ADDIS ABABA UNIVERSITY

ADDIS ABABA INSTITUTE OF TECHNOLOGY

SCHOOL OF CIVIL AND ENVIRONMENTAL ENGINEERING

Parametric Study on the Behavior of Eccentrically Braced Frame Links

A Thesis in Structural Engineering

By Abel Berhanemeskel

December, 2021

Addis Ababa

A Thesis

Submitted in Partial Fulfillment of the Requirements for the Degree of Master of Science

The undersigned have examined the thesis entitled '**Parametric Study on the Behavior of Eccentrically Braced Frame Links**' presented by **Abel Berhanemeskel**, a candidate for the degree of **Master of Science,** and hereby certify that it is worthy of acceptance.

Dr. Abrham Gebre		
Advisor	Signature	Date
Dr. Bedilu Habte		
Internal Examiner	Signature	Date
Dr. Shifferaw Taye		
External Examiner	Signature	Date
Dr. Ing. Mebruk Mohammed		
Chairperson	Signature	Date

UNDERTAKING

I certify that the research work titled "**Parametric Study on the Behavior of Eccentrically Braced Frame Links**" is my work. The work has not been presented elsewhere for assessment. When a material has been used from other sources it has been properly acknowledged and referenced.

Abel Berhanemeskel

ABSTRACT

Eccentrically Braced Frames (EBFs) link's behavior is affected by their link length, web/flange slenderness, stiffener spacing, stiffener cross-sectional behavior, and the axial load ratio present in the link. Even though various research has been conducted on the effect of these parameters on the link's behavior, a sensitivity analysis to determine which of these parameters is the most influential on the link's behavior has not been conducted. Additionally, most of the previous research conducted on EBF links was done using the American wide flange sections and not much research has been conducted using the European IPE sections. The purpose of this research is to conduct a parametric sensitivity analysis using nonlinear finite element analysis on the behavior of EBF links made up of European IPE sections subjected to cyclic loading. Latin hypercube sampling (LHS) method was employed to generate samples for the nonlinear finite element analysis. A total of 45 samples with 15 samples for each of the three link types (Short, Intermediate, and Long) was generated. From the nonlinear finite element analysis results, a sensitivity analysis was conducted using the differential sensitivity analysis method. From the sensitivity analysis, it was found out that short links plastic rotation capacity was the most influenced by axial load ratio and stiffener spacing, while their overstrength ratio was the most influenced by stiffener spacing and link length ratio. Short link energy dissipation capacity and ductility were the most influenced by axial load ratio, link length ratio, and stiffener spacing. Intermediate links plastic rotation capacity and ductility were the most influenced by stiffener spacing, axial load ratio, link length ratio, and flange slenderness the most. Intermediate links' overstrength ratio was the most influenced by stiffener spacing and link length ratio, while their energy dissipation capacity was the most influenced by stiffener spacing and flange slenderness. Long links' entire behavior was influenced by their flange slenderness and axial load ratio the most. It was also observed that tensile axial load increases the overstrength ratio in short links. The higher overall overstrength ratio observed for IPE sections in previous research was also observed in this research as well where most of the samples surpassed the seismic code recommended value of 1.5.

Keywords: Eccentrically braced frames, Links, axial load ratio, Link length ratio, Web slenderness, Flange slenderness, Stiffener spacing, Plastic rotation capacity, Overstrength ratio, Ductility, Energy dissipation capacity, Cyclic Loading

ACKNOWLEDGMENTS

First and foremost, I would like to thank my advisor, Dr. Abrham Gebre, for his encouragement and thoughtful guidance throughout this research. This research would not have been possible without his support, guidance, and patience.

Special thanks to the Ethiopian Road Authority for funding this research.

I would also like to thank ANSYS forum members and moderators for their quick and insightful responses to any question.

I am extremely grateful to my mother Etaferahu Fikreselassie for her support, love, prayers, sacrifices, and for educating and preparing me for my future. Last but not least I would like to thank my brother Tsega Fikreselassie, my friend Eyob Tariku, and my fellow graduate student Mahlet Wondwosen for their help and support.

TABLE OF CONTENTS

LIST OF TABLES

LIST OF FIGURES

NOTATIONS

a	Stiffener Spacing
A	Gross Cross-Sectional Area of a Member
A_f	Area of the Flange
A_w	Area of the Web
b	Width of Cross-Section
b_f	Width of the Flange
C_f	Compressed Width of Flange
C_w	Compressed Width of Web
d	Depth of Cross-Section
e	Link Length
E	Elastic Modulus of a Material
E^*	Energy Absorbed During the Half Cycle in Which Buckling Occurs
E_e	Elastic Energy Stored by a beam at Yield
f_y	Yield Strength
G	Shear Modulus of a Material
I	Moment of inertia of a Cross-Section
M	Flexural Moment
M_p	Plastic Moment Capacity
$M_{p,r}$	Reduced Plastic Moment Capacity
P	Axial Load
P_y	Axial Load Capacity
R	Eurocode Factor for Plastic Capacity Reduction due to Axial Load
t_f	Flange Thickness
t_w	Web Thickness
t_s	Stiffener Thickness
V	Shear Force
V_{Ed}	Design Shear Force
V_n	Nominal Shear Force
V_{max}	Maximum Link Shear Force
V_p	Plastic Shear Force Capacity

$V_{p,r}$	Reduced Plastic Shear Capacity
V_u	Ultimate Shear Force
ν	The ratio of Max Shear Force to 1.5 Times Plastic Shear Capacity
ν_{max}	Maximum Relative End Displacement
ν_y	Relative End Displacement at Yield
γ	Total Link Rotation
γ_p	Plastic Link Rotation
ν	Poisson's Ratio
Ω	Overstrength Ratio
ρ	Link Length Ratio
μ	Displacement Ductility
Δ_p	Plastic Drift
Θ_p	Plastic Drift Angle
σ	Stress Tensor
α	Back Stress Tensor
σ_s	Current Yield Stress
ε_p	Equivalent Yield Strain
$\mathbf{s}$	Deviatoric Stress Tensor
α^{dev}	Deviatoric Back Stress Tensor
C	Kinematic Hardening Modulus
γ	Parameters that determine Decrease in Kinematic Hardening
σ_0	Initial Yield Stress
R_∞	Saturation Stress
b	Material Constant in Voce Hardening Model

CHAPTER 1 INTRODUCTION

1.1 General

Eccentrically braced frames (EBFs), which combine high lateral stiffness and good ductility, are a preferred alternative to moment resisting frames (MRFs) and concentrically braced frames (CBFs) as seismic-resistant steel building systems. EBFs are braced frame systems distinguished by an eccentricity induced in the beam that isolates a segment of the beam known as the link. Figure 1.1(a) shows an EBF configuration with the link located at the center of the beam, between the two braces, and Figure 1.1(b) shows an EBF configuration where one end of the link is attached to a column. The link is important in the seismic performance of EBFs, as will be explained later.

Figure 1-1: Example of EBF Buildings

Eccentrically braced frames were proposed as seismic resisting steel systems in the 1970s in Japan to create a structure with high elastic stiffness and great energy dissipation during strong earthquakes (FUJIMOTO et al., 1972; Tanabashi et al., 1974). Roeder and Popov were the first to investigate the EBF system in the United States (1977). Numerous research on link behavior published in the 1980s shed light on the cyclic response of EBFs (Engelhardt & Popov, 1989; Hjelmstad & Popov, 1983b, 1984; K. Kasai & Popov, 1986; Kazuhiko Kasai & Popov, 1986a; Malley & Popov, 1984; Daniel N. Manheim & Popov, 1983). In the mid-to-late-1980s, experimental verifications of EBF response at the system level were also carried out (Roeder, 1977; Whittaker et al., 1989).

EBFs can be considered as a hybrid system between moment resisting frames (MRFs) and Concentrically Braced Frames (CBFs). They have the stable cyclic behavior of MRFs and the high lateral stiffness of CBFs. EBFs combine the best features of MRFs and CBFs. Even though MRFs display a stable hysteretic behavior without pinching or strength degradation if properly designed, it is often necessary to use a section bigger than required for strength to satisfy drift requirements. While CBFs show pinching and strength degradation with limited energy dissipation capacity. EBFs can be proportioned to balance stiffness and ductility, by preserving the frame stiffness similar to that of CBFs, while selecting a reasonable link length to dissipate seismic energy efficiently.

In EBF the ductility of the link beam is crucial to the ductile performance of the EBF. To enable large rotations or deformations in the links without severe strength degradation the links should be designed and proportioned to delay any premature local buckling, fracture, and lateral-torsional buckling. The links also limit the force that develops in the adjoining members such as columns, braces, and the beam outside of the link.

By bending and shear in the link, EBFs convey the axial load produced in the diagonal brace to the column or another brace. In EBF, inelastic deformation is limited to the link beam, while all other frame components are intended to be elastic.

The behavior and performance of EBF links are affected by different parameters such as stiffener spacing, web and flange slenderness, presence and amount of axial load, loading history, link length, presence of composite slabs, connection types, and others. The most relevant topics are discussed in the next chapter.

In addition to the above experimental investigations mentioned above, several numerical simulations using shell and solid elements have been conducted on EBF links and frames. Various researchers (Berman et al., 2010; Chao et al., 2006; Daneshmand & Hosseini Hashemi, 2012; Della Corte et al., 2013; Kanvinde et al., 2015; Mohebkhah & Chegeni, 2014; Ramadan & Ghobarah, 1991; Paul W. Richards & Uang, 2005) have conducted a numerical study on isolated links. While a numerical study using a portal frame and frame sub-assemblage has been conducted by other researchers (Dusicka et al., 2004; Hong et al., 2015; Imani & Bruneau, 2015; Pirmoz et al., 2016; Prinz & Richards, 2009; Yiğitsoy et al., 2014).

1.2 Problem Statement

Eccentrically Braced Frames (EBFs) link's behavior is affected by their link length, web/flange slenderness, stiffener spacing, stiffener cross-sectional behavior, and the axial load ratio present in the link. Even though various research has been conducted on the effect of these parameters on the link's behavior, a sensitivity analysis to determine which of these parameters is the most influential on the link's behavior has not been conducted. Additionally, most of the previous research conducted on EBF links was done using the American wide flange sections and not much research has been conducted using the European IPE sections. The purpose of this research is to conduct a parametric sensitivity analysis using nonlinear finite element analysis on the behavior of EBF links made up of European IPE sections subjected to cyclic loading.

1.3 The objective of the Study

General Objective

- To perform a parametric sensitivity analysis on the behavior of links using European IPE Sections.
- To evaluate the cyclic response and failure mechanism of EBF links under the varying parameters

Specific Objective

- To conduct a 3D nonlinear finite element analysis of isolated links made up of European IPE sections subjected to cyclic loading.
- To conduct a sensitivity analysis to determine which parameters affect the EBF link's overstrength factor, energy dissipation capacity, inelastic rotation capacity, and ductility the most.
- To evaluate the driving failure mechanism under the different parameters and provide an insight

1.4 Scope of the Study

- No laboratory experiments were conducted only finite element analysis was used.
- Material damage models were not incorporated into the finite element model.
- Composite slabs were not modeled thus their contribution to the link's behavior is not considered.
- Only S-355 steel is considered in this paper.
- Since the finite element simulation is conducted on an isolated link beam the effect of other members on link behavior is not considered.
- Initial imperfection and residual stress are not considered.

1.5 Methodology

A 3D nonlinear finite element analysis using the general-purpose finite element software package ANSYS 2021 R2 was conducted. 15 samples for each of the 3 link length types (Short, Intermediate, and Long) were generated using the Latin hypercube sampling method. Link length ratio, axial load ratio, flange/web slenderness, stiffener spacing constant C_B, and stiffener thickness multiplier were the parameters used in this study. Model validation was done using previous experimental data.

Following this, a sensitivity analysis was conducted to determine the effect of each parameter on the inelastic rotation capacity, overstrength ratio, ductility, and energy dissipation capacity of the link.

1.6 Organization of the Thesis

To achieve the aforementioned objective, a thorough relevant literature review was undertaken, followed by finite element analysis and sensitivity analysis.

Chapter 2 of this thesis is a comprehensive look at previous literature on EBF links. Emphasis is put on the relevant studies that were done on the parameters chosen for this study. The review is compiled and evaluated to offer a comprehensive overview of the research program.

Chapter 3 reviews the material model, test setup boundary condition, and other relevant information used in validating the finite element model. It also compares the finite element model to the experimental model and reviews its accuracy in predicting the actual behavior.

Chapter 4 presents the parametric study. The sampling method, the material property used in the finite element simulation, boundary conditions, and other relevant information will be discussed.

Chapter 5 presents the finite element simulation results and discusses the failure methods and any notable things observed during the simulation.

Chapter 6 uses the results from the finite element simulation for the sensitivity analysis. The sensitivity analysis method and its result will be discussed in this chapter.

Chapter 7 summarizes the findings of the research. The literature review and finite element's key observations and discussions are compiled. Finally, recommendations are made, as well as suggestions for further study.

CHAPTER 2 LITERATURE REVIEW

2.1 Introduction

Eccentrically braced frames (EBFs) are braced frame systems where an eccentricity is introduced between two adjacent brace-to-beam connections, or between adjacent brace-to-beam connections and beam-to-column connections. The beam that is created by the eccentricity between the braces or between a brace and a column is referred to as the link. There are several EBF arrangements and some of them are shown in Figure 2-1 below and the links are designated by their length e. EBFs are an attractive architectural option since they don't restrict the placement of doors and windows as much as the widely used concentrically braced frames.

EBFs transmit the axial load that is developed in the diagonal brace to the column or another brace by bending and shear in the link. In EBF inelastic deformation is concentrated at the link beam only and all other members of the frame are designed to remain essentially elastic.

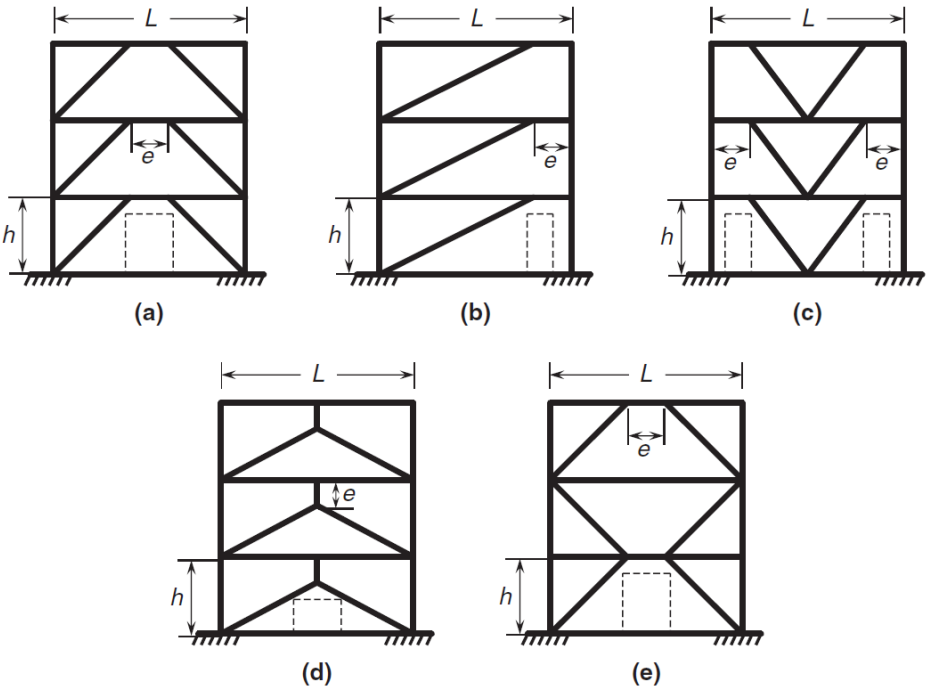

Figure 2-1: Typical EBF arrangements

In EBF the ductility of the link beam is crucial to the ductile performance of the EBF. To enable large rotations or deformations in the links without severe strength degradation the links should be designed and proportioned to delay any premature local buckling, fracture, and lateral-torsional buckling. The links also limit the force that develops in the adjoining members such as columns, braces, and the beam outside of the link.

2.2 Link Characteristics

2.2.1 Yield Behavior

One of the main factors that determine the stiffness, strength, ductility, and behavior of an EBF system is the length of a link segment e. The link length which controls the plastic mechanism is the ratio of the plastic bending moment to the plastic shear of the link's cross-section. The link length ratio which also offers a simple measure of yield behavior is defined as follows

$$\rho = \frac{e}{M_p / V_p} \tag{2.1}$$

Where M_P and V_P are the plastic moment and plastic shear capacity of the link respectively. For I sections they are calculated as follows

$$M_p = f_y b t_f \left(d - t_f\right) \tag{2.2}$$

$$V_p = \left(f_y / \sqrt{3}\right) t_w \left(d - t_f\right) \tag{2.3}$$

In the above equation, f_y is the yield strength of the steel, while *b, d,* t_w*, and* t_f are the depth of the cross-section, the width of the cross-section, the thickness of the web, and thickness of the flange respectively.

Typical force distribution for two types of EBF configuration is shown in Figure 2-2. The force in an EBF link is characterized by constant shear, V, along its length, reverse curvature bending, M, and typically a small axial force, N. The end moments are equal for EBF configuration a and e in Figure 2-1, while EBF configuration b, c, and d have unequal end moments as a result of the stiffness difference between the column at one

end and the beam brace connection at the other. The EBF configuration with unequal end restraints will be discussed later.

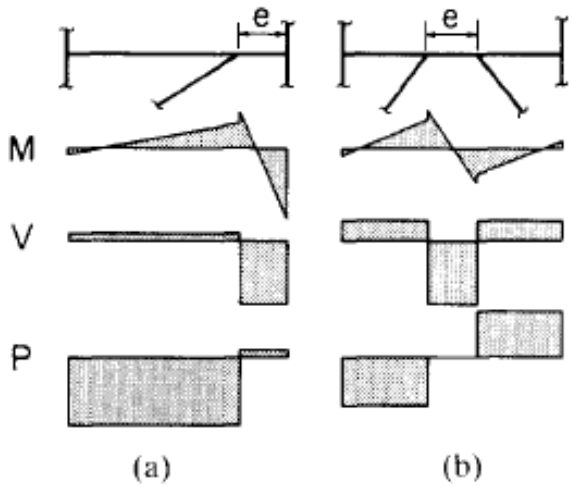

Figure 2-2: An EBF's Typical Force Distribution

The free-body diagram of an isolated link is shown in Figure 2-3. Considering equal end moments based on equilibrium at the ultimate state with negligible axial load the static equilibrium of the link reduces to the expression in equation (2.4). For elastic-perfectly plastic material with no moment-shear interaction, the theoretical dividing link length ratio between shear and flexure dominated behavior is $\rho = 2.0$. A shear hinge will form when $\rho \leq 2$. While a flexural (or moment) hinge forms at both ends of the link when $\rho > 2$.

$$Ve = 2M \tag{2.4}$$

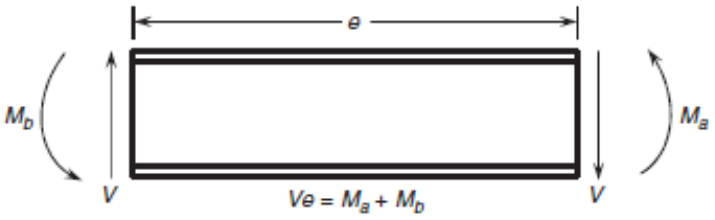

Figure 2-3: Free Body Diagram of Link

The above no-moment-shear interaction assumption is based on experimental results that revealed the moment-shear interaction to be weak for short links and that it may be ignored (Kazuhiko Kasai & Popov, 1986b). Figure 2-4 shows the M-V interaction surface recorded in the experiments with other plastic theory models for M-V interaction.

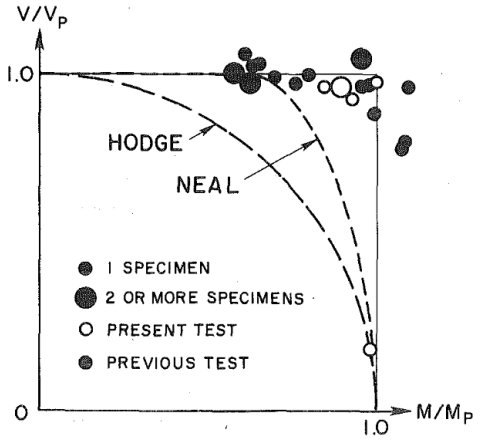

Figure 2-4: M-V Interaction of Links

A suitably stiffened short link may also strain harden and generate a shear strength of $1.5V_p$, according to test data. Due to this strain hardening, the end moments of a link that has yielded in shear might continue to grow, and flexural hinges can form. These end moments are limited to $1.2M_p$, to avoid excessive bending stresses that might cause severe flange buckling or failure of link flange-to-column welds. Therefore, taking these considerations into equation (2.4) the link must adhere to the following length restriction to ensure shear yielding behavior (Kazuhiko Kasai & Popov, 1986a).

$$e \le 1.6 \frac{M_p}{V_p} \qquad \text{or} \qquad \rho \le 1.6 \tag{2.5}$$

There are significant variations in how short and long Links behave. Although longer links allow for greater architectural flexibility with openings, early experimental investigations by Roeder and Popov (Roeder, 1977) and Hjelmstad and Popov (Hjelmstad & Popov, 1983b, 1983a) demonstrated that short links outperform long links in terms of strength and ductility under severe cyclic loadings.

Engelhardt and Popov conducted the first thorough investigation on the behavior of intermediate and long links (ρ >1.6) (Engelhardt & Popov, 1989). The report was an experimental investigation on fourteen 2/3 scale sub assemblages with ρ ranging from 1.45 to 4.25 subjected to cyclic loads. Based on the result the report concluded Shear dominates the inelastic behavior of short links while flexure dominates for very long links. The transition zone between short and long links with intermediate length is significantly affected by both shear and flexure in the inelastic range. In addition to the varying yielding mechanisms, the behavior of short and very long links is distinguished by unique inelastic rotation capabilities and failure mechanisms, with intermediate length links serving as a transition. based on the results Links may be classified into three length groups more organically as follows

$$\text{Short Links:} \quad e \leq 1.6 M_P / V_P \tag{2.6}$$

$$\text{Intermediate Links:} \quad 1.6 M_P / V_P < e \leq 3 M_P / V_P \tag{2.7}$$

$$\text{Long Links:} \quad e > 3 M_P / V_P \tag{2.8}$$

The above link length classification has been adopted into the European and the Ethiopian seismic codes (EBCS EN 1998-1:2014, 2014; EN 1998-1:2004, 2004). The American seismic code (AISC 341-16, 2016) uses the same length specification for Short links but the intermediate-range becomes $1.6 < \rho \leq 2.6$, and the long links are defined by $\rho > 2.6$. High axial loads modify the above categorization and it will be discussed later.

Engelhardt and Popov also reported that intermediate links behavior is affected by moment-shear interaction while long and short links are generally unaffected (Engelhardt & Popov, 1989).

Very short links ($\rho < 1$) were investigated by Ji and Wang where 12 cyclic load tests on shear links with link length ratio ranging from 0.58 to 0.97 (Ji et al., 2016a). Based on the experiment very short links exhibited large inelastic rotation capacity and a higher overstrength ratio than short links.

2.2.2 Shear Capacity and Overstrength

A sensible approximation of the shear force and end moments that develop in the EBF link during intense loading is necessary to achieve the objective of the capacity design

procedure. An underestimation of the developed link forces in the links leads to the untimely failure of the members outside of the link. A properly designed link can achieve a high amount of inelastic deformation and develop a significant level of strain hardening. The strain hardening is accounted for in design codes by the overstrength factor. The overstrength factor is the ratio between the maximum link shear force (V_{max}) to the nominal shear capacity of the link. The nominal shear capacity (V_n) of a link is defined as follows

$$V_n = \min\left[V_P, 2M_P/e\right] \tag{2.9}$$

$$\Omega = V_{max}/V_n \tag{2.10}$$

In early tests, Popov and his colleagues recommended the value of Ω = 1.5 for design purposes (Engelhardt & Popov, 1989; Hjelmstad & Popov, 1983b; K. Kasai & Popov, 1986; Roeder, 1977; Uang & Bertero, 1986), and this value is still (implicitly) used in most seismic design codes to this day.

Figure 2-5 shows the link overstrength observed in prior experimental research on horizontal I-shaped links (Dusicka et al., 2010; Engelhardt & Popov, 1989; K. Kasai & Popov, 1986; McDaniel et al., 2003; Okazaki, 2004; Okazaki et al., 2005b, 2009; Okazaki & Engelhardt, 2007; Popov, 1983; Roeder, 1977). The conventional Ω = 1.5 line is also included in this diagram. The picture only shows cyclic test results for links with f_y > 200 MPa.

As shown in Figure 2.5, a value of Ω =1.5 appears to be an acceptable upper bound for links with ρ > 1. However, for some intermediate links, this overstrength value overestimates V_{max}, whereas, for very short links (ρ < 1), it severely underestimates V_{max}. These differences have various causes, which can be described as follows.

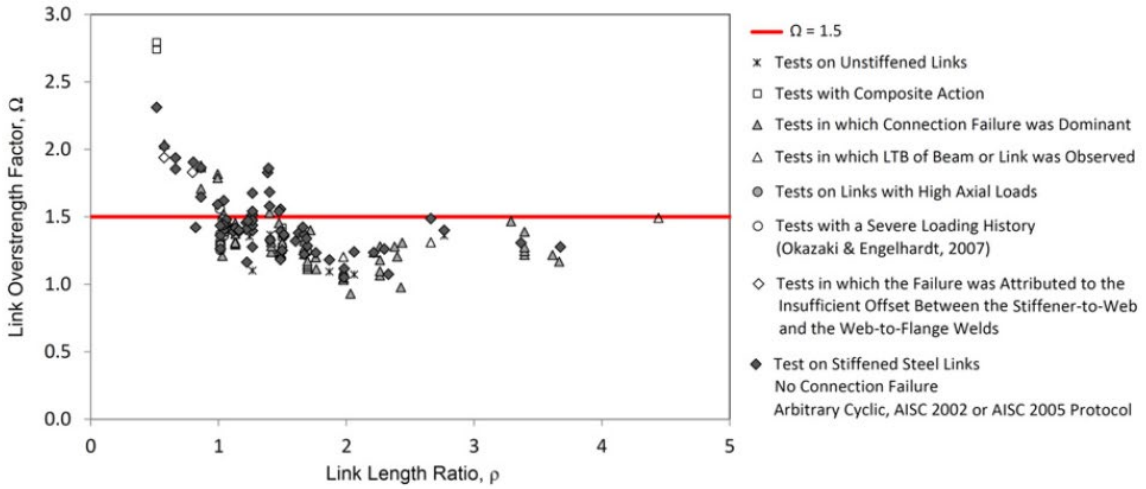

Figure 2-5: M-V Overstrength factors observed in several experimental investigations

The impact of moment-shear (M-V) interaction is ignored while using a constant value of 1.5 for the overstrength factor. However, Engelhardt and Popov (Engelhardt & Popov, 1989) demonstrated that this interaction can be significant for intermediate links where values of Ω less than 1.5 were observed. The effect of moment shear interaction can be best described by Figure 2-6, where maximum shear V_{max} normalized by the plastic shear capacity V_p is plotted against the link length ratio. In the figure, two lines representing the constant overstrength factor of 1.5 and the overstrength calculated based on the theoretical link strength proposed by Engelhardt and Popov (Engelhardt & Popov, 1989) are plotted. Comparisons of the two models show that the overstrength calculated using the theoretical link strength integrating shear-moment interaction yields a superior estimate compared to the constant 1.5 overstrength factor. The lines are plotted according to the following equations

Engelhardt and Popov Moment-shear interaction

$$v = 1 \qquad 0 \le \rho \le 4/3 \qquad (2.11)$$

$$\left(\frac{3\rho v - 4}{2}\right)\sqrt{1 - v^2} + v^2 = 1 \qquad \rho \ge 4/3 \qquad (2.12)$$

Where,

$$v = \frac{V_{\max}}{1.5V_P} \qquad (2.13)$$

For the constant overstrength ratio of 1.5

$$\frac{V_{max}}{V_P} = 1.5 \qquad 0 \le \rho \le 2 \qquad (2.14)$$

$$\frac{V_{max}}{V_P} = \frac{3}{\rho} \qquad \rho \ge 2 \qquad (2.15)$$

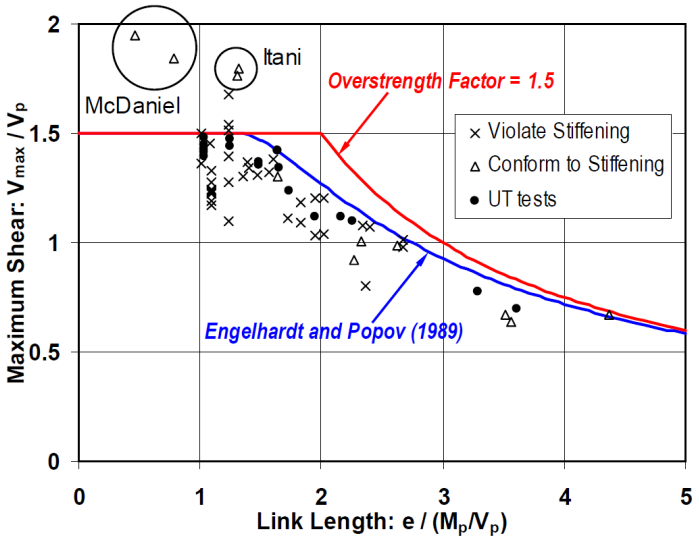

Figure 2-6: Link Overstrength vs Link Length Ratio

Short links nominal shear capacity is often estimated based on the web area, with the flanges' contribution ignored. However, as McDaniel (McDaniel et al., 2003) pointed out, there is substantial shear stress carried by the flanges in short links with relatively thick flanges. Methods for calculating the link plastic shear capacity while incorporating the flange effect have been presented by Manheim, Popov and, Richards (Daniel N. Manheim & Popov, 1983; P.W. Richards, 2004). Richards proved, using a nonlinear FE analysis of isolated links, that the over-strength factor of 1.5 is a realistic limit even for extremely short links when the flange effect is taken into account while estimating V_P. When earlier test findings on short and very short built-up links were evaluated by incorporating flange contribution to the shear capacity, the same conclusion was not found. The computed overstrength for these links fell marginally, but they were still substantially greater than 1.5 in most situations. Okazaki and Engelhardt (Okazaki & Engelhardt, 2007) published the test findings for a total of 37 ASTM A992 steel links the

tested links had a high flange to web area (A_f/A_w) ratios but they did not show overstrength above 1.5. Other recent findings (Ji et al., 2016a), on the other hand, suggested that extremely short links with even smaller flange to web area ratios may reach astonishingly high overstrength, in some cases exceeding 2.0. Ji's subsequent numerical study indicated that the shear contribution of flanges in the tested specimens may be as high as $0.2V_P$. Other variables, in addition to the flange effect, were shown to be important in producing the observed significant overstrength. As a result, it is concluded that computational and experimental research on the contribution of flanges to link overstrength is inconclusive.

Due to nonlinear geometric effects tension can occur (especially at high rotations) during shearing if axial restraints are present at the link ends. Della Corte (Della Corte et al., 2013) used comprehensive FE studies to explore this critical problem, which took into account both geometric and material nonlinearities. Based on the numerical findings, it was shown that the inclusion of axial restraints can considerably increase the overstrength (up to 15% in some models), especially for shorter links.

Excessive cyclic hardening of steel owing to very large plastic strains is another possible explanation for the extremely high overstrength reported in some experiments. It was recently proposed that very short links reported high overstrength is related to their high inelastic rotation capacity (Ji et al., 2016a). Ji et al. hypothesized that since high plastic rotation is experienced by very short links (substantially higher than 0.08 rad) subsequently their webs are exposed to high shear strains which may lead to high cyclic hardening. A finite element study on very short links was conducted by Ji et al. and it was discovered that the cyclic hardening effect can enhance shear strength by roughly 70% for a link plastic rotation of 0.15 rad.

2.2.3 Link Rotation Capacity and Demand

Figure 2-7 depicts the predicted plastic mechanisms of the split D and Split V type EBF systems. The total link rotation angle which is designated by γ is the angle between the link and the beam outside of the link, while γ_p shown in the figure is the inelastic/plastic link rotation angle (which is the total link rotation minus the elastic portion). In general, a link's plastic rotation capacity, γ_p^{max}, is defined as the link's maximum plastic rotation angle sustained during a cyclic test, for at least one full cycle of loading, before the shear

resisted by the link drops below 80% of the maximum link shear measured throughout the cyclic test. The plastic rotation capacity calculation method is shown in Figure 2-8.

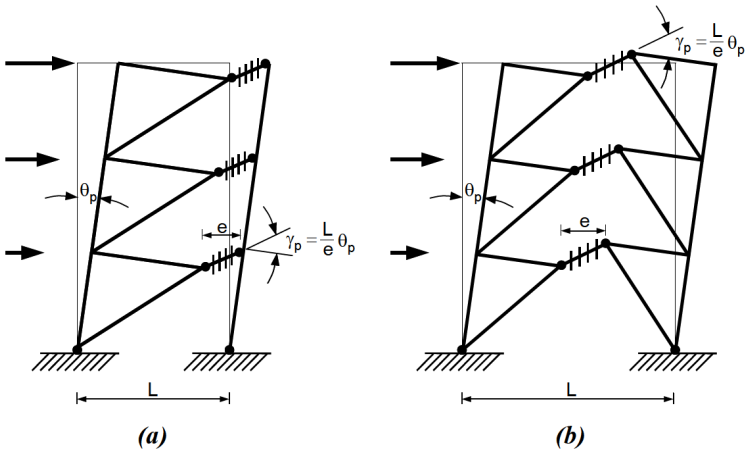

Figure 2-7: Energy Dissipation Mechanisms

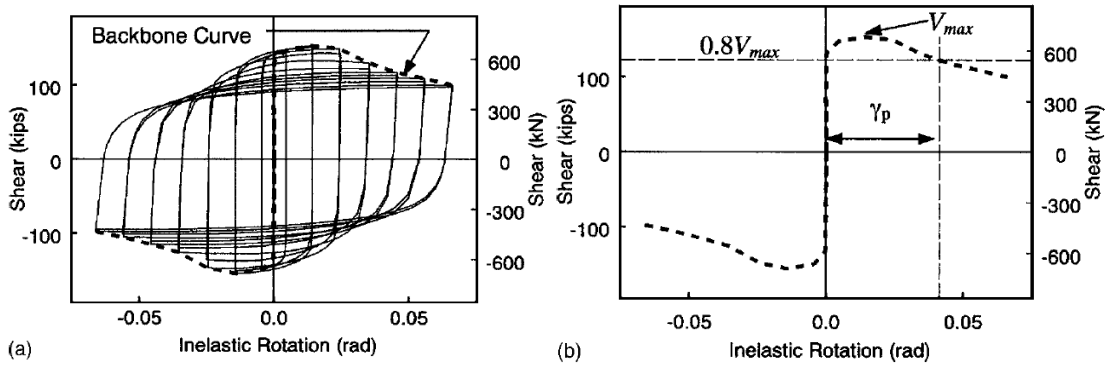

Figure 2-8: Plastic Rotation Angle Calculation (Paul W. Richards & Uang, 2005)

Experiments have revealed that various parameters, such as the link length ratio, loading history, compactness, and web stiffening, have a substantial impact on the rotation capacity of links. A summary of previous experiments on links plastic rotation capacity plotted against link length ratio as presented in a paper by Okazaki (Okazaki, 2004) is shown in Figure 2-9. In the figure tests that were affected by premature link end connection fracture or the presence of axial force were excluded. Monotonic loading experiments were also left out. It should be mentioned here that monotonic tests exhibit a higher plastic rotation capacity sometimes in an order of two times the cyclic plastic rotation capacity. From the figure, it can be seen that short links have a higher link rotation capacity compared to intermediate and long links. The Ethiopian and European

codes (EBCS EN 1998-1:2014, 2014; EN 1998-1:2004, 2004) specify a design limit based on the above-discussed experiments. The limit is defined as 0.08 rad for short links, 0.02 rad for long links while for intermediate links the inelastic rotation limit is calculated using interpolation between the 0.02 rad and 0.08rad based on their link length ratio. The AISC code (AISC 341-16, 2016) inelastic rotation limit is shown by the red line in Figure2-8.

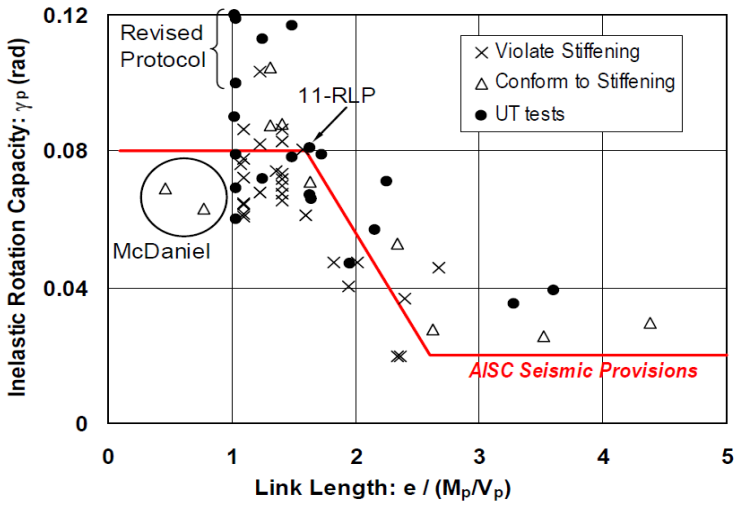

Figure 2-9: Link Rotation Capacity (Okazaki, 2004)

At the design stage, the inelastic link rotation demand must be calculated. Inelastic dynamic analysis is the most accurate method for finding this value. A rigid plastic mechanism as the one shown in Figure 2-7 can be used to calculate the inelastic link rotation angle instead. The inelastic link rotation angle, γ_p, is linked to the plastic story drift, Δ_p ($\Delta_p = \Theta_p H$), using geometrical relationships and the relationship is shown in Figure 2-7. Koboevic et al. (Koboevic et al., 2012; Koboevic & David, 2010) conducted extensive nonlinear time-history studies on low, mid, and high-rise EBFs, which further proved the validity of assuming such a relationship. However, Koboevic et al. and other recent research(Koboevic et al., 2012; Koboevic & David, 2010) have found that calculating Δ_p based on elastic analysis results utilizing the coded displacement amplification factors or the equal-displacement rule can provide unconservative estimates of γ_p.

In Figure 2-8 some link rotation capacities fail well below the required rotation demand and others especially very short links far exceeded the required/code specified inelastic rotation limit. These findings, especially those published by (Dusicka et al., 2010; Ji et al., 2016b), showed that the rotation capacity of very short links might be significantly greater than that of short links. As McDaniel and his colleagues (McDaniel et al., 2003) describe, several of the tested very short links failed early owing to brittle fracture of the web of the link, which was triggered by an inadequate offset between the stiffener-to-web and web-to-flange welds. Okazaki and Engelhardt (Okazaki & Engelhardt, 2007), Pedro Galvez (Gálvez, 2004), and others reported that the measured rotation capacity which falls substantially below the code stated limit was due to the use of a severe loading protocol.

2.2.4 Effect of Cyclic Loading Protocol

Popov and his colleagues (Hjelmstad & Popov, 1983b; Popov, 1983) observed that loading protocol has a significant effect on the recorded inelastic rotation capacity of EBF links during experimental study. A broad study on this effect was conducted by Richards and Uang (Paul W. Richards & Uang, 2004, 2006).

Unexpected link web fractures were reported by Okazaki and his colleagues (Okazaki et al., 2005a) for several short links before reaching the code specified inelastic rotation demand of 0.08 rad. Richards and Uang (Paul W. Richards & Uang, 2004, 2006) attributed the issue of web fractures to the loading protocol used by Okazaki. The loading protocol used by Okazaki was based on Appendix S of AISC 341-02 (AISC 341-02, 2002) which is derived from the standard moment frame loading protocol. Richards and Uang conducted a nonlinear time history analysis on 3 prototype EBF structures exposed to 20 large-magnitude-small-distance Los Angeles ground motions. The obtained cumulative and maximum link rotation demands were used to come up with a new protocol which was ultimately adopted by AISC 341-05 (AISC 341-05, 2005) for the cyclic testing of link-to-column connections. The proposed new loading protocol has fewer cycles with large rotations compared to the old loading protocol. Furthermore, the new loading protocol is a more sensible representation of seismic demands.

Okazaki et al. used the newly proposed loading protocol to retest the specimens that failed to meet the code-specified plastic rotation limit. The rotation capacities of all the retested specimens were higher than the code-specified limit, with an average increase of

52% in γ_P. Further research by Okazaki and his colleagues (Okazaki et al., 2009; Okazaki & Engelhardt, 2007) supported the conclusion that the previous loading protocol for shear links is excessively demanding when compared to the updated loading protocol.

If the new loading protocol is employed to test intermediate and long links, a slight rise in γ_P for intermediate links and a small drop in γ_P for long links may be seen, according to Richards (Paul W Richards, 2004). The cyclic demand exerted on moment(long) links by both the old and the new loading protocol is comparable, according to Okazaki and his colleagues (Okazaki et al., 2005a). Several experimental and numerical investigations on intermediate and long connections employed the new loading protocol. Daneshmand and Hashemi (Daneshmand & Hosseini Hashemi, 2012) proved the sensitivity of intermediate link rotation capacity to the loading protocol used. Based on the results of a nonlinear FE analysis when an intermediate link was loaded by the old loading protocol instead of the newly revised loading protocol, the value of γ_P decreased by 18%. The old and new loading protocols are shown in Table 2-1 below.

Table 2-1: Loading Protocols

(a) AISC Protocol	
Amplitude: γ (rad)	Number of cycles
0.0025	3
0.005	3
0.01	3
0.02	2
0.03	2
0.04	2
0.05	2
0.06	2
0.07	2
Continued at increments of 0.01 rad with two cycles at each amplitude	

(b) Revised Protocol	
Amplitude: γ (rad)	Number of cycles
0.00375	6
0.005	6
0.0075	6
0.01	6
0.015	4
0.02	2
0.03	2
0.04	1
0.05	1
Continued at increments of 0.02 rad with one cycle at each amplitude	

2.2.5 Effect of Composite Slab

Ricles and Popov (Popov & Ricles, 1989) studied the impact of a concrete slab put over a steel frame as a floor system on EBF links. The stiffness and strength of the composite links were initially stronger than those of the bare steel links, but the composite action degraded in subsequent cycles. The maximum shear forces that the composite link could withstand were 1 to 13% greater than those for the bare steel links. However, the hysteretic behavior was similar to that of naked steel links with the slab damage concentrated at the link section while no damage was seen outside of the link section.

In their experimental investigation, Engelhardt and Popov (Engelhardt & Popov, 1989; Popov & Ricles, 1989) found that if a diagonal brace is attached to the bottom flange of a link, the presence of a concrete slab can significantly improve the link's stability by constraining the top flange. During experiments on large EBF sub-assemblages done at National Taiwan University (Tsai et al., 1993) made a similar observation.

Mansour and his colleagues (Mansour et al., 2011) also looked at how a concrete slab affected link behavior. The replaceable link section had a smaller depth than the floor beam in the details examined. As a result, the link and the composite slab had no direct interaction. Despite this, the specimen with the concrete slab was found to have a greater shear force, 14% higher than the bare steel specimen, with no discernible difference in link rotation capacity.

2.2.6 Effect of Axial Load

The axial force in links is generally minimal if links are correctly positioned within EBFs, but some configurations can result in a considerable axial load in the links. The axial restraining effect of neighboring members, as well as the loading scheme and/or geometry of a structural system, can subject links to axial loads. In the event of seismic loading, for example, the EBF configuration shown in Figure 2-1(b) will impose more axial forces on link segments than the insignificant link axial forces generated in the arrangement shown in Figure 2-1(a).

Kasai and Popov (Kazuhiko Kasai & Popov, 1986b) demonstrated that the presence of axial force can have a degrading effect on link behavior. In the presence of axial force, these researchers presented new expressions for the plastic moment and shear capacity of links. A modified shear link length limit was also specified. The modified capacity is

usually connected to the axial load ratio P/P_y, where P is the applied axial force and P_y is the nominal axial yield strength. This work has shown that, when this proportion surpasses 0.15, plastic capacities must be decreased according to P/P_y.

In 1990, Ghobarah and Ramadan (Ghobarah & Ramadan, 1990) analyzed the influence of the axial force on the performance of the EBF links with a nonlinear FE analysis. Numerical results show that the presence of the axial force affects not only the plastic strength of the link but also its plastic rotation capacity and energy dissipation. The highest reduction in γ_P was found to be 37%. It was also discovered that the influence of axial force is most noticeable in links with a link length ratio close to 1.6.

Mansour and his colleagues (Mansour et al., 2011) studied the behavior of replaceable shear links inside a frame system. During these tests, cyclic loading was applied to the floor beam from one end, transferring half of the applied force axially across the link. The greatest value of P/P_y recorded was 0.26, indicating a reasonably high axial force level. Mansour discovered that when the links were exposed to tension rather than compression, the peak shear forces were greater, with a maximum difference of 12% (Mansour, 2010). In his dissertation, Mansour also quantitatively illustrated this issue and presented a simple equation for calculating the increase in shear capacity owing to axial stress.

Dastmalchi (Dastmalchi, 2014) performed non-linear time-history analyses of a three-story, eccentric brace construction comparable to the one in Figure 2-1(c). The results showed that the peak value of P/P_y measured for the links surpassed 0.15 by a considerable margin in most earthquake recordings, indicating a high chance of significant axial forces occurring in shear links with the chosen configuration. Dastmalchi also conducted nonlinear FE studies to investigate the behavior of Shear links under extremely high axial forces ($0.15 < P/P_y < 0.5$). The monotonic and cyclic shearing of short links under continuous axial compression showed its adverse influence on the shear strength and ductility of short links, especially when the length of the shear link was increased. It was also discovered that the shear capacity formula published in AISC 341-10 (AISC 341-10, 2010) understates this impact for $P/P_y < 0.2$, thus a numerically calibrated modification factor was included for this formula.

It should be noted that the effect of high axial force on the behavior of long and intermediate links has not been properly studied. As a result, if links have a large axial force, it is recommended to use a short link by many codes. The Ethiopian seismic code (EBCS EN 1998-1:2014, 2014) uses the following expression for link length limit and shear and moment capacity reduction for links with $P/P_y > 0.15$.

$$V_{P,r} = V_P \sqrt{1- \left(P / P_y\right)^2} \tag{2.16}$$

$$M_{P,r} = M_P \left(1- \left(P / P_y\right)\right) \tag{2.17}$$

If $P/P_y \geq 0.15$, the link length "e" should not exceed:

$$e \leq 1.6\, M_P/V_P \qquad \text{when } R < 0.3 \tag{2.18}$$

$$e \leq (1.15 - 0.5\, R)\, 1.6\, M_P/V_P \qquad \text{when } R \geq 0.3 \tag{2.19}$$

Where,

$$R = P\, t_w\, (d - 2t_f)/(V_{Ed}/A) \tag{2.20}$$

In the above expression, V_{Ed} and A are the design shear force and the gross cross-sectional area respectively.

2.2.7 Effect of Unequal End Moments

EBF configuration with links connected to columns, such as types (a) and (c) shown in Figure 2-1, the rotational restraint of the link is generally considerably larger at the column end than at the beam-brace end, resulting in unequal link end moments as shown in Figure 2-2.

As the link goes through large inelastic deformation the end moments tend to equalize. However, in some cases, the link may approach its shear or flexural capacity before reaching full moment equalization. The assumption of moment equalization in such circumstances might lead to an underestimation of design link moments.

The impact of unequal end restraints was studied by Kasai and Popov (K. Kasai & Popov, 1986; Kazuhiko Kasai & Popov, 1986b). Shear link specimens with link length ratios ρ = 1.08, 1.36, and 1.64 were evaluated in a test configuration that applied more rotational restraint at one end of the link than the other. The originally unequal end

moment in the ρ =1.08 link remained unequal throughout the loading history until the link failed. In the links with link length ratio ρ = 1.36 and ρ = 1.64, full moment equalization was accomplished. In all cases, the link moments at both ends were roughly bounded at M_p. The unequal end restraints had minimal influence on the shear links' overall behavior and rotation capacity.

Ricles and Popov (Ricles & Popov, 1987) discovered that links with ρ = 1.4 and unequal end restraints could not achieve moment equalization. Engelhardt and Popov (Engelhardt & Popov, 1989) reported that moment equalization may not be accomplished in links of any length connected to columns for the direction of loading that causes compression in the beam segment outside of the link. Even in the absence of instability, large compression in the beam may reduce its flexural rigidity. The beam with reduced stiffness attracts less moment from the column end to the beam end of the connection, preventing moment equalization. It was advised that, as a result of this process, the moment at the column end might be more than would be predicted from assuming complete moment equalization, putting additional strain on the link-to-column connection. Significant yielding and instability in the beam lead to a considerable loss of stiffness at the beam end of the connection and prevent moment equalization.

2.3 Link Detailing

2.3.1 Web and Flange Slenderness/Compactness

The slenderness limit of the link flange is required to avoid severe degradation of strength during heavy loads due to local buckling of the flange. Kasai and Popov (Kazuhiko Kasai & Popov, 1986b) calculated the link flange stress and related moments under the 1.5 V_P shear limit for 156 links with four different yield stresses and two link length ratio, ρ = 1.6 (short) and ρ = 2 (intermediate), with and without axial force. The maximum stress obtained in the flange is compared with the conservative critical plastic buckling stress determined based on Haaijer's method. Kasai and Popov did not detect buckling of the link flange with ρ = 1.6 when the link flange slenderness (ie, $b_f / 2t_f$) was limited to $0.38\sqrt{E/F_y}$, and there was no axial force, where b_f and t_f are flange width and thickness respectively while E is the elastic modulus of the steel and F_y is the yield strength of the steel. However, if these links are subjected to axial forces, a strict flange slenderness limit of $0.3\sqrt{E/F_y}$ is recommended to prevent flange buckling. On the other

hand, some intermediate links with ρ = 2 are prone to flange buckling even if the flange slenderness is kept below the stricter limit of $0.3\sqrt{E/F_y}$, particularly when they're subjected to axial force. Based on these, it is recommended to limit the flange slenderness of the link to $0.3\sqrt{E/F_y}$. This restriction was adopted by the earlier EBF codes.

Using the flange Slenderness limit of $0.3\sqrt{E/F_y}$ excludes many proficient wide-flanged sections constructed from A992 steel from being utilized as links. Trying to satisfy the flange slenderness limit leads to selecting larger sections but this is not efficient from a capacity design point of view. Richards and Uang (Paul W. Richards & Uang, 2005) carried out a comprehensive numerical study to further investigate this problem. A total of 112 models of isolated I-shaped links with various flange slenderness were analyzed. The numerical results show that the flange slenderness limit can be relaxed from $0.3\sqrt{E/F_y}$ to $0.38\sqrt{E/F_y}$. Although some intermediate links couldn't reach the required link inelastic rotation capacity, this problem was related to the requirements of the web stiffener spacing, not the slenderness of the flange.

Okazaki and his colleagues (Okazaki et al., 2005a; Okazaki & Engelhardt, 2007) subsequently conducted experimental studies on wide flange links made of A992 steel, which confirmed that relaxation of the flange slenderness limit proposed by Richards and Uang can be safely applied to the short links. However, they also observed that the strength of some intermediate links samples was reduced due to flange buckling. Taking into consideration the above research the AISC 314-05 (AISC 341-05, 2005) relaxed the flange slenderness ratio to $0.38\sqrt{E/F_y}$ for shear yielding links (ρ < 1.6). It should be mentioned here that in both the numerical study by Richards and Uang and the experimental study by Okazaki and his colleagues no axial force was imposed on the links.

Generally, compact webs are used in links to prevent or delay the deteriorating effects of web buckling. The European and Ethiopian seismic codes (EBCS EN 1998-1:2014, 2014; EN 1998-1:2004, 2004) do not give a specific web or flange slenderness limit for EBF links but they require all seismic yielding members to be class 1.

2.3.2 Link Transverse Stiffeners

End and intermediate web stiffeners in EBF links are key to establishing consistent and regulated hysteresis behavior. End stiffeners are full-depth stiffeners positioned on both sides of the web at link ends for all link length ratios. Roeder and Popov (Roeder, 1977) showed the need for end stiffeners to maintain local stability at a brace-link-beam connection panel in their experimental study. The use of end stiffeners was always deemed necessary in previous and current EBF standards to enhance shear force transmission to reaction components and to prevent early local buckling in links.

Popov and his colleagues' early experiments (Hjelmstad & Popov, 1983b; Kazuhiko Kasai & Popov, 1986a) revealed that in short links, tearing of the web and significant strength degradation generally happened quickly after web buckling. Popov and his colleagues proved that adding intermediate stiffeners to links might significantly increase their strength and energy dissipation capability. Hjelmstad and Popov (Hjelmstad & Popov, 1983a) developed the first relation (Shown by the expressions 2.21-2.23) for calculating the required transverse stiffener spacing based on the link's estimated energy dissipation. Later experiments by Kasai and Popov (Kazuhiko Kasai & Popov, 1986b) revealed that such a relationship mentioned above does not exist and that the required stiffener spacing is instead determined by the predicted final link rotation, γ_u. Kasai and Popov (Kazuhiko Kasai & Popov, 1986a) published conservative stiffener spacing formulas (expression 2.24) based on cyclic plastic theory and experimental results conducted on short links. For three distinct ultimate rotations, the stiffener spacing was calculated as a function of the I-shaped link's depth and web thickness.

$$\frac{a}{t_w} = 94 - 14\ln\left(\frac{E^*}{E_e}\right) \tag{2.21}$$

$$\frac{E^*}{E_e} = 2\mu - 1 \tag{2.22}$$

$$\mu = v_{\max} / v_y \tag{2.23}$$

$$\frac{a}{t_w} + \frac{1}{5}\frac{d}{t_w} = C_B \tag{2.24}$$

For γ_u = 0.03, 0.06, and 0.09 the constant C_B is 56, 38, and 29, respectively. For other values of the γ_u C_B can be linearly interpolated. It is also required for C_B to be less than or equal to d. The EBCS, Eurocode, and AISC (AISC 341-16, 2016; EBCS EN 1998-1:2014, 2014; EN 1998-1:2004, 2004)use the above spacing formula with slight modification.

$$a = C_B t_w - \frac{d}{5} \tag{2.25}$$

C_B values in the above-mentioned codes are related to the inelastic rotation demand. C_B is taken as 30 for γ_p values greater than or equal to 0.08rad and 52 for γ_p values less than or equal to 0.02rad and linear interpolation for γ_p values between 0.08rad and 0.02 rad.

Stiffeners must have sufficient axial strength to provide tension field action. The bending stiffness of the stiffeners must also be adequate to prevent the entire link web from buckling as a single panel. Malley and Popov (Malley & Popov, 1984) used Basler's theory for plate girders and Bleich's method to analyze the necessary area and moment of inertia of link intermediate stiffeners. This method was never incorporated into design codes instead, the standard requirements of plate girder web stiffeners with the addition of a minimum thickness restriction were proposed for estimating the needed moment of inertia of link stiffeners. The Ethiopian and European seismic codes (EBCS EN 1998-1:2014, 2014; EN 1998-1:2004, 2004) specify that transverse stiffeners shall be the full depth with a width no less than b-2t_w and have a thickness equal to the link web thickness or 10mm whichever is greater. The AISC code (AISC 341-16, 2016) gives roughly the same stiffener specification as the above codes.

In links with flexure dominant behavior, intermediate stiffeners are also needed. The extensive experimental research on long links conducted by Engelhardt and Popov (Engelhardt & Popov, 1989, 1992) demonstrated that, unlike shear links, local buckling of flanges does not always result in strength loss in stiffened long links. It was determined that putting stiffeners 1.5b_f from either end of the link will reduce the strength loss due to flange buckling while not stopping it (Engelhardt & Popov, 1992). The benefits of putting stiffeners outside the link region, in the brace-link-beam connection panel, were also noted by Engelhardt and Popov. In addition, intermediate links that will suffer both shear and flexural yielding should include intermediate stiffeners 1.5b_f from the link ends, as well as evenly spaced further stiffeners throughout

the link length according to the requirements of short links. Tsai and his colleagues (Tsai et al., 1993) conducted large-scale pseudo-dynamic testing and found that adding stiffeners $1.5b_f$ from link ends may be advantageous if the link has a significant amount of axial force.

Experiments have shown that, unlike end stiffeners, intermediate stiffeners may be one-sided in links of varied lengths (Engelhardt & Popov, 1992; Kazuhiko Kasai & Popov, 1986b; Malley & Popov, 1984; Okazaki et al., 2009). Using one-sided stiffeners can lower the rotation capacity of intermediate and long links, according to Daneshmand and Hashemi (Daneshmand & Hosseini Hashemi, 2012), although this reduction rarely reduces γ_p below the code-specified rotation capacity. Furthermore, for links in the $1.8 < \rho < 2.2$ range, the reduction was observed to be more significant. However, the Ethiopian and European seismic codes (EBCS EN 1998-1:2014, 2014; EN 1998-1:2004, 2004) allow one-sided stiffener for sections with depth lower than 600mm while the AISC code (AISC 341-16, 2016) also allows one-sided stiffener but for depth less than 635mm.

During their numerical investigation, Richards and Uang (Paul W. Richards & Uang, 2005) discovered that several of the intermediate links did not reach the rotation capacity indicated by the provisions, with a maximum discrepancy of 11%. Similarly, Arce (Arce, 2002) made similar observations. The problem was attributed by Richards and Uang to the AISC (AISC 341-02, 2002) seismic provision's intermediate stiffener spacing restrictions. Kasai and Popov (Kazuhiko Kasai & Popov, 1986a) provided their stiffener spacing formula for short links; nevertheless, the provisions expanded its application to intermediate links, ignoring the substantial moment-shear interaction inherent in the web panels of these links.

2.3.3 Lateral bracing

Lateral torsional buckling (LTB) can harm the cyclic performance of a link. To achieve a steady inelastic response, the lateral bracing requirements are designed to restrict the link against out-of-plane displacement and twisting. Although lateral bracing was included in earlier testing (Roeder, 1977), the necessity of adequate link lateral bracing was fully appreciated during Manheim's (Daniel Nissim Manheim, 1982) tests on three-story prototypes, where LTB was seen in certain test specimens. As a result, Manheim proposed lateral bracing of link ends with moment connections between the lateral braces and the link ends to enhance the link's torsional rigidity.

The lateral buckling of beams in EBFs was investigated by Hjelmstad and Lee in 1989 (Hjelmstad & Sang-Gab Lee, 1989). In the same paper, they found that providing full rotational constraints at the link ends is important based on the experimental findings of five tests on propped cantilever beams with varied lateral bracing schemes at the link ends and a numerical parametric study. Furthermore, the forces produced on the lateral braces were significantly larger than the conventional design load of 2% of the flange yield force, P_y^{flange}, as observed by these researchers. Some specimens showed strength loss owing to the LTB of the link or the beam outside the link in Engelhardt and Popov's experimental investigation on long links (Engelhardt & Popov, 1989, 1992). These findings reinforced the need for strong and stiff lateral bracing at link ends. Engelhardt and Popov, like Hjelmstad and Lee, said that the demand on link lateral braces is many times greater than the minimum load of 1.5 % of P_y^{flange}, which was considered in the 1980s' design codes. For the design of lateral bracing of short and long links, these researchers recommended a minimum load of 6% of P_y^{flange}. To avoid imposing an excessive in-plane restraint on the link, it was also suggested that the lateral braces should only frame into the link ends from one side. The Ethiopian and European seismic codes (EBCS EN 1998-1:2014, 2014; EN 1998-1:2004, 2004) specify that the end lateral supports of links should have a design axial resistance sufficient to provide lateral support for forces of 6% of the expected nominal axial strength of the link flange, which is the same as the above recommendation.

CHAPTER 3 FINITE ELEMENT MODEL AND VALIDATION

3.1 Introduction

This section will go into the details of the finite element model that was used to conduct the parametric analysis. ANSYS 2021 R2 was the FE platform used for the simulation. Test specimens, model parameters, material properties, components, loading protocol, and other considerations will be addressed in the following sections.

3.2 Test Specimens

Experiments by Okazaki and Engelhardt (Okazaki & Engelhardt, 2007) at the University of Texas at Austin was used to validate the numerical models. The experimental program and specimens' specifications will be shown in the next section

3.2.1 Experiment by Okazaki and Engelhardt

The experimental program was conducted to examine flange buckling and overstrength in links constructed of A992 steel. A total of 37 link specimens were built from five different ASTM A992 steel wide-flange sections, with link lengths ranging from short shear yielding links to long flexural yielding links.

A test setup was designed to replicate the force and deformation environment exerted on a link in an EBF with one end of the link attached to a column. The kinematics of the test setup is shown in Figure 3-1. Figure 3-2 depicts the full features and dimensions of the test setup. As illustrated in Figure 3-3, the link specimens were welded to heavy endplates at either end. The endplates were then bolted into place between the vertical column and horizontal beam. Five different wide-flange shapes were used to construct the test specimens. All sections were of ASTM A992 steel.

The loading system consists of a vertical column stub and a horizontal beam, both of which connect to the link-column specimen; a 450-kip hydraulic loading ram that applies vertical cyclic load and displacement to the column; and four reaction rods, one on each end of the vertical column or horizontal beam. Lateral bracing was provided at the link ends.

Four different cyclic loading protocols were used in the tests. The four loading protocols are the old AISC (AISC 341-02, 2002)Loading protocol, the revised loading protocol by Richards and Uang, the severe loading protocol, and a random loading protocol.

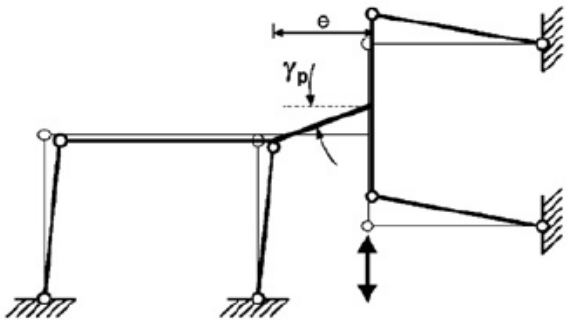

Figure 3-1: Schematic Representation of Test Setup by Okazaki and Engelhardt

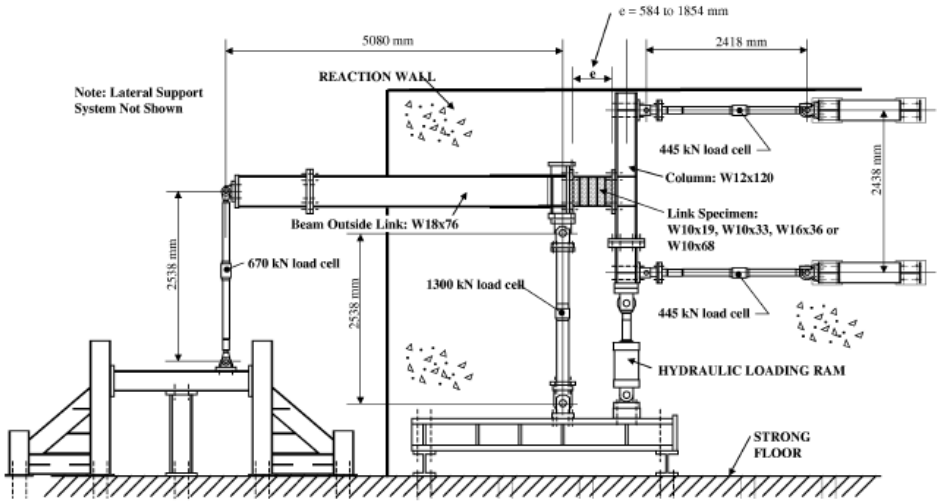

Figure 3-2: Test Setup Details and Dimensions

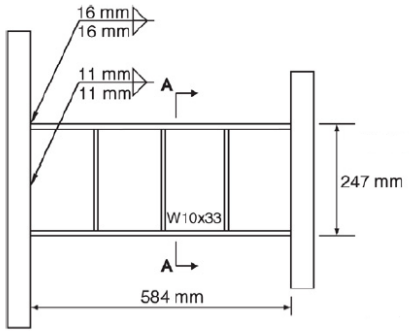

Figure 3-3: Details of Link Specimens

The test specimen chosen for finite element validation is a short shear link with a link length ratio of 1.04 made up of a W10x33 wide flange section. The loading protocol used was the old AISC loading protocol and it is shown in Table 2-1 (a). The relevant cross-sectional dimensions and material properties are listed in Table 3-1and Table 3-2.

Table 3-1: Specimen Cross-Sectional Dimension

Specimen	Section	Width b (mm)	Depth d (mm)	t_f (mm)	t_w (mm)	Stiffener thickness (mm)
4B	W10x33	202.2	247	10.53	7.4	10

Table 3-2: Specimen Details

Specimen	Section	Link Length		Stiffener Spacing	F_y (MPa)		F_u (MPa)	
		e (mm)	$e/(M_p/V_p)$		Flange	Web	Flange	Web
4B	W10x33	584	1.04	3@146	379	402	518	530

3.3 Finite Element Model

3.3.1 Introduction

This section will go into the details of the finite element models that were developed for the experiments discussed in section 3.2. ANSYS 2021 was the general finite element program used to conduct the finite element analysis.

3.3.2 General Notes on the Model

Here are a few general assumptions and limitations considered in all of the finite element models

- Residual stresses were not taken into account. In their numerical research, Della Corte and his colleagues noted that only the initial yield point is affected by residual stresses, but not the fully plastic response (Della Corte et al., 2013).
- No initial imperfection was considered in this model.
- Welds were not modeled to keep the model size within a reasonable range
- Stiffener details such as cut off at the K and weld areas are not considered,
- Shell elements are chosen for the analysis so cross-sections are modeled using the mid surface.
- Displacement control was applied to capture link rotation.

3.3.3 Material Model

Observations of cyclically loaded structural steels in the laboratory reveal several distinguishing characteristics. Strain hardening, the Bauschinger effect, and ratcheting are three of the more common examples. Strain hardening encapsulates the observation that the stress carried after some degree of permanent deformation tends to increase. The Bauschinger effect describes the fact that increasing flow stress in one direction reduces yield stress when loading is applied in the opposite direction. Finally, in constant stress amplitude and nonzero mean stress cyclic testing, an accumulation of plastic strain in the direction of the average stress is generally seen with each cycle. This is known as ratcheting or cyclic creep.

An accurate constitutive model that incorporates the above-explained behavior of steel under cyclic loading is quite important to the numerical simulation. A brief explanation of the material model is given here.

An initial yielding condition, a flow rule, and a hardening rule are necessary to explain the work-hardening material behavior. The initial hardening rule specifies the stress level at which plasticity occurs for the first time.

Plastic materials have a range of elasticity within which they behave solely elastically. The yield surface is the boundary of this range in either stress or strain space. Its shape is determined by the total history of deformation from the reference state. The yield surface is the separator surface between elastic and plastic regions in the stress space. It is defined by the von Mises yield criterion. Von Mises criterion is obtained by assuming that yielding occurs at a particle subjected to a general triaxial state of stress when the value of the corresponding distortional strain energy density is equal to the distortional strain density energy density when the particle yields while subjected to a state of uniaxial stress. For this reason, the von Mises yield criterion is also known as the distortional energy density yield criterion. The expression for the von Mises yield criterion is shown by the expression (3.1) and (3.2).

Any point inside the yield surface region will not cause permanent deformation upon unloading. There are three possible circumstances when considering a point on the yield surface: unloading, neutral loading, and loading. When unloaded, the condition of stress returns to the surface, causing it to return to the elastic domain. Plasticity will not

occur in this scenario. If neutral loading occurs, the condition of stress moves on the yield surface, resulting in no plasticity. When loading occurs, the condition of stress shifts away from the yield surface, and plasticity occurs. After plasticity, two forms of hardening may occur: isotropic and kinematic hardening.

The isotropic hardening accounts for the change in the size of the yield surface. If a specimen is loaded in uniaxial tension beyond the yield stress (see Figure 3-1 & Figure 3-2), then unloaded and reloaded in uniaxial compression, the new yield stress in compression will be equal to the new yield stress in tension, indicating that the yield surface has expanded. Kinematic hardening, on the other hand, accounts for the deviatoric stress space translation of the yield surface (see Figure 3-1 & Figure 3-3). If a specimen is loaded beyond yield stress in uniaxial tension, then unloaded and reloaded in uniaxial compression, the new yield stress point in compression will be lower in magnitude than the original. which is also called the Bauschinger effect.

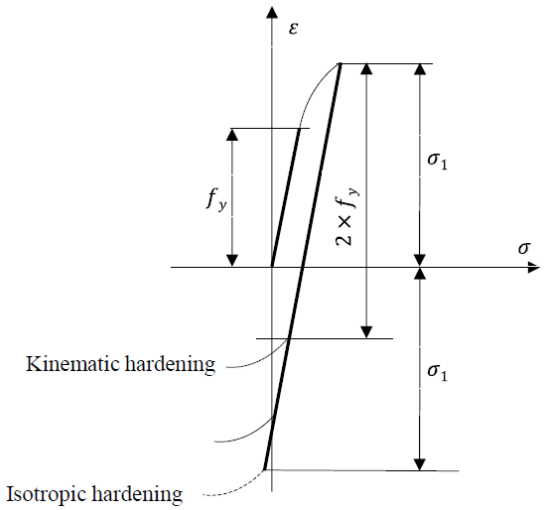

Figure 3-4: Stress-Strain Curve for Uniaxial Loading

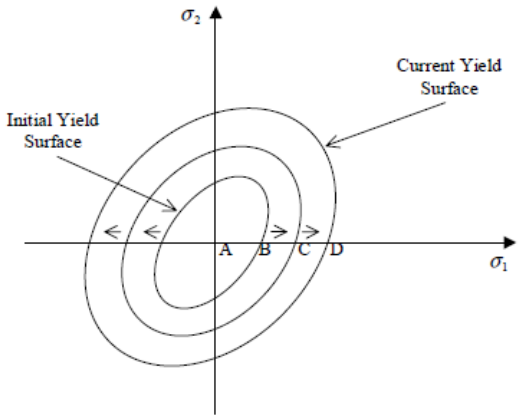

Figure 3-5: Isotropic Hardening - Same Shape, Different Size

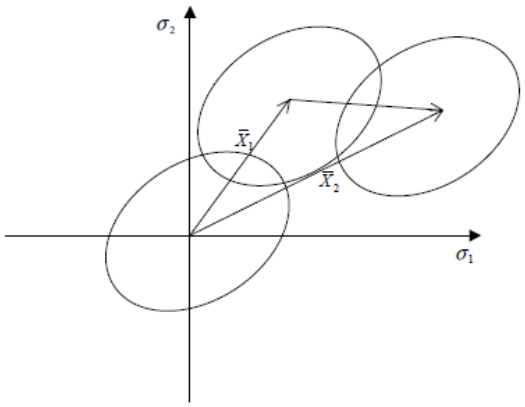

Figure 3-6: Kinematic Hardening - Same Shape, Same Size

The two types of hardening rules described above, isotropic and kinematic, are used in the vast majority of cyclic material models. The difference between isotropic and kinematic hardening for a uniaxial cyclically loaded steel sample is shown in the figures above. The yield surface retains the same form during isotropic hardening, but it expands as the stress increases (see Figure 3-2). The initial yield function determines the form of the yield function, which changes in size when the hardening parameter varies. The Bauschinger effect, as well as related responses in which a hardening in tension leads to softening in compression, cannot be modeled using the isotropic hardening rule. According to this concept, symmetric yield surface about the stress axes will stay symmetric as the yield surface develops with plastic strains. A kinematic hardening rule must be specified to account for such effects. The yield surface retains the same form and

size in this model, but it translates in stress space. The distance between the centers of the surfaces is defined as the back-stress or shift-stress.

The material model used here is the Voce-Chaboche Combined Isotropic-Kinematic hardening model. The nonlinear isotropic hardening rule, which was proposed by Voce (expression 3.6), defines the evolution of the yield surface size σ_s as a function of the equivalent plastic strain ε_p. While the nonlinear kinematic hardening rule, which was proposed by Chaboche and his colleagues (Chaboche, 1986) (3.4), is a superposition of several Armstrong-Frederick (Armstrong & Frederick, 1966) hardening rules (3.3), each with its specific purpose. The Chaboche model describes the translation of the yield surface in stress space (through the back-stress). A further investigation into the subject matter is out of the scope of this paper. All the relevant Constitutive model expressions are shown below.

$$f\left(\sigma-\alpha\right)-\sigma_s\left(\varepsilon_p\right)=0 \tag{3.1}$$

$$f\left(\sigma-\alpha\right)=\sqrt{\frac{3}{2}\left(s-\alpha^{dev}\right):\left(s-\alpha^{dev}\right)} \tag{3.2}$$

$$d\alpha=\frac{C}{\sigma_s}\left(\sigma-\alpha\right)d\varepsilon_p-\gamma\alpha d\varepsilon_p \tag{3.3}$$

$$d\alpha_i=\frac{C_i}{\sigma_s}\left(\sigma-\alpha\right)d\varepsilon_p-\gamma\alpha d\varepsilon_p \tag{3.4}$$

$$\alpha=\sum_{i=1}^{N}\alpha_i \tag{3.5}$$

$$\sigma_s=\sigma_0+R_\infty\left(1-e^{-b\varepsilon_p}\right) \tag{3.6}$$

In the above equation $f(\sigma-\alpha)$ is the equivalent stress expressed in terms of the stress tensor σ and the back stress tensor α, while σ_s is the current yield stress under the equivalent plastic strain ε_p. The equivalent stress is defined by the expression (3.2) where $\boldsymbol{s}$ is the deviatoric stress tensor and $\boldsymbol{\alpha^{dev}}$ is the deviatoric back stress tensor.

In the Armstrong and Frederick model, C is the kinematic hardening modulus γ is the parameter that determines the decrease of kinematic hardening. The Chaboche model as

explained is a superimposing of several Armstrong-Frederick hardening rules. In the equation above N is the number of components of the back stress tensor. Chaboche recommended using 3 components.

In the isotropic hardening model R_∞ is the saturation stress, b is the material constant that defines the change in the rate of the yield surface size, and σ_0 is the initial yield stress.

The material parameters for the nonlinear isotropic-kinematic hardening model need a calibration process and uniaxial cyclic test result. There are various methods for this calibration like using a genetic algorithm or particle swarm optimization. Evaluation and calibration of the Voce-Chaboche parameter are out of the scope of this study.

Voce-Chaboche hardening model is one of the hardening models available in ANSYS. ANSYS only needs the material model parameters. In this research, the Voce-Chaboche parameters for the finite element validation are taken from the numerical research conducted by Hu (Hu, 2015) where the material model parameters for the A992 steel used by Okazaki and Engelhardt is calibrated and the Voce-Chaboche parameters are given in Table 4-1 below.

Table 3-3: Voce-Chaboche Parameter for Validation

Material	A992
E [GPa]	200
ν	0.30
σ_0 [MPa]	380
R_∞ [MPa]	50
b	1.2
C_1 [MPa]	7,993
γ_1	175
C_2 [MPa]	7,100
γ_2	116
C_3 [MPa]	2,650
γ_3	60

3.3.4 Boundary Conditions, Loading Protocol, and Solution Setup

The boundary conditions used for the finite element model validation and the one that will be used in the analysis are adopted from the numerical research done by Richards and Uang (Paul W. Richards & Uang, 2005). In their research, they used experimental research conducted by Arce (Arce, 2002) at the University of Texas, Austin where the

test setup is approximately the same as the test setup explained in a previous section of this chapter and used by Okazaki and Uang. The boundary condition used is shown in the figure below.

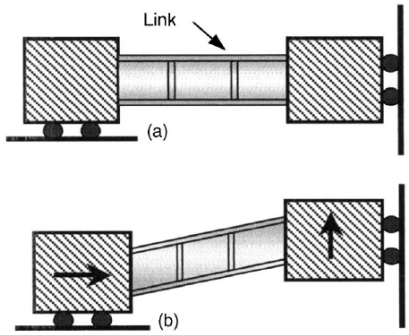

Figure 3-7: Boundary condition Used by Richards and Uang

In the boundary condition, all nodes in the links were restrained against all rotations. Out of plane displacement was restrained at both ends. The left side nodes were free to move in the horizontal direction but they were restrained against the movement in the vertical direction. The left side nodes were free to move in the vertical direction but they were restrained against horizontal movement. Loading was applied by imposing a vertical displacement to the right side. This kind of loading produced constant shear over the length of the link, with equal end moments and no axial force.

The boundary conditions in this research were applied to a reference point (master node) where all other nodes at the end are tied to the reference node. The reference point and the boundary condition are shown in the figure below.

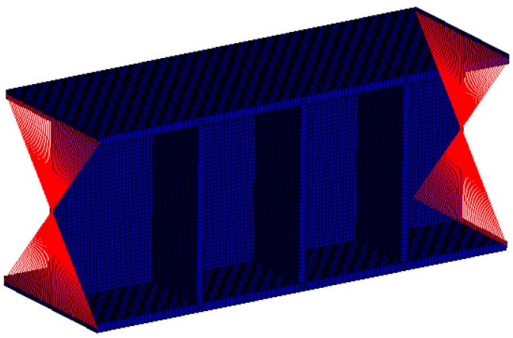

Figure 3-8: Reference point Tied to Edge Nodes

The loading protocol used in the experiment is shown in Table 2-1 and it is the old AISC (AISC 341-02, 2002) loading protocol. The load is applied as a displacement to the right end. The applied displacements are calculated by multiplying the loading protocol rotation angles with the link length.

Geometric nonlinearity was considered by turning on the large displacement option in ANSYS. A sufficient amount of sub-steps per every load step was used to capture the behavior correctly.

3.3.5 Elements Types and Mesh

A shell element was chosen for this study to limit the run time within a reasonable amount of time. Links have been modeled using shell elements in various studies (Berman et al., 2010; Della Corte et al., 2013; Paul W. Richards & Uang, 2005). ANSYS recommends and uses Shell181 for plastic analysis. Shell181 is a four-node shell element with six degrees of freedom at each node. Shell181 is well-suited for linear, large rotation, and/or large strain nonlinear applications (ANSYS, 2021).

The model's mesh refinement studies were carried out to determine the amount of mesh refinement required to meet the objectives. Equivalent plastic strain (PEEQ) and von Mises stress versus the mesh size were used to determine convergence. It was tested at the most impacted area, which was the web of the link at the middle of the section. The graph below shows the mesh convergence results study.

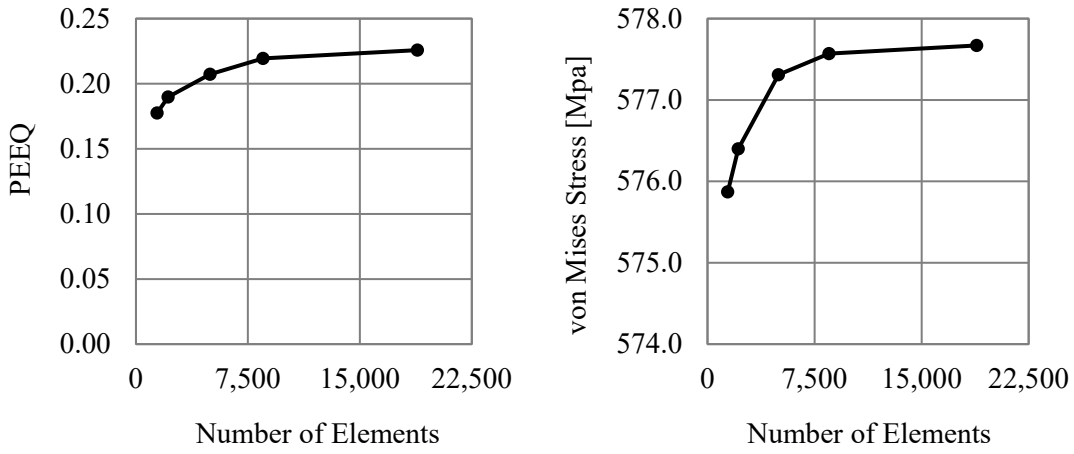

Figure 3-9: Mesh Convergence Study

The final mesh convergence required 18,864 elements with a maximum mesh size of 5mm. The PEEQ and von Mises stress difference for the maximum mesh size of 5mm and 7.5mm was minimal (less than 3%), so for the finite element analysis, a maximum mesh size of 7.5mm was adopted.

3.3.6 Comparison of Experimental and Numerical Results

The shear-force vs plastic rotation graph for the experimental and the finite element is shown in the figure below.

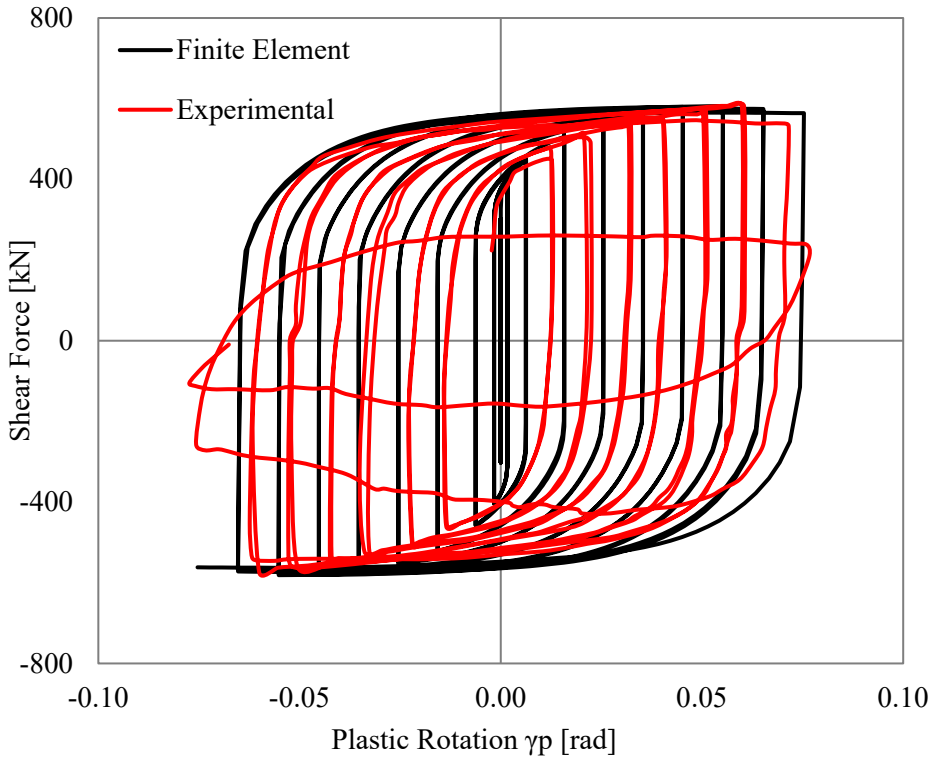

Figure 3-10: Finite Element Analysis vs Experimental Results

It can be seen from the graph that the numerical simulation closely resembles the experimental result until web fracture occurs. The slight variation in results can be attributed to the sensitivity of the material model parameter calibration process and the type of test result (monotonic or cyclic) used in calibrating the parameters (Crișan, 2016; Kalnins et al., 2015).

The maximum difference between the finite element and experimental results at the end of every cycle is 5.85% for the shear force and 7.45% for the plastic rotation.

CHAPTER 4 PARAMETRIC STUDY

4.1 Parameters

In this parametric study, the following parameters were chosen to study their effects on EBF links made up of the European IPE Sections.

- Link Length Ratio, ρ
- Axial Load Ratio, P/P_y
- Web Slenderness, C_w/t_w
- Flange Slenderness, C_f/t_f
- Stiffener Spacing Constant, C_B
- Stiffener Thickness Multiplier
- End Stiffener Spacing Multiplier

The above parameters were chosen based on the reviewed literature in chapter 2. The web slenderness is used only for short links ($\rho < 1.6$) while flange slenderness is used for the rest. The stiffener spacing constant C_B shown in section 2.3.2 is used to vary the stiffener spacing for short and intermediate links. In section 2.3.2 the end stiffener spacing was calculated as a proportion of the cross-section's width (1.5 in the relevant codes). In this study, the end stiffener spacing for long links is calculated by varying this multiplier. The Stiffener thickness is varied in this study by varying the multiplier for t_w, as discussed in section 2.3.2 the stiffener thickness is usually calculated as a proportion of the web thickness (equal to the web thickness).

Since EBF links behavior varies with their link length ratio as discussed in chapter 2 the parametric study was subdivided into the 3-link length ratio.

- Short ($0.5 \leq \rho \leq 1.6$)
- Intermediate ($1.6 < \rho \leq 3$)
- Long ($3 < \rho \leq 5$)

4.2 Sampling

The process of selecting a set of data points from a population to study and characterize the population as a whole is called sampling. All members of a given group, as well as all conceivable outcomes or measures, are included in the population. The exact population will be determined by the study's scope. The sample is a subset of the population, consisting of some observations taken from the population. A good sample should be representative of the population, be accurate to avoid bias, and should have a good size to represent the population.

There are several sampling techniques and they can be subdivided into two groups probability sampling and non-probability sampling. Probability sampling is one in which every unit in the population has a probability (greater than zero) of being chosen and this probability can be properly measured. The combination of these characteristics allows for the generation of unbiased estimates of population by weighting sampled units based on their likelihood of selection.

When performing large research, probability sampling is usually chosen. There are four types of probability sampling techniques simple random sampling, cluster sampling, systematic sampling, and stratified random sampling.

In this research, a type of stratified sampling method called the Latin hypercube sampling (LHS) is used. Latin hypercube sampling (LHS) was developed by McKay and his colleagues in 1979 (McKay et al., 1979). Latin Hypercube sampling is a sampling method that can precisely recreate the input distribution through sampling in fewer iterations when compared with the Monte Carlo method (random sampling type). The stratification of the input probability distributions is the key to Latin Hypercube sampling. On the cumulative probability scale, stratification splits the cumulative curve into equal intervals. After that, a sample is drawn at random from each interval or "stratification" of the input distribution. Sampling is forced to represent values in each interval, and therefore to reproduce the input probability distribution.

Latin Hypercube Sampling selects n distinct values from each of k random variables X_1,....., X_k. Based on an equal chance of occurrence, the range of each variable is split into n non-overlapping intervals (therefore the area of each interval under the density function should be equal to the probability value of P(X)=1/n). Figure 4-1 shows the

LHS method for a random variable with uniform distribution and a sample size of n=5. Because n=5, the probability density function (PDF) should be split into five equal probability parts P(X)=0.20. The cumulative distribution function (CDF) makes it simple to compute these interval boundaries. Then a random sample is taken from the intervals. However, once a stratum is sampled, it is not sampled again since its value is already reflected in the sampled set.

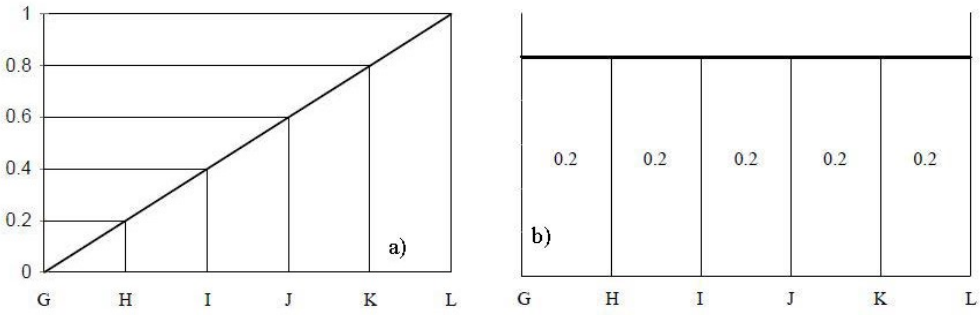

Figure 4-1: a) CDF, b) PDF Divided into 5 intervals With Equal Probability

The choice of the sample distribution function is down to the researcher. The book by Santner and his colleagues gives the following explanation on sample distribution "…Varying the size and position of the strata, as well as sampling according to different distributions within the strata, allows considerable flexibility in selecting a design. This may be more or less useful, depending on the purpose of the computer experiment. For example, one may wish to explore some portions of the experimental region more thoroughly than others. However, if the goal is simply to select points that are spread evenly throughout the experimental region, spacing the strata evenly and sampling each according to a uniform distribution would seem the most natural choice" (Santner et al., 2018).

In this research, a Latin hypercube sampling (LHS) with uniformly distributed parameters (variables) is used. As discussed earlier the sample points are divided into 3 blocks based on the link length ratio. 15 sample points for each of the blocks are generated using LHS. The LHS samples were generated using the statistical software package JMP Pro 16.1.0 (JMP, 2012). In a Latin Hypercube design in JMP, each factor has as many levels as there are runs in the design. The levels are spaced evenly from the lower bound to the upper bound of the factor. The Latin Hypercube method chooses

points to maximize the minimum distance between design points, but with a constraint. The constraint maintains the even spacing between factor levels. The maximum and minimum intervals for the variables/parameters for the short, intermediate, and long links are shown in the following tables.

Table 4-1: Variation of Variables for Short Links

Parameter/Variables	Minimum	Maximum
Link Length Ratio, ρ	0.5	1.6
Axial Load Ratio, P/P_y	0	0.4
Stiffener Spacing Constant, C_B	25	40
Web Slenderness Ratio, C_w/t_w	25.6	52.4
Stiffener Thickness Multiplier	0.5	1.9

Table 4-2: Variation of Variables for Intermediate Links

Parameter/Variables	Minimum	Maximum
Link Length Ratio, ρ	1.61	3
Axial Load Ratio, P/P_y	0	0.4
Stiffener Spacing Constant, C_B	30	52
Flange Slenderness Ratio, C_f/t_f	2.89	6.41
Stiffener Thickness Multiplier	0.5	1.9

Table 4-3: Variation of Variables for Long Links

Parameter/Variables	Minimum	Maximum
Link Length Ratio, ρ	3.01	5
Axial Load Ratio, P/P_y	0	0.4
End Stiffener Spacing Multiplier	0.5	2.5
Flange Slenderness Ratio, C_f/t_f	2.89	6.41
Stiffener Thickness Multiplier	0.5	1.9

In the above table, C_f and C_w are the flange and web compressed widths, respectively.

Axial load ratios range is taken from previous research where maximum axial load ratios in the range of 0.26 up to 0.5 were observed (Dastmalchi, 2014; Kazuhiko Kasai & Popov, 1986b; Mansour et al., 2011). Stiffener spacing constant ranges were chosen so that half of the generated samples fail below the required stiffener spacing while the other half were higher than the required stiffener spacing. The same criteria were used while selecting the ranges for the end stiffener spacing multiplier. Flange and web

slenderness ratio were taken from the European IPE section where the max and minimum flange and web slenderness ratio were used as the range. The stiffener thickness multiplier range was chosen so that half of the generated samples have stiffener thickness that falls below the required minimum thickness for a stiffener (minimum of t_w or 10mm) and the other half were above the required minimum for the stiffener thickness.

The above ranges were used as input for the software. JMP Pro uses a uniform distribution for the factors. 15 samples each were generated for the short, intermediate, and long links. The generated samples are shown in the tables below.

Table 4-4: LHS Generated Samples for Short Links

Sample	Link Length Ratio, ρ	Axial Load Ratio, P/P_y	Stiffener Spacing Constant, C_B	Web Slenderness Ratio, C_w/t_w	Stiffener Thickness Multiplier
Short-1	1.13	0.11	40.00	46.66	1.20
Short-2	0.81	0.26	36.79	31.34	0.70
Short-3	0.50	0.20	34.64	44.74	1.70
Short-4	1.60	0.31	32.50	37.09	1.30
Short-5	1.21	0.23	26.07	35.17	0.50
Short-6	0.89	0.37	35.71	29.43	1.80
Short-7	1.52	0.14	30.36	52.40	1.10
Short-8	0.58	0.29	29.29	50.49	0.80
Short-9	1.36	0.09	31.43	39.00	1.90
Short-10	0.66	0.17	27.14	25.60	1.40
Short-11	1.29	0.40	38.93	48.57	0.60
Short-12	1.44	0.03	33.57	33.26	0.90
Short-13	1.05	0.34	25.00	40.91	1.50
Short-14	0.74	0.00	28.21	42.83	1.00
Short-15	0.97	0.06	37.86	27.51	1.60

Table 4-5: LHS Generated Samples for Intermediate Links

Sample	Link Length Ratio, ρ	Axial Load Ratio, P/P_y	Stiffener Spacing Constant, C_B	Flange Slenderness Ratio, C_f/t_f	Stiffener Thickness Multiplier
Int-1	2.40	0.11	52.00	5.66	1.20
Int-2	2.01	0.26	47.29	3.64	0.70
Int-3	1.61	0.20	44.14	5.40	1.70
Int-4	3.00	0.31	41.00	4.40	1.30
Int-5	2.50	0.23	31.57	4.15	0.50
Int-6	2.11	0.37	45.71	3.39	1.80
Int-7	2.90	0.14	37.86	6.41	1.10
Int-8	1.71	0.29	36.29	6.16	0.80
Int-9	2.70	0.09	39.43	4.65	1.90
Int-10	1.81	0.17	33.14	2.89	1.40
Int-11	2.60	0.40	50.43	5.91	0.60
Int-12	2.80	0.03	42.57	3.90	0.90
Int-13	2.31	0.34	30.00	4.90	1.50
Int-14	1.91	0.00	34.71	5.15	1.00
Int-15	2.21	0.06	48.86	3.14	1.60

Table 4-6: LHS Generated Samples for Long Links

Sample	Link Length Ratio, ρ	Axial Load Ratio, P/P_y	End Stiffener Spacing Multiplier	Flange Slenderness Ratio, C_f/t_f	Stiffener Thickness Multiplier
Long-1	4.15	0.11	2.50	5.66	1.20
Long-2	3.58	0.26	2.07	3.64	0.70
Long-3	3.01	0.20	1.79	5.40	1.70
Long-4	5.00	0.31	1.50	4.40	1.30
Long-5	4.29	0.23	0.64	4.15	0.50
Long-6	3.72	0.37	1.93	3.39	1.80
Long-7	4.86	0.14	1.21	6.41	1.10
Long-8	3.15	0.29	1.07	6.16	0.80
Long-9	4.57	0.09	1.36	4.65	1.90
Long-10	3.29	0.17	0.79	2.89	1.40
Long-11	4.43	0.40	2.36	5.91	0.60
Long-12	4.72	0.03	1.64	3.90	0.90
Long-13	4.01	0.34	0.50	4.90	1.50
Long-14	3.44	0.00	0.93	5.15	1.00
Long-15	3.86	0.06	2.21	3.14	1.60

After the LHS samples were generated, using the web and flange slenderness ratio an appropriate IPE Section was selected. Subsequently, all the relevant data was generated using the dimensions and properties of the assigned cross-section.

Table 4-7: Short Link Sample Data

Sample	Section	Link Length [mm]	Number of Stiffener and Spacing [mm]	Stiffener Thickness [mm]	Applied Axial Load [kN]
Short-1	IPE A 400	604	2 @ 201 mm	8.40	281.20
Short-2	IPE V 400	424	-	-	942.42
Short-3	IPE A 360	257	1 @ 129 mm	11.22	434.59
Short-4	IPE O 550	935	2 @ 312 mm	16.51	1,686.17
Short-5	IPE300	473	3 @ 118 mm	3.55	420.97
Short-6	IPE O 270	343	1 @ 172 mm	13.50	684.39
Short-7	IPE A 600	1,036	5 @ 173 mm	10.78	669.81
Short-8	IPE A 500	346	1 @ 173 mm	6.72	987.02
Short-9	IPE400	668	3 @ 167 mm	16.34	245.49
Short-10	IPE O 200	178	1 @ 89 mm	8.68	186.99
Short-11	IPE A 450	730	3 @ 183 mm	4.56	1,161.00
Short-12	IPE270	522	2 @ 174 mm	5.94	44.64
Short-13	IPE A 300	412	3 @ 103 mm	9.15	542.78
Short-14	IPE600	444	1 @ 222 mm	12.00	0.00
Short-15	IPE V 550	536	-	-	399.69

Table 4-8: Intermediate Link Sample Data

Sample	Section	Link Length [mm]	Number of Stiffener and Spacing [mm]	Stiffener Thickness [mm]	Applied Axial Load [kN]
Int-1	IPE A 360	1,234	4 @ 247 mm	7.92	248.34
Int-2	IPE V 400	1,045	2 @ 348 mm	7.42	942.42
Int-3	IPE A 450	914	3 @ 229 mm	12.92	580.50
Int-4	IPE550	1,691	4 @ 338 mm	14.43	1,444.53
Int-5	IPE200	659	4 @ 132 mm	2.80	221.10
Int-6	IPE O 600	1,308	1 @ 654 mm	27.00	2,529.28
Int-7	IPE A 300	1,137	6 @ 162 mm	6.71	226.16
Int-8	IPE A 330	729	3 @ 182 mm	5.20	526.97
Int-9	IPE A 600	1,839	6 @ 263 mm	18.62	401.89
Int-10	IPE V 600	1,112	1 @ 556 mm	25.20	1,392.65
Int-11	IPE A 270	963	3 @ 241 mm	3.30	528.50
Int-12	IPE O 500	1,552	3 @ 388 mm	10.80	134.82
Int-13	IPE A 550	1,463	8 @ 163 mm	13.50	1,367.39
Int-14	IPE A 240	633	4 @ 127 mm	5.20	0.00
Int-15	IPE V 500	1,263	1 @ 632 mm	22.72	325.17

Table 4-9: Long Link Sample Data

Sample	Section	Link Length [mm]	End Stiffener and Spacing [mm]	Stiffener Thickness [mm]	Applied Axial Load [kN]
Long-1	IPE A 360	2,128	425 mm from each end	7.92	248.34
Long-2	IPE V 400	1,863	377 mm from each end	7.42	942.42
Long-3	IPE A 450	1,708	339 mm from each end	12.92	580.50
Long-4	IPE550	2,819	315 mm from each end	14.43	1,444.53
Long-5	IPE200	1,128	64 mm from each end	2.80	221.10
Long-6	IPE O 600	2,310	432 mm from each end	27.00	2,529.28
Long-7	IPE A 300	1,904	182 mm from each end	6.71	226.16
Long-8	IPE A 330	1,344	171 mm from each end	5.20	526.97
Long-9	IPE A 600	3,113	299 mm from each end	18.62	401.89
Long-10	IPE V 600	2,024	179 mm from each end	25.20	1,392.65
Long-11	IPE A 270	1,640	318 mm from each end	3.30	528.50
Long-12	IPE O 500	2,613	332 mm from each end	10.80	134.82
Long-13	IPE A 550	2,542	105 mm from each end	13.50	1,367.39
Long-14	IPE A 240	1,141	111 mm from each end	5.20	0.00
Long-15	IPE V 500	2,211	452 mm from each end	22.72	325.17

4.3 Finite Element Model

This section will discuss the finite element model used in the numerical analysis. Material model, mesh, boundary condition, and loading protocol will be discussed.

4.3.1 Material

The material chosen for this study is S-355. The S-355 was chosen because it is generally characterized by the lower variance between nominal and actual yield strength. As a result of its lower variance between nominal and actual yield, S355 may be considered "good seismic" steel (Landolfo et al., 2017).

The combined nonlinear isotopic kinematic hardening material model (Voce-Chaboche Model) discussed in section 3.3.3 is used here for the numerical analysis. As discussed in section 3.3.3 the calibration for the material model needs a uniaxial cyclic loading test. Since no experimental work is done in the research and no material model for cyclic loading is given in Ethiopian or European codes (EBCS EN 1998-1:2014, 2014; EN 1998-1:2004, 2004) the material model parameters are taken from previous research done by Sousa and his colleagues (Sousa et al., 2020). The research was conducted to establish a consistent set of material characteristics capable of properly representing a wide range of mechanical uniaxial cyclic load histories. The material used is S-355 with

3 Chaboche parameters with a yield strength of 355 MPa. The material parameters are listed in Table 4-10.

Table 4-10: Voce-Chaboche Parameter for the Numerical Analysis

Material	S355J2
E [GPa]	185.32
ν	0.30
σ_0 [MPa]	269.22
R_∞ [MPa]	107.01
b	6.00
C_1 [MPa]	12,659.43
γ_1	150.94
C_2 [MPa]	3,226.07
γ_2	51.55
C_3 [MPa]	1,345.22
γ_3	5.54

4.3.2 Finite Element Mesh

The same modeling procedure that was discussed in chapter 3 was used for the analysis model. 8 node shell elements with 6 degrees of freedom per node (SHELL 181) was used. The mesh size was based on the mesh sensitivity analysis conducted in chapter 3. An example of the typical mesh used for the numerical analysis is shown in Figure 4-2.

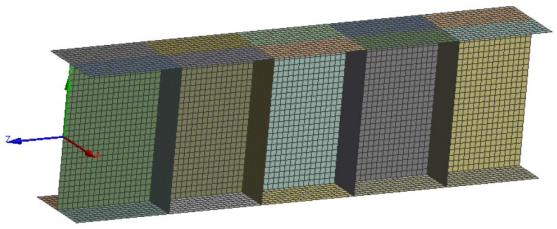

Figure 4-2: Finite Element Mesh for Int-5

4.3.3 Boundary Conditions

The boundary condition used for the analysis is the same as the one used in chapter 3 and the numerical research done by Richards (Paul W. Richards & Uang, 2005). The boundary conditions considered are shown in Figure 3-7. The same consideration as in section 3.3.4, where the end of the link is tied to a single reference point and all the boundary conditions applied to that reference point, is used here too.

4.3.4 Loading Protocol

The loading protocol used for this research is the revised loading protocol proposed by Richards and Uang (Paul W. Richards & Uang, 2004, 2006). The loading protocol is discussed in section 2.2.4. The loading protocol is shown in Table 2-1 and it is shown here graphically in Figure 4-4. The loading is applied as displacement (by multiplying the loading protocol rotation angel by the link length) to the right reference point.

The boundary condition considered in section 3.3.4 doesn't induce axial load in the link. To introduce axial load into the link a similar loading procedure to the one used in the experimental research done by Kasi and Popov (Kazuhiko Kasai & Popov, 1986b) is used here. The experimental setup is shown in Figure 4-3. In the research, link rotation is applied to the link by jack 1 and 2 while the cyclic axial load is applied to the link via jack 3. In the same manner, a cyclic axial load is applied as a force in the axial direction to the left side reference point in the finite element model. The cyclic axial loading protocol is calculated assuming that the axial load varies with the same proportion as the displacement loading protocol. The maximum or the final axial load is the applied axial load that is shown in Table 4-7 up to Table 4-9. The cyclic axial loading protocol closely resembles the cyclic axial loading protocol used by Huiling (Hu, 2015) in the numerical study of seismic behavior of high-strength steel replaceable shear links. The same method was used in that research but compressive axial loading-unloading is used instead of cyclic compressive-tensile axial loading.

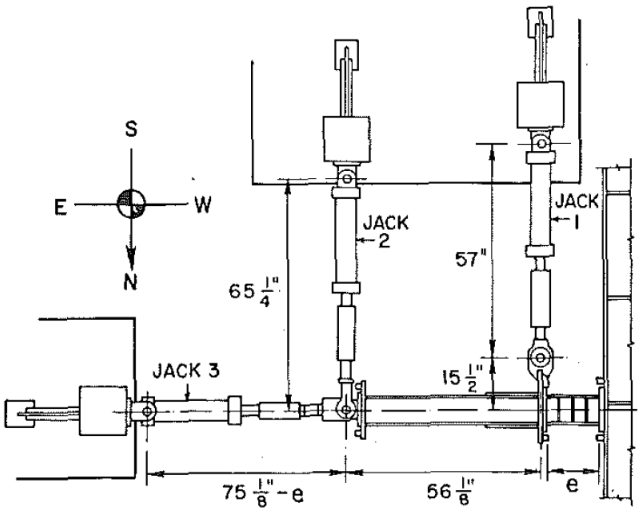

Figure 4-3: Experimental Setup Used by Kasi and Popov

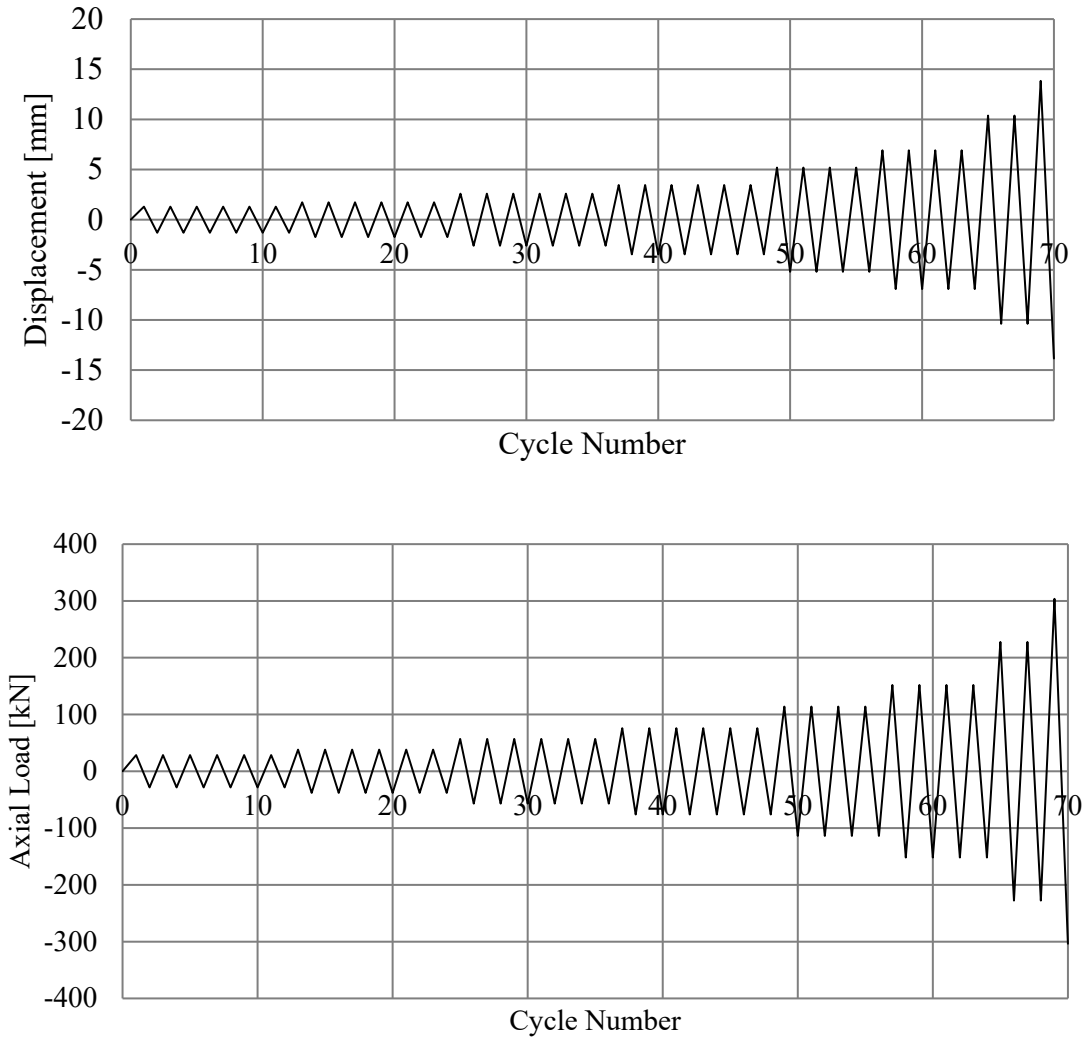

Figure 4-4: Loading Protocol for Int-7

CHAPTER 5 RESULTS AND DISCUSSIONS

The results from the finite element analysis are discussed in this section. The result calculation method, failure types observed, overstrength ratio, plastic rotation capacity, total dissipated energy, ductility, and maximum shear and moment in the links are reported.

5.1 Result Calculation

5.1.1 Link Rotation Angle

The link rotation angle γ is calculated as the ratio of the relative end displacement between the two link ends to the link length. As shown in the previous chapters the left side of the link end is restrained from vertical movement (see Figure 5-1) and the displacement loading is applied to the right side. Since the left side displacement of the link is zero the link rotation angle will be calculated as the ratio of the applied displacement at the right end to the link length. The calculation is shown below. The link rotation is considered positive when the right-side displacement is in the upward direction.

$$\gamma = \frac{\Delta_R}{e} \tag{5.1}$$

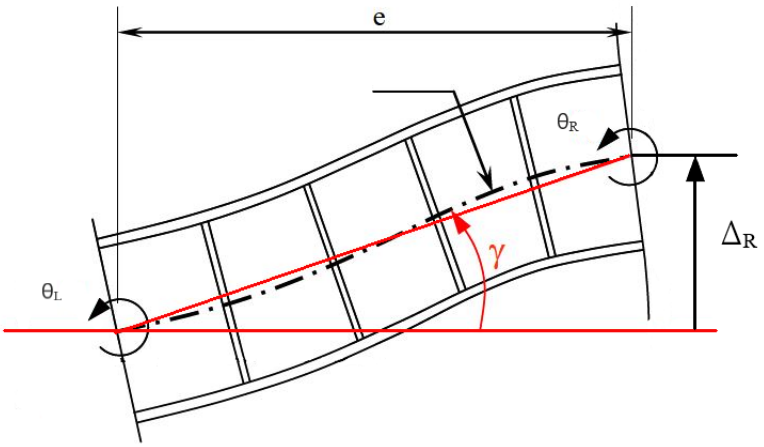

Figure 5-1: Link Deformation

The link plastic rotation angle as discussed in the previous chapter is calculated by subtracting the elastic part of the link rotation angle from the total link rotation angle. The expression for the calculation is shown below.

$$\gamma_P = \gamma - \frac{V}{K_e} \tag{5.2}$$

In the above expression, V is the shear force in the link and K_e is the elastic stiffness of the link which is the ratio of V/γ in the initial elastic loading cycles. K_e is the slope of the V-γ graph in the elastic range.

The elastic stiffness can also be calculated using the material and cross-sectional properties of the link. Della Corte and his colleagues (Della Corte et al., 2013) gave an expression (5.3) to calculate K_e in their research. This expression is used and compared to the finite element calculated elastic stiffness in this research.

$$K_e = \frac{1}{\frac{1}{GA_V} + \frac{e^2}{12EI}} \tag{5.3}$$

$$G = \frac{E}{2(1+\nu)} \tag{5.4}$$

$$A_V = dt_w \tag{5.5}$$

In the above expression G is the shear modulus of elasticity, A_V is the shear area, and I is the moment of inertia of the link.

The plastic rotation capacity calculation is shown in Figure 2-8. The link plastic rotation capacity is the maximum plastic rotation sustained for at least one full cycle of loading before the shear resisted by the link drops to 80% of the link's maximum shear measured throughout the cyclic test.

5.1.2 Energy Dissipation

Quantifying structural energy dissipation via plastic deformations is important for a variety of reasons. First, energy methods can be applied to the study and design of earthquake-resistant buildings. The primary concept of such approaches is to balance the earthquake energy input to a structure against the elastic vibrational energy (elastic strain energy and kinetic energy) of the structure and the energy lost by hysteretic damping (plastic deformations). Energy dissipation during severe earthquake ground movements is primarily provided by hysteretic damping. For the application of energy-based design approaches, knowledge of the energy dissipation capability of structural components is required. Calculations of energy dissipation are also useful for assessing the overall performance of various specimens. Comparisons based on energy dissipation capacity are more informative. The impacts of different post-yield behaviors, such as deteriorating hysteretic response, can be included in energy dissipation depending on the area contained by load-deformation response loops. As a result, energy dissipation capacity is a helpful measure for assessing the entire performance of a link.

Total dissipated energy E_{total} was computed as the total area enclosed by the hysteretic loops in the shear force versus relative link displacement graph. Comparing total energy dissipated of links with different cross-sections might be misleading as the maximum link shear that the link attains is based on the links cross-section, therefore the total dissipated energy needs to be normalized by the elastic energy stored by the link at yield, E_e. This eliminates the influence of the cross-section and makes it possible to compare among all of the samples. The elastic energy E_e is calculated as the area under the shear vs displacement graph at yield.

5.1.3 Overstrength and Shear Strength

The overstrength factor is discussed in section 2.2.2 and it is defined by the expression in (2.10). It is the ratio of maximum shear in the link to the nominal (plastic) shear capacity of the link. The maximum shear force in the link (shear strength) is the maximum shear force attained during the cyclic testing of the link.

5.1.4 Ductility

Ductility refers to a structure's capacity to withstand a considerable amount of permanent deformation without losing significant strength. In earthquake design, high ductility is required to postpone local failure of components by permitting plastic redistribution of

actions from one critical area to another, as well as to allow input energy absorption and dissipation capability.

The ductility ratio is a statistic that measures the maximal inelastic deformation capability of earthquake-resistant structures or components. Ductility factor is defined as the ratio of post-peak displacement at a 20% reduction in load-carrying capacity to the displacement at yield. This study adopts this definition for ductility factor as shown by the following expression.

$$\mu = \frac{\Delta_u}{\Delta_y} = \frac{\gamma_u}{\gamma_y} \tag{5.6}$$

γ_u is the link rotation angle when the shear force in the link reaches 80% of the maximum shear that was observed in the link during the cyclic loading. γ_y is the link rotation at yield. γ_u and γ_y are calculated as the average of the maximum ultimate and yield rotation achieved in positive and negative cycles respectively.

5.2 Results

5.2.1 Short Link Results

5.2.1.1 Observed Failures

All the tested samples deformed as a result of plastic shear yielding of the web. The links Short-1, Short-3, Short-12, and Short-14 exhibited a significant amount of web buckling that can be seen in their shear force-plastic rotation hysteretic graph. Figure 5-2 and Figure 5-3 show the deformed shape and the hysteretic graph for the link Short-1.

When web buckling has fully formed as a result of one-way loading, a tension field exists with the primary tension directed along the direction of the buckle. A compression field exists that is roughly perpendicular to the tension field, but the forces in it are considerably lower due to the deformed web's geometry. The tension and compression fields shift their orientation when the load sense is reversed. The principal tension acts to straighten the residual out-of-plane displacement left by buckling in the opposite direction as the loading proceeds, while the compressive stresses operate to produce a new buckle. Buckling occurs first and a loss of load-carrying capacity results. The

instability is usually not catastrophic because buckling is arrested by the formation of a tension field in the opposite direction. the load-carrying capacity increases when the tension field action becomes the predominant load carrying mechanism of the link which increases, often surpassing the buckling load. This mechanism is shown in Figure 5-3 where the load-carrying capacity of the link drops momentarily and gradually recovers until the tension field becomes the predominant load-carrying capacity mechanism.

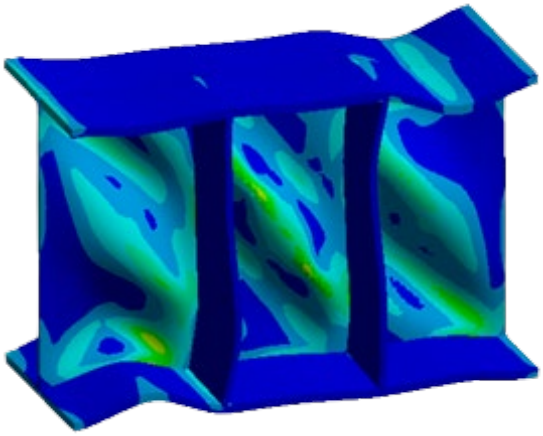

Figure 5-2: Deformed Geometry of Link Short-1

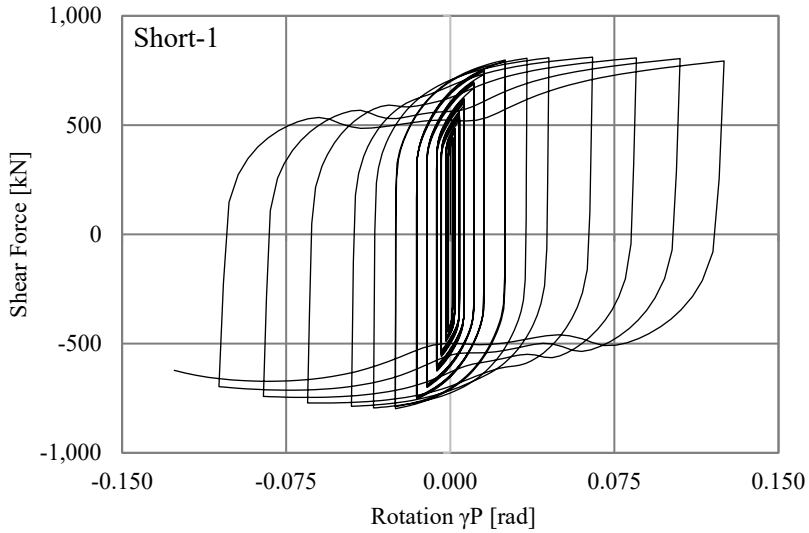

Figure 5-3: Shear Force vs Plastic Rotation Graph for Link Short-1

The links Short-7, Short-8, and Short-9 exhibited a moderate web buckling while the rest developed a slight web buckling. The web buckling was followed by flange buckling. The links that were able to sustain a large amount of inelastic rotation exhibited a higher flange buckling. Links that were also closer to the intermediate link range also exhibited higher flange buckling. Severe stiffener buckling was observed in the links Short-14, Short-12, Short-11, and Short-5. All of these samples had a stiffener thickness well below the required and all of them except Short-12 were unable to contain the buckling within the region bounded by the stiffeners. Figure 5-4 shows an example of the web buckling forming beyond the stiffener bounded region. In the figure, it can be seen that the middle stiffener is incapable of providing the required stiffness to arrest web buckling between the region bounded by the stiffeners.

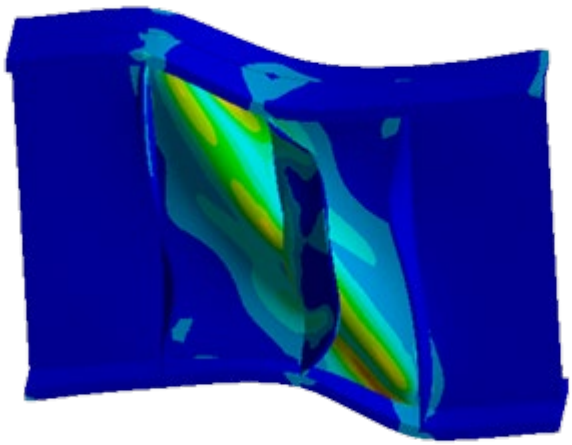

Figure 5-4: Deformed Geometry of Link Short-5

Links Short-7 and Short-8 experienced a noticeable stiffener buckling but it didn't affect the tension field being created between the region bounded by the stiffeners. All the deformed shapes with their equivalent plastic strain are shown in Appendix A.

5.2.1.2 Plastic Rotation Capacity and Overstrength

The calculation method for the overstrength ratio and plastic rotation capacity is shown in the previous section. The plastic rotation capacity and overstrength are calculated for both the positive and negative rotation cycles. This is done to see the effect of tensile axial load on the link behavior. In most of the links the shear force in the link degraded in the negative cycle where the compressive axial load was applied to the link. As

discussed before the link is loaded until the shear force in the link deteriorates to 80% of the maximum shear force attained during either the positive or negative loading cycle of the link. Therefore, if the link shear force in the negative cycle reaches the 80% mark before the positive cycle, then the plastic rotation capacity of the positive cycle is taken as the last plastic rotation sustained before the negative cycle failed and vice versa.

The plastic rotation capacity and overstrength ratio for the positive and negative cycles of the links are shown in Table 5-1 below. Only Short-4 and Short-11 failed to reach the required plastic rotation capacity. The shear-force vs plastic rotation graph for all of the samples is shown in Appendix B.

Table 5-1: Overstrength Ratio and Plastic Rotation Capacity for Short Links

Sample	Link Length Ratio, ρ	V_n [kN]	V_{max} [kN]		Overstrength Factor Ω		γ_P [rad]	γ_P (FE) [rad]	
			+ve	-ve	+ve	-ve	Req.	+ve	-ve
Short-1	1.13	552.37	810.98	797.83	1.468	1.444	0.080	0.125	0.119
Short-2	0.81	848.39	1,528.90	1,380.20	1.802	1.627	0.080	0.105	0.093
Short-3	0.50	468.72	859.36	813.05	1.833	1.735	0.080	0.145	0.141
Short-4	1.60	1,394.68	2,266.70	2,052.50	1.625	1.472	0.080	0.084	0.068
Short-5	1.21	420.99	779.20	687.97	1.851	1.634	0.080	0.124	0.113
Short-6	0.89	402.44	731.61	647.88	1.818	1.610	0.080	0.084	0.081
Short-7	1.52	1,163.98	2,030.20	1,926.30	1.744	1.655	0.080	0.164	0.146
Short-8	0.58	830.70	1,483.10	1,376.70	1.785	1.657	0.080	0.125	0.107
Short-9	1.36	681.26	1,173.60	1,145.30	1.723	1.681	0.080	0.164	0.157
Short-10	0.66	244.62	496.38	456.09	2.029	1.864	0.080	0.204	0.195
Short-11	1.29	675.88	1,094.30	973.08	1.619	1.440	0.080	0.064	0.046
Short-12	1.44	351.44	535.85	531.05	1.525	1.511	0.080	0.165	0.165
Short-13	1.05	359.82	697.25	588.67	1.938	1.636	0.080	0.124	0.106
Short-14	0.74	1,428.98	2,478.80	2,501.70	1.735	1.751	0.080	0.206	0.192
Short-15	0.97	1,895.40	3,453.70	3,367.60	1.822	1.777	0.080	0.145	0.142

The maximum moments measured for the links are shown in table 5-1 below. The links Short-4, Short-7, and Short-12 which are closer to the intermediate link range boundary experienced a moment close to 1.2, which is the ratio assumed when the short link length ratio range was derived.

Table 5-2: Maximum Moment in Short Shear Links

Sample	Link Length Ratio, ρ	M_p [kN]	M_{max} [kN]		M_{max}/M_p	
			+ve	-ve	+ve	-ve
Short-1	1.13	295.22	241.89	241.50	0.819	0.818
Short-2	0.81	441.53	305.56	307.71	0.692	0.697
Short-3	0.50	240.48	106.39	106.44	0.442	0.443
Short-4	1.60	814.55	1,003.10	979.42	1.231	1.202
Short-5	1.21	164.84	170.59	168.29	1.035	1.021
Short-6	0.89	154.20	115.91	114.87	0.752	0.745
Short-7	1.52	792.03	1,021.90	1,014.30	1.290	1.281
Short-8	0.58	496.73	246.77	244.71	0.497	0.493
Short-9	1.36	333.41	384.41	385.78	1.153	1.157
Short-10	0.66	66.22	41.83	41.82	0.632	0.632
Short-11	1.29	383.39	369.97	366.36	0.965	0.956
Short-12	1.44	127.00	139.54	138.58	1.099	1.091
Short-13	1.05	140.99	128.78	127.68	0.913	0.906
Short-14	0.74	862.15	547.82	553.03	0.635	0.641
Short-15	0.97	1,045.01	906.28	910.69	0.867	0.871

5.2.1.3 Energy Dissipation and Ductility

The normalized energy dissipation capacity and the ductility ratio are shown below.

Table 5-3: Energy Dissipation and Ductility Ratio for Short Links

Sample	Link Length Ratio, ρ	E_e [kN.mm]	E_{total} [kN.mm]	E_{total}/E_e	μ
Short-1	1.13	554.52	1,083,098.75	1,953.21	37.64
Short-2	0.81	556.09	1,100,446.42	1,978.88	33.29
Short-3	0.50	174.33	566,751.48	3,251.06	50.31
Short-4	1.60	2,213.27	3,066,475.19	1,385.50	23.19
Short-5	1.21	337.36	743,621.02	2,204.26	36.27
Short-6	0.89	216.92	346,496.57	1,597.36	27.71
Short-7	1.52	2,071.90	6,315,347.89	3,048.10	45.60
Short-8	0.58	421.14	1,091,074.44	2,590.79	40.68
Short-9	1.36	780.87	2,399,088.43	3,072.34	47.71
Short-10	0.66	62.59	360,937.47	5,766.92	69.50
Short-11	1.29	846.94	957,293.03	1,130.29	17.42
Short-12	1.44	333.42	839,925.47	2,519.15	46.28
Short-13	1.05	240.58	562,654.85	2,338.77	36.72
Short-14	0.74	926.76	4,569,789.71	4,930.91	68.25
Short-15	0.97	1,533.97	4,727,836.99	3,082.10	48.17

5.2.1.4 Elastic Stiffness

The elastic stiffness from the finite element simulation is compared to the theoretical values calculated. The theoretical calculation is discussed in section 5.1.1.

Table 5-4: Elastic Stiffness of Short Shear Links

Sample	Link Length Ratio, ρ	K_e (kN/rad)		Difference
		Calculated	FE	
Short-1	1.13	169,202.86	162,643.67	4.03%
Short-2	0.81	283,775.96	271,338.67	4.58%
Short-3	0.50	162,525.69	157,353.33	3.29%
Short-4	1.60	399,344.53	385,244.52	3.66%
Short-5	1.21	127,478.28	121,593.33	4.84%
Short-6	0.89	131,212.00	125,313.33	4.71%
Short-7	1.52	332,481.05	322,469.33	3.10%
Short-8	0.58	286,362.78	276,911.79	3.41%
Short-9	1.36	200,174.43	192,880.00	3.78%
Short-10	0.66	84,200.28	80,704.00	4.33%
Short-11	1.29	200,767.71	193,435.25	3.79%
Short-12	1.44	99,020.41	94,762.67	4.49%
Short-13	1.05	112,818.66	108,070.08	4.39%
Short-14	0.74	488,056.13	470,779.73	3.67%
Short-15	0.97	632,985.24	605,013.33	4.62%

5.2.2 Intermediate Link Results

5.2.2.1 Observed Failures

The links Int-1, Int-4, Int-5, Int-7, Int-9, Int-11, Int-12, Int-13, Int-14, and Int-15 exhibited flange buckling before web buckling and their strength deteriorated faster after the web buckling occurred. The rest of the links exhibited web buckling before flange buckling. Flange and web buckling were confined to the end region in links Int-1, Int-4, Int-5, Int-7, Int-9, Int-12, and Int-13 where a high flexural moment is present. Web buckling outside of the end regions was observed for the rest of the links. It should be mentioned here that the links that experienced web buckling first and web buckling in the mid panels have a link length ratio below or close to 2. A representative deformed shape for the two cases is shown in the figures below.

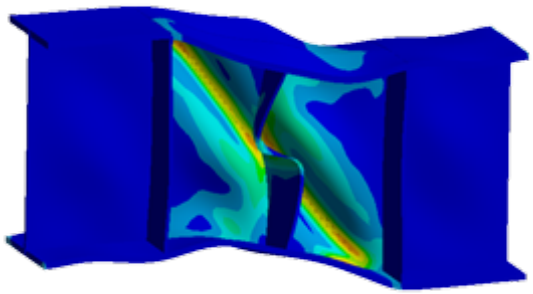

Figure 5-5: Deformed Geometry of Link Int-8

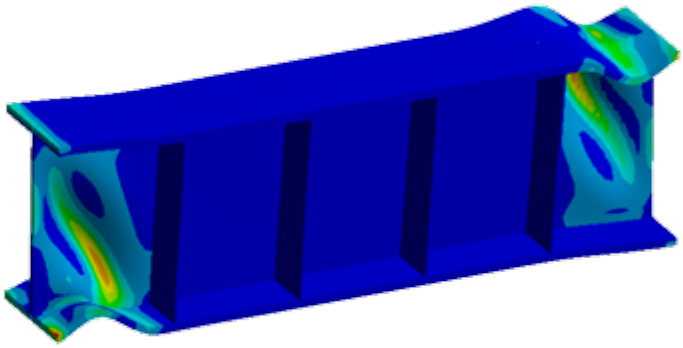

Figure 5-6: Deformed Geometry of Link Int-5

Only Int-8 stiffener suffered severe stiffener buckling and couldn't contain the tension field that was created by web buckling between the region bounded by the stiffener and it is shown in Figure 5-5. Int-5, Int-10, Int-12, Int-13, Int-14, and Int-5 stiffeners experienced a slight buckling. The rest didn't have a noticeable stiffener buckling. All the deformed geometry along with the equivalent plastic strain is shown in Appendix A.

5.2.2.2 Plastic Rotation Capacity and Overstrength

Almost half of the links had a plastic link rotation capacity greater than the required and an overstrength value greater than the recommended value. The maximum moments, maximum shear, overstrength ratio, and plastic rotation capacity that were observed in the analysis are shown in the tables below.

Table 5-5: Overstrength Ratio and Plastic Rotation Capacity for Intermediate Links

Sample	Link Length Ratio, ρ	V_n [kN]	V_{max} [kN]		Overstrength Factor Ω		γ_P [rad]	γ_P (FE) [rad]	
			+ve	-ve	+ve	-ve	Req.	+ve	-ve
Int-1	2.40	389.76	585.83	546.41	1.503	1.402	0.046	0.024	0.025
Int-2	2.01	845.03	1,254.30	1,172.40	1.484	1.387	0.063	0.064	0.049
Int-3	1.61	675.88	988.45	948.25	1.462	1.403	0.080	0.064	0.051
Int-4	3.00	808.03	1,438.70	1,361.40	1.781	1.685	0.020	0.024	0.025
Int-5	2.50	175.37	336.48	302.70	1.919	1.726	0.041	0.082	0.065
Int-6	2.11	1,710.04	2,407.50	2,256.30	1.408	1.319	0.058	0.025	0.026
Int-7	2.90	248.01	445.55	413.29	1.797	1.666	0.024	0.033	0.025
Int-8	1.71	422.32	648.15	596.71	1.535	1.413	0.075	0.064	0.059
Int-9	2.70	861.37	1,570.50	1,491.90	1.823	1.732	0.033	0.043	0.039
Int-10	1.81	2,176.67	3,318.00	3,217.70	1.524	1.478	0.071	0.105	0.088
Int-11	2.60	223.67	298.26	287.22	1.333	1.284	0.037	0.014	0.014
Int-12	2.80	855.07	1,636.90	1,605.60	1.914	1.878	0.029	0.085	0.064
Int-13	2.31	850.11	1,495.40	1,372.50	1.759	1.615	0.050	0.063	0.050
Int-14	1.91	243.75	375.09	371.81	1.539	1.525	0.067	0.105	0.086
Int-15	2.21	1,295.07	2,000.00	1,958.50	1.544	1.512	0.054	0.065	0.060

Table 5-6: Maximum Moment for Intermediate Links

Sample	Link Length Ratio, ρ	M_p [kN]	M_{max} [kN]		M_{max}/M_p	
			+ve	-ve	+ve	-ve
Int-1	2.40	240.48	356.98	339.05	1.484	1.410
Int-2	2.01	441.53	632.09	622.47	1.432	1.410
Int-3	1.61	383.39	442.95	436.40	1.155	1.138
Int-4	3.00	683.19	1,182.50	1,162.20	1.731	1.701
Int-5	2.50	57.79	104.54	102.27	1.809	1.770
Int-6	2.11	1,118.37	1,547.00	1,488.00	1.383	1.331
Int-7	2.90	140.99	248.36	237.02	1.762	1.681
Int-8	1.71	180.06	226.55	220.76	1.258	1.226
Int-9	2.70	792.03	1,425.40	1,378.20	1.800	1.740
Int-10	1.81	1,337.13	1,824.10	1,801.80	1.364	1.348
Int-11	2.60	107.70	139.75	139.31	1.298	1.294
Int-12	2.80	663.53	1,266.70	1,248.50	1.909	1.882
Int-13	2.31	621.85	1,030.20	1,029.90	1.657	1.656
Int-14	1.91	80.86	118.54	117.43	1.466	1.452
Int-15	2.21	817.84	1,256.60	1,240.40	1.536	1.517

5.2.2.3 Energy Dissipation and Ductility

The normalized energy dissipation capacity and ductility are shown in the table below.

Table 5-7: Energy Dissipation and Ductility Ratio for Intermediate Links

Sample	ρ	E_e	E_{total}	E_{total}/E_e	μ
		[kN.mm]	[kN.mm]		
Int-1	2.40	860.42	581,770.87	676.14	7.61
Int-2	2.01	1,429.93	1,586,658.64	1,109.60	16.53
Int-3	1.61	1,112.21	1,136,977.59	1,022.27	16.93
Int-4	3.00	1,962.67	1,994,598.32	1,016.27	9.41
Int-5	2.50	190.92	301,668.22	1,580.12	21.76
Int-6	2.11	3,208.50	2,620,614.96	816.77	8.98
Int-7	2.90	484.36	436,792.91	901.79	9.43
Int-8	1.71	552.82	572,985.18	1,036.48	17.67
Int-9	2.70	2,285.10	2,929,854.85	1,282.16	14.26
Int-10	1.81	3,750.87	6,626,409.60	1,766.63	29.61
Int-11	2.60	383.54	156,714.98	408.60	4.98
Int-12	2.80	1,823.32	3,059,667.52	1,678.07	24.93
Int-13	2.31	1,903.15	2,552,437.78	1,341.17	18.02
Int-14	1.91	272.80	413,930.07	1,517.35	25.67
Int-15	2.21	2,495.64	3,117,207.17	1,249.06	19.46

5.2.2.4 Elastic Stiffness

The elastic stiffness for the theoretical and finite element calculated are shown in the table below and it can be seen that the difference is smaller than the values observed for the short links.

Table 5-8: Elastic Stiffness of Intermediate Links

Sample	Link Length Ratio, ρ	K_e (kN/rad)		Difference
		Calculated	FE	
Int-1	2.40	91,770.471	89,786.550	2.21%
Int-2	2.01	202,261.403	195,732.120	3.34%
Int-3	1.61	183,016.642	177,330.205	3.21%
Int-4	3.00	232,110.034	228,281.150	1.68%
Int-5	2.50	43,275.573	42,125.391	2.73%
Int-6	2.11	453,524.654	440,044.800	3.06%
Int-7	2.90	61,454.060	60,330.678	1.86%
Int-8	1.71	110,039.239	106,007.617	3.80%
Int-9	2.70	231,529.902	228,128.448	1.49%
Int-10	1.81	600,721.840	578,960.000	3.76%
Int-11	2.60	53,890.428	52,697.100	2.26%
Int-12	2.80	235,175.532	230,506.730	2.03%
Int-13	2.31	220,094.362	215,846.798	1.97%
Int-14	1.91	57,959.205	56,041.267	3.42%
Int-15	2.21	337,167.869	327,296.890	3.02%

5.2.3 Long Link Results

5.2.3.1 Observed Failures

Flange buckling preceded web buckling in all of the analyzed samples except for the Long-3, Long-8, and Long-10 in which web buckling occurred first. These links have a link length ratio closer to the intermediate range. Lateral torsional buckling (LTB) occurred in the links Long-2 and Long-12 and it was the controlling failure mode in these links. The links closer to the intermediate-range (Long-3, Long-8, Long-10, and Long-14) experienced web buckling in the middle panels. In the links Long-3, Long-8, and Long-10 web buckling was severe and it was the controlling mode of failure for the three links. The web buckling is reflected in the shear-force vs plastic rotation graph of Link-3 in Figure 5-7. As can be seen from the graph and as explained in the short link results section, the temporary decrease in the load-carrying capacity of the link followed

by load-carrying capacity recovery seen in web buckled links is apparent in the V-γ_p graph of the Long-3 link. The deformed shape for an LTB, flange buckling, and web buckling failure mode is shown in Figure 5-8 up to 5-9. Stiffener buckling was slight in most of the links except for links Long-5 and Long-12 which suffered a relatively high stiffener buckling that didn't adversely affect the links' behavior. The deformed shapes and the shear-force vs plastic rotation for all of the links can be found in Appendix A and B.

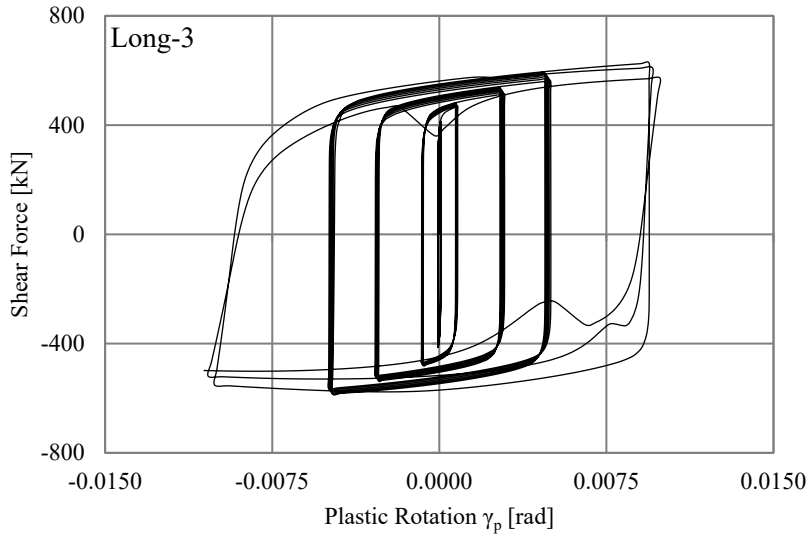

Figure 5-7: Shear Force vs Plastic Rotation Graph for Link Long-3

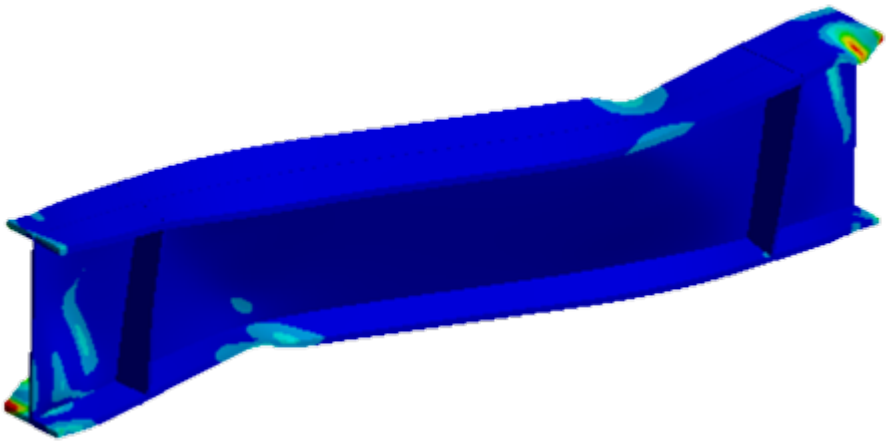

Figure 5-8: Deformed shape for Link Long-12

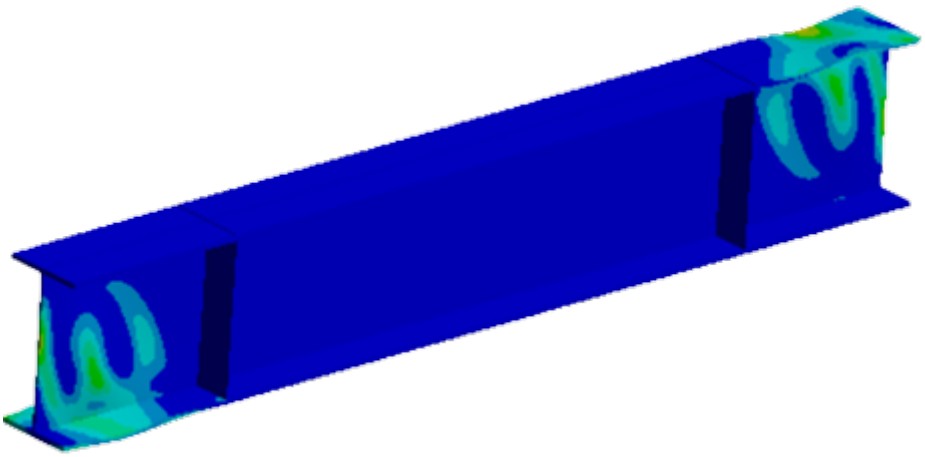

Figure 5-9: Deformed shape for Link Long-11

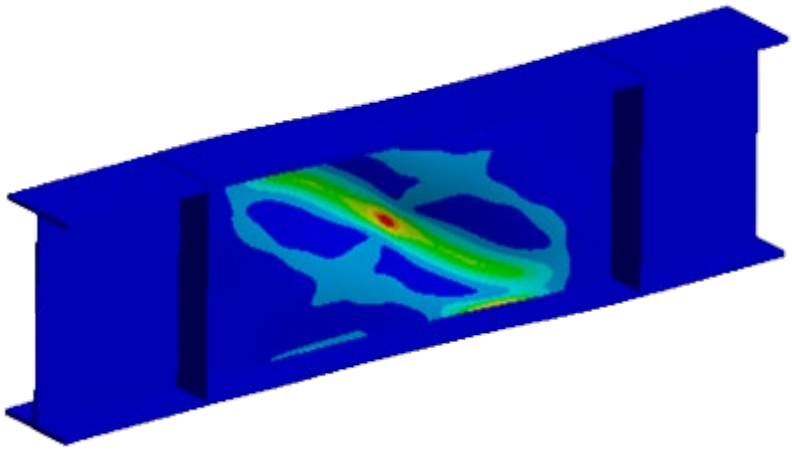

Figure 5-10: Deformed shape for Link Long-3

5.2.3.2 Plastic Rotation Capacity and Overstrength

Half of the links have plastic link rotation capacity less than the required while all of the links with exception of 4 links have an overstrength value greater than the recommended value. The maximum moments, maximum shear, overstrength ratio, and plastic rotation capacity that were observed in the analysis are shown in the tables below.

Table 5-9: Overstrength Ratio and Plastic Rotation Capacity for Long Links

Sample	Link Length Ratio, ρ	V_n [kN]	V_{max} [kN]		Overstrength Factor Ω		γ_P [rad]	γ_P (FE) [rad]	
			+ve	-ve	+ve	-ve	Req.	+ve	-ve
Long-1	4.15	226.01	387.25	363.52	1.713	1.608	0.02	0.012	0.014
Long-2	3.58	474.00	955.04	885.39	2.015	1.868	0.02	0.042	0.039
Long-3	3.01	448.94	627.08	583.59	1.397	1.300	0.02	0.010	0.011
Long-4	5.00	484.70	863.02	795.06	1.781	1.640	0.02	0.013	0.013
Long-5	4.29	102.46	211.86	190.46	2.068	1.859	0.02	0.041	0.036
Long-6	3.72	968.29	1,794.40	1,723.10	1.853	1.780	0.02	0.023	0.025
Long-7	4.86	148.10	256.73	238.46	1.733	1.610	0.02	0.012	0.013
Long-8	3.15	267.94	414.09	385.11	1.545	1.437	0.02	0.014	0.015
Long-9	4.57	508.85	960.54	897.16	1.888	1.763	0.02	0.022	0.018
Long-10	3.29	1,321.27	2,816.60	2,710.50	2.132	2.051	0.02	0.063	0.057
Long-11	4.43	131.34	158.61	152.74	1.208	1.163	0.02	0.004	0.005
Long-12	4.72	507.87	1,093.20	1,074.30	2.153	2.115	0.02	0.063	0.043
Long-13	4.01	489.26	637.67	609.75	1.303	1.246	0.02	0.005	0.006
Long-14	3.44	141.74	259.81	256.77	1.833	1.812	0.02	0.061	0.043
Long-15	3.86	739.79	1,649.70	1,590.40	2.230	2.150	0.02	0.084	0.069

Table 5-10: Maximum Moment for Long Links

Sample	Link Length Ratio, ρ	M_p [kN]	M_{max} [kN]		M_{max}/M_p	
			+ve	-ve	+ve	-ve
Long-1	4.15	240.48	403.94	391.86	1.680	1.629
Long-2	3.58	441.53	848.39	841.77	1.921	1.906
Long-3	3.01	383.39	528.65	501.47	1.379	1.308
Long-4	5.00	683.19	1,178.00	1,135.80	1.724	1.662
Long-5	4.29	57.79	113.46	110.33	1.963	1.909
Long-6	3.72	1,118.37	2,009.00	2,009.70	1.796	1.797
Long-7	4.86	140.99	237.96	229.30	1.688	1.626
Long-8	3.15	180.06	271.71	261.78	1.509	1.454
Long-9	4.57	792.03	1,475.80	1,404.20	1.863	1.773
Long-10	3.29	1,337.13	2,797.90	2,803.00	2.092	2.096
Long-11	4.43	107.70	127.61	134.74	1.185	1.251
Long-12	4.72	663.53	1,419.60	1,410.10	2.139	2.125
Long-13	4.01	621.85	794.68	778.19	1.278	1.251
Long-14	3.44	80.86	148.13	146.48	1.832	1.811
Long-15	3.86	817.84	1,798.80	1,770.60	2.199	2.165

5.2.3.3 Energy Dissipation and Ductility

Table 5-11: Energy Dissipation and Ductility Ratio for Long Links

Sample	Link Length Ratio, ρ	E_e [kN.mm]	E_{total} [kN.mm]	E_{total}/E_e	μ
Long-1	4.15	1,044.11	501,250.35	480.07	4.35
Long-2	3.58	1,516.87	1,718,954.44	1,133.22	13.15
Long-3	3.01	1,340.83	476,880.39	355.66	4.28
Long-4	5.00	2,254.40	1,201,412.24	532.92	5.43
Long-5	4.29	225.27	222,357.03	987.08	11.06
Long-6	3.72	3,484.65	3,061,675.54	878.62	8.91
Long-7	4.86	620.30	268,666.34	433.13	4.35
Long-8	3.15	653.62	316,878.75	484.81	5.43
Long-9	4.57	2,833.95	2,067,837.44	729.67	7.36
Long-10	3.29	3,252.09	6,761,276.88	2,079.05	22.68
Long-11	4.43	423.87	88,161.18	207.99	2.06
Long-12	4.72	2,401.69	3,036,108.42	1,264.16	16.57
Long-13	4.01	2,157.33	444,885.51	206.22	2.78
Long-14	3.44	317.96	326,022.49	1,025.36	14.01
Long-15	3.86	2,210.43	5,067,237.60	2,292.42	25.76

5.2.3.4 Elastic Stiffness

Table 5-12: Elastic Stiffness of Long Links

Sample	Link Length Ratio, ρ	K_e (kN/rad)		Difference
		Calculated	FE	
Long-1	4.15	48,344.657	48,211.736	0.28%
Long-2	3.58	115,642.653	114,662.843	0.85%
Long-3	3.01	113,780.577	112,245.864	1.37%
Long-4	5.00	126,828.418	127,114.550	-0.23%
Long-5	4.29	22,973.793	22,917.661	0.24%
Long-6	3.72	275,624.271	273,675.093	0.71%
Long-7	4.86	31,586.249	31,586.322	0.00%
Long-8	3.15	66,428.612	65,424.889	1.53%
Long-9	4.57	126,537.179	126,585.658	-0.04%
Long-10	3.29	384,940.468	379,963.653	1.31%
Long-11	4.43	28,040.370	28,076.069	-0.13%
Long-12	4.72	127,972.203	128,055.569	-0.07%
Long-13	4.01	125,580.825	125,272.930	0.25%
Long-14	3.44	32,835.966	32,477.856	1.10%
Long-15	3.86	195,288.268	194,257.463	0.53%

5.3 Discussion

The results presented in the previous section will be discussed in-depth for each link type (Short, Intermediate, and long) and an overall comparison between the link type behavior will also be discussed. Scatter plots will be used to see a trend and relation between the input and the output variables.

5.3.1 Short Links

5.3.1.1 Plastic Rotation Capacity and Overstrength

As shown in Table 5-1 the link overstrength surpassed the code-defined overstrength value of 1.5 in all but one of the links in the positive cycle and all but 3 of the links in the negative cycle. A similar trend was observed for the link plastic rotation capacity. A scatter plot of the positive and negative plastic rotation capacity to the parameters used in the study is shown in the figures below.

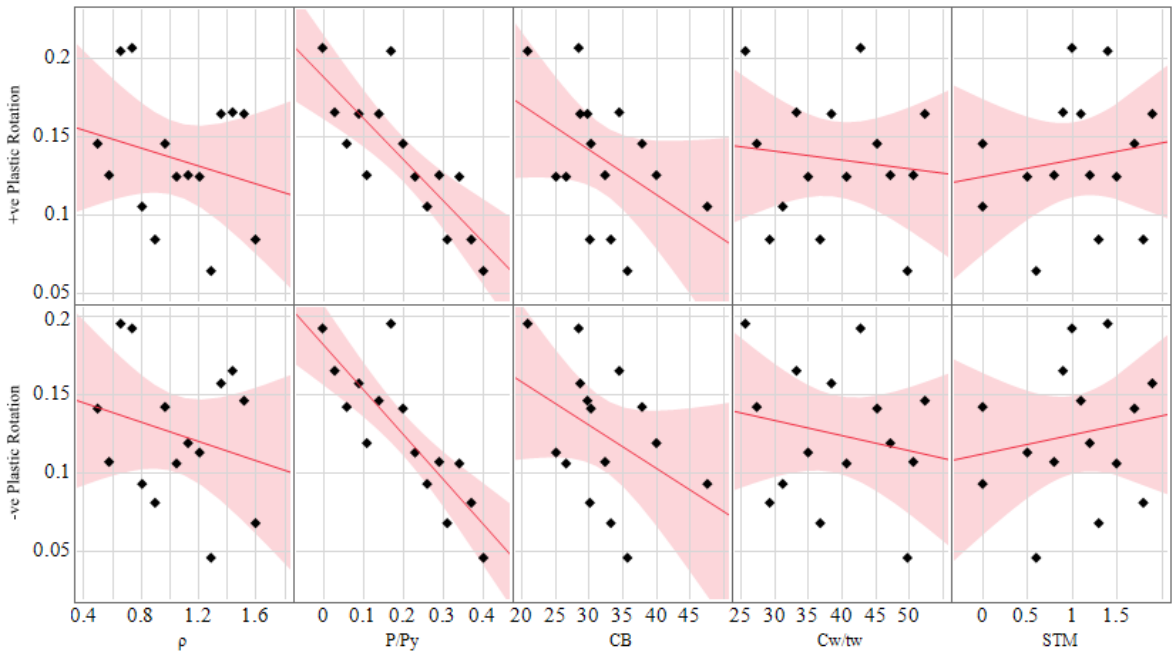

Figure 5-11: Scatter Plot of +ve and -ve Plastic Rotation Capacity vs Parameters for Short Links

The scatter plot above also shows a trend line (linear regression) to predict the relation between the parameters and the positive and negative plastic rotation. As can be seen from the scatter plot the plastic rotation capacity in both the positive and negative cycle is negatively influenced by the axial load ratio and stiffener spacing constant. The scatter plot for the plastic rotation capacity vs axial load ratio and stiffener spacing constant

show a better trend than the rest of the parameters i.e., almost all of the sample's plastic rotation capacity decrease with the increasing axial load ratio and stiffener spacing constant.

The plastic rotation capacity decreased with increasing link length ratio but the decrease was slight and the fit to the trend line is small. This could mean that the influence of the link length ratio on the plastic rotation capacity is slight. Regardless of the scatter plot the links with a link length ratio less than one have a plastic rotation capacity on average greater than (14% and 18% for positive and negative cycles respectively) the links with a link length ratio greater than 1.

A slight decrease and a slight increase in plastic rotation capacity were observed when the web slenderness and stiffener thickness multiplier (STM) was increased respectively.

A thin stiffener won't contain the web buckling inside the region between two successive stiffeners. In the links where severe stiffener buckling occurred the web buckling was contained between the stiffener links until the stiffeners buckled. When stiffener buckles and it is no longer capable of containing the web buckling within the stiffener regions, it acts as if the stiffener spacing has increased since the buckled stiffener no longer has a significant influence in arresting the web buckling. This might explain the slight plastic rotation capacity increase with increasing stiffener thickness.

The overstrength scatter plot is shown in the figure below. In the axial load vs overstrength scatter plot it can be seen that the direction of the slope’s changes for the positive and negative cycle which means that tensile axial load increases overstrength while compressive axial load decreases overstrength. This observation is in line with previous experiments (discussed in chapter 2) where it was hypothesized that tensile axial load increases overstrength in shear links.

The overstrength for both the negative and positive cycles decreased when the link length ratio increased. It was discussed in chapter 2 that very short shear links have a high overstrength value and a similar observation was made here too. The very short links in this study exhibited an overstrength value (on average) of 9% and 10% higher than the short links with link length ratio greater than 1 in the positive and negative cycle respectively.

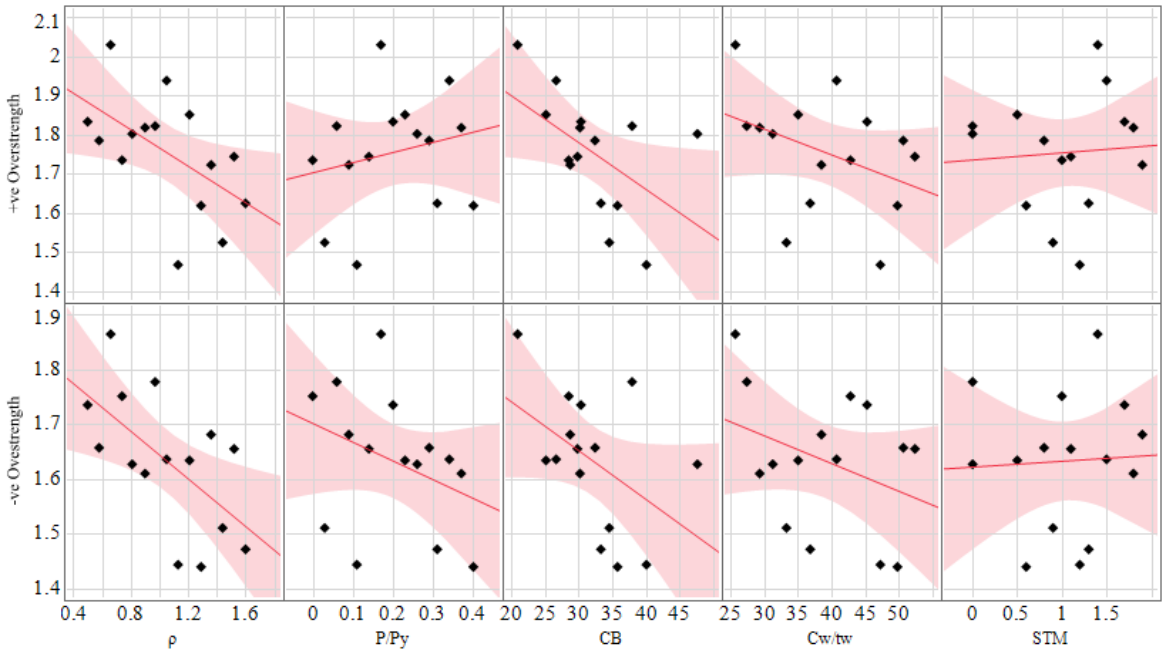

Figure 5-12: Scatter Plot of +ve and -ve Overstrength Ratio vs Parameters for Short Links

It can also be seen from the figure that overdesigning i.e., providing too many stiffeners increases the overstrength ratio. While having a compact section with a higher stiffener thickness also slightly increases the overstrength ratio.

5.3.1.2 Energy Dissipation Capacity and Ductility

The normalized energy dissipation and ductility scatter plot is shown in the figure below. The ductility and the normalized energy dissipation capacity almost mirror one another in their response to the parameter variation. Link length ratio, axial load ratio, and stiffener spacing constant decrease the ductility and energy dissipation as they increase.

The scatter for the slenderness ratio and stiffener thickness shows a slight gain in energy dissipation capacity and ductility as the web slenderness ratio decreases and as the stiffener thickness increases.

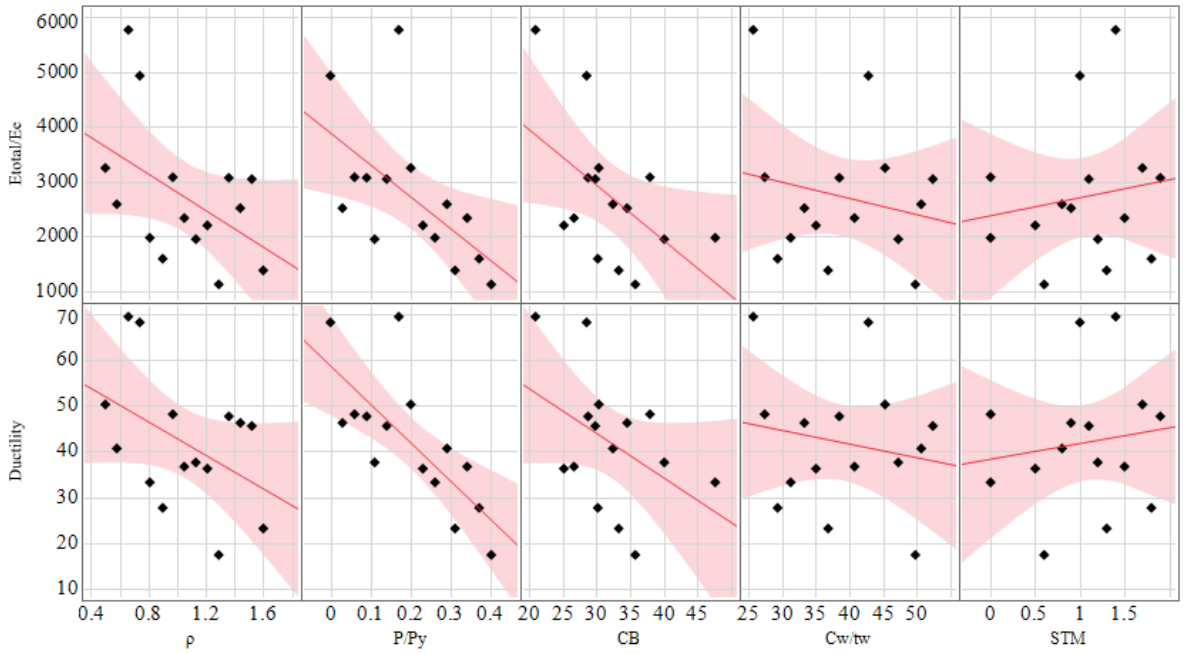

Figure 5-13: Scatter Plot of E_{total}/E_e and Ductility vs Parameter for Short Links

5.3.2 Intermediate Links

5.3.2.1 Plastic Rotation Capacity and Overstrength

As discussed earlier 11 out of the 15 intermediate samples have an overstrength ratio above the recommended value of 1.5 and all but 7 samples have a plastic rotation capacity less than the required. The scatter plot of the positive and negative plastic rotation capacity to the parameters in the study is shown in the graph below.

From the graph, it can be seen that the plastic rotation capacity for both the positive and negative cycle decreases with an increasing link length ratio. This observation is the same as previous experiments and the code specified plastic rotation capacities for intermediate links where plastic rotation capacity decreases with increasing link length ratio. The plastic rotation capacity also decreases when stiffener spacing increases. Both axial load ratio and flange slenderness decrease plastic rotation capacity when they increase.

The stiffener thickness multiplier vs plastic rotation capacity scatter plot doesn't show a considerable amount of trend. In the result, it was shown that not many of the stiffeners buckled or failed to stop the plastic deformations being formed within the stiffener spacing region. Only the link Int-8 stiffener suffered severe buckling. This link has a link

length ratio of 1.71 and the stiffener buckling affected the link's behavior in the same way as the short links with buckled stiffener did in the last section. So, this means that stiffener thickness doesn't affect the plastic rotation capacity significantly.

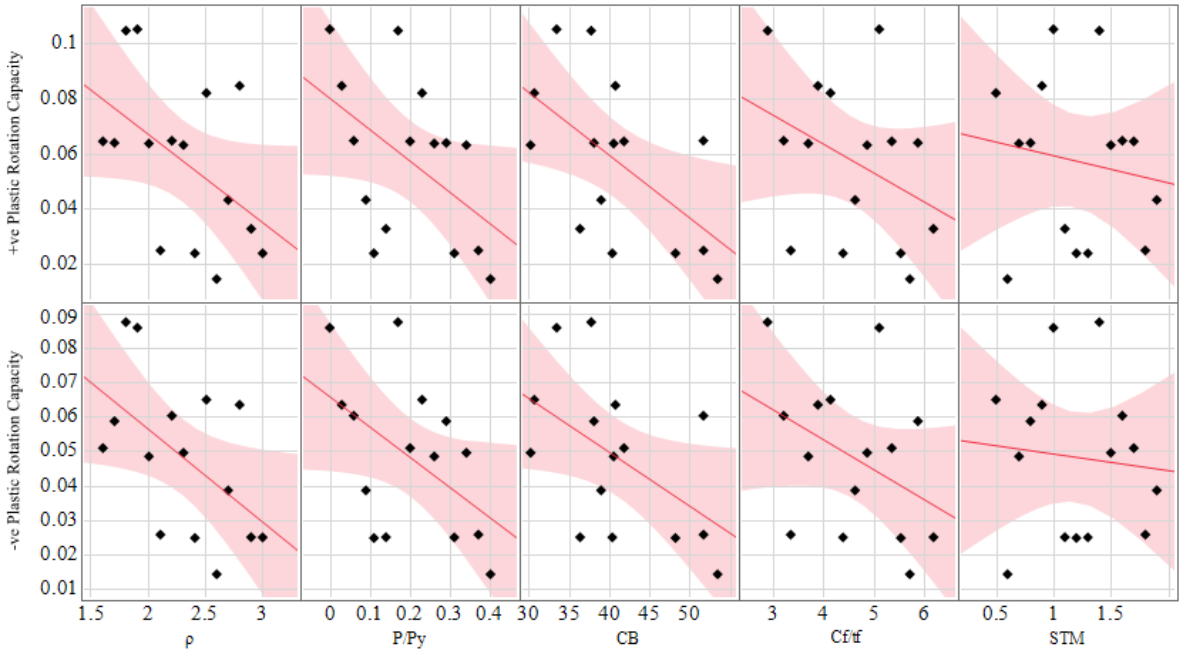

Figure 5-14: Scatter Plot of +ve and -ve Plastic Rotation Capacity vs Parameters for Intermediate Links

The scatter plot for the overstrength ratio is shown in the figure below. In the figure, it can be seen that the overstrength ratio increases when the link length ratio increases. This apparent increase in the overstrength ratio is the result of the high shear-moment interaction that is present in the intermediate link. This issue was discussed in chapter 2 where experimental results showed a lower overstrength value in the region of the link with a link length ratio of 1.6-2.4 (where high shear-moment interaction is apparent) and a slight increase in overstrength ratio beyond this range. The same observation was made here where the links with a link length ratio less than 2.4 have a 1.53 average overstrength ratio for the positive cycle and a 1.45 average overstrength ratio for the negative cycle. While links with a link length ratio greater than 2.4 have an average overstrength ratio of 1.76 and 1.66 for the positive and negative cycles respectively.

The scatter plot for the overstrength ratio vs stiffener spacing constant shows that the overstrength increases with increasing the stiffener spacing constant, which means overdesigning leads to a higher overstrength.

Overstrength also decreases with increasing axial load ratio. Both the positive and negative cycles have the same slope which is different from the observation made in the short links.

A slight decrease in the overstrength ratio is observed with an increasing flange slenderness ratio.

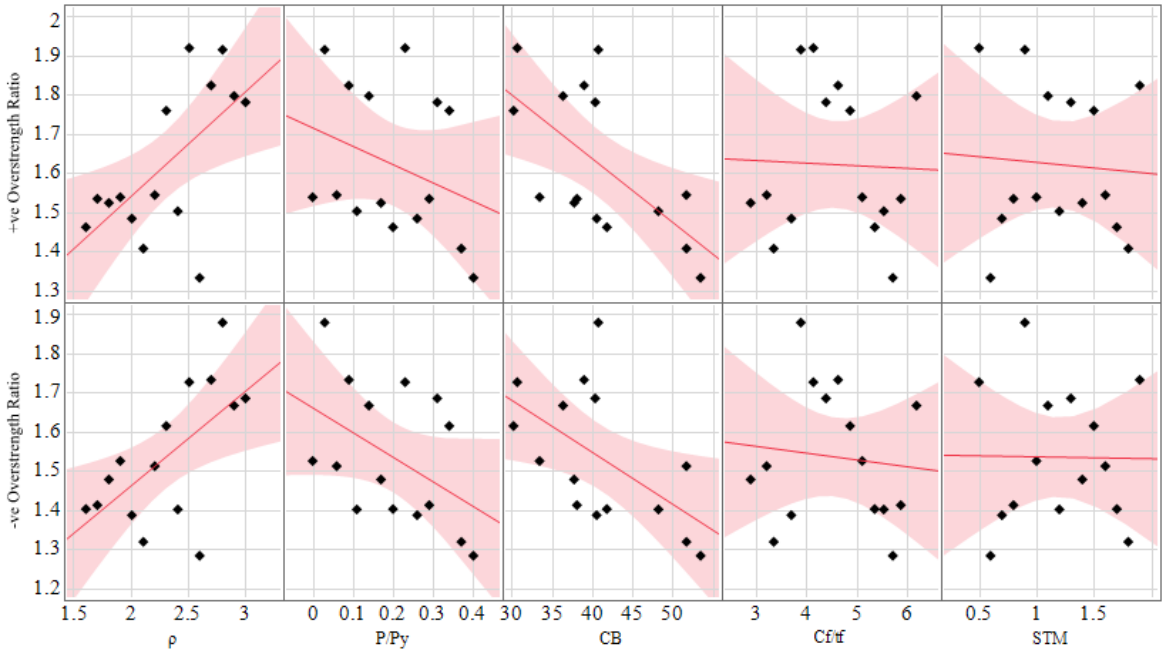

Figure 5-15: Scatter Plot of +ve and -ve Overstrength Ratio vs Parameters for Intermediate Links

5.3.2.2 Energy Dissipation Capacity and Ductility

From the scatter plot it is can be deduced that having a compact flange section with closely spaced stiffener with a small axial load will dissipate more energy and is also more ductile.

An increase in the link length ratio decreases ductility. This is due to the decrease in the plastic rotation capacity when the link length ratio was increased which was observed earlier. A decrease in plastic rotation capacity implicitly means a decrease in ultimate rotation capacity which is one of the variables used in ductility calculation. The same

wasn't observed for the normalized energy dissipation capacity. The reason for this is that lower overstrength values were observed when the link length ratio was decreased. This means the links with smaller link length ratios developed a smaller maximum shear force for a larger deformation and the links with a longer link length ratio developed a higher shear force for a smaller deformation. The implication of this is that the area under the shear-deformation hysteretic plot used to calculate total energy dissipated can't show as a definitive trend with an increasing link length ratio as ductility has shown.

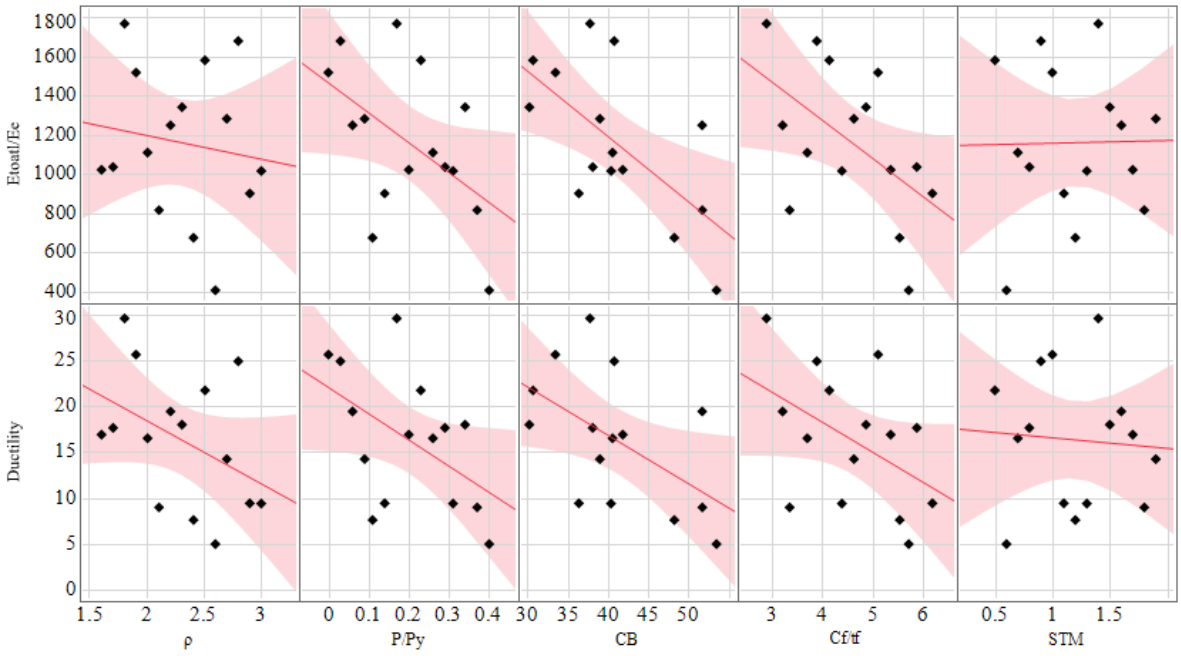

Figure 5-16: Scatter Plot of E_{total}/E_e and Ductility vs Parameter for Intermediate Links

5.3.2.3 Other Observations

The link Int-4 and Int-13 with a link length ratio 3 and 2.3 respectively which have a high axial load ratio, an average flange slenderness ratio, slightly higher stiffness thickness than required, and closely spaced stiffeners performed very well. As discussed earlier the axial load ratio affects the plastic rotation capacity of the links. These observations signify that closely spaced stiffeners help the links achieve their required plastic rotation capacity with a higher overstrength ratio.

Intermediate links also need to obey the end stiffener spacing recommendation (1.5b from the ends) set by seismic codes. In this research, this parameter wasn't considered as a direct parameter but the stiffener spacing constant range was chosen so that half of the generated link samples obey the end stiffener criteria while the rest didn't. The scatter

plot of the end stiffener spacing multiplier to the output parameters is shown in the figure below. It can be seen here that the end stiffener spacing doesn't greatly affect the plastic rotation capacity, energy dissipation, and ductility that much since the graph doesn't show a considerable amount of trend, but the overstrength ratio shows a slight decrease with increasing end stiffener spacing multiplier.

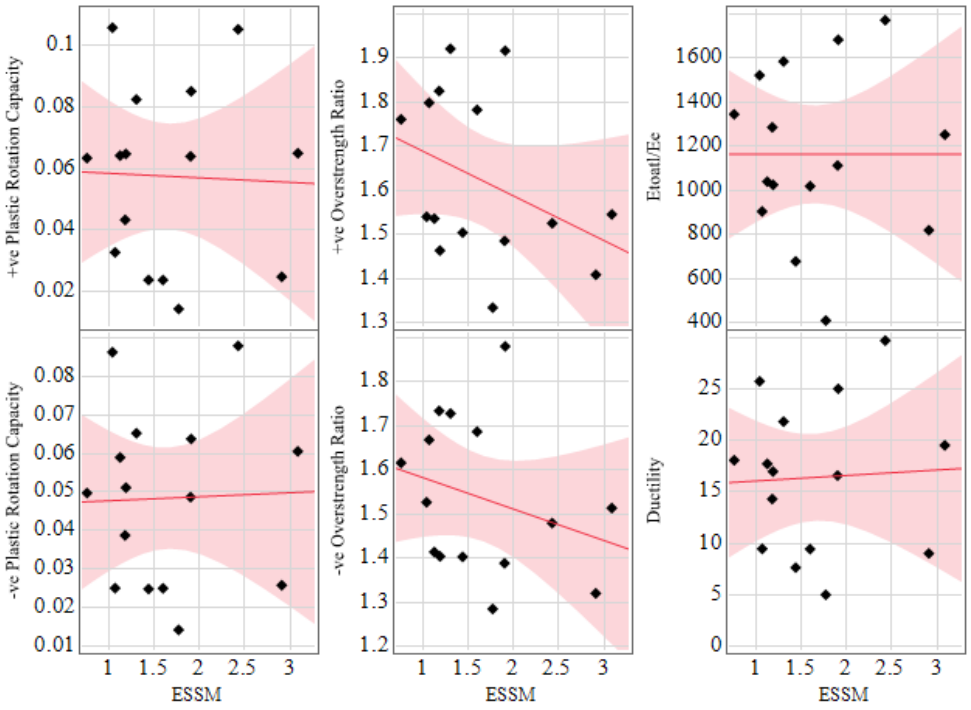

Figure 5-17: Scatter Plot of End Stiffener Spacing Multiplier to the output parameters

5.3.3 Long Links

5.3.3.1 Plastic Rotation Capacity and Overstrength

The plastic rotation capacity and overstrength ratio exceeded the required limit for most of the samples as discussed in the previous section. The scatter plot for the plastic rotation vs the parameters is shown below.

In the graph, it can be seen that the plastic rotation capacity decreases with increasing axial load ratio and flange slenderness ratio the most. While the link plastic rotation capacity moderately decreases with increasing link length ratio.

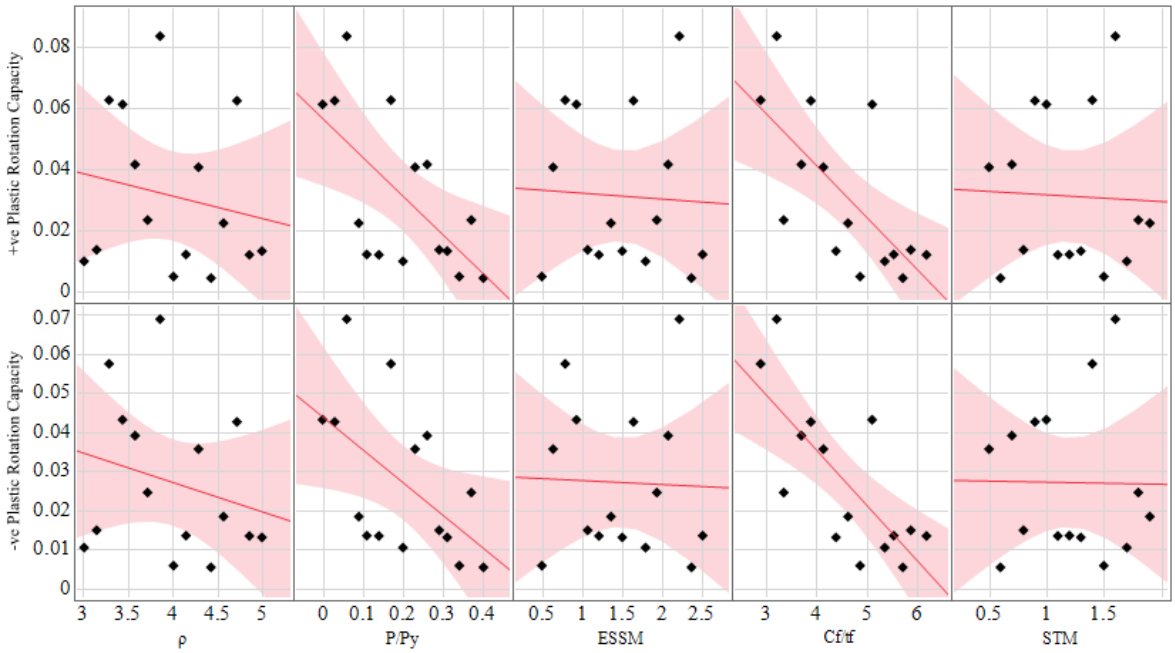

Figure 5-18: Scatter Plot of +ve and -ve Plastic Rotation Capacity vs Parameters for Long Links

The stiffener spacing and thickness multiplier didn't show any trend and exhibited a minimal effect on the plastic rotation capacity.

The scatter-plot of the overstrength ratio to the parameters shows that increasing axial load ratio and flange slenderness ratio decreases the overstrength ratio. The scatter for the two parameters shows a good trend.

The link overstrength ratio slightly increases with increasing link length ratio. As discussed for intermediate links overstrength ratio is smaller in the intermediate range due to moment shear interaction, therefore in the long links near the intermediate link range where there is still some moment shear interaction the overstrength will be lower and the overstrength will increase when the interaction fades away with the increase of link length ratio.

The stiffener spacing and thickness multiplier didn't show any trend and they exhibited a minimal effect on the overstrength ratio.

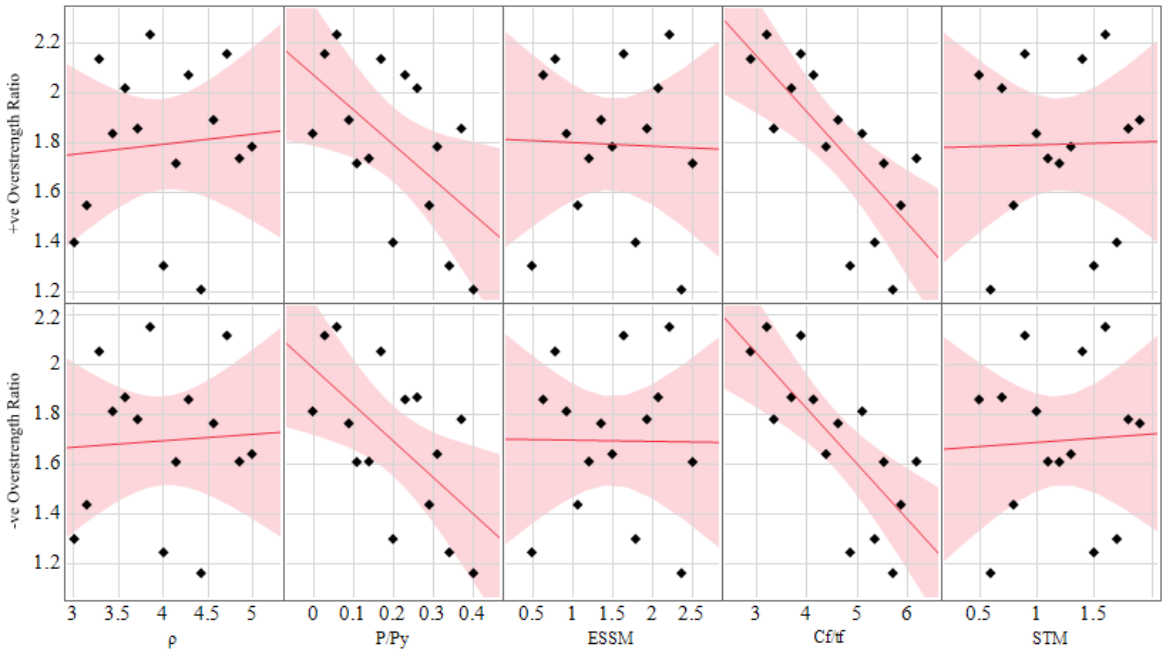

Figure 5-19: Scatter Plot of +ve and -ve Overstrength Ratio vs Parameters for Long Links

5.3.3.2 Energy Dissipation Capacity and Ductility

The normalized energy dissipation capacity and ductility show a similar trend where they both decrease with increasing axial load ratio and flange slenderness ratio. A moderate loss of ductility and energy dissipation capacity is observed when link length is increased. A moderately positive effect in normalized energy dissipation capacity and ductility is noticed when the stiffener thickness was increased.

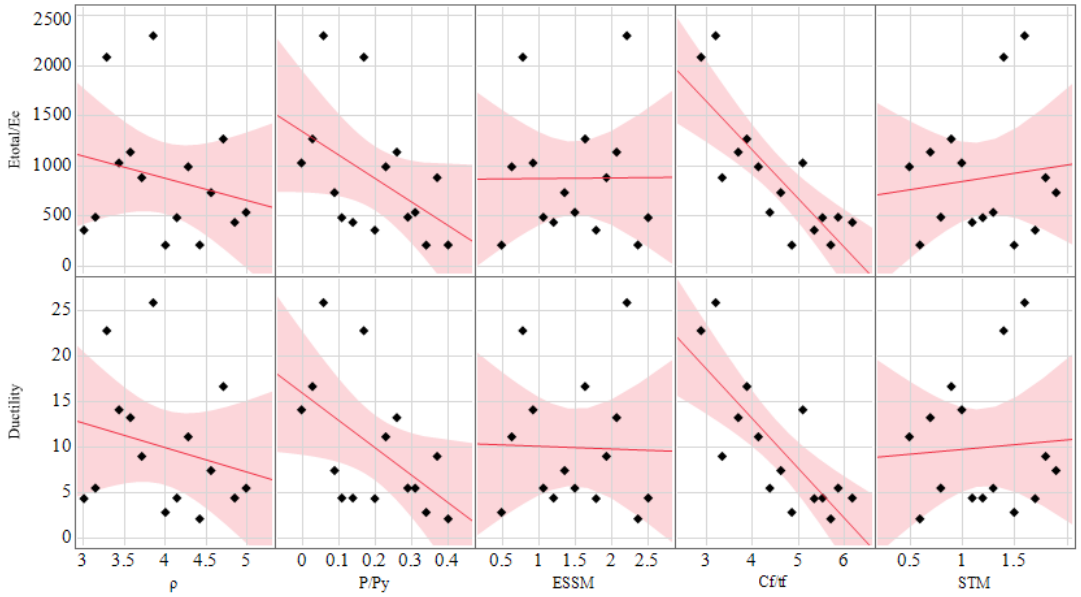

Figure 5-20: Scatter Plot of E_{total}/E_e and Ductility vs Parameter for Long Links

5.3.3.3 Other Observations

The links Long-3, Long-8, and Long-10 failed by web buckling as discussed in the results section of this chapter. All the links that failed by web buckling have a link length ratio closer to the intermediate range. In this range, there is still some moment shear interaction that could affect the failure of the links. All the links experienced a high shear force very close to V_p. The link long-10 went through high rotations and thus developed a high shear force than usual. Long 8 which has a large web slenderness ratio with a link length ratio closer to the intermediate link range underwent a small amount of rotation but still developed a high shear force. This could mean in the long links closer to the intermediate link range might need a web stiffener in the middle panel since shear yielding and web buckling are still active.

Long-3 has a link length ratio of 3.01 which is essentially an intermediate link, so the shear yielding and web buckling are still important.

The questionable performance of the Links Long-3 and Long-8 coupled with the excellent performance of Int-4 and Int-13 which are closer to the long link range limit implies that adding an intermediate stiffener might be beneficial for the long links with a link length ratio close to 3.

5.3.4 Overall Link Behavior

In this section, a comparison between the Short, Intermediate, and long links will be made. Figure 5-21 and Figure 5-22 show the plastic rotation capacity vs the link length ratio for the positive and negative cycle respectively.

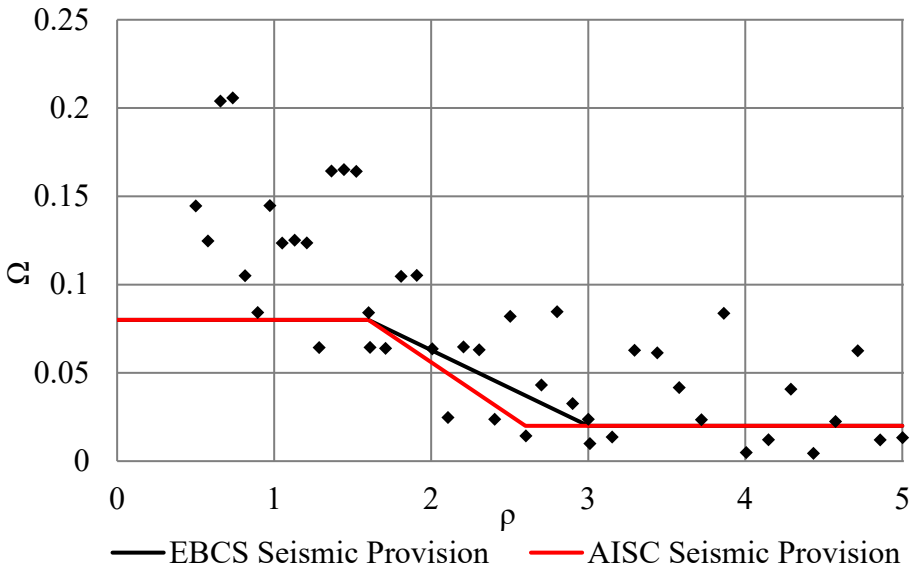

Figure 5-21: Plastic Rotation Capacity vs Link Length Ratio in the Positive Cycle

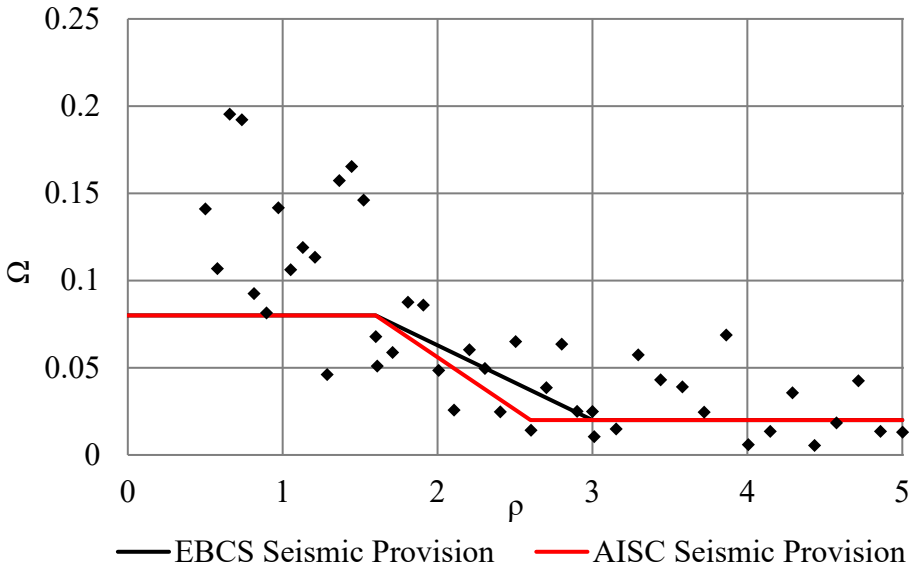

Figure 5-22: Plastic Rotation Capacity vs Link Length Ratio in the Negative Cycle

The code specified plastic Rotation capacity was specified by setting a lower bound on all the experimental data gathered on plastic rotation capacity. Thus, from the graph, it can be seen that short links performed significantly better than the intermediate and long links since almost all of the links' plastic rotation capacity was above the lower bound set by previous experiments and seismic codes. This implies that short links can perform better under varying conditions (for example under high axial load) than the longer links.

This is also true for intermediate and long links where a smaller number of links for the intermediate links fall below the line than long links.

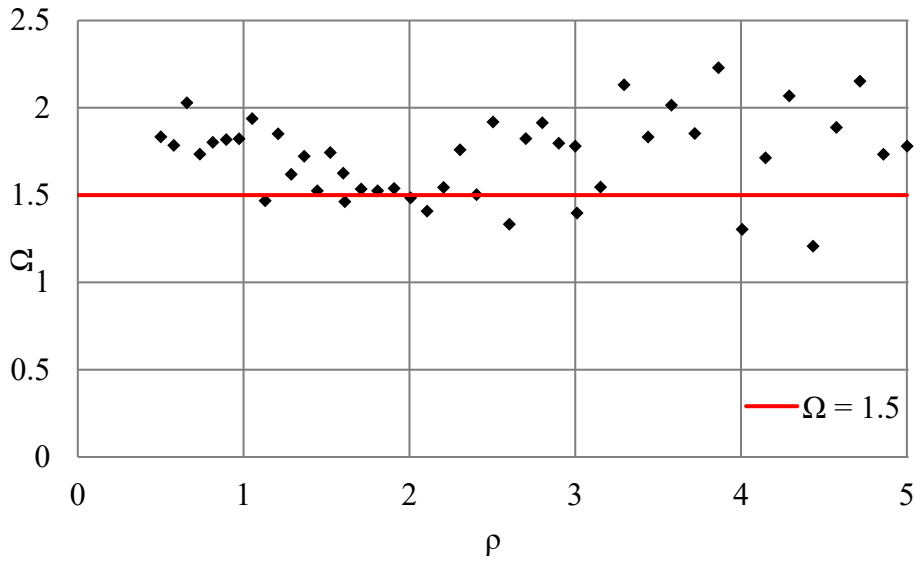

Figure 5-23: Overstrength Factors vs Link Length Ratio in the Positive Cycle

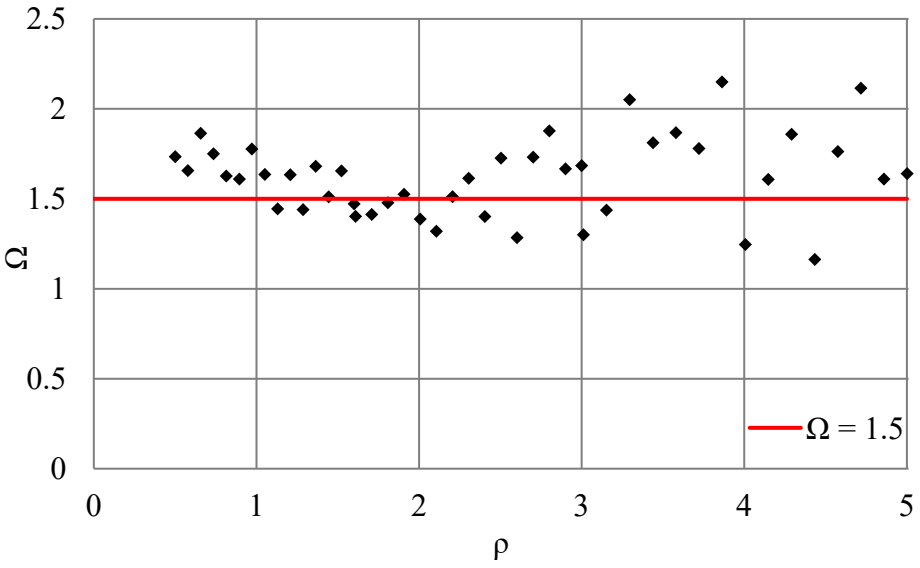

Figure 5-24: Overstrength Factors vs Link Length Ratio in the Negative Cycle

The above figures show the overstrength ratio vs the link length ratio for all of the links in this research. It can be seen in the graph the lower overstrength ratio experienced in the link length ratio range of 1.6-2.4. It was shown in chapter 2 that in this link length

range ($1.6 < \rho < 2.4$) the moment shear interaction is high and the overstrength is low as a result of this interaction. This is reflected in this graph even though the overstrength values here are higher than the values reported in previous experimental studies.

Seismic provisions usually prohibit calculation of overstrength value only using isolated links since the overstrength value is affected by beam, brace, and connections outside of the link. Thus, the overstrength results using an isolated link will be higher than the actual. The other factor that might contribute to the high overstrength is that the links are not under the normal design requirements meaning there is some level of over-designing in the links. Another factor which was also mentioned by Mohebkhah and Chegeni (Mohebkhah & Chegeni, 2014) in their research is that most of the test conducted in the development of the design method for EBF links is conducted on American wide flange sections, and in their research, they put forward the idea that the overstrength ratio for IPE sections should be higher than the one currently in use. They suggested increasing the overstrength ratio by 10% for IPE sections.

Another interesting thing that was noticed was that in the overstrength vs axial load ratio scatterplot for short links the overstrength ratio in the positive cycle increased when the axial load ratio was increased. This trend was not seen in the scatter plots for intermediate and long links but a further look into the shear force-plastic deformation diagram of long and intermediate links revealed that in the positive cycle the graph was still hardening when the negative cycle was in the softening range. To visualize this hardening behavior under the positive (tensile axial load) cycle, intermediate and long links with a high axial load ratio were loaded beyond what was defined as the failure point in this paper (when 80% of max shear is reached). All of the links were loaded with the next rotation in the loading protocol while keeping the axial load the same as the last load step. For example, the original link Int-4 last applied rotation was 0.04 rad so the next rotation in the cyclic loading protocol is 1 cycle of 0.05 rad and that is what is applied to the original link while keeping the axial load the same as the axial load applied at the rotation 0.04 rad. In the figures below, it can be seen clearly that in the positive (tensile axial load) cycle the links were still hardening and thereby achieving a higher overstrength ratio. This shows that tensile axial load increases the overstrength of links. In the scatterplot, this could not be seen because the max shear in the positive cycle is taken as the last maximum shear achieved in the link in the positive cycle before

failure in the negative cycle occurs which was usually when failure was observed. Since an increase in axial load ratio decreases the overstrength ratio in the negative cycle and how much overstrength that can develop in the positive cycle is bounded by the negative cycle the scatter plot for the positive overstrength ratio vs axial load ratio will follow the same trend as a negative one.

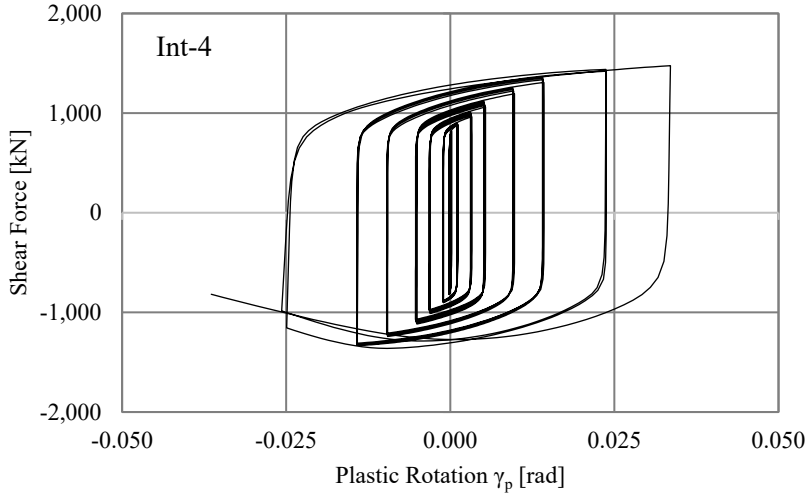

Figure 5-25: Shear-Force vs Plastic Rotation Graph for Link Int-4

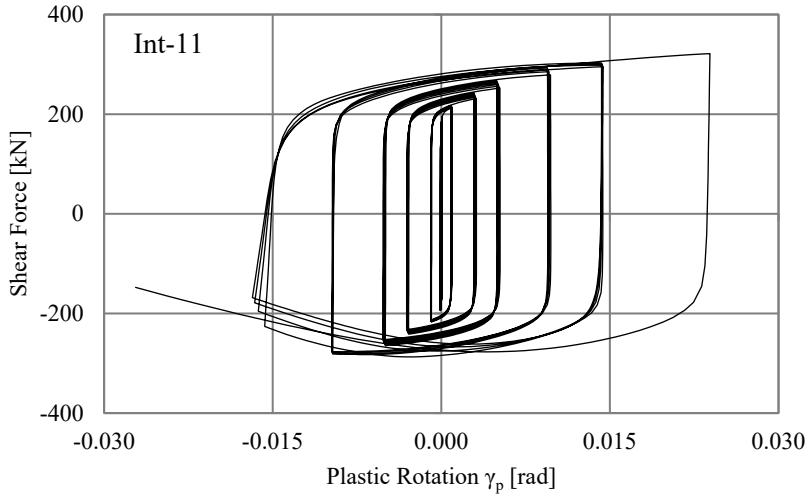

Figure 5-26: Shear-Force vs Plastic Rotation Graph for Link Int-11

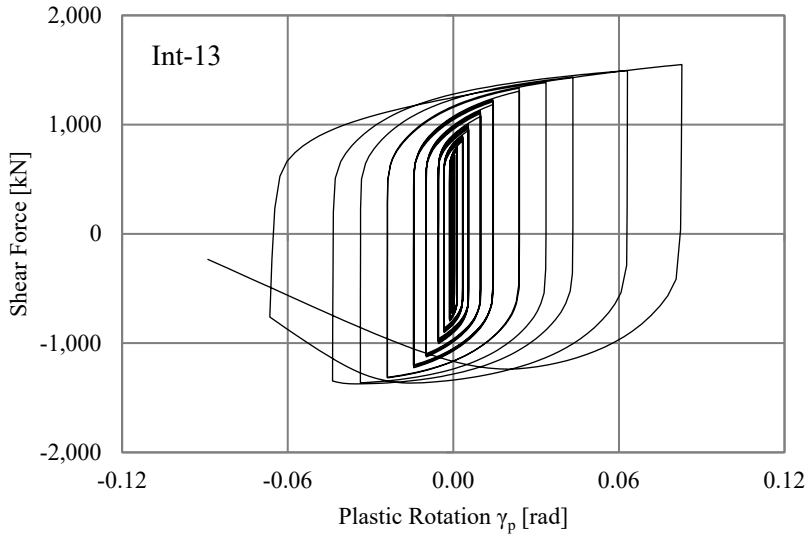

Figure 5-27: Shear-Force vs Plastic Rotation Graph for Link Int-13

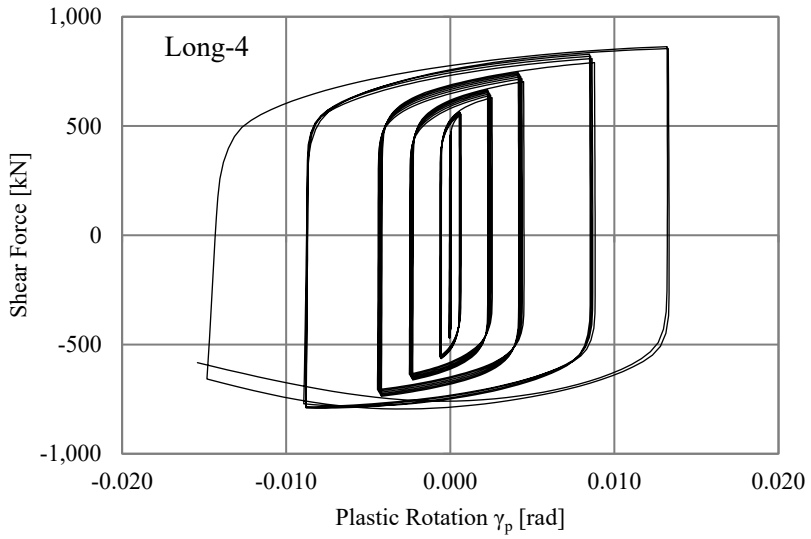

Figure 5-28: Shear-Force vs Plastic Rotation Graph for Link Long-4

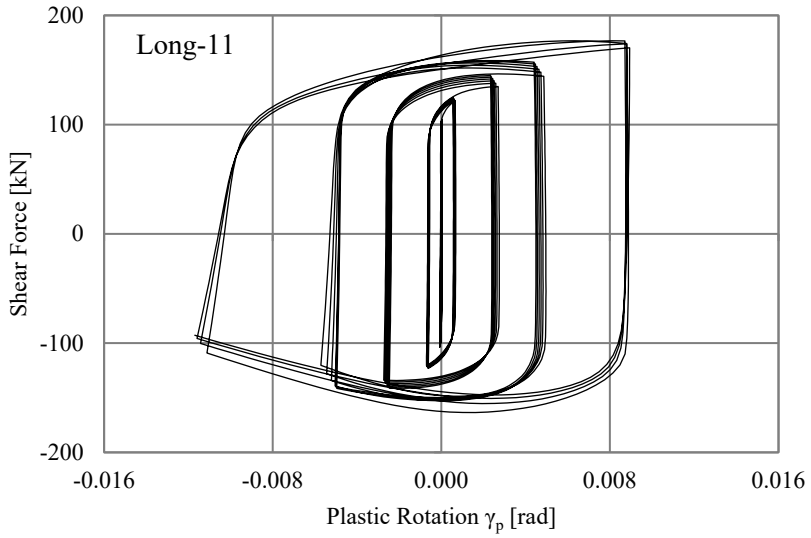

Figure 5-29: Shear-Force vs Plastic Rotation Graph for Link Long-11

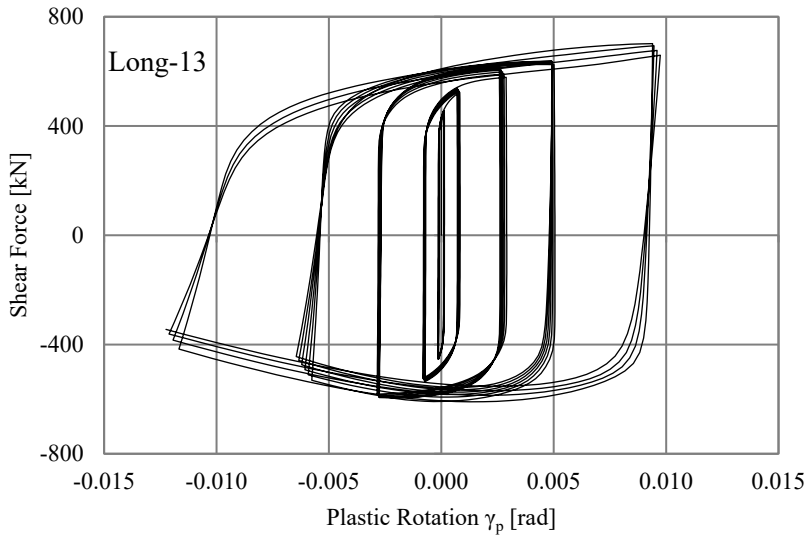

Figure 5-30: Shear-Force vs Plastic Rotation Graph for Link Long-13

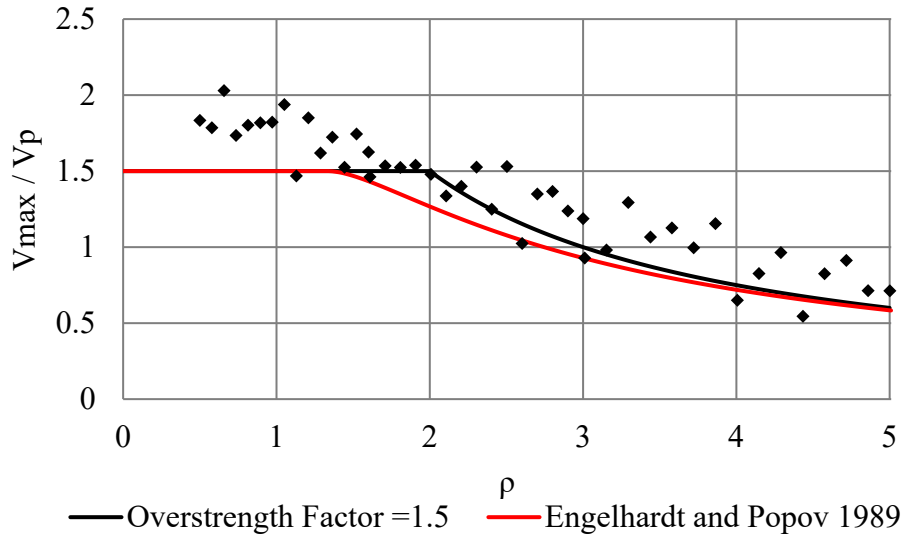

Figure 5-31: V_{max}/V_p vs Link Length Ratio in the Positive Cycle

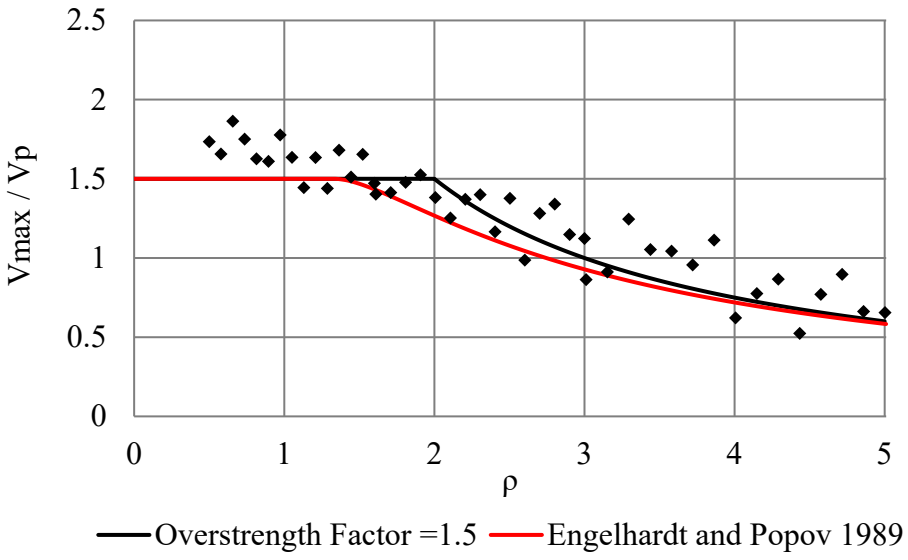

Figure 5-32: V_{max}/V_p vs Link Length Ratio in the Negative Cycle

The V_{max}/V_p vs link length ratio is shown in the figures above. This is the same as the overstrength ratio but it is used to show moment shear interaction. This concept is discussed in chapter 2. The Engelhardt and Popov formula that considers moment shear interaction is shown in the graph. It can be seen here also the numerical analysis results roughly follow previous experiments and theoretical works.

The energy dissipation capacity and ductility of links decrease with increasing link length ratio as can be seen in the figures below. This is in line with previous experiments where it was shown that as link length ratios decrease the ductility and energy dissipation capacity of the link increases. This was expressed in the literature where it was discussed that shear yielding links where the entire web of the link can participate in the yielding process has a higher capacity for sustaining a large amount of plastic deformation and thus can dissipate a large amount of energy.

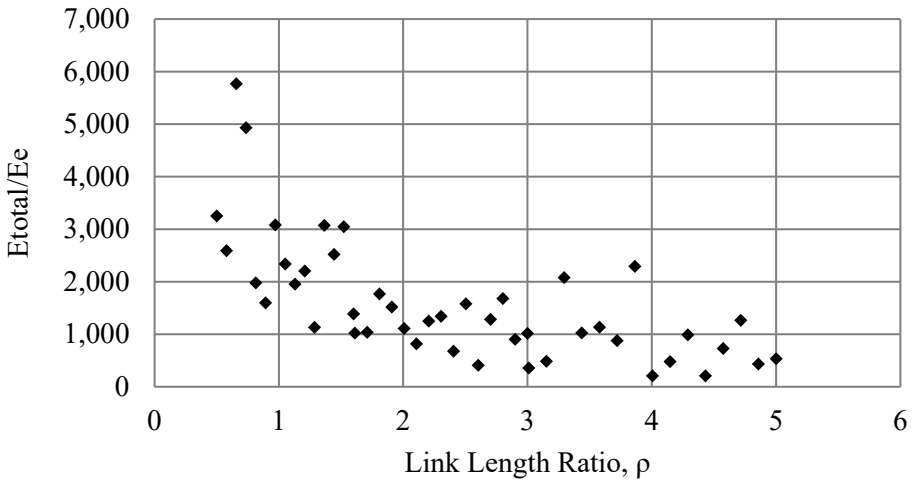

Figure 5-33: E_{total}/E_e vs Link Length Ratio

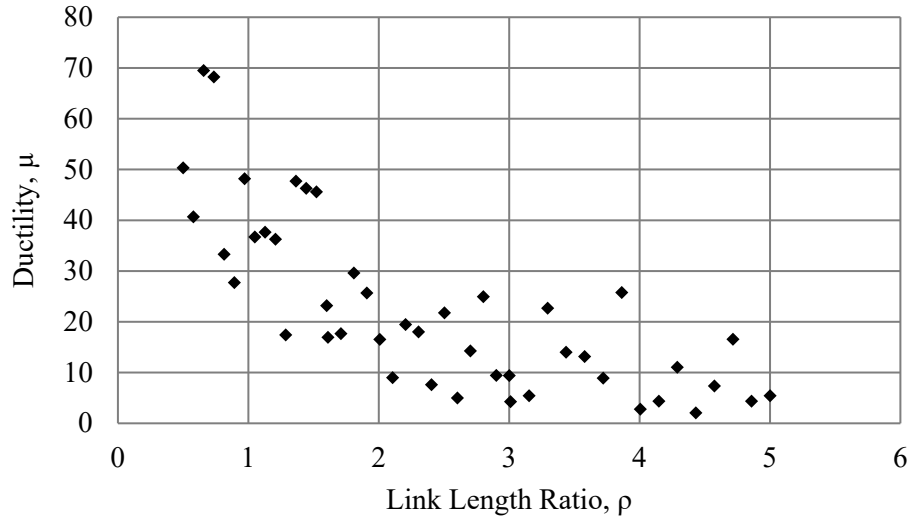

Figure 5-34: Ductility vs Link Length Ratio

In previous sections, the elastic stiffness of the links calculated from the finite element models was presented along with the theoretical calculated elastic stiffness. Here in the figure below the ratio of the elastic stiffness calculated from the finite element analysis to the theoretical elastic stiffness values are shown against their link length ratio. It can be seen that the theoretical and finite element calculated elastic stiffness become approximately equal as the links move away from a shear-dominated behavior into a flexural-dominated behavior.

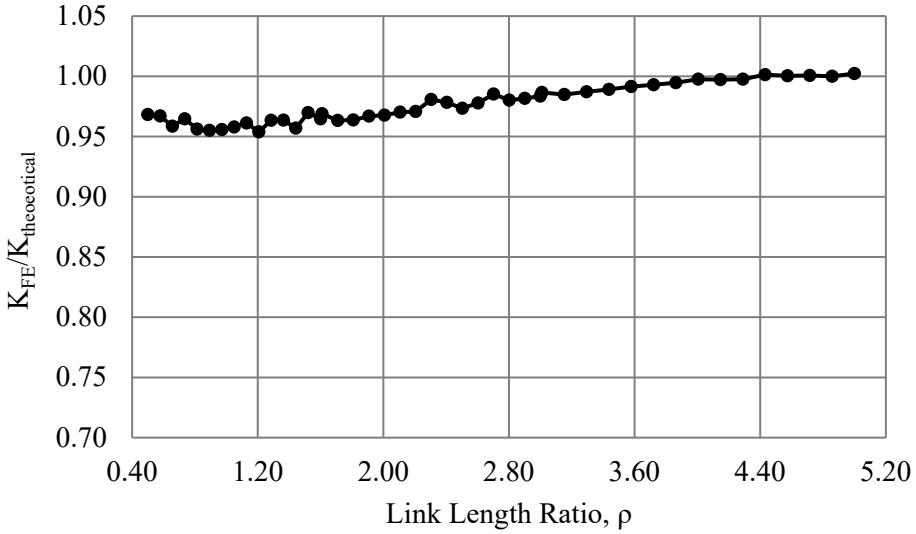

Figure 5-35: $K_{FE}/K_{Theoretical}$ vs Link Length Ratio

CHAPTER 6 SENSITIVITY ANALYSIS

The examination of how uncertainty in a model's output (numerical or otherwise) may be apportioned to various sources of uncertainty in the model input is known as a sensitivity analysis (Saltelli et al., 2008). Sensitivity analysis identifies the model parameters that have the greatest impact on model outcomes.

Various highly complex engineering, physical and environmental phenomena are approximated using mathematical models. Sensitivity analysis identifies the model parameters that have the greatest impact on model findings.

Sensitivity Analysis may be conducted for several reasons including the need to determine:

- Which parameters require more investigation to increase the knowledge base and reduce output uncertainty
- Which parameters are unimportant and should be removed from the final model?
- Which inputs have the greatest impact on output variability
- Which parameters have the strongest relationship with the output; and
- What effect does modifying a given input parameter has on the model

Sensitivity analyses are typically carried out by:

- Defining the model and its independent and dependent variables
- Assigning probability density functions to each input parameter
- Creating an input matrix using a suitable random sampling method, calculating an output vector, and
- Assessing the influences and relative importance of each input/output relationship

Many authors interchangeably use the phrases sensitive, important, most influential, major contributor, effective, or correlated when referring to the degree to which an input parameter influences the model output. Important parameters, according to Crick et al. (Crick & Hill, 1987), are those whose uncertainty adds significantly to the uncertainty in assessment results, whereas sensitive parameters are those that have a major influence on

assessment results. The consensus among authors is that models are indeed sensitive to input parameters in two distinct ways:

- The uncertainty or variability associated with a sensitive input parameter is transmitted through the model, resulting in a significant contribution to overall output variability, and
- Model output can be highly correlated with an input parameter so that small changes in the input value result in significant changes in the output.

The difference between important and sensitive parameters is determined by the type of study performed: uncertainty analysis (parameter importance) or sensitivity analysis (parameter sensitivity). Because parameter variability will not manifest in the output unless the model is sensitive to the input, an important parameter is always sensitive. A sensitive parameter, on the other hand, may be unimportant since it is known accurately, resulting in little unpredictability in the output.

There are various methods of sensitivity analysis. Some are discussed below.

The first one is differential sensitivity analysis. A sensitivity coefficient is the ratio of change in output to change in input while all other variables stay constant. The base case is defined as the model output when all parameters are maintained constant. Differential methods are based on the model's behavior given a certain set of parameter values, such as assuming the base-case scenario has all parameter values set to their mean. One significant disadvantage of this method is that this local behavior may not be relevant in realms far from the basic case.

In differential sensitivity analysis, the sensitivity analysis is simple to do when an explicit algebraic equation defines the relationship between the independent variables and the dependent variable. In this situation, the sensitivity coefficient α_i, for a certain independent variable may be computed using the partial derivative of the dependent variable to the independent variable. In the formula, the quotient, X_i/Y, is used to normalize the coefficient by eliminating the impact of units. It is based on the aggregated partial differentiation of the model (Hamby, 1994).

$$\alpha_i = \frac{\partial Y}{\partial X_i}\left(\frac{\overline{X}_i}{\overline{Y}}\right) \tag{6.1}$$

Another method is the Pearson correlation coefficient. A simple correlation coefficient on the parameter values of input and output may be used to obtain a quantitative estimate of linear correlation. It was proposed by Gardner and his colleagues (Gardner et al., 1981) proposed using simple correlation coefficients generated from simulations to rank model parameters based on their contribution to prediction uncertainty. Pearson's product-moment correlation coefficient (r) is defined as follows.

$$r = \frac{\sum_{j=1}^{n}\left(X_{ij}-\overline{X}_i\right)\left(Y_j-\overline{Y}\right)}{\left[\sum_{j=1}^{n}\left(X_{ij}-\overline{X}_i^2\sum_{j=1}^{n}\left(Y_j-\overline{Y}\right)^2\right)\right]^{1/2}} \tag{6.2}$$

The greater the absolute value of r, the more linear the connection between the input and output values. When r is negative, it means that the output is inversely linked to the input. In this study, the correlation coefficient is used for sensitivity analysis.

As indicated in the equation below, the uncertainty coefficients were computed by multiplying the coefficient of variation by the sensitivity factor. The percentage contribution of the variables is stated in the uncertainty analysis. If the Ui value is positive, the factors contribute positively. That is, an increase in those specific factors leads to an increase in the value of the dependent variable, whereas a decrease in those specific variables increases the value of the dependent variable. The coefficient of variation, or COV, is used to calculate the dispersion of data points. This statistic is defined as the ratio of the standard deviation to the mean. As a result, it provides a standardized measure of the spread.

$$CoV = \frac{\sigma_i}{\overline{X}} \times 100\% \tag{6.3}$$

$$U_i = CoV_i \times \alpha_i \tag{6.4}$$

The sensitivity analysis method used in this research is differential sensitivity analysis. The results for the sensitivity analysis are shown below. The objective function was generated from a multilinear regression analysis. The fitness of the objective function is evaluated based on the coefficient of determination (R^2). The coefficient of

determination is the proportion of the variation in the dependent variable that is predictable from the independent variable.

6.1 Short Links

The sensitivity and uncertainty index along with the objective function are shown below. From the sensitivity analysis, it can be seen that axial load decreases the plastic rotation capacity of the short links in both the positive and negative cycles of loading. Link length ratio and stiffener spacing constant also have a moderately negative impact on the plastic rotation capacity when their values are increased. The web slenderness and stiffener thickness multiplier (STM) have a minimal negative effect on the plastic rotation capacity.

$$\gamma_p^{+ve} = 0.303 - 2.684\times10^{-2}\rho - 0.264\,P/P_y - 2.765\times10^{-3}C_B + 9.976\times10^{-5}\,C_w/t_w - 1.445\times10^{-3}STM \qquad R^2 = 90.2\% \qquad (6.5)$$

Table 6-1: Sensitivity Analysis Parameters for +ve Plastic Rotation Capacity (Short)

	$\overline{x}_i$	$\overline{y}$	$(CoV)_i$	$\frac{\delta y}{\delta x_i}$	α_i	U_i	%
ρ	1.05	0.14	33.5%	-0.046	-0.360	-12.1%	-22.3%
P/P_y	0.20	0.14	63.9%	-0.232	-0.343	-21.9%	-40.5%
C_B	32.13	0.14	20.4%	-0.003	-0.767	-15.7%	-29.0%
C_w/t_w	39.08	0.14	22.5%	-0.0003	-0.073	-1.6%	-3.0%
STM	1.05	0.14	56.6%	0.006	0.049	2.8%	5.1%

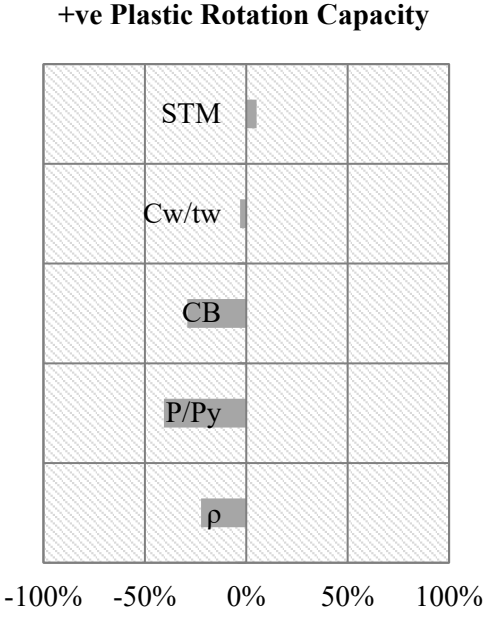

Figure 6-1: Sensitivity Analysis of +ve Plastic Rotation Capacity (Short)

$$\gamma_p^{-ve} = 0.298 - 2.906\times10^{-2}\rho - 0.286\,P/P_y - 2.398\times10^{-3}C_B - 3.147\times10^{-4}\,C_w/t_w + 3.689\times10^{-3}STM \qquad R^2 = 93.8\% \qquad (6.6)$$

Table 6-2: Sensitivity Analysis Parameters for -ve Plastic Rotation Capacity (Short)

	$\overline{x}_i$	$\overline{y}$	$(CoV)_i$	$\frac{\delta y}{\delta x_i}$	α_i	U_i	%
ρ	1.05	0.12	33.5%	-0.045	-0.375	-12.5%	-21.2%
P/P_y	0.20	0.12	63.9%	-0.237	-0.380	-24.2%	-41.0%
C_B	32.13	0.12	20.4%	-0.003	-0.776	-15.9%	-26.8%
C_w/t_w	39.08	0.12	22.5%	-0.0004	-0.130	-2.9%	-4.9%
STM	1.05	0.12	56.6%	0.007	0.063	3.6%	6.0%

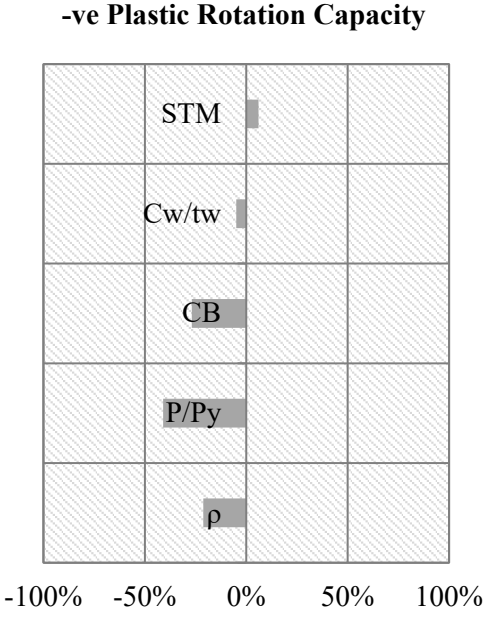

Figure 6-2: Sensitivity Analysis of -ve Plastic Rotation Capacity of Short Links

The overstrength ratio will decrease with increasing link length ratio for both the positive and negative cycles. It was discussed in chapter 2 that very short links have a higher overstrength ratio and this is reflected in the sensitivity analysis. A higher stiffener thickness multiplier will result in a higher overstrength ratio. Stiffener spacing constant and web slenderness both have a negative correlation to the overstrength ratio and they decrease the overstrength ratio when their values are increased.

The interesting thing that was also noticed in chapter 5 is that tensile axial load has a positive effect on the overstrength ratio. This was observed in previous research done by Della Corte and his colleagues where axial restraint that was placed on the link produced a tensile axial load on the link increased the overstrength ratio of the link compared to a link without the tensile axial load (Della Corte et al., 2013).

Axial load ratio has a moderate effect on the overstrength ratio in both the positive and negative cycles.

$$\Omega^{+ve} = 2.627 - 0.194\rho + 0.313\,P/P_y - 1.429\times10^{-2}\,C_B - 5.169\times10^{-3}\,C_w/t_w - 6.699\times10^{-2}\,STM \qquad R^2 = 74.5\% \qquad (6.7)$$

Table 6-3: Sensitivity Analysis Parameters for +ve Overstrength Ratio (Short)

	$\overline{x}_i$	$\overline{y}$	$(CoV)_i$	$\frac{\delta y}{\delta x_i}$	α_i	U_i	%
ρ	1.05	1.75	33.5%	-0.194	-0.116	-3.9%	-23.7%
P/P_y	0.20	1.75	63.9%	0.317	0.036	2.3%	14.0%
C_B	32.13	1.75	20.4%	-0.014	-0.263	-5.4%	-32.7%
C_w/t_w	39.08	1.75	22.5%	-0.0052	-0.115	-2.6%	-15.8%
STM	1.05	1.75	56.6%	-0.067	-0.040	-2.3%	-13.7%

+ve Overstrength Ratio

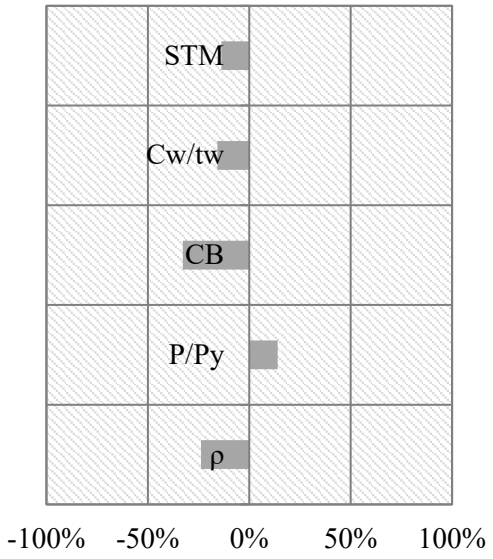

Figure 6-3: Sensitivity Analysis of +ve Overstrength Ratio (Short)

$$\Omega^{-ve} = 2.374 - 0.196\rho - 0.318\,P/P_y - 9.772\times10^{-2}C_B - 3.015\times10^{-3}\,C_w/t_w - 0.037STM \qquad R^2 = 76.5\% \qquad (6.8)$$

Table 6-4: Sensitivity Analysis Parameters for -ve Overstrength Ratio

	$\overline{x}_i$	$\overline{y}$	$(CoV)_i$	$\frac{\delta y}{\delta x_i}$	α_i	U_i	%
ρ	1.05	1.63	33.5%	-0.198	-0.128	-4.3%	-31.2%
P/P_y	0.20	1.63	63.9%	-0.316	-0.039	-2.5%	-18.0%
C_B	32.13	1.63	20.4%	-0.010	-0.193	-3.9%	-28.8%
C_w/t_w	39.08	1.63	22.5%	-0.0030	-0.072	-1.6%	-11.8%
STM	1.05	1.63	56.6%	-0.038	-0.025	-1.4%	-10.1%

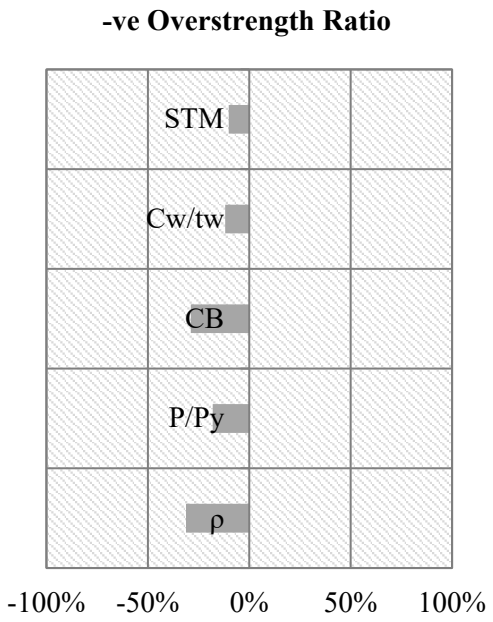

Figure 6-4: Sensitivity Analysis of -ve Plastic Rotation Capacity (Short)

The normalized energy dissipation capacity and ductility are the most affected by axial load ratio, stiffener spacing constant, and link length ratio. The three parameters affect the energy dissipation and ductility negatively, thus decreasing ductility and energy dissipation as they increase. Stiffener thickness multiplier and web slenderness have minimal effect on the ductility and energy dissipation capacity of the link.

$$E_{total}/E_e = 9,281.566 - 1,548.229\rho - 5,736.671 P/P_y - 101.941 C_B - 8.344 C_w/t_w - 174.321 STM \qquad R^2 = 82.9\% \qquad (6.9)$$

Table 6-5: Sensitivity Analysis Parameters for E_{total}/E_e (Short)

	$\overline{x_i}$	$\overline{y}$	$(CoV)_i$	$\frac{\delta y}{\delta x_i}$	α_i	U_i	%
ρ	1.05	2,723.31	33.5%	-2,278.991	-0.879	-29.42%	-32.5%
P/P_y	0.20	2,723.31	63.9%	-5,262.173	-0.386	-24.69%	-27.3%
C_B	32.13	2,723.31	20.4%	-124.099	-1.464	-29.94%	-33.1%
C_w/t_w	39.08	2,723.31	22.5%	-18.7409	-0.269	-6.06%	-6.7%
STM	1.05	2,723.31	56.6%	19.735	0.008	0.43%	0.5%

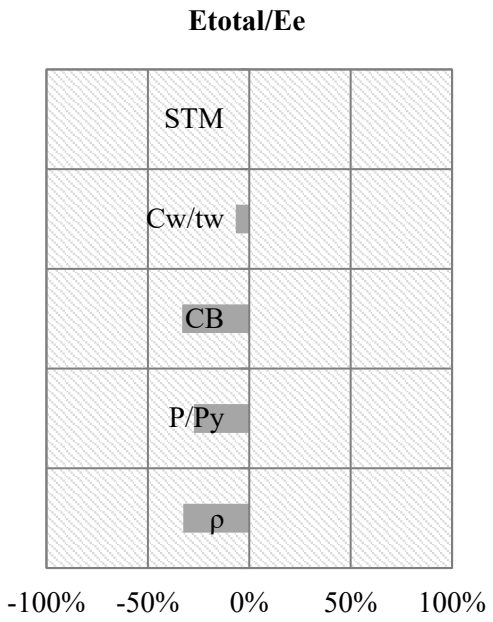

Figure 6-5: Sensitivity Analysis of E_{total}/E_e (Short)

$$\mu = 108.667 - 17.641\rho - 84.358\,P/P_y - 0.904C_B - 4.858\times10^{-2}\,C_w/t_w - 0.382STM \qquad R^2 = 92.4\% \qquad (6.10)$$

Table 6-6: Sensitivity Analysis Parameters for Ductility (Short)

	$\overline{x}_i$	$\overline{y}$	$(CoV)_i$	$\frac{\delta y}{\delta x_i}$	α_i	U_i	%
ρ	1.05	41.92	33.5%	-23.928	-0.600	-20.1%	-31.6%
P/P_y	0.20	41.92	63.9%	-71.980	-0.343	-21.9%	-34.5%
C_B	32.13	41.92	20.4%	-1.072	-0.822	-16.8%	-26.4%
C_w/t_w	39.08	41.92	22.5%	-0.1152	-0.107	-2.4%	-3.8%
STM	1.05	41.92	56.6%	1.667	0.042	2.4%	3.7%

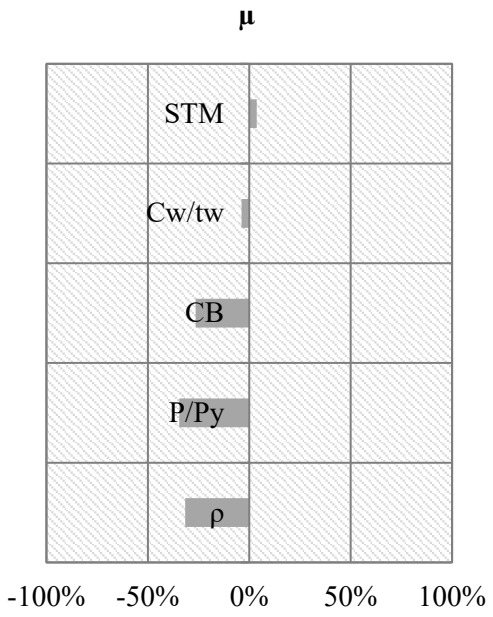

Figure 6-6: Sensitivity Analysis of Ductility (Short)

6.2 Intermediate Links

The plastic rotation capacity is almost equally affected by the link length ratio, axial load ratio, stiffener spacing constant, and flange slenderness for both the positive and negative plastic rotation capacity. They all have a negative correlation with the plastic rotation capacity. Stiffener thickness multiplier has a negative moderate effect on the plastic rotation capacity.

The flange slenderness effect is pronounced in the negative cycle because flange buckling in the negative cycle is increased by compressive axial load present in the link.

$$\gamma_p^{+ve} = 0.302 - 3.093\times10^{-2}\rho - 9.854\times10^{-2}\,P/P_y - 1.971\times10^{-3}C_B - 1.145\times10^{-2}\,C_f/t_f - 1.704\times10^{-2}\,STM \qquad R^2 = 91.6\% \qquad (6.11)$$

Table 6-7: Sensitivity Analysis Parameters for +ve Plastic Rotation Capacity (Intermediate)

	$\overline{x}_i$	$\overline{y}$	$(CoV)_i$	$\frac{\delta y}{\delta x_i}$	α_i	U_i	%
ρ	2.31	0.06	19.3%	-0.031	-1.246	-24.0%	-22.7%
P/P_y	0.20	0.06	63.9%	-0.099	-0.344	-22.0%	-20.8%
C_B	40.95	0.06	18.0%	-0.002	-1.411	-25.4%	-24.1%
C_f/t_f	4.59	0.06	22.7%	-0.0115	-0.919	-20.8%	-19.7%
STM	1.20	0.06	37.3%	-0.017	-0.357	-13.3%	-12.6%

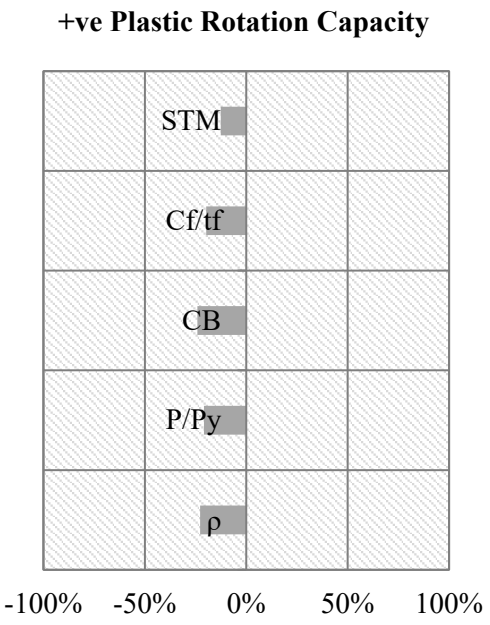

Figure 6-7: Sensitivity Analysis of +ve Plastic Rotation Capacity (Intermediate)

$$\gamma_p^{-ve} = 0.233 - 2.594\times10^{-2}\rho - 7.708\times10^{-2}\,P/P_y - 1.348\times10^{-3}C_B - 8.953\times10^{-3}\,C_f/t_f - 1.124\times10^{-2}\,STM \qquad R^2 = 90.4\% \qquad (6.12)$$

Table 6-8: Sensitivity Analysis Parameters for -ve Plastic Rotation Capacity (Intermediate)

	$\overline{x}_i$	$\overline{y}$	$(CoV)_i$	$\frac{\delta y}{\delta x_i}$	α_i	U_i	%
ρ	2.31	0.05	19.3%	-0.026	-1.240	-23.9%	-25.2%
P/P_y	0.20	0.05	63.9%	-0.077	-0.320	-20.4%	-21.6%
C_B	40.95	0.05	18.0%	-0.001	-1.144	-20.6%	-21.8%
C_f/t_f	4.59	0.05	22.7%	-0.0090	-0.852	-19.3%	-20.4%
STM	1.20	0.05	37.3%	-0.011	-0.280	-10.4%	-11.0%

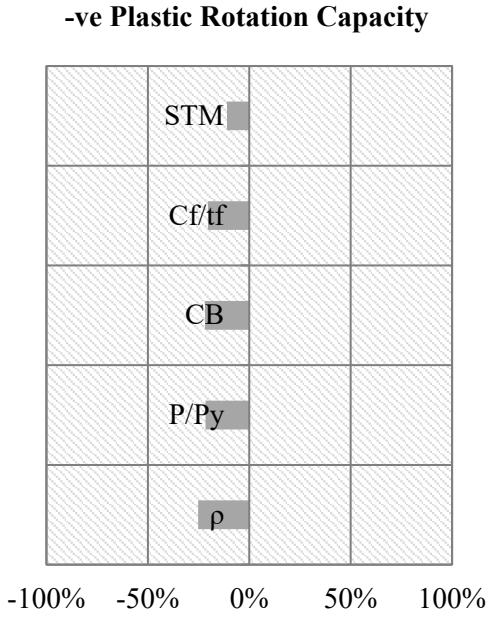

Figure 6-8: Sensitivity Analysis of -ve Plastic Rotation Capacity (Intermediate)

The overstrength ratio for both the positive and negative cycle showed the same type of trend where link length ratio and stiffener spacing constant affected the overstrength the most while axial load ratio and flange slenderness showed a moderate effect and stiffener thickness multiplier showed a minimal effect. The overstrength ratio increased with increasing link length ratio again showing the M-V interaction present in this range. Axial load ratio and stiffener spacing constant increased overstrength ratio when their values were decreased.

It can also be seen here that the influence of the axial load ratio in the negative cycle is higher than the positive cycle. This is because intermediate links experience flange buckling and negative (compressive) axial load expedite the flange buckling thereby decreasing the maximum shear the link can attain and, in the process, decreasing the overstrength ratio.

$$\Omega^{+ve} = 1.812 + 0.283\rho - 0.244\,P/P_y - 1.683\times10^{-2} C_B - 3.097\times10^{-2}\, C_f/t_f + 3.112\times10^{-2}\, STM \qquad R^2 = 87.6\% \qquad (6.13)$$

Table 6-9: Sensitivity Analysis Parameters for +ve Overstrength Ratio (Intermediate)

	$\overline{x}_i$	$\overline{y}$	$(CoV)_i$	$\frac{\delta y}{\delta x_i}$	α_i	U_i	%
ρ	2.31	1.62	19.3%	0.283	0.403	7.8%	38.4%
P/P_y	0.20	1.62	63.9%	-0.244	-0.030	-1.9%	-9.5%
C_B	40.95	1.62	18.0%	-0.017	-0.425	-7.7%	-38.0%
C_f/t_f	4.59	1.62	22.7%	-0.0310	-0.088	-2.0%	-9.8%
STM	1.20	1.62	37.3%	0.031	0.023	0.9%	4.3%

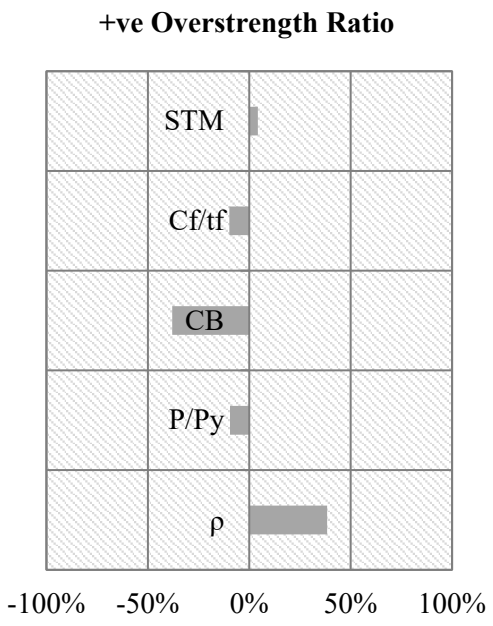

Figure 6-9: Sensitivity Analysis of +ve Overstrength Ratio (Intermediate)

$$\Omega^{-ve} = 1.699 + 0.256\rho - 0.437\,P/P_y - 1.333\times10^{-2}C_B - 3.491\times10^{-2}\,C_f/t_f + 3.212\times10^{-2}\,STM \qquad R^2 = 88.8\% \qquad (6.14)$$

Table 6-10: Sensitivity Analysis Parameters for -ve Overstrength Ratio (Intermediate)

	$\overline{x_i}$	$\overline{y}$	$(CoV)_i$	$\frac{\delta y}{\delta x_i}$	α_i	U_i	%
ρ	2.31	1.54	19.3%	0.256	0.385	7.4%	35.7%
P/P_y	0.20	1.54	63.9%	-0.437	-0.057	-3.6%	-17.5%
C_B	40.95	1.54	18.0%	-0.013	-0.356	-6.4%	-30.9%
C_f/t_f	4.59	1.54	22.7%	-0.0349	-0.104	-2.4%	-11.4%
STM	1.20	1.54	37.3%	0.032	0.025	0.9%	4.5%

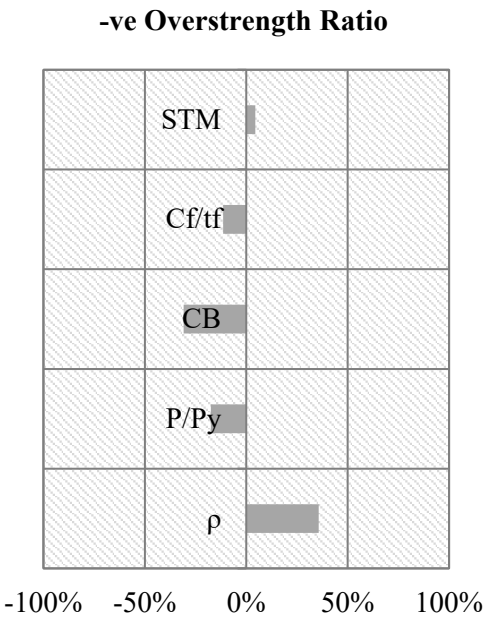

Figure 6-10: Sensitivity Analysis of for -ve Overstrength Ratio (Intermediate)

Normalized energy dissipation is the most affected by stiffener spacing constant, axial load ratio, and flange slenderness ratio all of which decrease the energy dissipation capacity when they increase.

Ductility is almost equally affected by axial load ratio, link length ratio, flange slenderness, and stiffener spacing constant. They all are negatively correlated to ductility. Stiffener thickness multiplier has a moderate effect on ductility.

$$E_{total}/E_e = 3{,}933.739 - 61.209\rho - 1{,}089.313\,P/P_y - 33.428C_B - 215.182\,C_f/t_f - 48.021STM \qquad R^2 = 92.4\% \qquad (6.15)$$

Table 6-11: Sensitivity Analysis Parameters for E_{total}/E_e (Intermediate)

	$\bar{x}_i$	$\bar{y}$	$(CoV)_i$	$\frac{\delta y}{\delta x_i}$	α_i	U_i	%
ρ	2.31	1,160.17	19.3%	-61.209	-0.122	-2.34%	-4.1%
P/P_y	0.20	1,160.17	63.9%	-1,089.313	-0.188	-12.00%	-21.1%
C_B	40.95	1,160.17	18.0%	-33.428	-1.180	-21.28%	-37.5%
C_f/t_f	4.59	1,160.17	22.7%	-215.1819	-0.852	-19.30%	-34.0%
STM	1.20	1,160.17	37.3%	-48.021	-0.050	-1.85%	-3.3%

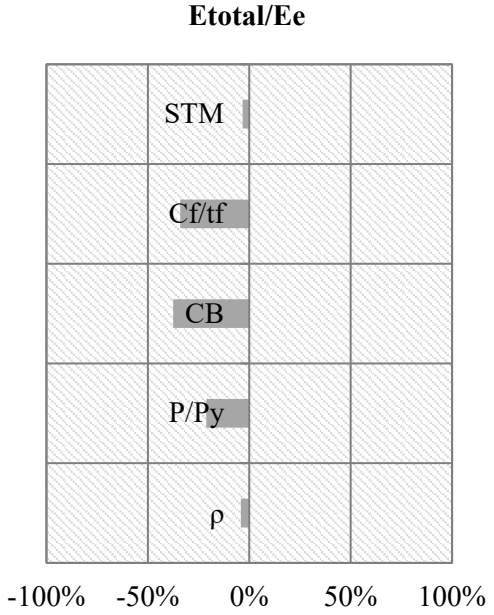

Figure 6-11: Sensitivity Analysis of E_{total}/E_e (Intermediate)

$$\mu = 74.862 - 6.277\rho - 23.793\,P/P_y - 0.479C_B - 3.466\,C_f/t_f - 3.138STM \qquad R^2 = 88\% \qquad (6.16)$$

Table 6-12: Sensitivity Analysis Parameters for Ductility (Intermediate)

	$\overline{x}_i$	$\overline{y}$	$(CoV)_i$	$\frac{\delta y}{\delta x_i}$	α_i	U_i	%
ρ	2.31	16.35	19.3%	-6.277	-0.885	-17.0%	-19.4%
P/P_y	0.20	16.35	63.9%	-23.793	-0.291	-18.6%	-21.2%
C_B	40.95	16.35	18.0%	-0.479	-1.199	-21.6%	-24.6%
C_f/t_f	4.59	16.35	22.7%	-3.4657	-0.973	-22.1%	-25.1%
STM	1.20	16.35	37.3%	-3.138	-0.230	-8.6%	-9.8%

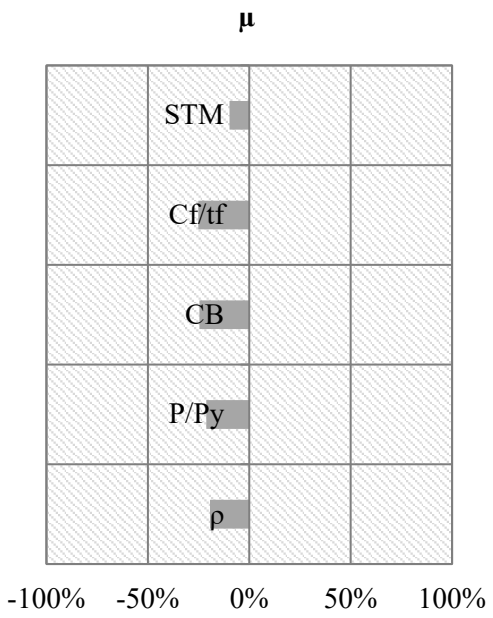

Figure 6-12: Sensitivity Analysis of Ductility (Intermediate)

6.3 Long Links

The sensitivity analysis for plastic rotation capacity of the long links revealed that the axial load ratio and flange slenderness as the most influential parameters in determining the links plastic rotation capacity in both the positive and negative cycles. A slight influence in plastic rotation capacity for an increase in link length ratio and stiffener thickness multiplier is seen from the sensitivity analysis. End stiffener spacing multiplier (ESSM) shows little effect or correlation.

$$\gamma_p^{+ve} = 0.179 - 5.899\times10^{-3}\rho - 0.124\,P/P_y - 8.971\times10^{-5}\,ESSM - 1.714\times10^{-2}\,C_f/t_f - 1.721\times10^{-2}\,STM \qquad R^2 = 91\% \qquad (6.17)$$

Table 6-13: Sensitivity Analysis Parameters for +ve Plastic Rotation Capacity (Long)

	$\overline{x}_i$	$\overline{y}$	$(CoV)_i$	$\frac{\delta y}{\delta x_i}$	α_i	U_i	%
ρ	4.01	0.03	15.9%	-0.006	-0.756	-12.0%	-8.3%
P/P_y	0.20	0.03	63.9%	-0.124	-0.790	-50.5%	-35.0%
ESSM	1.50	0.03	42.6%	0.000	-0.004	-0.2%	-0.1%
C_f/t_f	4.59	0.03	22.7%	-0.0171	-2.517	-57.0%	-39.5%
STM	1.20	0.03	37.3%	-0.017	-0.661	-24.6%	-17.1%

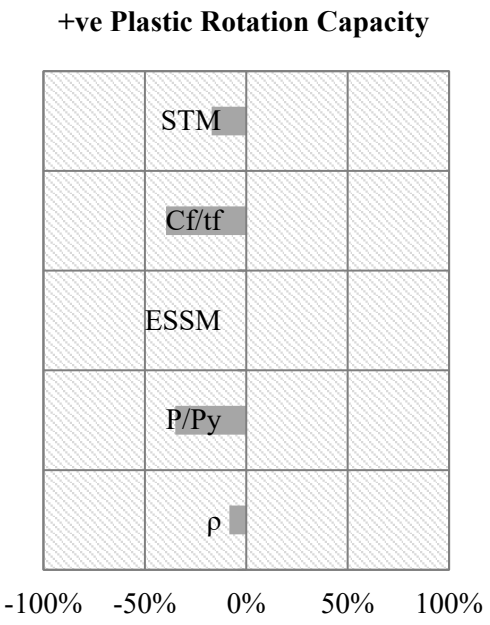

Figure 6-13: Sensitivity Analysis of for +ve Plastic Rotation Capacity (Long)

$$\gamma_p^{-ve} = 0.147 - 6.067\times10^{-3}\rho - 8.019\times10^{-2}\,P/P_y - 4.384\times10^{-4}\,ESSM - 0.141\,C_f/t_f - 1.244\times10^{-2}\,STM \qquad R^2 = 90.3\% \qquad (6.18)$$

Table 6-14: Sensitivity Analysis Parameters for -ve Plastic Rotation Capacity (Long)

	$\overline{x_i}$	$\overline{y}$	$(CoV)_i$	$\frac{\delta y}{\delta x_i}$	α_i	U_i	%
ρ	4.01	0.03	15.9%	-0.006	-0.897	-14.2%	-11.1%
P/P_y	0.20	0.03	63.9%	-0.080	-0.592	-37.8%	-29.6%
ESSM	1.50	0.03	42.6%	0.000	0.024	1.0%	0.8%
C_f/t_f	4.59	0.03	22.7%	-0.0141	-2.392	-54.2%	-42.4%
STM	1.20	0.03	37.3%	-0.012	-0.551	-20.5%	-16.1%

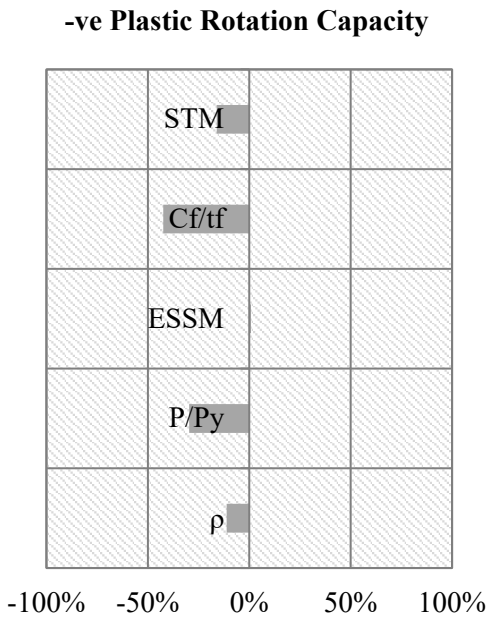

Figure 6-14: Sensitivity Analysis of for -ve Plastic Rotation Capacity (Long)

The overstrength ratio is negatively correlated to the flange slenderness ratio and axial load ratio. these two parameters affect the overstrength ratio in both the positive and negative cycles the most while the others are minimal.

From the plastic rotation capacity and overstrength ratio sensitivity analysis, it can be seen that axial load ratio and flange slenderness are the parameters that affect the behavior of long links the most. This can be attributed to the failure mode of long links where flange buckling is the driving mechanism. The two parameters that enable early flange buckling are the flange slenderness ratio and axial load ratio.

$$\Omega^{+ve} = 3.03 + 0.069\rho - 1.293\,P/P_y - 6.913\times10^{-3}\,ESSM - 0.232\,C_f/t_f - 0.153\,STM \qquad R^2 = 87.5\% \qquad (6.19)$$

Table 6-15: Sensitivity Analysis Parameters for +ve Overstrength Ratio (Long)

	$\overline{x}_i$	$\overline{y}$	$(CoV)_i$	$\frac{\delta y}{\delta x_i}$	α_i	U_i	%
ρ	4.01	1.79	15.9%	0.069	0.155	2.5%	8.4%
P/P_y	0.20	1.79	63.9%	-1.293	-0.144	-9.2%	-31.6%
ESSM	1.50	1.79	42.6%	-0.007	-0.006	-0.2%	-0.8%
C_f/t_f	4.59	1.79	22.7%	-0.2317	-0.594	-13.5%	-46.1%
STM	1.20	1.79	37.3%	-0.153	-0.103	-3.8%	-13.1%

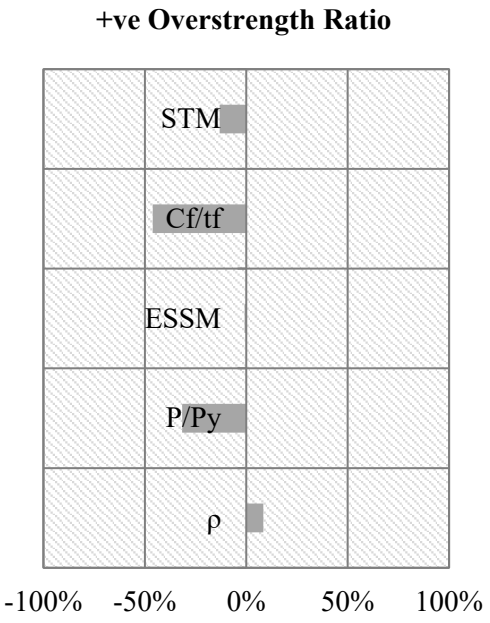

Figure 6-15: Sensitivity Analysis of for +ve Overstrength Ratio (Long)

$$\Omega^{-ve} = 2.944 + 5.367\times10^{-2}\rho - 1.357\,P/P_y + 3.811\times10^{-3}\,ESSM - 0.226\,C_f/t_f - 0.134\,STM \qquad R^2 = 91.9\% \qquad (6.20)$$

Table 6-16: Sensitivity Analysis Parameters for -ve Overstrength Ratio (Long)

	$\overline{x_i}$	$\overline{y}$	$(CoV)_i$	$\frac{\delta y}{\delta x_i}$	α_i	U_i	%
ρ	4.01	1.69	15.9%	0.054	0.127	2.0%	6.8%
P/P_y	0.20	1.69	63.9%	-1.357	-0.160	-10.2%	-34.3%
ESSM	1.50	1.69	42.6%	0.004	0.003	0.1%	0.5%
C_f/t_f	4.59	1.69	22.7%	-0.226	-0.613	-13.9%	-46.5%
STM	1.20	1.69	37.3%	-0.134	-0.095	-3.6%	-11.9%

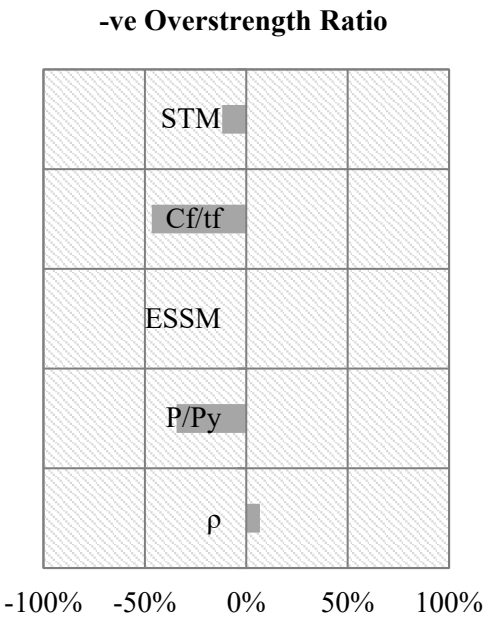

Figure 6-16: Sensitivity Analysis of for -ve Overstrength Ratio (Long)

The normalized energy dissipation and ductility followed the same trend as the plastic rotation capacity and overstrength ratio sensitivity analysis in which flange slenderness and axial load ratio was the most influential parameter. Here a slight negative correlation can be seen with the stiffener thickness multiplier and link length ratio.

$$E_{total}/E_e = 4,280.351 - 154.478\rho - 2,146.764\,P/P_y + 40.733ESSM - 472.184\,C_f/t_f - 210.31STM \qquad R^2 = 85.6\% \qquad (6.21)$$

Table 6-17: Sensitivity Analysis Parameters for E_{total}/E_e (Long)

	$\overline{x}_i$	$\overline{y}$	$(CoV)_i$	$\frac{\delta y}{\delta x_i}$	α_i	U_i	%
ρ	4.01	872.69	15.9%	-154.478	-0.709	-11.26%	-10.0%
P/P_y	0.20	872.69	63.9%	-2,146.764	-0.492	-31.43%	-27.9%
ESSM	1.50	872.69	42.6%	40.733	0.070	2.98%	2.6%
C_f/t_f	4.59	872.69	22.7%	-472.184	-2.484	-56.29%	-49.9%
STM	1.20	872.69	37.3%	-210.310	-0.289	-10.78%	-9.6%

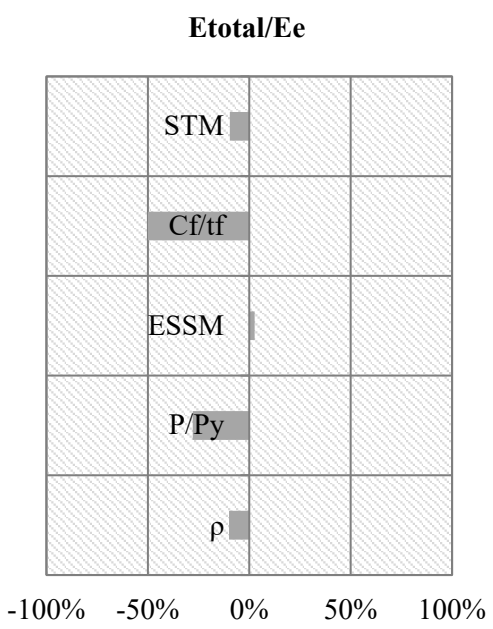

Figure 6-17: Sensitivity Analysis of for E_{total}/E_e (Long)

$$\mu = 51.959 - 2.014\rho - 28.269\,P/P_y + 0.167\,ESSM - 5.354\,C_f/t_f - 3.352\,STM \qquad R^2 = 88.8\% \qquad (6.22)$$

Table 6-18: Sensitivity Analysis Parameters for Ductility (Long)

	$\overline{x}_i$	$\overline{y}$	$(CoV)_i$	$\frac{\delta y}{\delta x_i}$	α_i	U_i	%
ρ	4.01	9.88	15.9%	-2.014	-0.817	-13.0%	-10.6%
P/P_y	0.20	9.88	63.9%	-28.269	-0.572	-36.6%	-29.9%
ESSM	1.50	9.88	42.6%	0.167	0.025	1.1%	0.9%
C_f/t_f	4.59	9.88	22.7%	-5.3538	-2.489	-56.4%	-46.2%
STM	1.20	9.88	37.3%	-3.352	-0.407	-15.2%	-12.4%

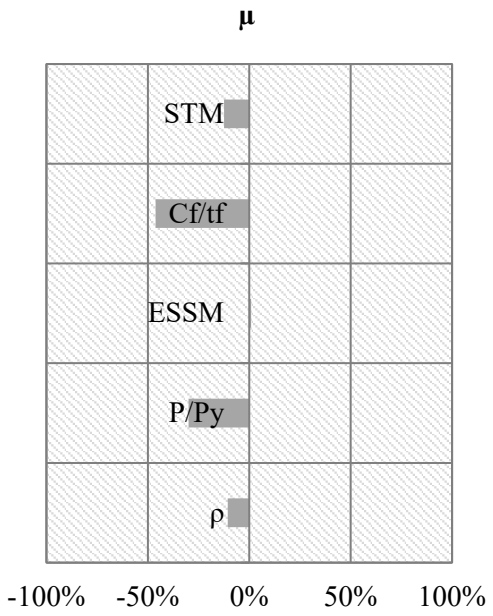

Figure 6-18: Sensitivity Analysis of for Ductility (Long)

CHAPTER 7 CONCLUSION AND RECOMMENDATION

7.1 Conclusion

In this research, a parametric study on the behavior of EBF links was conducted using a nonlinear finite element subjected to cyclic loading. The link types short, intermediate, and long links were evaluated separately. Link length ratio, axial load ratio, web/flange slenderness, stiffener spacing constant C_B, end stiffener spacing, stiffener thickness multiplier were the parameters used in the study. 15 samples for each of the 3 link types were generated using the LHS sampling method. The sensitivity of the links' plastic rotation capacity, overstrength ratio, normalized energy dissipation capacity, and ductility to the above parameters was calculated using the differential sensitivity analysis method.

The following conclusion was made based on the sensitivity analysis

- Short links plastic rotation capacity was negatively influenced by high axial load and high stiffener spacing constant. The web slenderness has a minimal negative effect on the plastic rotation capacity. while the link length ratio also moderately affected the plastic rotation capacity negatively. The stiffener thickness multiplier even though small has a positive correlation with the plastic rotation capacity meaning an adequate or stiff stiffener will positively affect the plastic rotation capacity of the link.
- Short shear link overstrength ratio is the most affected by link length ratio and stiffener spacing constant with stiffener spacing constant being the most influential. They both have a negative correlation with an overstrength ratio meaning a short link that is over stiffened will have a higher overstrength ratio, and as the link length ratio increases the moment shear interaction is also getting higher meaning a lower overstrength ratio.
- Short shear links overstrength ratio are positively affected by axial load ratio in the positive cycle and negatively affected by the link length ratio in the negative cycle meaning that tensile axial load increase overstrength values. While the overstrength ratio was slightly affected by the stiffener thickness multiplier and

web slenderness ratio, both of which decreased over strength when their values increased.

- The normalized energy dissipation capacity was the most affected by link length ratio and stiffener spacing constant, while axial load ratio has a slightly less influence than link length ratio and stiffener spacing. They all have a negative effect on the normalized energy dissipation capacity.
- The ductility of short links was the most affected by the axial load ratio and it was negatively correlated to ductility. While link length ratio and stiffener spacing constant moderately influenced ductility. They were also negatively correlated to ductility. Web slenderness and stiffener thickness effect were minimal.
- Intermediate links plastic rotation capacity was almost equally influenced by axial load ratio, link length ratio, flange slenderness, and stiffener spacing constant while stiffener thickness multiplier was less influential. All the parameters were negatively correlated to the plastic rotation capacity.
- The influential parameters for the overstrength ratio for the intermediate links were found to be the link length ratio which was the highest and a close second was the stiffener spacing constant, while axial load ratio moderately influenced the overstrength ratio. The rest of the parameters had minimal effect on the overstrength ratio. The overstrength ratio was positively correlated to the link length ratio while being negatively correlated to the rest of the parameters.
- The normalized energy dissipation capacity was highly influenced by stiffener spacing constant and flange slenderness. Axial load ratio has a moderate influence on the normalized energy dissipation. They are all negatively correlated meaning an increase in the parameters will result in a decrease in the energy dissipation capacity of the intermediate link.
- The ductility of intermediate links was highly influenced by stiffener spacing constant and flange slenderness while link length ratio and axial load ratio were slightly less influential. They all had a negative impact on the ductility of intermediate links.

- The most influential parameters for long links behavior are axial load ratio and flange slenderness ratio. Flange slenderness is the most influential with axial load ratio being second. An increase in flange slenderness ratio and axial load ratio decreased

plastic rotation capacity, overstrength ratio, normalized energy dissipation, and ductility of long links.

Other observations that were made during the analysis are listed below

- Short links performed better under even extreme cases of loading (high axial load) and poor design (high stiffener spacing and low stiffener thickness) compared to long and intermediate links. Therefore, it is recommended that short links be used when high axial loads are anticipated or when unexpectedly high loading conditions might occur.
- The performance of intermediate links with a link length ratio close to 3 that have a closely spaced stiffener at the middle panel was excellent even during a high axial load ratio, while long links with a link length ratio close to 3 with only stiffeners at the end performed inadequately and failed prematurely by web buckling in the middle panel. This led to the conclusion that long links that have a link length ratio close to 3 should be fitted with intermediate stiffeners at the middle panel for better performance.
- The overstrength value recorded for most of the links surpassed the seismic code recommended value of 1.5 which is in line with previous research done on the European IPE sections.

7.2 Recommendation

The following recommendations are given for future works

- An experimental investigation of this numerical study is needed to corroborate the findings of this research.
- More comprehensive finite element research with a lot more samples that also incorporates a material failure model needs to be conducted.
- An empirical equation to predict the overstrength ratio and plastic rotation capacity of links when the various parameters studied in this research are varied is needed.
- A finite element analysis using a portal or frame sub-assemblage is needed to take into account the contribution of other members to the link's behavior.
- A further study into the tensile axial load contribution in increasing the overstrength ratio is needed.

- A flange slenderness limit is needed for longer links especially those that might encounter high axial loads.
- The higher overstrength ratio experienced by IPE sections needs to be validated by experimental research and the overstrength ratio needs to be updated for European IPE sections.

REFERENCE

AISC 341-02. (2002). ANSI/AISC 341-02: Seismic Provisions for Structural Steel Buildings. *American Institute of Steel Construction (Chicago, Illinois)*.

AISC 341-05. (2005). ANSI/AISC 341-05: Seismic Provisions for Structural Steel Buildings. *American Institute of Steel Construction (Chicago, Illinois)*.

AISC 341-10. (2010). ANSI/AISC 341-10:Seismic Provisions for Structural Steel Buildings. *American Institute of Steel Construction (Chicago, Illinois)*.

AISC 341-16. (2016). ANSI/AISC 341-16:Seismic Provisions for Structural Steel Buildings. *American Institute of Steel Construction (Chicago, Illinois)*.

ANSYS, I. (2021). Mechanical User's Guide. *ANSYS*, *15317*(July), 1028.

Arce, G. (2002). *Impact of higher strength steels on local buckling and overstrength of links in eccentrically braced frames*. University of Texas at Austin.

Armstrong, P. J., & Frederick, C. O. (1966). A Mathematical Representation of the Multi Axial Bauschinger Effect. *Materials at High Temperatures*, *24*(1), 1–26.

Berman, J. W., Okazaki, T., & Hauksdottir, H. O. (2010). Reduced link sections for improving the ductility of eccentrically braced frame link-to-column connections. *9th US National and 10th Canadian Conference on Earthquake Engineering 2010, Including Papers from the 4th International Tsunami Symposium*, *5*(May), 3546–3555.

Chaboche, J. L. (1986). Time-independent constitutive theories for cyclic plasticity. *International Journal of Plasticity*, *2*(2), 149–188. https://doi.org/10.1016/0749-6419(86)90010-0

Chao, S. H., Khandelwal, K., & El-Tawil, S. (2006). Ductile web fracture initiation in steel shear links. *Journal of Structural Engineering*, *132*(8), 1192–1200. https://doi.org/10.1061/(ASCE)0733-9445(2006)132:8(1192)

Crick, M. J., & Hill, M. D. (1987). The role of sensitivity analysis in assessing uncertainty. In *Uncertainty analysis for performance assessments of radioactive waste disposal systems*.

Crișan, A. (2016). Material calibration for static cyclic analyses. *Intersections/IntersectII*, *13*(2), 43–58.

Daneshmand, A., & Hosseini Hashemi, B. (2012). Performance of intermediate and long links in eccentrically braced frames. *Journal of Constructional Steel Research*, *70*, 167–176. https://doi.org/10.1016/j.jcsr.2011.10.011

Dastmalchi, S. (2014). *Numerical study of axial load effect on the seismic behavior of shear links in eccentrically braced frames*. University of Maryland, College Park.

Della Corte, G., D'Aniello, M., & Landolfo, R. (2013). Analytical and numerical study of plastic overstrength of shear links. *Journal of Constructional Steel Research*, *82*, 19–32. https://doi.org/10.1016/j.jcsr.2012.11.013

Dusicka, P., Itani, A. M., & Buckle, I. G. (2004). Finite element investigation of steel built-up shear links subjected to inelastic deformations. *Earthquake Engineering and Engineering Vibration*, *3*(2), 195–203. https://doi.org/10.1007/BF02858234

Dusicka, P., Itani, A. M., & Buckle, I. G. (2010). Cyclic Behavior of Shear Links of Various Grades of Plate Steel. *Journal of Structural Engineering*, *136*(4), 370–378. https://doi.org/10.1061/(asce)st.1943-541x.0000131

EBCS EN 1998-1:2014. (2014). EBCS 8: Design of Structures for Earthquake Resistance Part 1: General Rules, Seismic Actions, and Rules for Buildings. *Ministry of Urban Development, Housing, and Construction (Addis Ababa, Ethiopia)*.

EN 1998-1:2004. (2004). Eurocode 8: Design of Structures for Earthquake Resistance Part 1: General Rules, Seismic Actions, and Rules for Buildings. *European Committee for Standardization (CEN) (Brussels, Belgium)*.

Engelhardt, M. D., & Popov, E. P. (1989). Behavior of Long Links in Eccentrically Braced Frames. *Earthquake Engineering Research Center*, *Report No.* (January). https://nehrpsearch.nist.gov/static/files/NSF/PB92143056.pdf

Engelhardt, M. D., & Popov, E. P. (1992). Experimental Performance of Long Links in Eccentrically Braced Frames. *Journal of Structural Engineering*, *118*(11), 3067–3088. https://doi.org/10.1061/(asce)0733-9445(1992)118:11(3067)

FUJIMOTO, M., AOYAGI, T., UKAI, K., WADA, A., & SAITO, K. (1972). Structural Characteristics of Eccentric K-Braced Frames. *Transactions of the Architectural Institute of Japan*, *195*(0), 39-49,97. https://doi.org/10.3130/aijsaxx.195.0_39

Gálvez, P. (2004). *Investigation of factors affecting web fractures in shear links*. University of Texas at Austin.

Gardner, R. H., O'Neill, R. V, Mankin, J. B., & Carney, J. H. (1981). A comparison of sensitivity analysis and error analysis based on a stream ecosystem model. *Ecological Modelling*, *12*(3), 173–190. https://doi.org/https://doi.org/10.1016/0304-3800(81)90056-9

Ghobarah, A., & Ramadan, T. (1990). Butterworth & Co (Publishers) Ltd 106 Eng. *Struct*, *12*, 106–113.

Hamby, D. M. (1994). A Review of Techniques for Parameter Sensitivity. *Environmental Monitoring and Assessment*, *32*(c), 135–154. https://deepblue.lib.umich.edu/bitstream/handle/2027.42/42691/10661_2004_Article_BF00547132.pdf?sequence=1

Hjelmstad, K. D., & Popov, E. P. (1983a). Cyclic Behavior and Design of Link Beams. *Journal of Structural Engineering (United States)*, *109*(10), 2387–2403.

Hjelmstad, K. D., & Popov, E. P. (1983b). Seismic behavior of active beam links in eccentrically braced frames. *NASA STI/Recon Technical Report N*, *84*(July), 18480.

Hjelmstad, K. D., & Popov, E. P. (1984). Characteristics of eccentrically braced frames. *Journal of Structural Engineering (United States)*, *110*(2), 340–353. https://doi.org/10.1061/(ASCE)0733-9445(1984)110:2(340)

Hjelmstad, K. D., & Sang-Gab Lee. (1989). Lateral buckling of beams in eccentrically-braced frames. *Journal of Constructional Steel Research*, *14*(4), 251–272. https://doi.org/10.1016/0143-974X(89)90039-4

Hong, J. K., Uang, C. M., Okazaki, T., & Engelhardt, M. D. (2015). Link-to-Column Connection with Supplemental Web Doublers in Eccentrically Braced Frames. *Journal of Structural Engineering (United States)*, *141*(8), 1–8. https://doi.org/10.1061/(ASCE)ST.1943-541X.0001170

Hu, H. (2015). *Numerical study of seismic behavior of high strength steel replaceable shear links*. University of Maryland, College Park.

Imani, R., & Bruneau, M. (2015). Effect of link-beam stiffener and brace flange alignment on inelastic cyclic behavior of eccentrically braced frames. *Engineering Journal*, *52*(2), 109–124.

Ji, X., Wang, Y., Ma, Q., & Okazaki, T. (2016a). Cyclic behavior of very short steel shear links. *Journal of Structural Engineering (United States)*, *142*(2). https://doi.org/10.1061/(ASCE)ST.1943-541X.0001375

Ji, X., Wang, Y., Ma, Q., & Okazaki, T. (2016b). Cyclic Behavior of Very Short Steel Shear Links. *Journal of Structural Engineering*, *142*(2), 04015114. https://doi.org/10.1061/(asce)st.1943-541x.0001375

JMP. (2012). *Discovering JMP*. 1–154. papers2://publication/uuid/06CF8B81-7B00-49E5-94E8-5F30387CF6F4

Kalnins, A., Rudolph, J., & Willuweit, A. (2015). Using the nonlinear kinematic hardening material model of Chaboche for elastic-plastic ratcheting analysis. *Journal of Pressure Vessel Technology, Transactions of the ASME*, *137*(3). https://doi.org/10.1115/1.4028659

Kanvinde, A. M., Marshall, K. S., Grilli, D. A., & Bomba, G. (2015). Forensic analysis of link fractures in eccentrically braced frames during the February 2011 Christchurch earthquake: Testing and simulation. *Journal of Structural Engineering (United States)*, *141*(5), 1–15. https://doi.org/10.1061/(ASCE)ST.1943-541X.0001043

Kasai, K., & Popov, E. P. (1986). A study of seismically resistant eccentrically braced steel frame systems. *Journal of Structural Engineering*, *121*(11), 1574–1580.

Kasai, Kazuhiko, & Popov, E. P. (1986a). Cyclic web buckling control for shear link beams. *Journal of Structural Engineering (United States)*, *112*(3), 505–523. https://doi.org/10.1061/(ASCE)0733-9445(1986)112:3(505)

Kasai, Kazuhiko, & Popov, E. P. (1986b). General Behavior of WF Steel Shear Link Beams. *Journal of Structural Engineering*, *112*(2), 362–382. https://doi.org/10.1061/(asce)0733-9445(1986)112:2(362)

Koboevic, S., & David, S. O. (2010). Design and seismic behaviour of taller eccentrically braced frames. *Canadian Journal of Civil Engineering*, *37*(2), 195–208. https://doi.org/10.1139/L09-131

Koboevic, S., Rozon, J., & Tremblay, R. (2012). Seismic Performance of Low-to-Moderate Height Eccentrically Braced Steel Frames Designed for North American Seismic Conditions. *Journal of Structural Engineering*, *138*(12), 1465–1476. https://doi.org/10.1061/(asce)st.1943-541x.0000433

Landolfo, R., Mazzolani, F., Dubina, D., And, L. S. da S., & D'Aniello, M. (2017). *Design of Steel Structures for Buildings in Seismic Areas* (1st Editio). ECCS – European Convention for Constructional Steelwork.

Malley, J. O., & Popov, E. P. (1984). Shear Links in Eccentrically Braced Frames. *Journal of Structural Engineering*, *110*(9), 2275–2295. https://doi.org/10.1061/(asce)0733-9445(1984)110:9(2275)

Manheim, Daniel N., & Popov, E. P. (1983). Plastic Shear Hinges in Steel Frames. *Journal of Structural Engineering*, *109*(10), 2404–2419. https://doi.org/10.1061/(asce)0733-9445(1983)109:10(2404)

Manheim, Daniel Nissim. (1982). *On the design of eccentrically braced frames*. University of California, Berkeley.

Mansour, N. (2010). *Development of the design of eccentrically braced frames with replaceable shear links*.

Mansour, N., Christopoulos, C., & Tremblay, R. (2011). Experimental validation of replaceable shear links for eccentrically braced steel frames. *Journal of Structural Engineering*, *137*(10), 1141–1152. https://doi.org/10.1061/(ASCE)ST.1943-541X.0000350

McDaniel, C. C., Uang, C. M., & Seible, F. (2003). Cyclic testing of built-up steel shear links for the new bay bridge. *Journal of Structural Engineering*, *129*(6), 801–809. https://doi.org/10.1061/(ASCE)0733-9445(2003)129:6(801)

McKay, M. D., Beckman, R. J., & Conover, W. J. (1979). A comparison of three methods for selecting values of input variables in the analysis of output from a computer code. *Technometrics*, *42*(1), 55–61. https://doi.org/10.1080/00401706.2000.10485979

Mohebkhah, A., & Chegeni, B. (2014). Overstrength and rotation capacity for EBF links made of European IPE sections. *Thin-Walled Structures*, *74*, 255–260. https://doi.org/10.1016/j.tws.2013.10.013

Okazaki, T. (2004). *Seismic performance of link-to-column connections in steel eccentrically braced frames*. 647.

Okazaki, T., Arce, G., Ryu, H.-C., & Engelhardt, M. D. (2005a). Experimental Study of Local Buckling, Overstrength, and Fracture of Links in Eccentrically Braced Frames. *Journal of Structural Engineering*, *131*(10), 1526–1535. https://doi.org/10.1061/(asce)0733-9445(2005)131:10(1526)

Okazaki, T., Arce, G., Ryu, H. C., & Engelhardt, M. D. (2005b). Experimental study of local buckling, overstrength, and fracture of links in eccentrically braced frames. *Journal of Structural Engineering*, *131*(10), 1526–1535. https://doi.org/10.1061/(ASCE)0733-9445(2005)131:10(1526)

Okazaki, T., & Engelhardt, M. D. (2007). Cyclic loading behavior of EBF links constructed of ASTM A992 steel. *Journal of Constructional Steel Research*, *63*(6), 751–765. https://doi.org/10.1016/j.jcsr.2006.08.004

Okazaki, T., Engelhardt, M. D., Drolias, A., Schell, E., Hong, J. K., & Uang, C. M. (2009). Experimental investigation of link-to-column connections in eccentrically braced frames. *Journal of Constructional Steel Research*, *65*(7), 1401–1412. https://doi.org/10.1016/j.jcsr.2009.02.003

Pirmoz, A., Ahadi, P., & Farajkhah, V. (2016). Finite element analysis of extended stiffened end plate link-to-column connections. *Steel Construction*, *9*(1), 46–57. https://doi.org/10.1002/stco.201350003

Popov, E. P. (1983). Design Considerations for Shear Links in. *Design Considerations for Shear Links in Eccentrically Braced Frames*, *November*.

Popov, E. P., & Ricles, J. M. (1989). Composite Action in Eccentrically Braced Frames. *Journal of Structural Engineering*, *115*(8), 2046–2066. https://doi.org/https://doi.org/10.1061/(ASCE)0733-9445(1989)115:8(2046)

Prinz, G. S., & Richards, P. W. (2009). Eccentrically braced frame links with reduced web sections. *Journal of Constructional Steel Research*, *65*(10–11), 1971–1978. https://doi.org/10.1016/j.jcsr.2009.04.017

Ramadan, T., & Ghobarah, A. (1991). Prediction of the ultimate capacity of wide flange link beams under cyclic loading. *Computers and Structures*, *40*(2), 409–418. https://doi.org/10.1016/0045-7949(91)90366-T

Richards, P.W. (2004). *Cyclic stability and capacity design of steel eccentrically braced frames*.

Richards, Paul W., & Uang, C.-M. (2004). Development of Testing Protocol for Links in Eccentrically Braced Frames. *13th World Conference on Earthquake Engineering*, *2795*.

Richards, Paul W., & Uang, C.-M. (2006). Testing Protocol for Short Links in Eccentrically Braced Frames. *Journal of Structural Engineering*, *132*(8), 1183–1191. https://doi.org/10.1061/(asce)0733-9445(2006)132:8(1183)

Richards, Paul W., & Uang, C. M. (2005). Effect of flange width-thickness ratio on eccentrically braced frames link cyclic rotation capacity. *Journal of Structural Engineering*, *131*(10), 1546–1552. https://doi.org/10.1061/(ASCE)0733-9445(2005)131:10(1546)

Richards, Paul W. (2004). *Cyclic stability and capacity design of steel eccentrically braced frames*. University of California, San Diego.

Ricles, J. M., & Popov, E. P. (1987). *Experiments on eccentrically braced frames with composite floors*. Earthquake Engineering Research Center, University of California Berkeley, CA.

Roeder, C. W. (1977). Inelastic Behavior of Eccentrically Braced. *Research Report No. UCB/EERC-77/18*.

Saltelli, A., Ratto, M., Andres, T., Cariboni, F. C. J., Gatelli, D., Saisana, M., & Tarantola, S. (2008). Global Sensitivity Analysis: The Primer. In *International Statistical Review* (Vol. 76, Issue 3). https://doi.org/10.1111/j.1751-5823.2008.00062_17.x

Santner, T. J., Williams, B. J., & Notz, W. I. (2018). *The Design and Analysis of Computer Experiments* (S. Z. Peter Diggle, Ursula Gather (ed.); 2nd ed.). Springer Series in Statistics. https://doi.org/https://doi.org/10.1007/978-1-4939-8847-1

Sousa, A. de C. e, Suzuki, Y., & Lignos, D. (2020). Consistency in Solving the Inverse Problem of the Voce-Chaboche Constitutive Model for Plastic Straining. *Journal of Engineering Mechanics*, *146*(9), 04020097. https://doi.org/10.1061/(asce)em.1943-7889.0001839

Tanabashi, R., Kaneta, K., & Ishida, T. (1974). On the rigidity and ductility of steel bracing assemblages. In *5th World Conference on Earthquake Engineering*.

Tsai, K. C., Yang, Y. F., & Lin, J. L. (1993). Seismic eccentrically braced frames. *The Structural Design of Tall Buildings*, *2*(1), 53–74. https://doi.org/10.1002/tal.4320020105

Whittaker, A. S., Uang, C. M., & Bertero, V. V. (1989). Seismic testing of eccentrically braced dual steel systems. *Earthquake Spectra*, *5*(2), 429–449. https://doi.org/10.1193/1.1585531

Yiğitsoy, G., Topkaya, C., & Okazaki, T. (2014). Stability of beams in steel eccentrically braced frames. *Journal of Constructional Steel Research*, *96*, 14–25. https://doi.org/10.1016/j.jcsr.2014.01.002

APPENDIX A DEFORMED SHAPES AND EQUIVALENT PLASTIC STRAIN

Deformed shapes and equivalent plastic strain at the last load step are shown below.

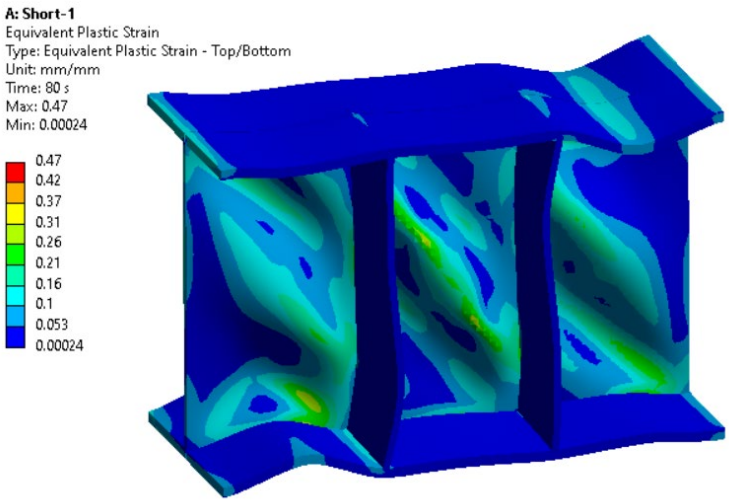

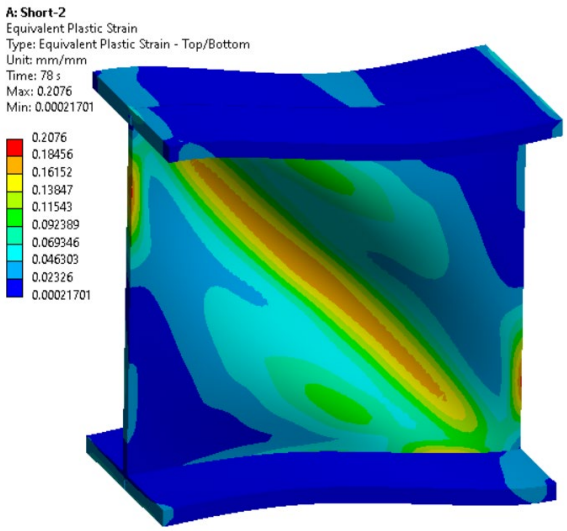

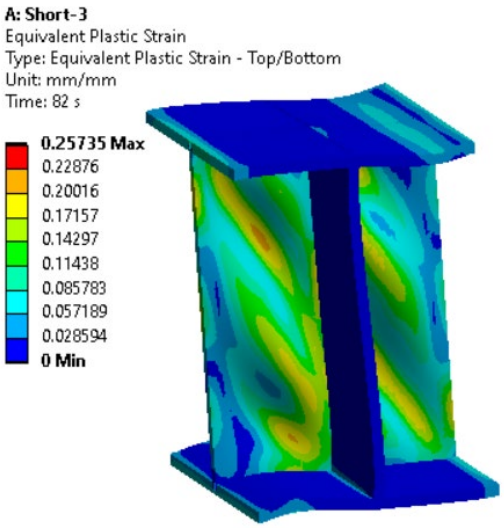

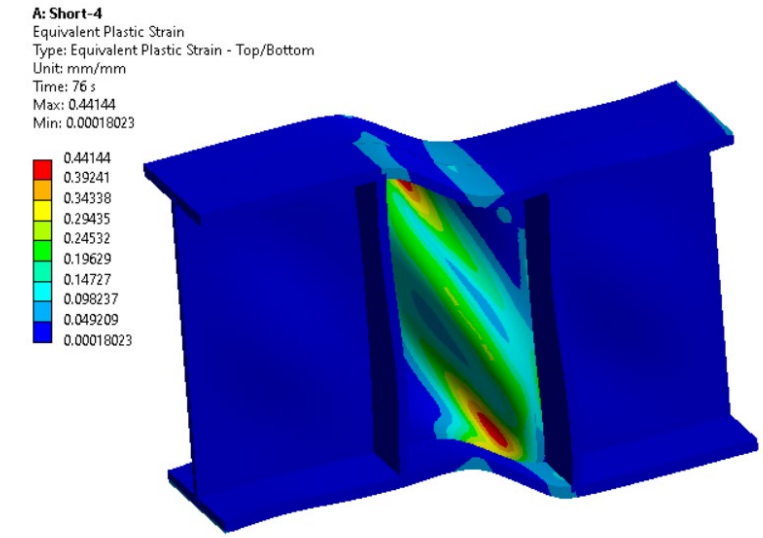
A: Short-4
Equivalent Plastic Strain
Type: Equivalent Plastic Strain - Top/Bottom
Unit: mm/mm
Time: 76 s
Max: 0.44144
Min: 0.00018023
0.44144
0.39241
0.34338
0.29435
0.24532
0.19629
0.14727
0.098237
0.049209
0.00018023

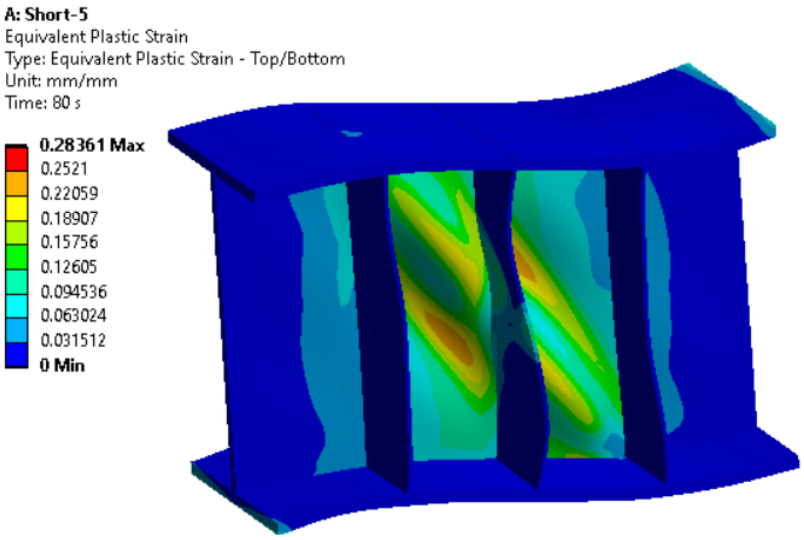
A: Short-5
Equivalent Plastic Strain
Type: Equivalent Plastic Strain - Top/Bottom
Unit: mm/mm
Time: 80 s
0.28361 Max
0.2521
0.22059
0.18907
0.15756
0.12605
0.094536
0.063024
0.031512
0 Min

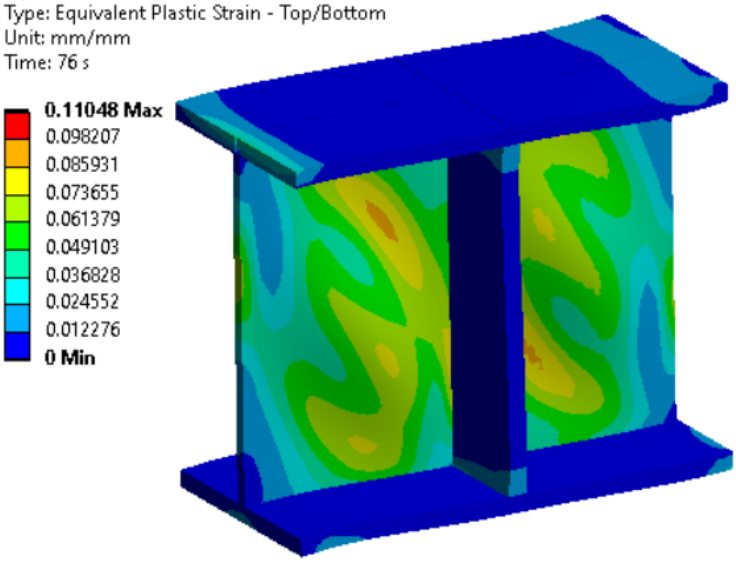
A: Short-6
Equivalent Plastic Strain
Type: Equivalent Plastic Strain - Top/Bottom
Unit: mm/mm
Time: 76 s
0.11048 Max
0.098207
0.085931
0.073655
0.061379
0.049103
0.036828
0.024552
0.012276
0 Min

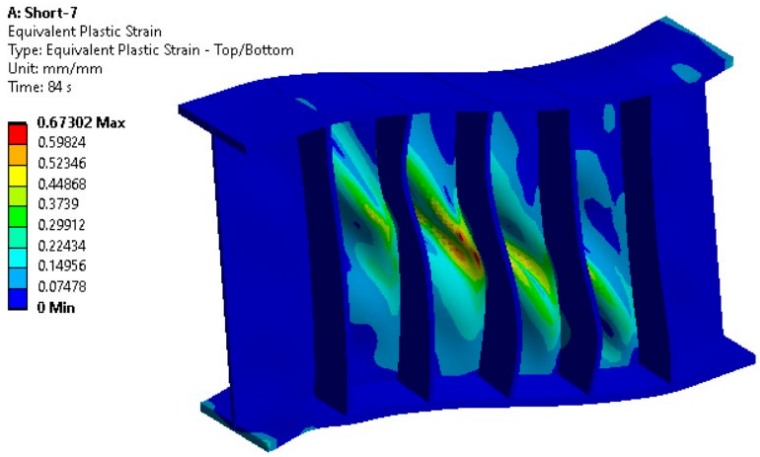
A: Short-7
Equivalent Plastic Strain
Type: Equivalent Plastic Strain - Top/Bottom
Unit: mm/mm
Time: 84 s
0.67302 Max
0.59824
0.52346
0.44868
0.3739
0.29912
0.22434
0.14956
0.07478
0 Min

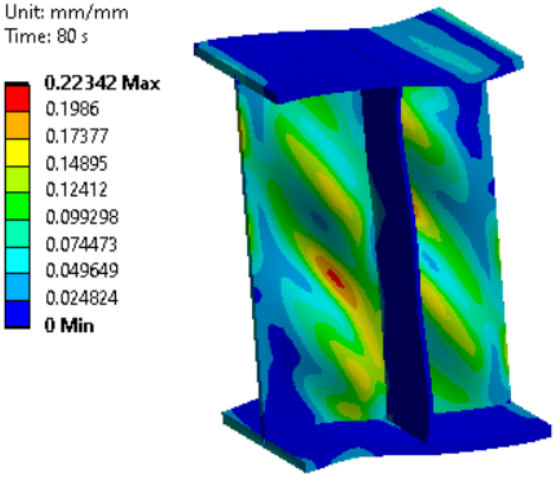
A: Short-8
Equivalent Plastic Strain
Type: Equivalent Plastic Strain - Top/Bottom
Unit: mm/mm
Time: 80 s
0.22342 Max
0.1986
0.17377
0.14895
0.12412
0.099298
0.074473
0.049649
0.024824
0 Min

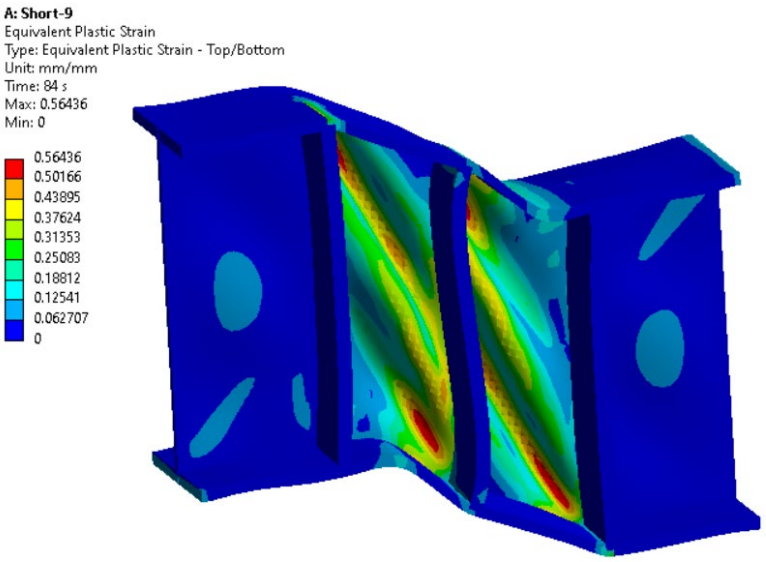
A: Short-9
Equivalent Plastic Strain
Type: Equivalent Plastic Strain - Top/Bottom
Unit: mm/mm
Time: 84 s
Max: 0.56436
Min: 0
0.56436
0.50166
0.43895
0.37624
0.31353
0.25083
0.18812
0.12541
0.062707
0

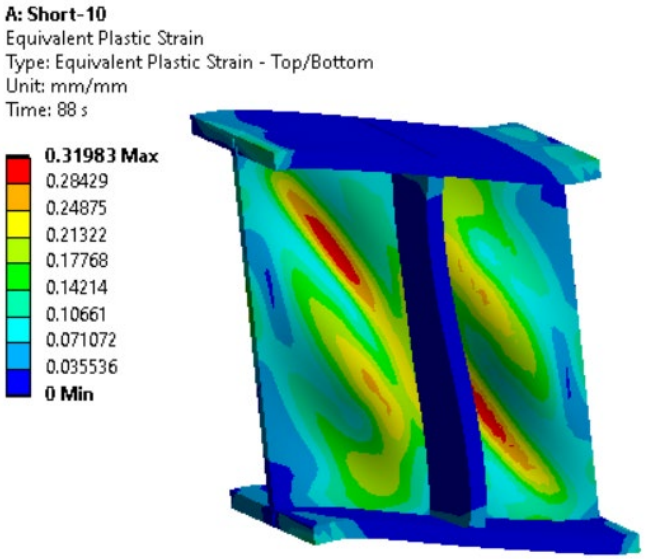
A: Short-10
Equivalent Plastic Strain
Type: Equivalent Plastic Strain - Top/Bottom
Unit: mm/mm
Time: 88 s
0.31983 Max
0.28429
0.24875
0.21322
0.17768
0.14214
0.10661
0.071072
0.035536
0 Min

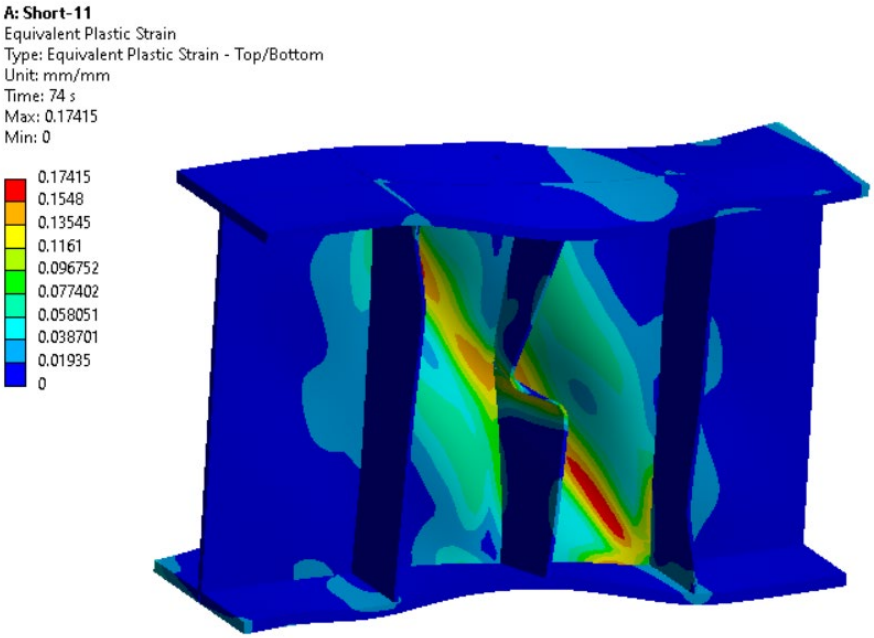
A: Short-11
Equivalent Plastic Strain
Type: Equivalent Plastic Strain - Top/Bottom
Unit: mm/mm
Time: 74 s
Max: 0.17415
Min: 0
0.17415
0.1548
0.13545
0.1161
0.096752
0.077402
0.058051
0.038701
0.01935
0

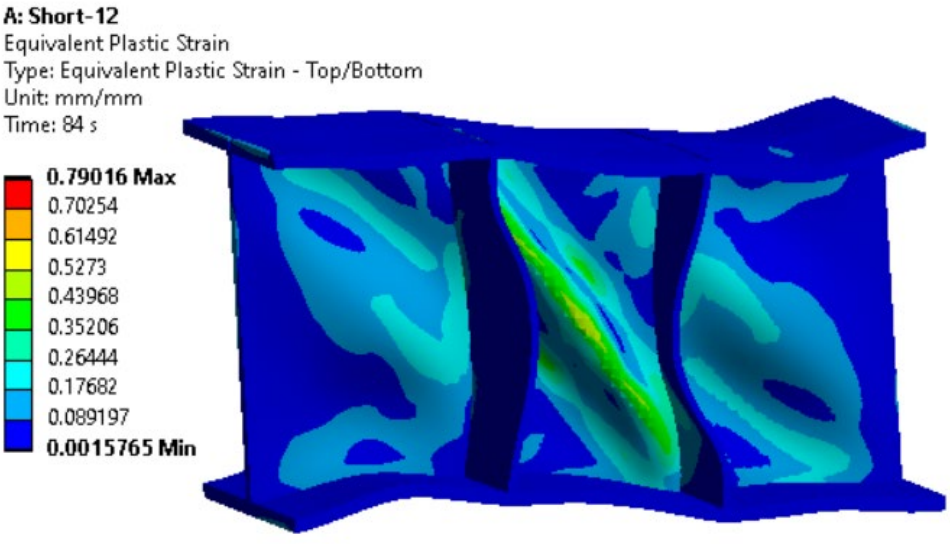
A: Short-12
Equivalent Plastic Strain
Type: Equivalent Plastic Strain - Top/Bottom
Unit: mm/mm
Time: 84 s
0.79016 Max
0.70254
0.61492
0.5273
0.43968
0.35206
0.26444
0.17682
0.089197
0.0015765 Min

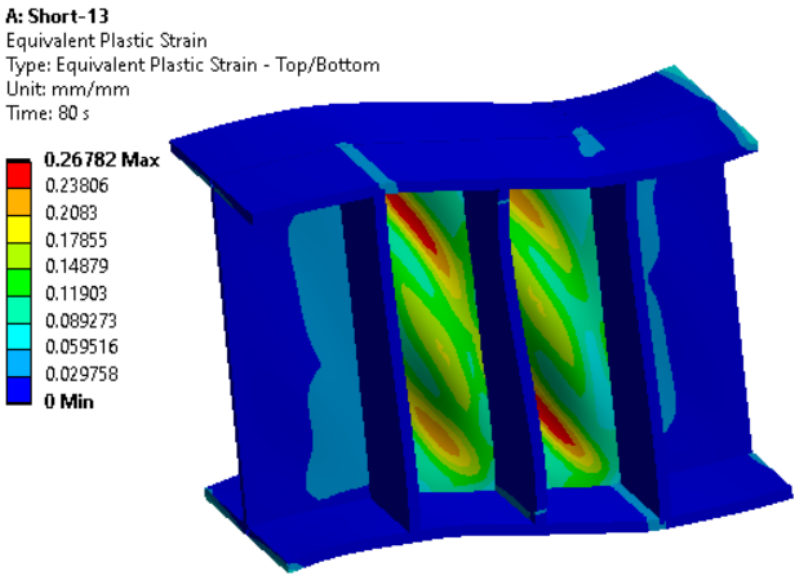
A: Short-13
Equivalent Plastic Strain
Type: Equivalent Plastic Strain - Top/Bottom
Unit: mm/mm
Time: 80 s
0.26782 Max
0.23806
0.2083
0.17855
0.14879
0.11903
0.089273
0.059516
0.029758
0 Min

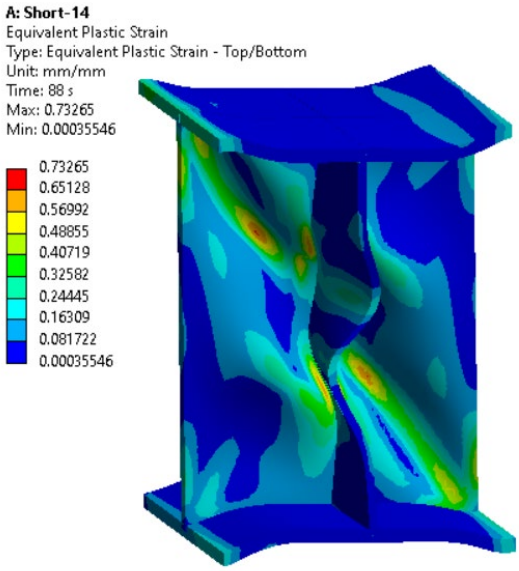
A: Short-14
Equivalent Plastic Strain
Type: Equivalent Plastic Strain - Top/Bottom
Unit: mm/mm
Time: 88 s
Max: 0.73265
Min: 0.00035546
0.73265
0.65128
0.56992
0.48855
0.40719
0.32582
0.24445
0.16309
0.081722
0.00035546

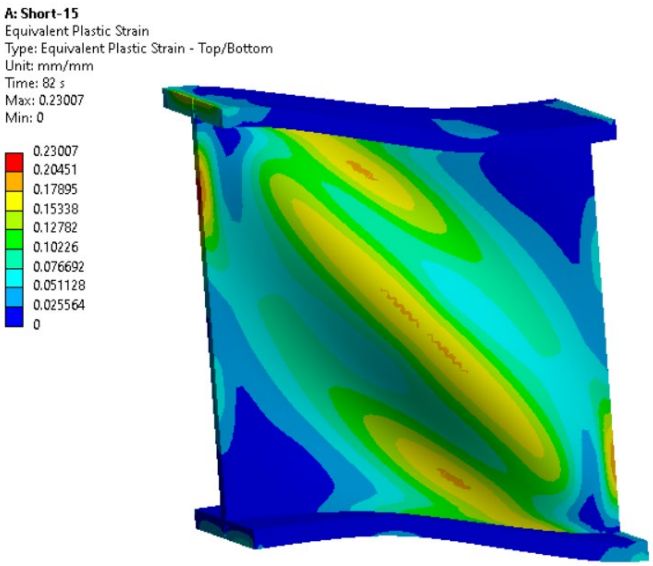
A: Short-15
Equivalent Plastic Strain
Type: Equivalent Plastic Strain - Top/Bottom
Unit: mm/mm
Time: 82 s
Max: 0.23007
Min: 0
0.23007
0.20451
0.17895
0.15338
0.12782
0.10226
0.076692
0.051128
0.025564
0

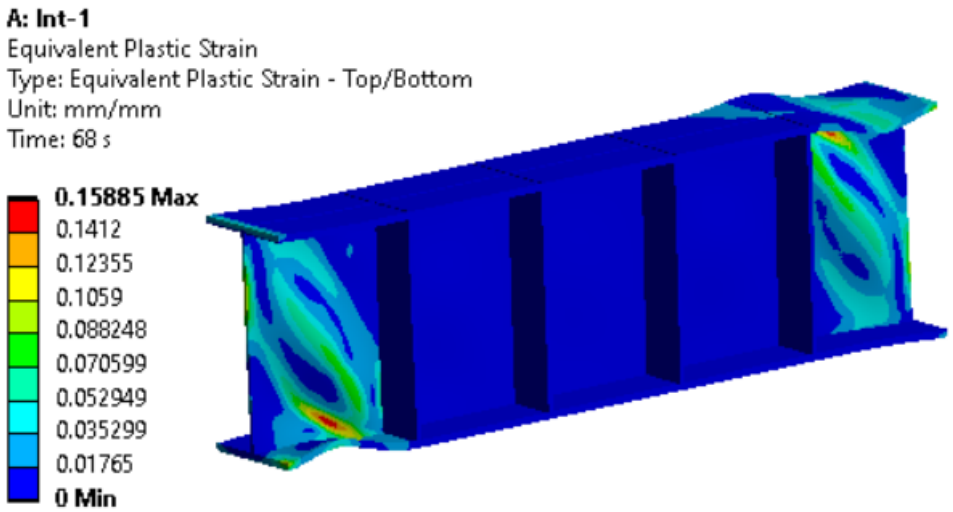
A: Int-1
Equivalent Plastic Strain
Type: Equivalent Plastic Strain - Top/Bottom
Unit: mm/mm
Time: 68 s
0.15885 Max
0.1412
0.12355
0.1059
0.088248
0.070599
0.052949
0.035299
0.01765
0 Min

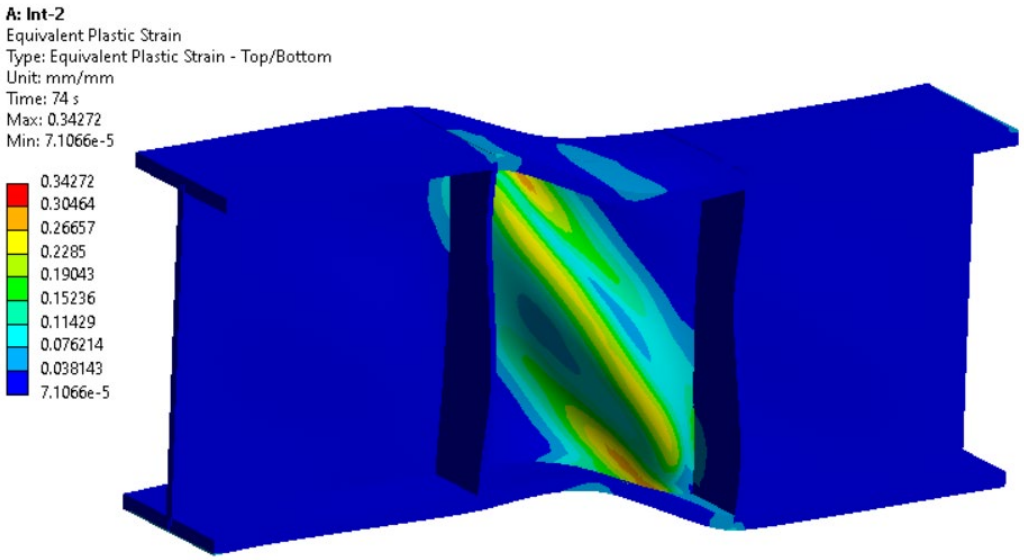
A: Int-2
Equivalent Plastic Strain
Type: Equivalent Plastic Strain - Top/Bottom
Unit: mm/mm
Time: 74 s
Max: 0.34272
Min: 7.1066e-5
0.34272
0.30464
0.26657
0.2285
0.19043
0.15236
0.11429
0.076214
0.038143
7.1066e-5

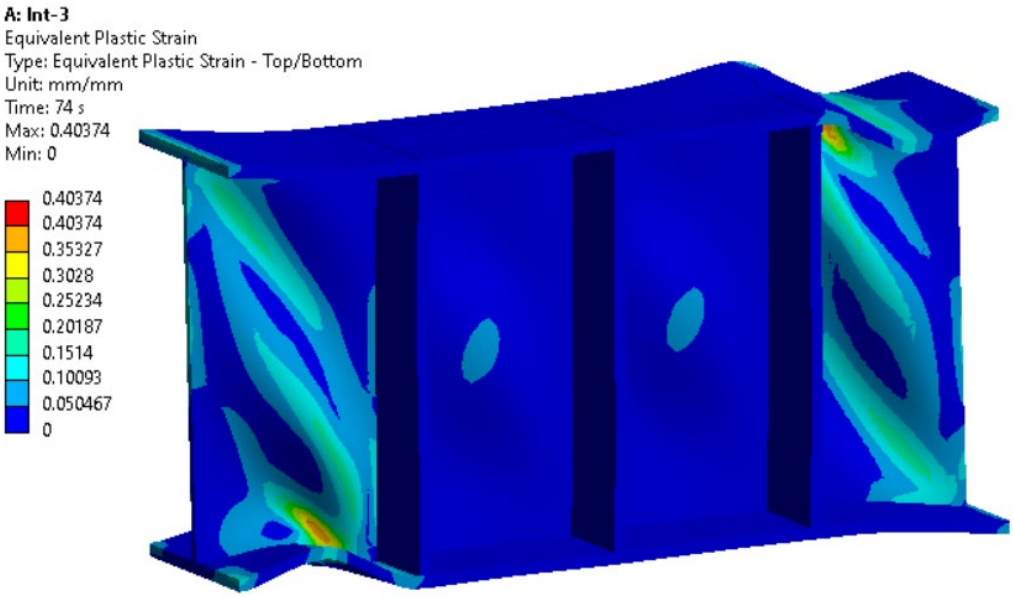
A: Int-3
Equivalent Plastic Strain
Type: Equivalent Plastic Strain - Top/Bottom
Unit: mm/mm
Time: 74 s
Max: 0.40374
Min: 0
0.40374
0.40374
0.35327
0.3028
0.25234
0.20187
0.1514
0.10093
0.050467
0

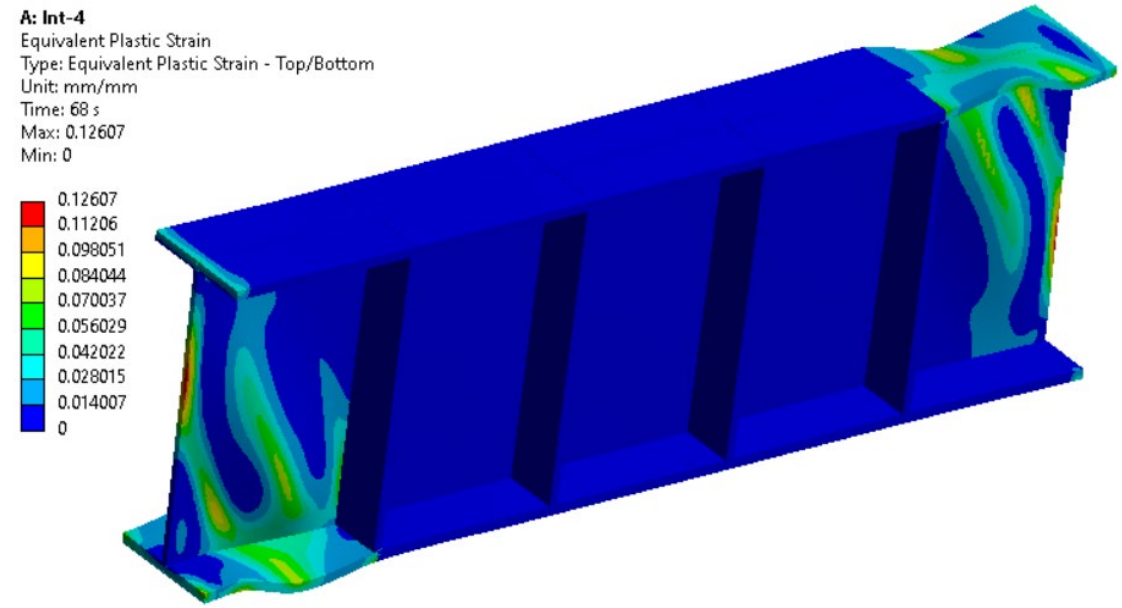
A: Int-4
Equivalent Plastic Strain
Type: Equivalent Plastic Strain - Top/Bottom
Unit: mm/mm
Time: 68 s
Max: 0.12607
Min: 0
0.12607
0.11206
0.098051
0.084044
0.070037
0.056029
0.042022
0.028015
0.014007
0

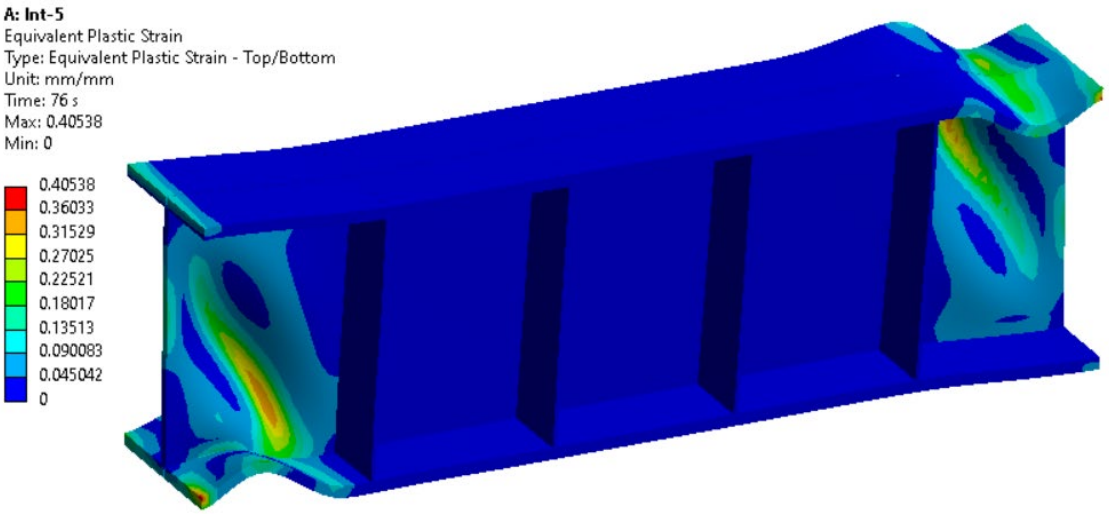
A: Int-5
Equivalent Plastic Strain
Type: Equivalent Plastic Strain - Top/Bottom
Unit: mm/mm
Time: 76 s
Max: 0.40538
Min: 0
0.40538
0.36033
0.31529
0.27025
0.22521
0.18017
0.13513
0.090083
0.045042
0

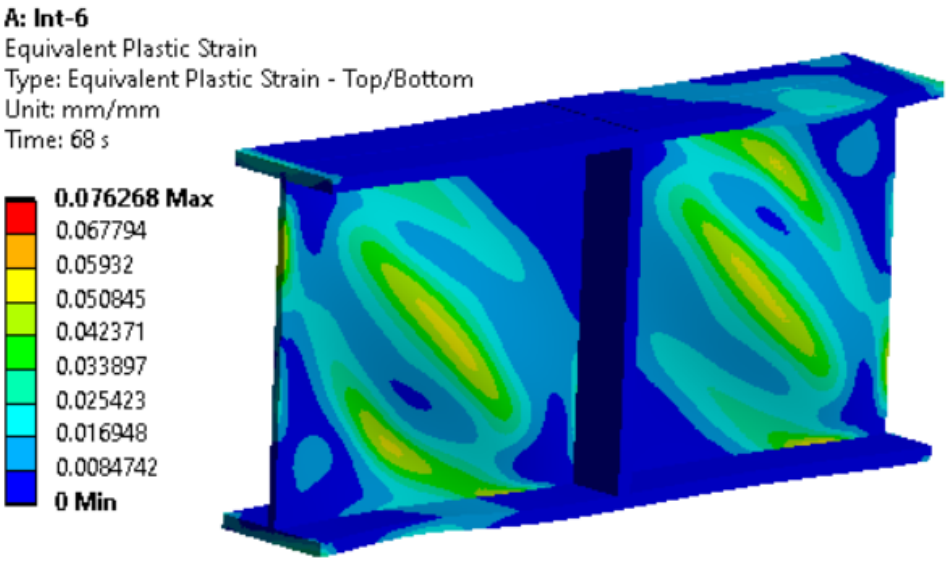
A: Int-6
Equivalent Plastic Strain
Type: Equivalent Plastic Strain - Top/Bottom
Unit: mm/mm
Time: 68 s
0.076268 Max
0.067794
0.05932
0.050845
0.042371
0.033897
0.025423
0.016948
0.0084742
0 Min

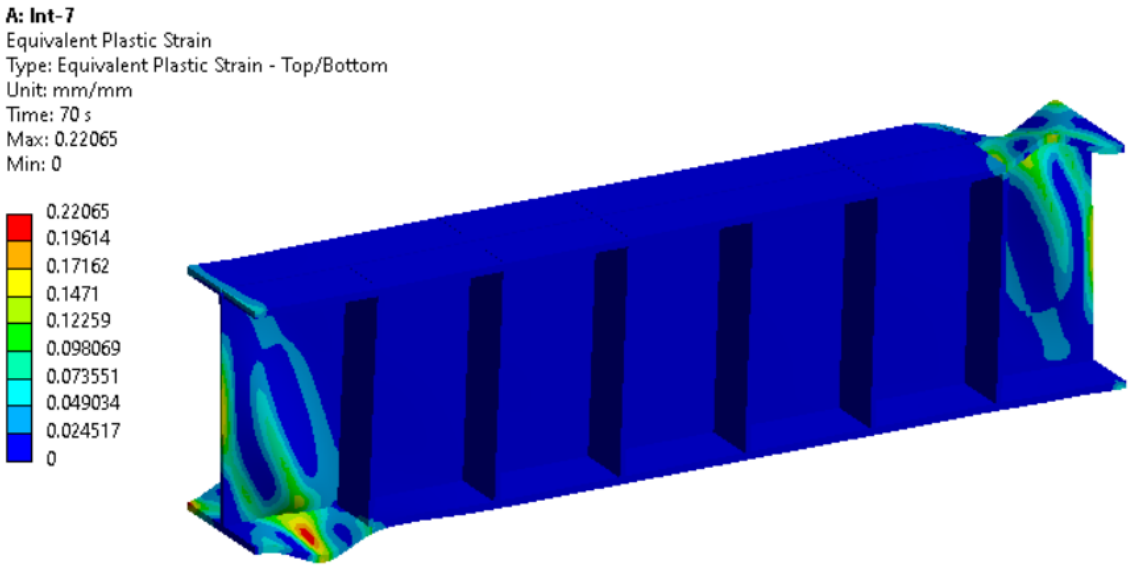
A: Int-7
Equivalent Plastic Strain
Type: Equivalent Plastic Strain - Top/Bottom
Unit: mm/mm
Time: 70 s
Max: 0.22065
Min: 0
0.22065
0.19614
0.17162
0.1471
0.12259
0.098069
0.073551
0.049034
0.024517
0

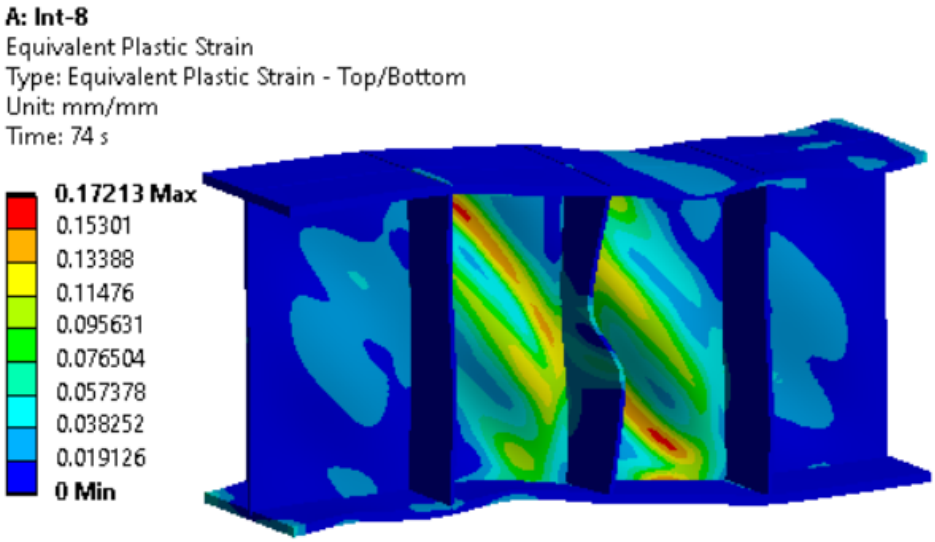
A: Int-8
Equivalent Plastic Strain
Type: Equivalent Plastic Strain - Top/Bottom
Unit: mm/mm
Time: 74 s
0.17213 Max
0.15301
0.13388
0.11476
0.095631
0.076504
0.057378
0.038252
0.019126
0 Min

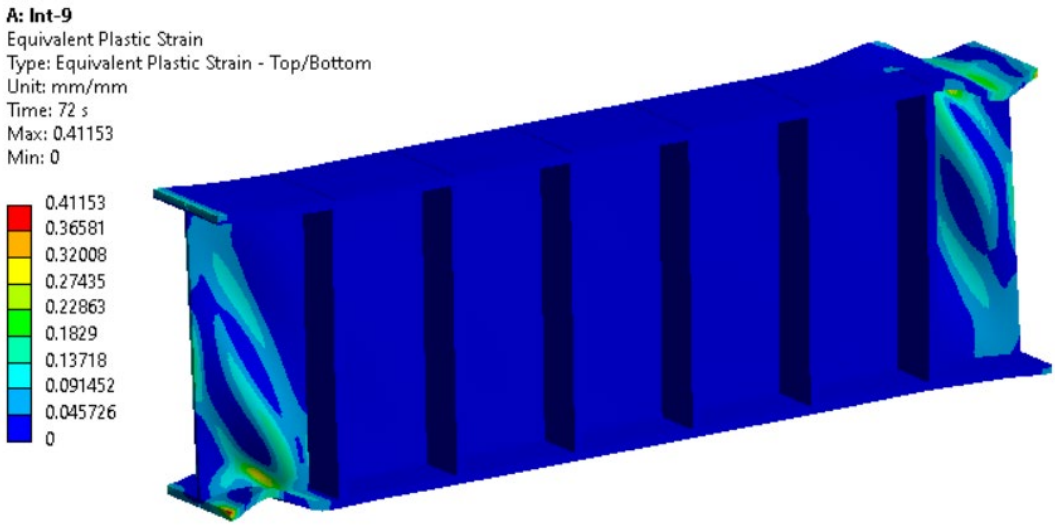
A: Int-9
Equivalent Plastic Strain
Type: Equivalent Plastic Strain - Top/Bottom
Unit: mm/mm
Time: 72 s
Max: 0.41153
Min: 0
0.41153
0.36581
0.32008
0.27435
0.22863
0.1829
0.13718
0.091452
0.045726
0

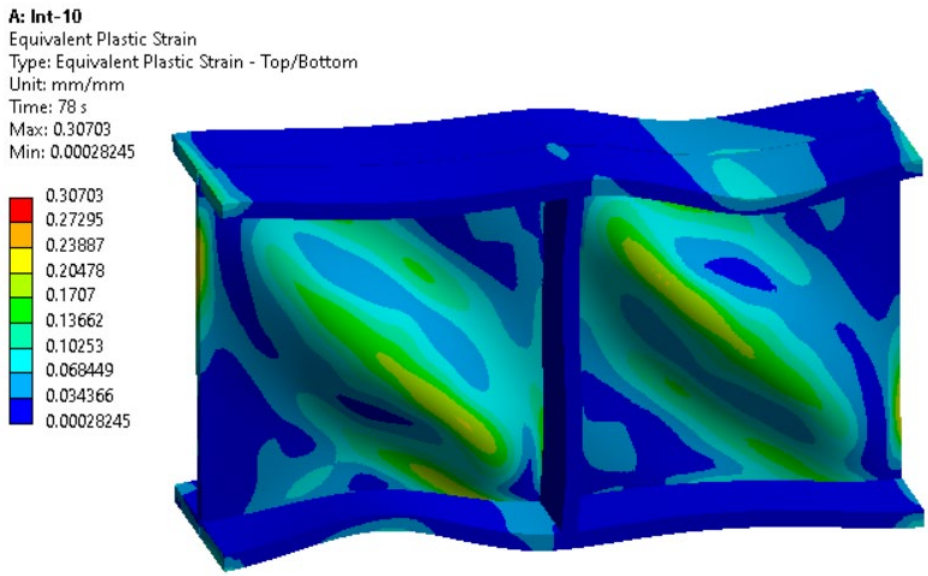
A: Int-10
Equivalent Plastic Strain
Type: Equivalent Plastic Strain - Top/Bottom
Unit: mm/mm
Time: 78 s
Max: 0.30703
Min: 0.00028245
0.30703
0.27295
0.23887
0.20478
0.1707
0.13662
0.10253
0.068449
0.034366
0.00028245

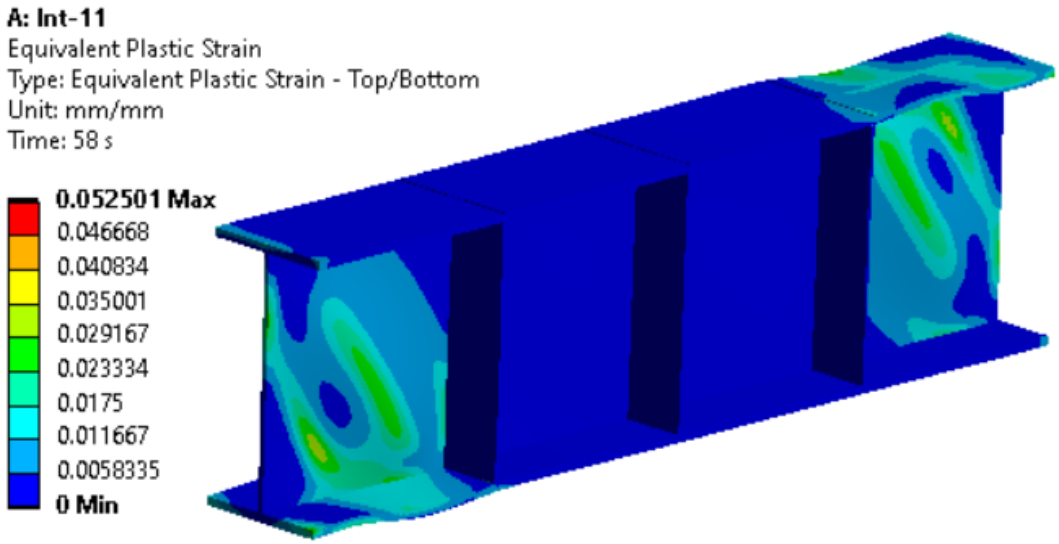
A: Int-11
Equivalent Plastic Strain
Type: Equivalent Plastic Strain - Top/Bottom
Unit: mm/mm
Time: 58 s
0.052501 Max
0.046668
0.040834
0.035001
0.029167
0.023334
0.0175
0.011667
0.0058335
0 Min

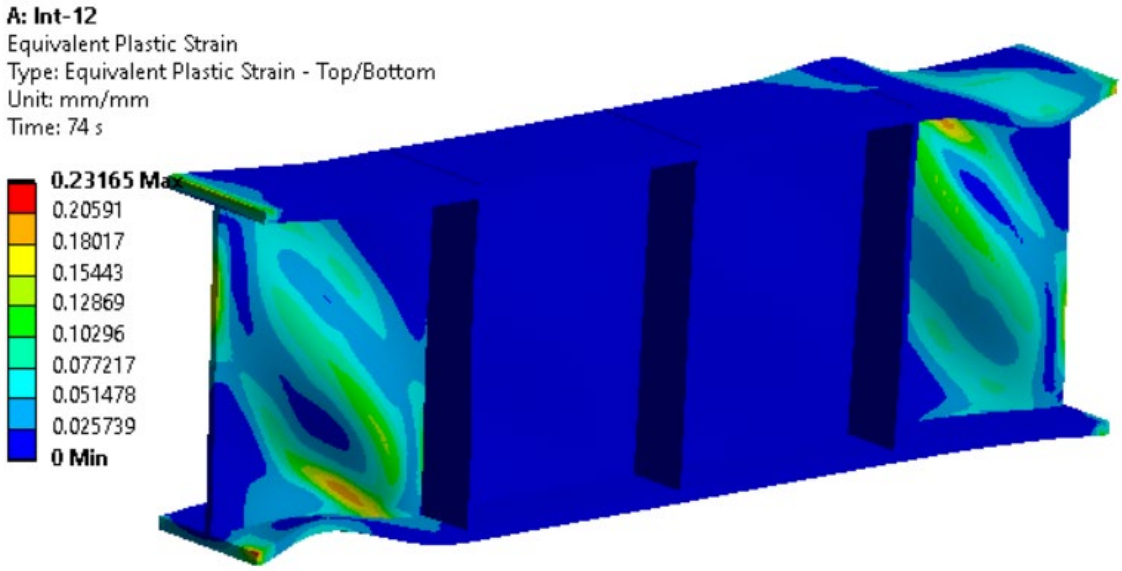
A: Int-12
Equivalent Plastic Strain
Type: Equivalent Plastic Strain - Top/Bottom
Unit: mm/mm
Time: 74 s
0.20591
0.18017
0.15443
0.12869
0.10296
0.077217
0.051478
0.025739
0 Min

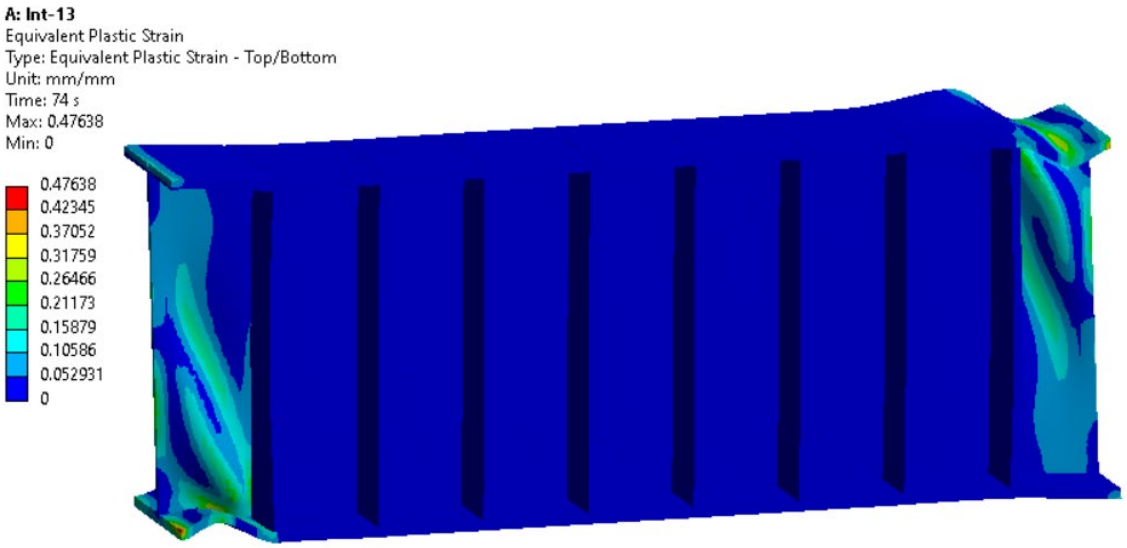
A: Int-13
Equivalent Plastic Strain
Type: Equivalent Plastic Strain - Top/Bottom
Unit: mm/mm
Time: 74 s
Max: 0.47638
Min: 0
0.47638
0.42345
0.37052
0.31759
0.26466
0.21173
0.15879
0.10586
0.052931
0

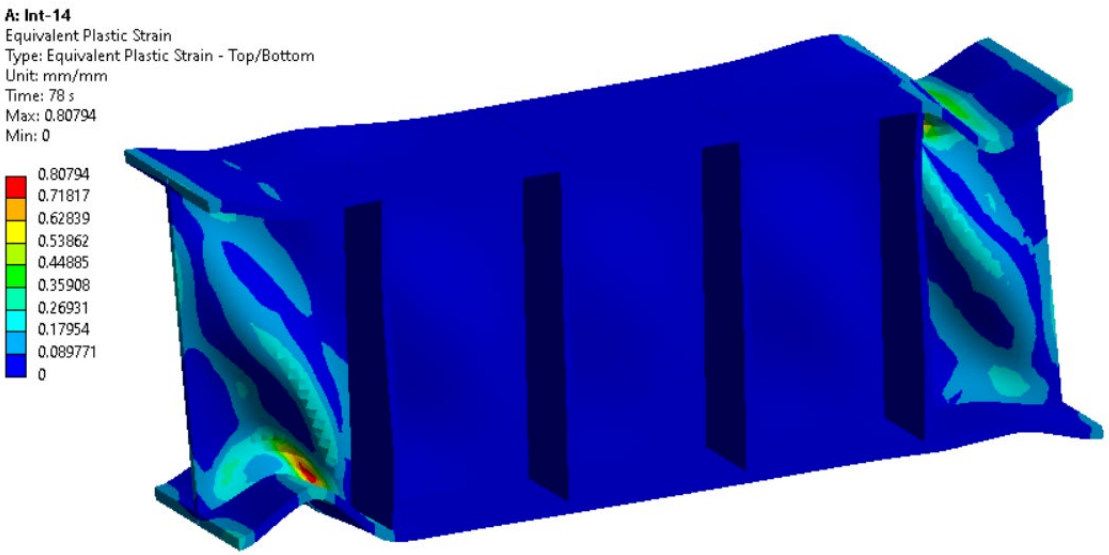
A: Int-14
Equivalent Plastic Strain
Type: Equivalent Plastic Strain - Top/Bottom
Unit: mm/mm
Time: 78 s
Max: 0.80794
Min: 0
0.80794
0.71817
0.62839
0.53862
0.44885
0.35908
0.26931
0.17954
0.089771
0

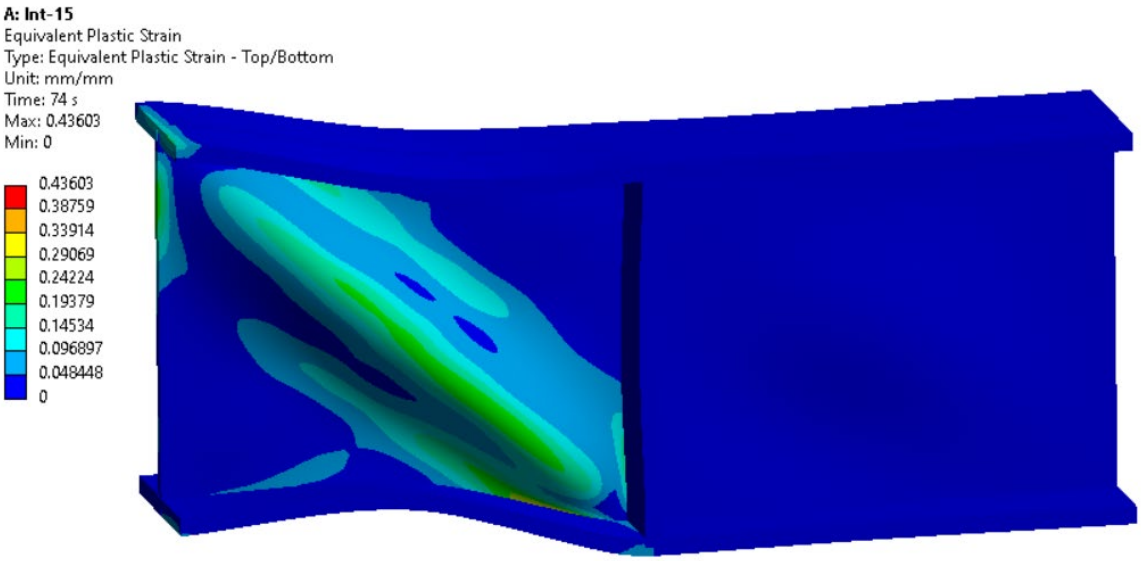
A: Int-15
Equivalent Plastic Strain
Type: Equivalent Plastic Strain - Top/Bottom
Unit: mm/mm
Time: 74 s
Max: 0.43603
Min: 0
0.43603
0.38759
0.33914
0.29069
0.24224
0.19379
0.14534
0.096897
0.048448
0

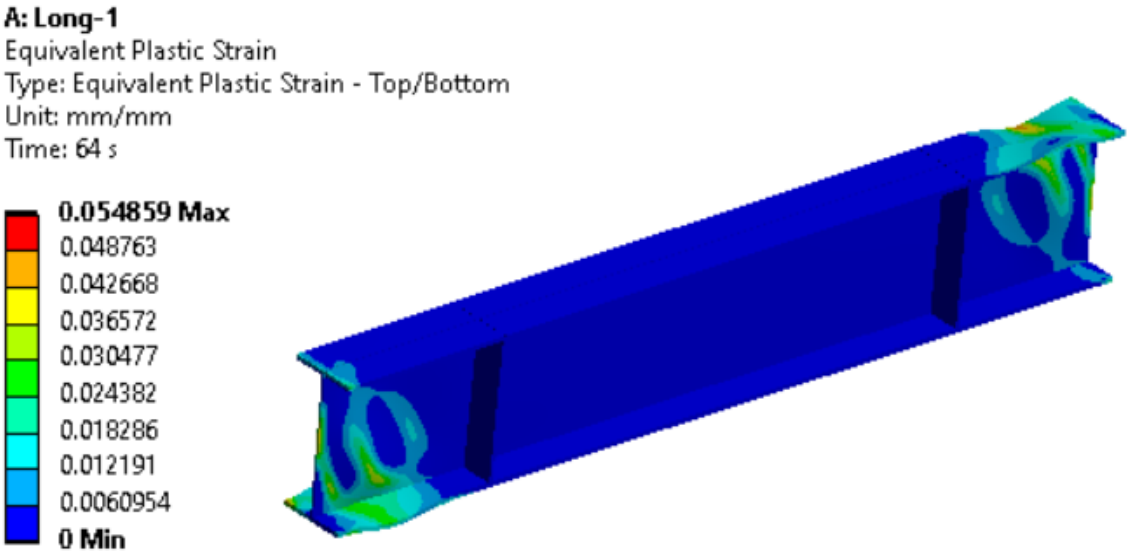
A: Long-1
Equivalent Plastic Strain
Type: Equivalent Plastic Strain - Top/Bottom
Unit: mm/mm
Time: 64 s
0.054859 Max
0.048763
0.042668
0.036572
0.030477
0.024382
0.018286
0.012191
0.0060954
0 Min

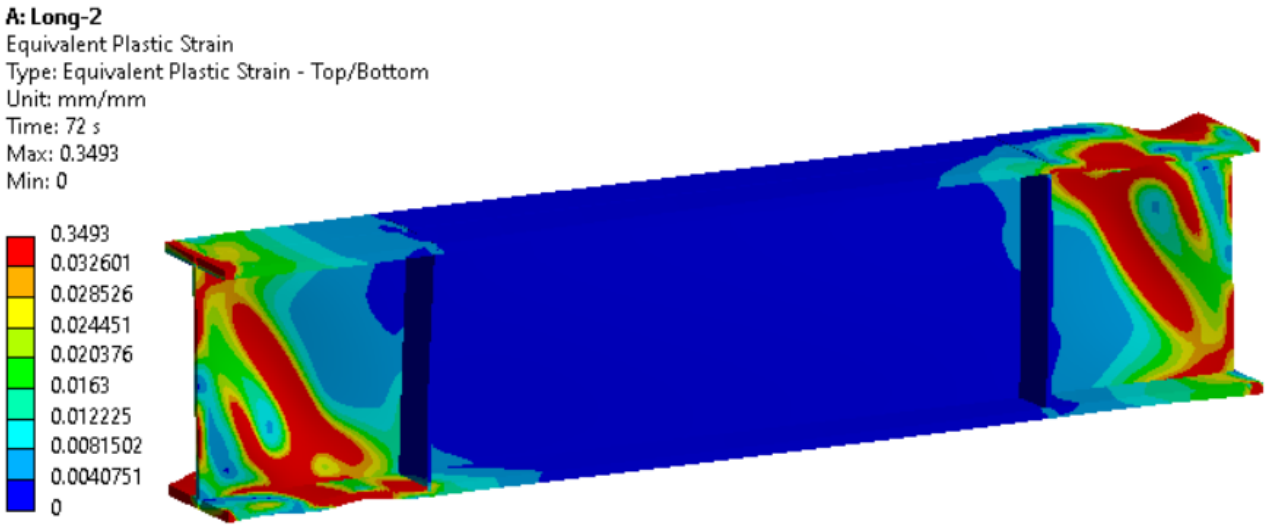
A: Long-2
Equivalent Plastic Strain
Type: Equivalent Plastic Strain - Top/Bottom
Unit: mm/mm
Time: 72 s
Max: 0.3493
Min: 0
0.3493
0.032601
0.028526
0.024451
0.020376
0.0163
0.012225
0.0081502
0.0040751
0

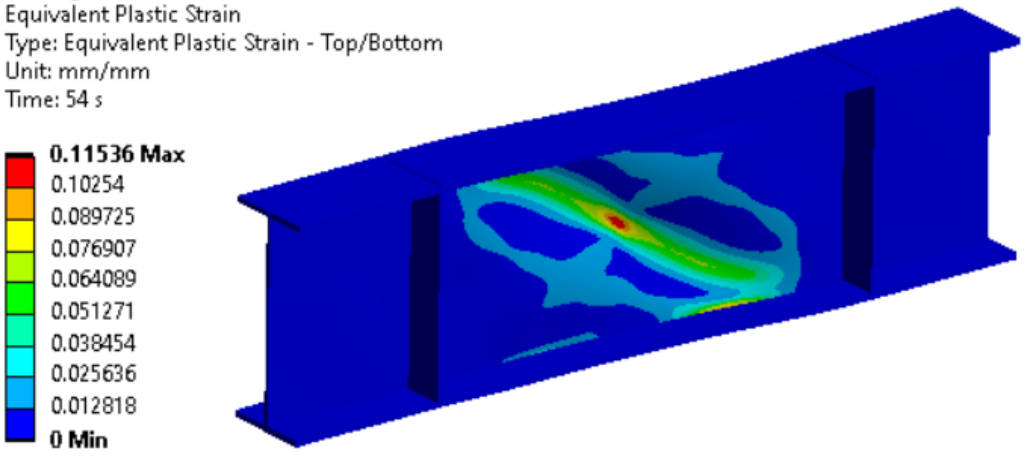
A: Long-3
Equivalent Plastic Strain
Type: Equivalent Plastic Strain - Top/Bottom
Unit: mm/mm
Time: 54 s
0.11536 Max
0.10254
0.089725
0.076907
0.064089
0.051271
0.038454
0.025636
0.012818
0 Min

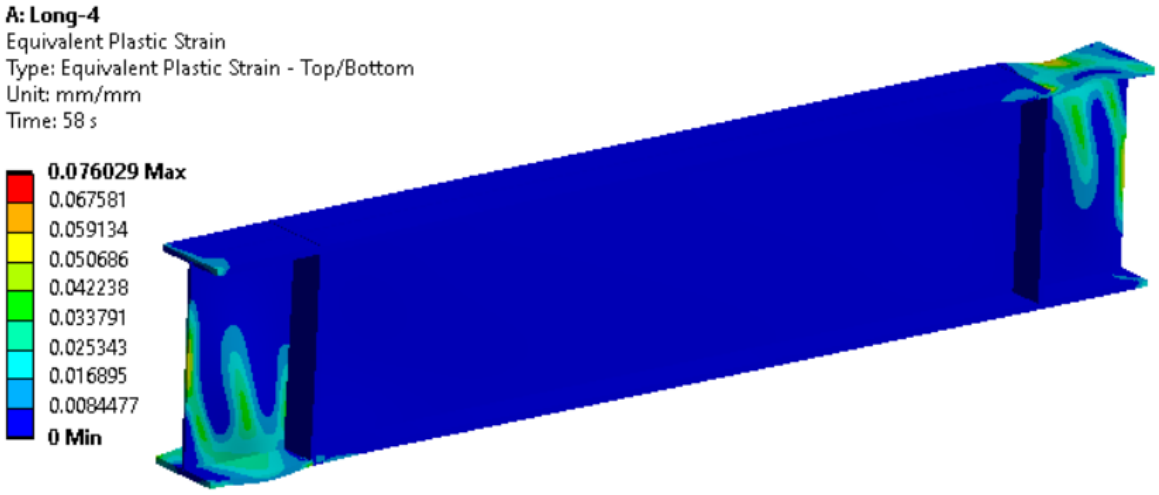
A: Long-4
Equivalent Plastic Strain
Type: Equivalent Plastic Strain - Top/Bottom
Unit: mm/mm
Time: 58 s
0.076029 Max
0.067581
0.059134
0.050686
0.042238
0.033791
0.025343
0.016895
0.0084477
0 Min

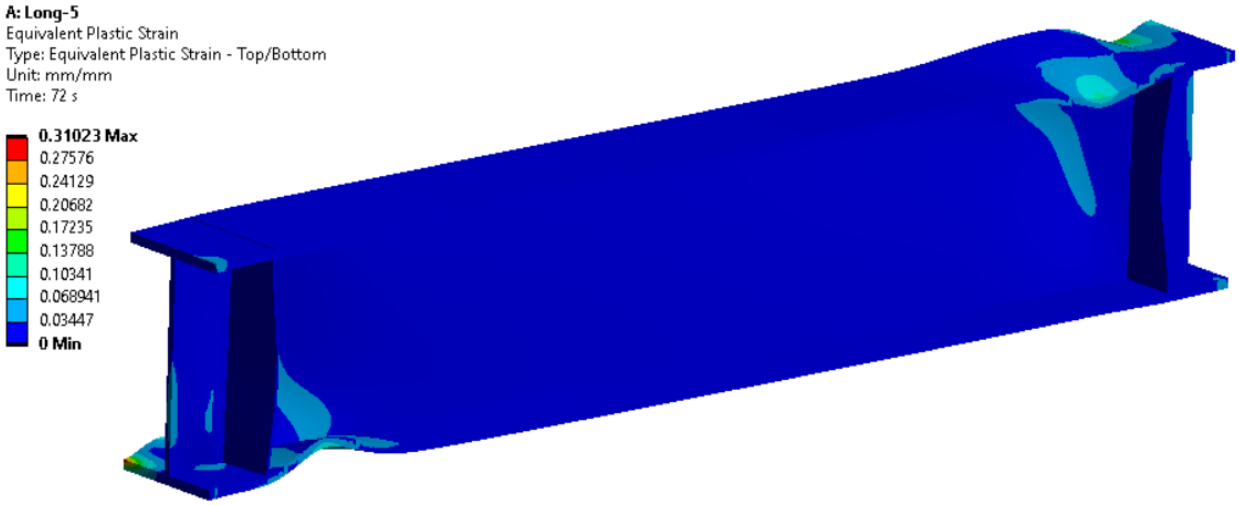
A: Long-5
Equivalent Plastic Strain
Type: Equivalent Plastic Strain - Top/Bottom
Unit: mm/mm
Time: 72 s
0.31023 Max
0.27576
0.24129
0.20682
0.17235
0.13788
0.10341
0.068941
0.03447
0 Min

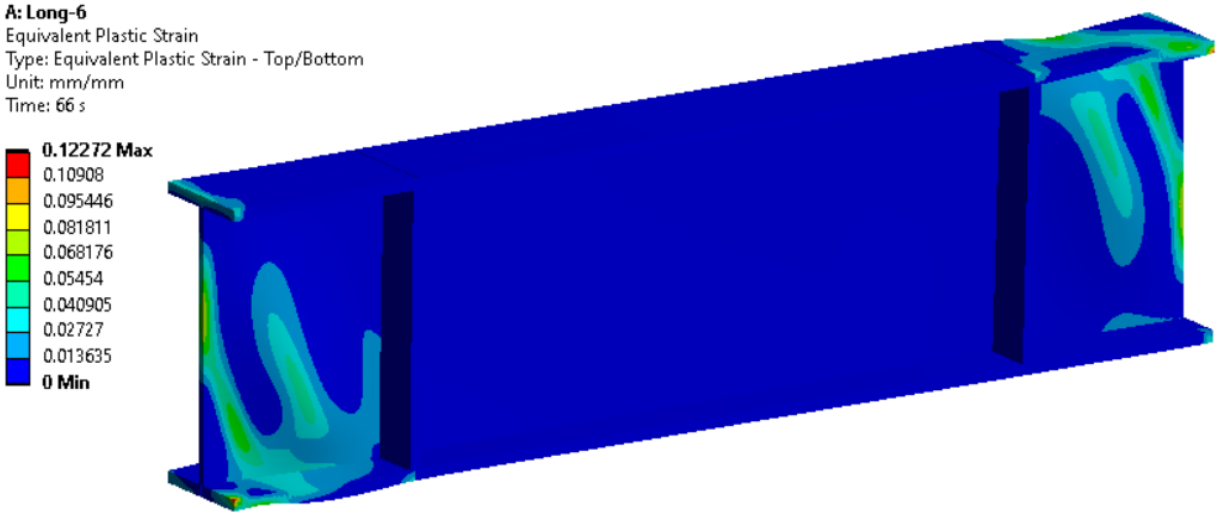
A: Long-6
Equivalent Plastic Strain
Type: Equivalent Plastic Strain - Top/Bottom
Unit: mm/mm
Time: 66 s
0.12272 Max
0.10908
0.095446
0.081811
0.068176
0.05454
0.040905
0.02727
0.013635
0 Min

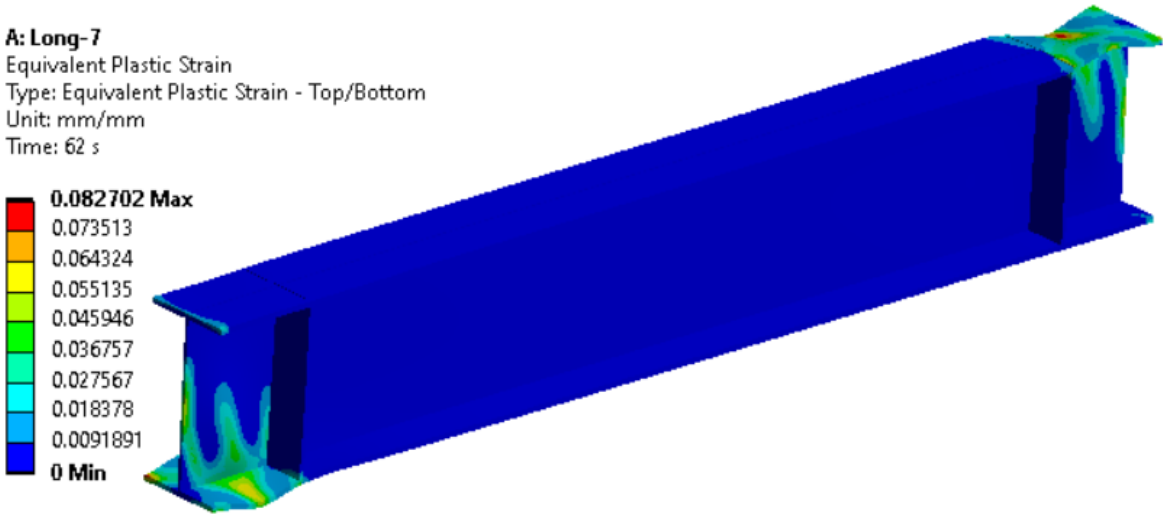
A: Long-7
Equivalent Plastic Strain
Type: Equivalent Plastic Strain - Top/Bottom
Unit: mm/mm
Time: 62 s
0.082702 Max
0.073513
0.064324
0.055135
0.045946
0.036757
0.027567
0.018378
0.0091891
0 Min

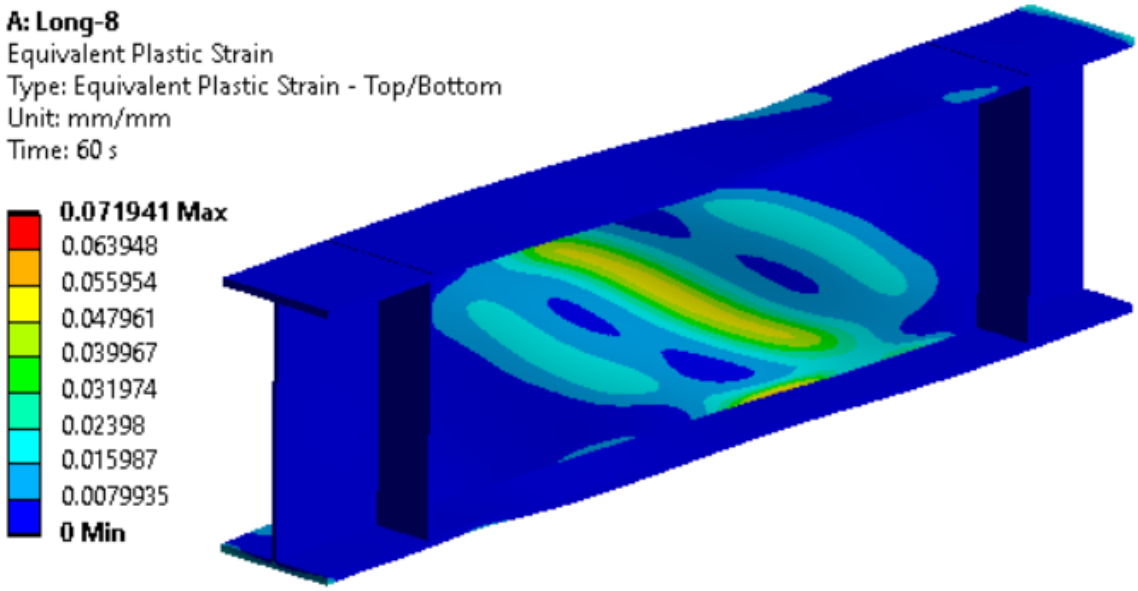
A: Long-8
Equivalent Plastic Strain
Type: Equivalent Plastic Strain - Top/Bottom
Unit: mm/mm
Time: 60 s
0.071941 Max
0.063948
0.055954
0.047961
0.039967
0.031974
0.02398
0.015987
0.0079935
0 Min

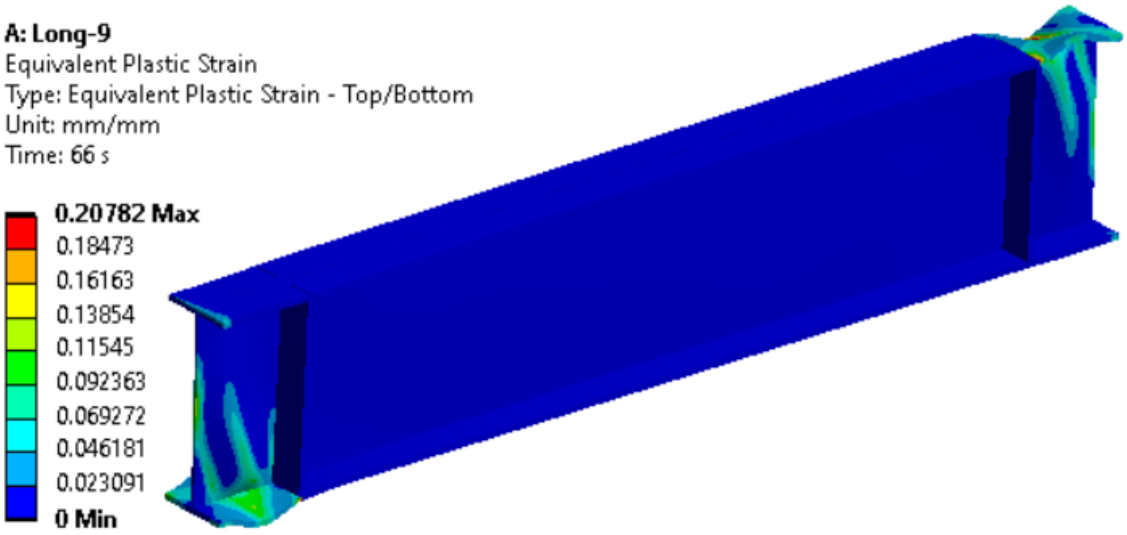
A: Long-9
Equivalent Plastic Strain
Type: Equivalent Plastic Strain - Top/Bottom
Unit: mm/mm
Time: 66 s
0.20782 Max
0.18473
0.16163
0.13854
0.11545
0.092363
0.069272
0.046181
0.023091
0 Min

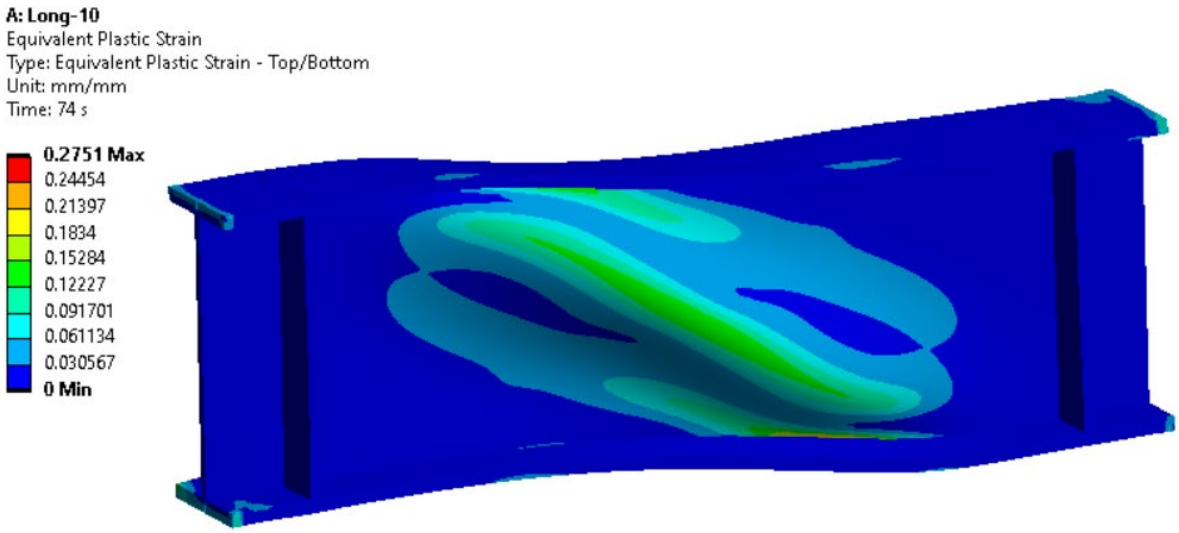
A: Long-10
Equivalent Plastic Strain
Type: Equivalent Plastic Strain - Top/Bottom
Unit: mm/mm
Time: 74 s
0.2751 Max
0.24454
0.21397
0.1834
0.15284
0.12227
0.091701
0.061134
0.030567
0 Min

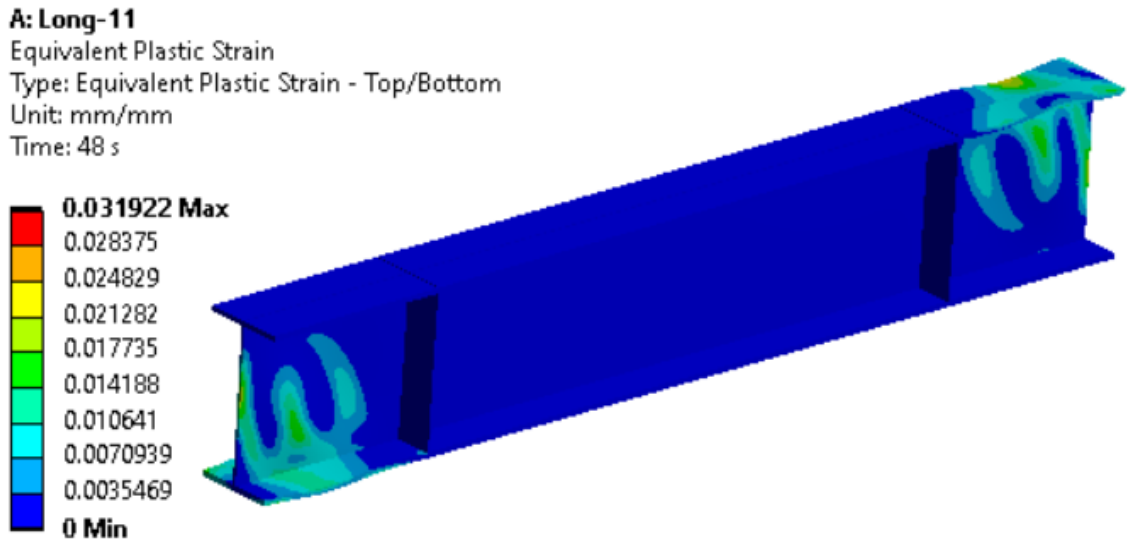
A: Long-11
Equivalent Plastic Strain
Type: Equivalent Plastic Strain - Top/Bottom
Unit: mm/mm
Time: 48 s
0.031922 Max
0.028375
0.024829
0.021282
0.017735
0.014188
0.010641
0.0070939
0.0035469
0 Min

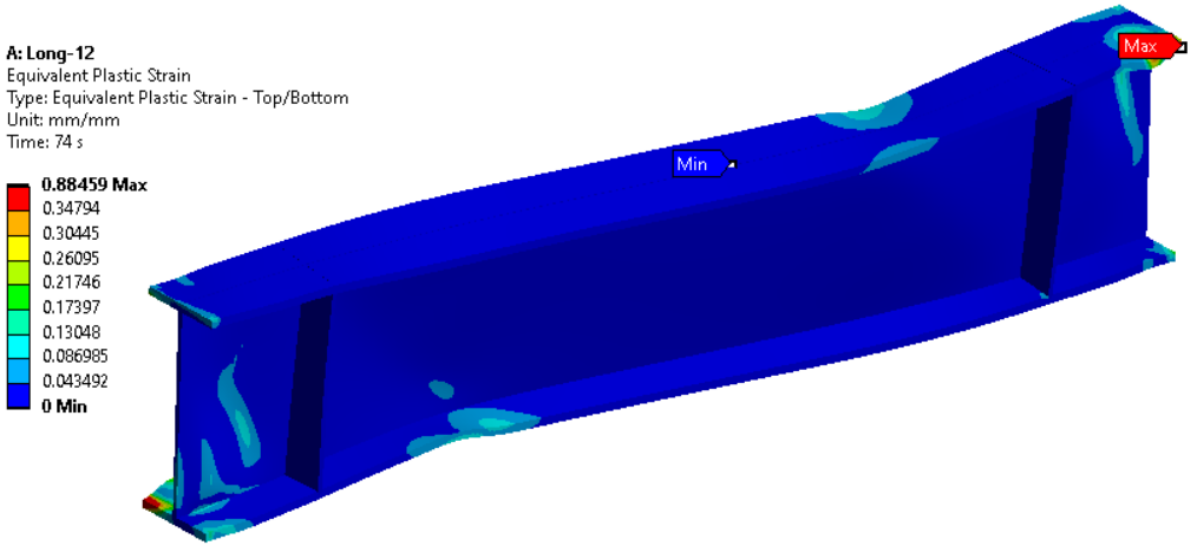
A: Long-12
Equivalent Plastic Strain
Type: Equivalent Plastic Strain - Top/Bottom
Unit: mm/mm
Time: 74 s
0.88459 Max
0.34794
0.30445
0.26095
0.21746
0.17397
0.13048
0.086985
0.043492
0 Min
Max
Min

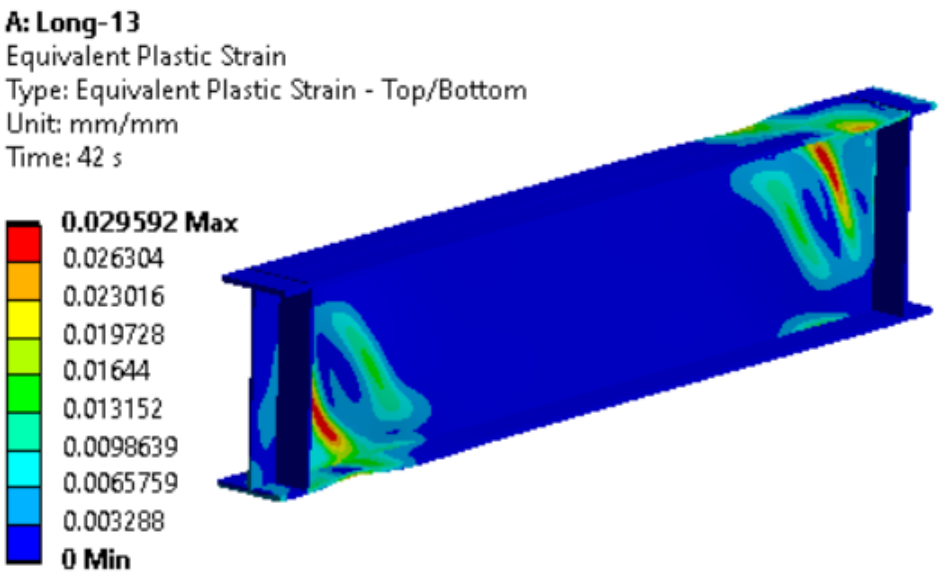
A: Long-13
Equivalent Plastic Strain
Type: Equivalent Plastic Strain - Top/Bottom
Unit: mm/mm
Time: 42 s
0.029592 Max
0.026304
0.023016
0.019728
0.01644
0.013152
0.0098639
0.0065759
0.003288
0 Min


A: Long-14
Equivalent Plastic Strain
Type: Equivalent Plastic Strain - Top/Bottom
Unit: mm/mm
Time: 74 s
Max: 0.42051
Min: 0
0.42051
0.37378
0.32706
0.28034
0.23361
0.18689
0.14017
0.093446
0.046723
0

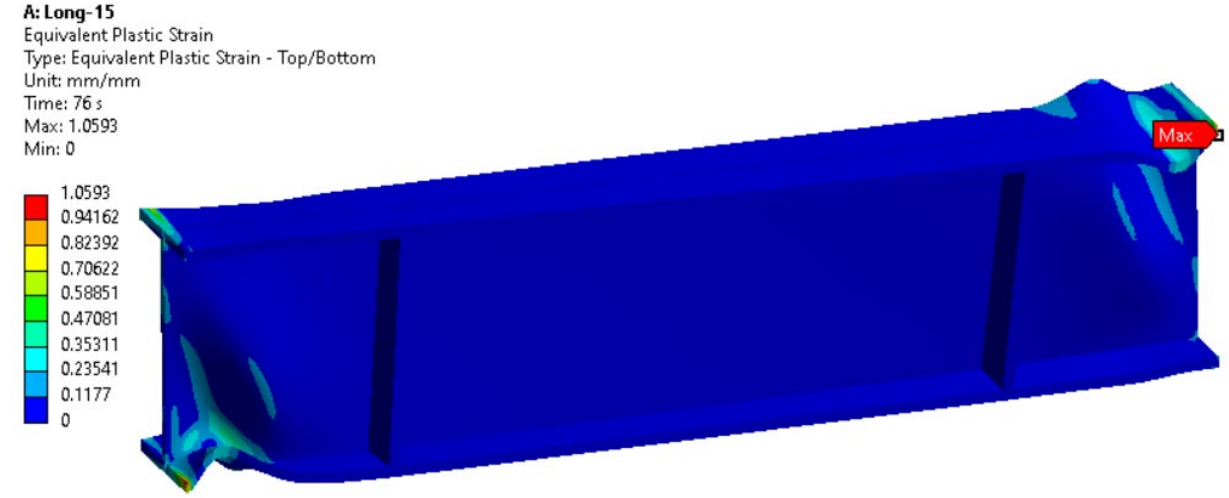
A: Long-15
Equivalent Plastic Strain
Type: Equivalent Plastic Strain - Top/Bottom
Unit: mm/mm
Time: 76 s
Max: 1.0593
Min: 0
1.0593
0.94162
0.82392
0.70622
0.58851
0.47081
0.35311
0.23541
0.1177
0
Max

APPENDIX B SHEAR FORCE-PLASTIC ROTATION GRAPHS

The shear force-plastic rotation hysteresis loops for the analyzed samples is shown in this section.

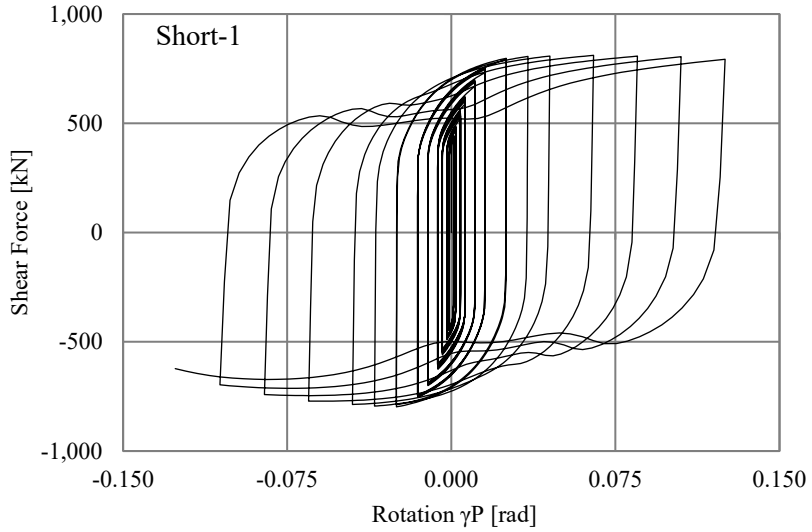

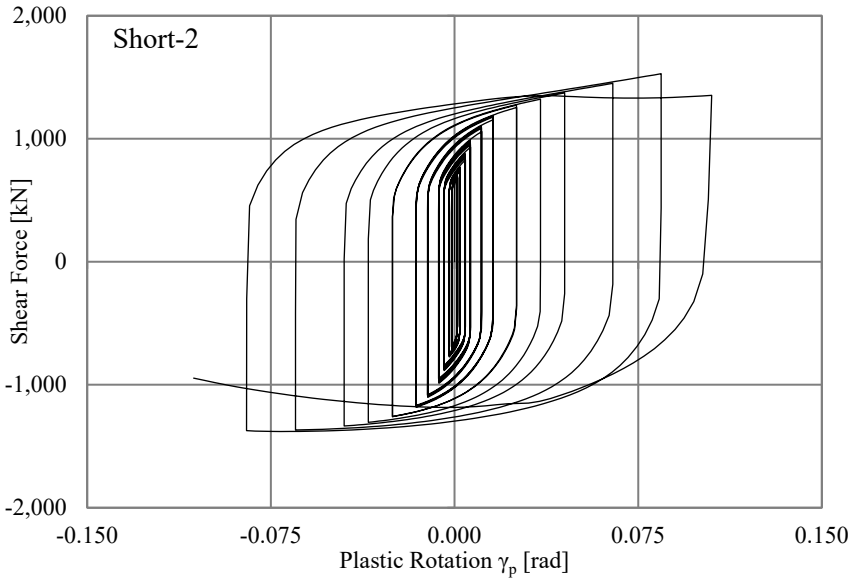

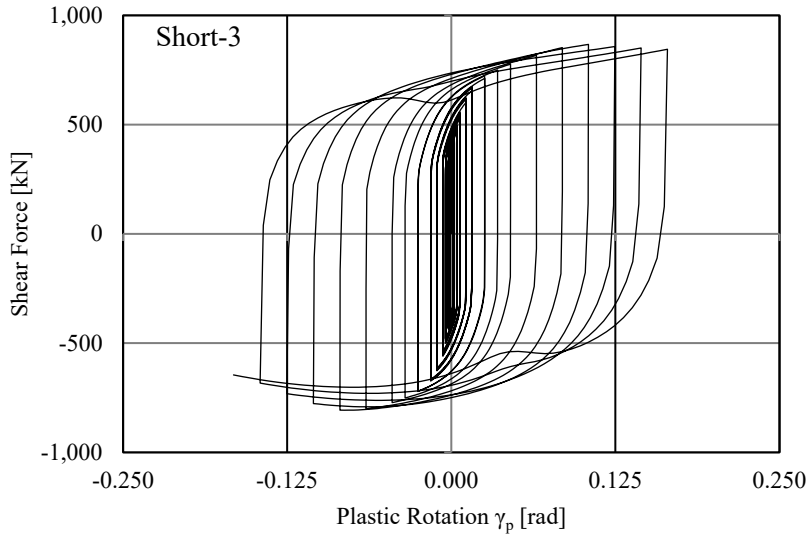
Short-3
1,000
500
0
-500
-1,000
Shear Force [kN]
-0.250
-0.125
0.000
0.125
0.250
Plastic Rotation γp [rad]

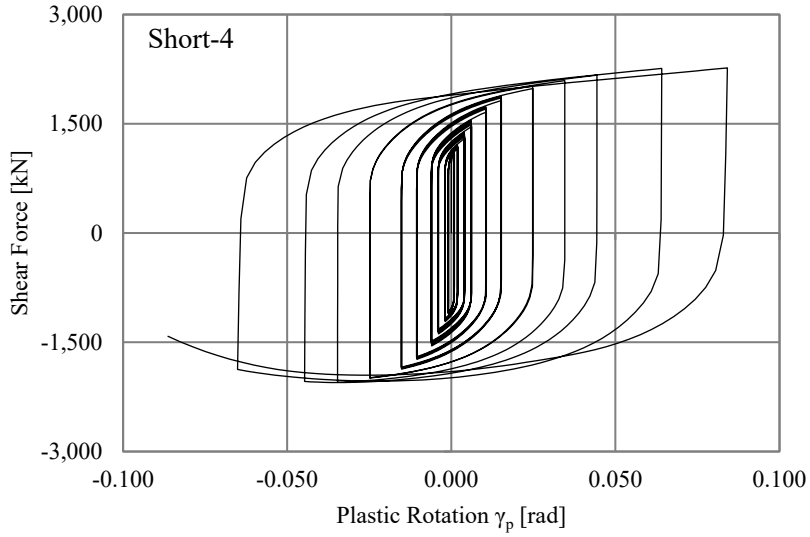
Short-4
3,000
1,500
0
-1,500
-3,000
Shear Force [kN]
-0.100
-0.050
0.000
0.050
0.100
Plastic Rotation γp [rad]

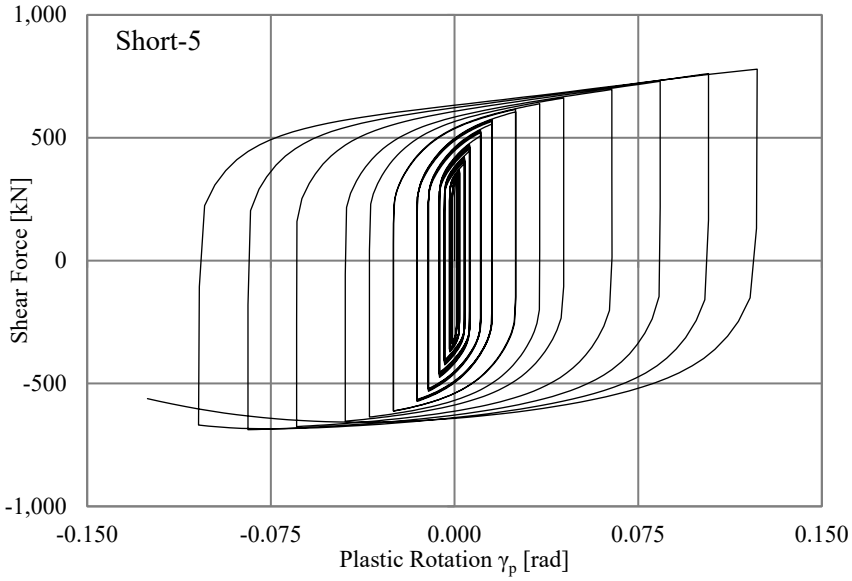
Short-5
1,000
500
0
-500
-1,000
Shear Force [kN]
-0.150
-0.075
0.000
0.075
0.150
Plastic Rotation γp [rad]

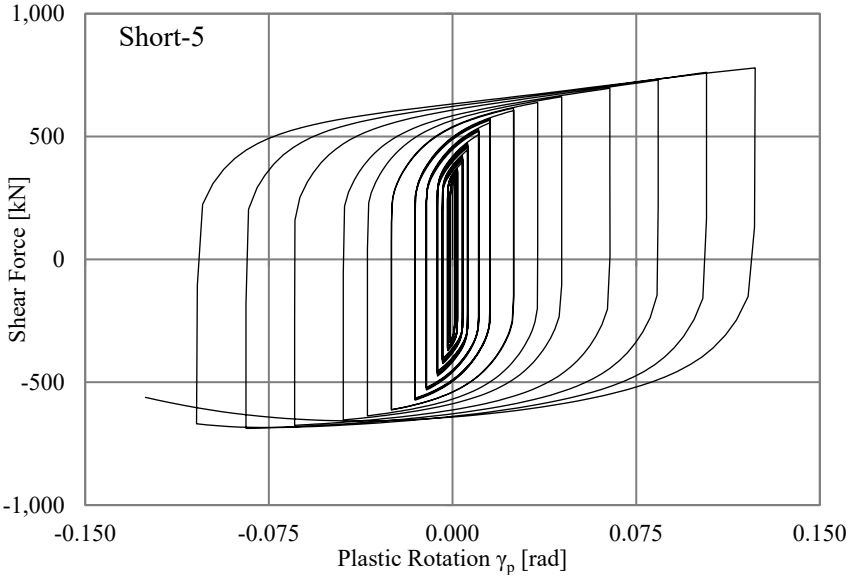
Short-5
1,000
500
0
-500
-1,000
Shear Force [kN]
-0.150
-0.075
0.000
0.075
0.150
Plastic Rotation γp [rad]

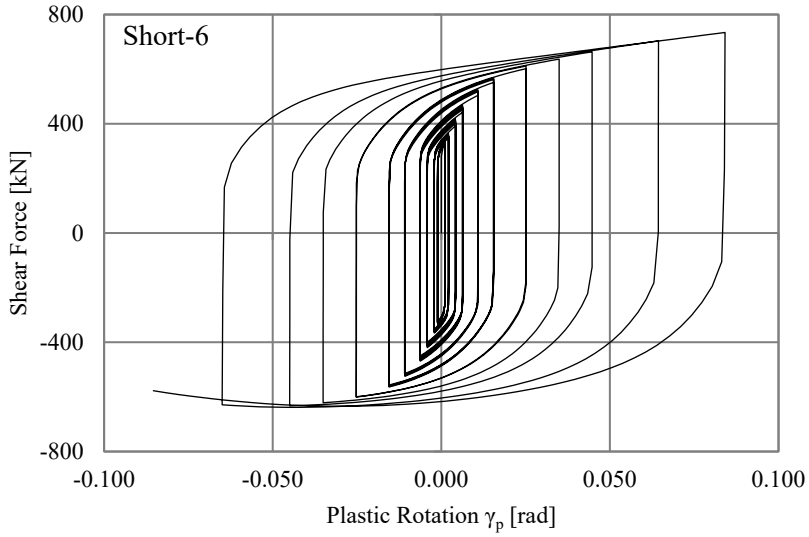
Short-6
800
400
0
-400
-800
Shear Force [kN]
-0.100
-0.050
0.000
0.050
0.100
Plastic Rotation γp [rad]

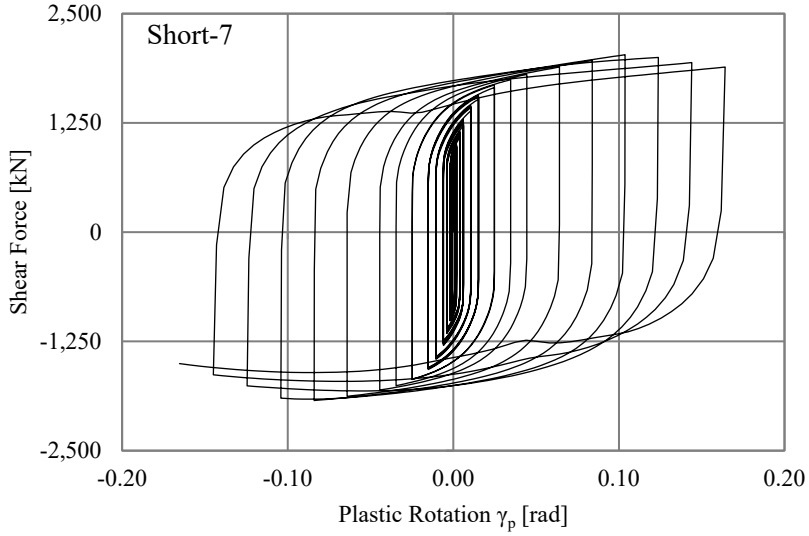
Short-7
2,500
1,250
0
-1,250
-2,500
Shear Force [kN]
-0.20
-0.10
0.00
0.10
0.20
Plastic Rotation γp [rad]

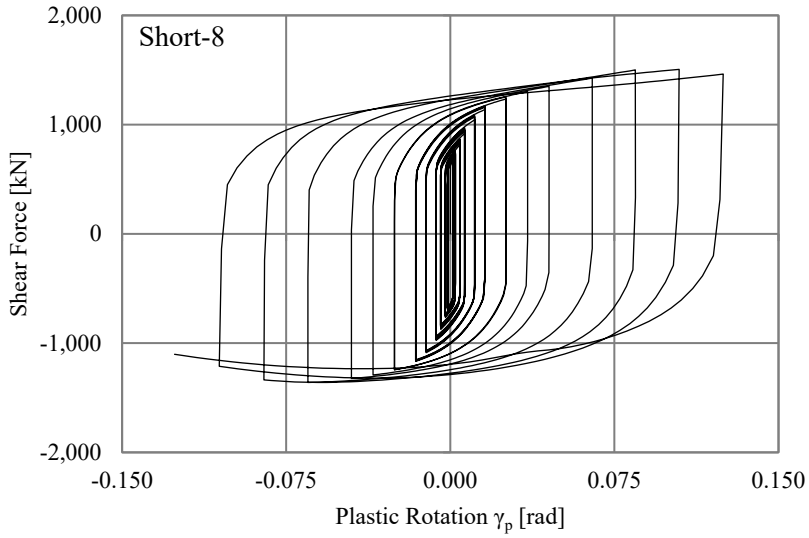
Short-8
2,000
1,000
0
-1,000
-2,000
Shear Force [kN]
-0.150
-0.075
0.000
0.075
0.150
Plastic Rotation γp [rad]

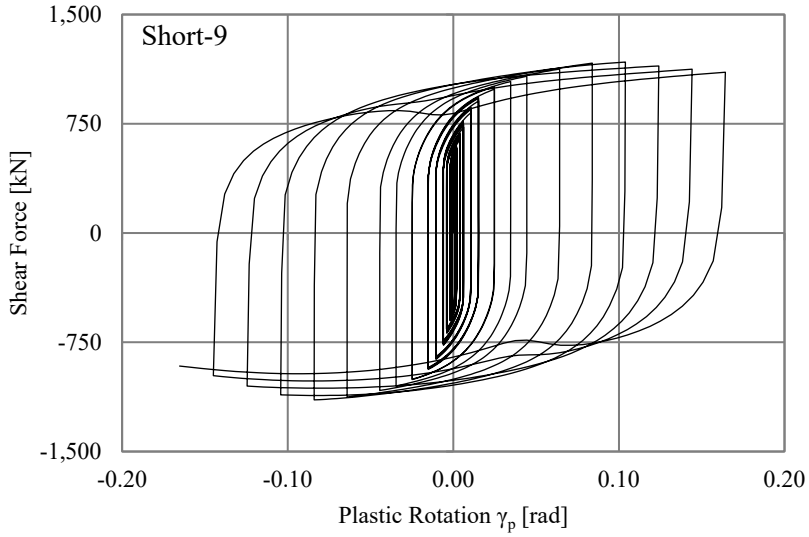
Short-9
1,500
750
0
-750
-1,500
Shear Force [kN]
-0.20
-0.10
0.00
0.10
0.20
Plastic Rotation γp [rad]

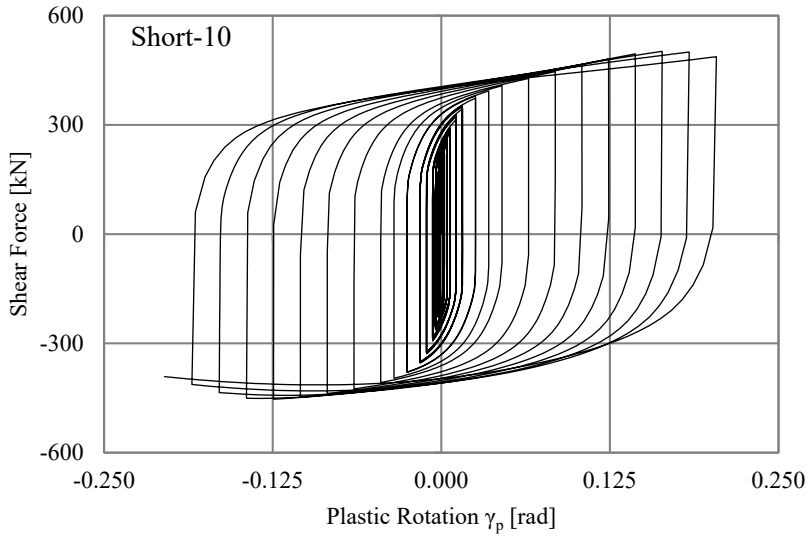
Short-10
600
300
0
-300
-600
Shear Force [kN]
-0.250
-0.125
0.000
0.125
0.250
Plastic Rotation γp [rad]

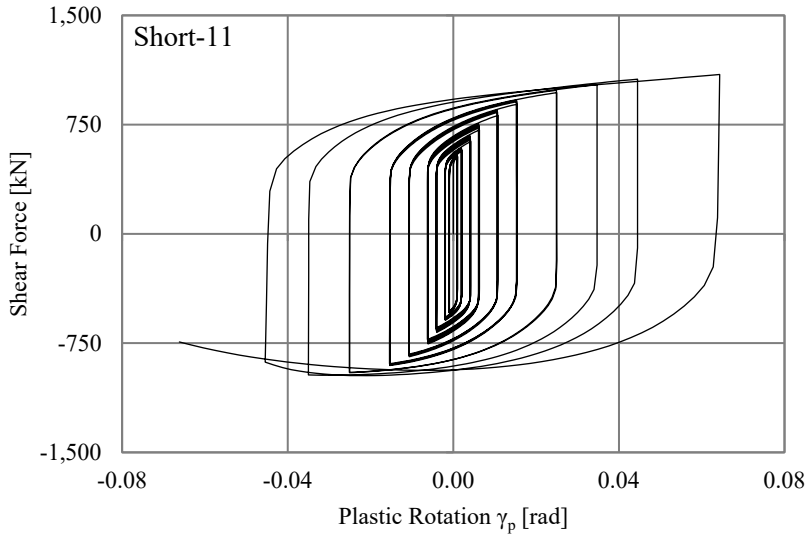
Short-11
1,500
750
0
-750
-1,500
Shear Force [kN]
-0.08
-0.04
0.00
0.04
0.08
Plastic Rotation γp [rad]

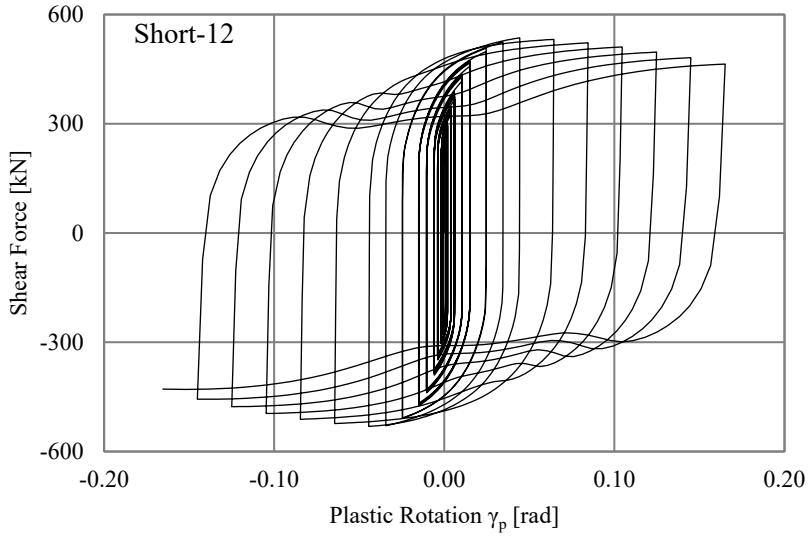
Short-12
600
300
0
-300
-600
Shear Force [kN]
-0.20
-0.10
0.00
0.10
0.20
Plastic Rotation γp [rad]

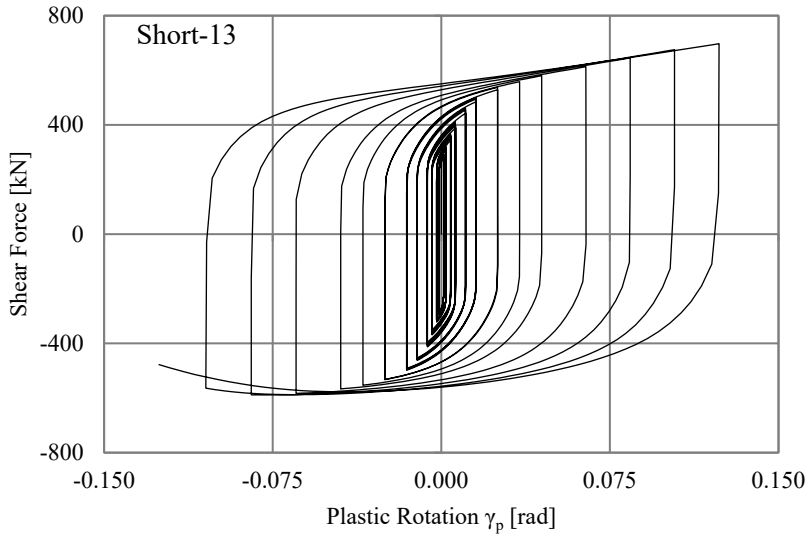
Short-13
800
400
0
-400
-800
Shear Force [kN]
-0.150
-0.075
0.000
0.075
0.150
Plastic Rotation γp [rad]

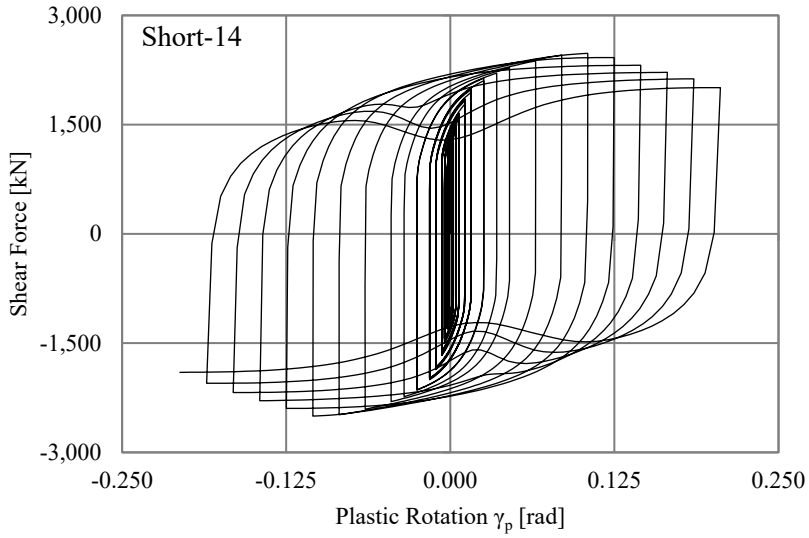
Short-14
3,000
1,500
0
-1,500
-3,000
Shear Force [kN]
-0.250
-0.125
0.000
0.125
0.250
Plastic Rotation γp [rad]

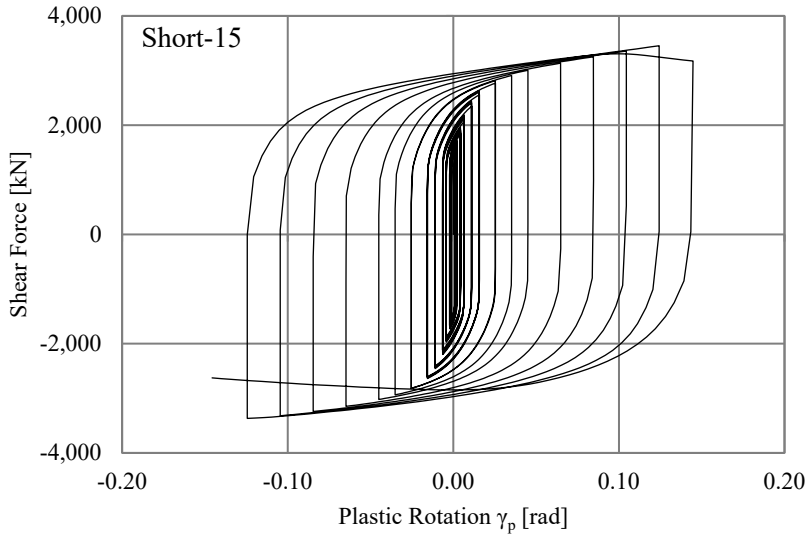
Short-15
4,000
2,000
0
-2,000
-4,000
Shear Force [kN]
-0.20
-0.10
0.00
0.10
0.20
Plastic Rotation γp [rad]

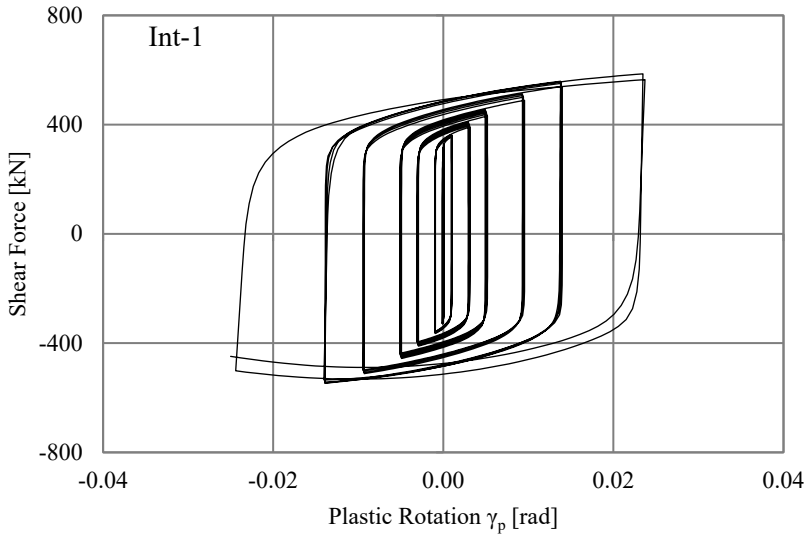
Int-1
800
400
0
-400
-800
Shear Force [kN]
-0.04
-0.02
0.00
0.02
0.04
Plastic Rotation γp [rad]

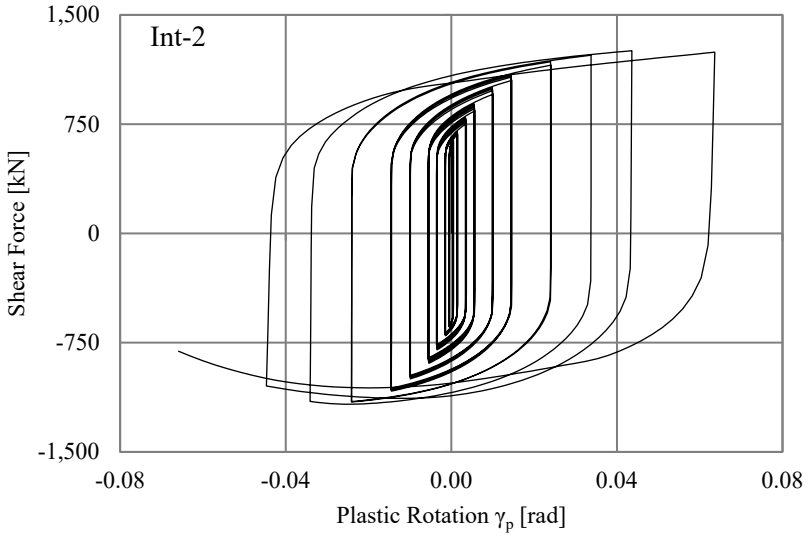
Int-2
1,500
750
0
-750
-1,500
Shear Force [kN]
-0.08
-0.04
0.00
0.04
0.08
Plastic Rotation γp [rad]

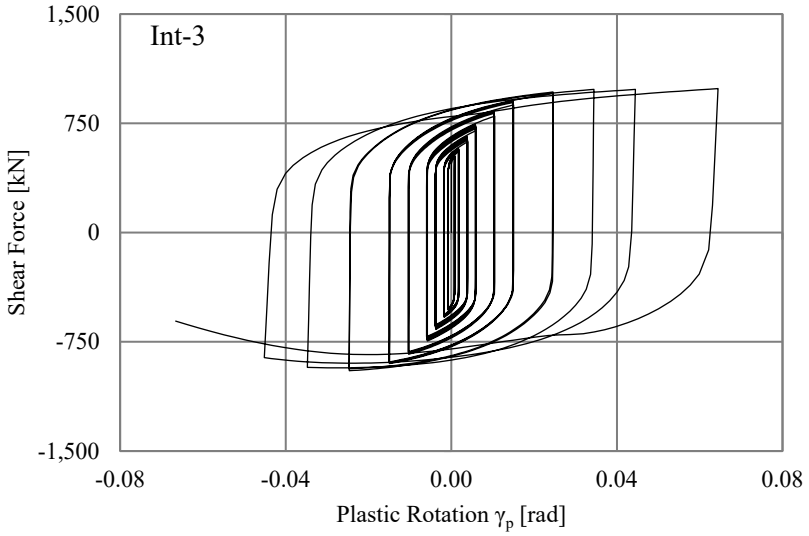
Int-3
1,500
750
0
-750
-1,500
Shear Force [kN]
-0.08
-0.04
0.00
0.04
0.08
Plastic Rotation γp [rad]

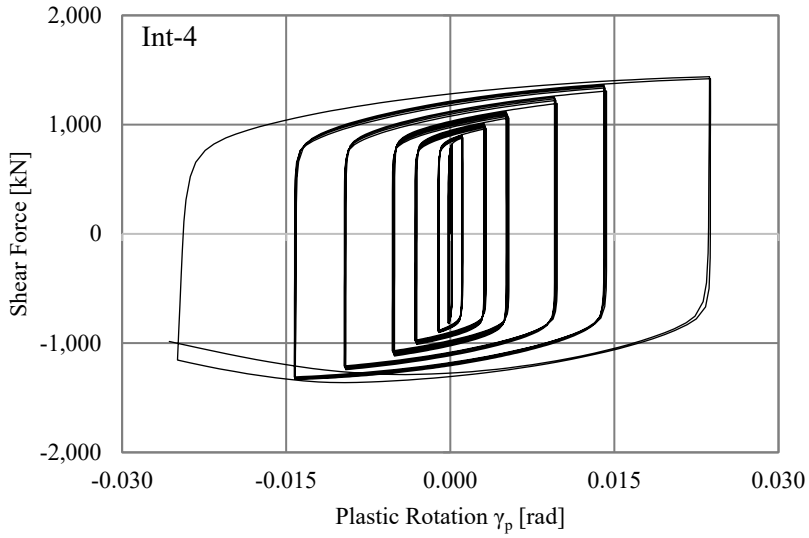
Int-4
2,000
1,000
0
-1,000
-2,000
Shear Force [kN]
-0.030
-0.015
0.000
0.015
0.030
Plastic Rotation γp [rad]

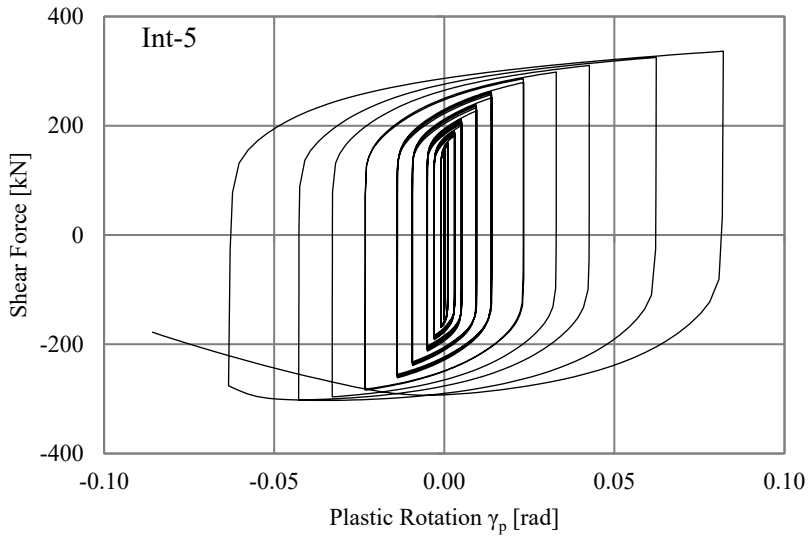
Int-5
400
200
0
-200
-400
Shear Force [kN]
-0.10
-0.05
0.00
0.05
0.10
Plastic Rotation γp [rad]

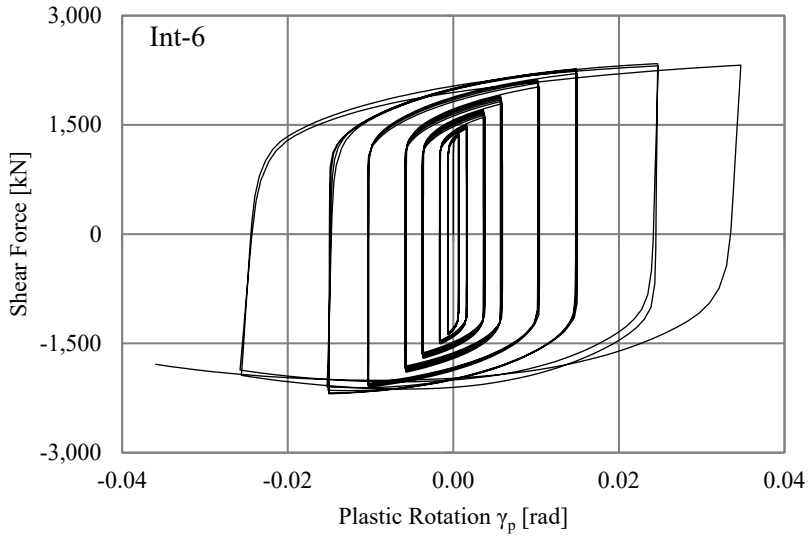
Int-6
3,000
1,500
0
-1,500
-3,000
Shear Force [kN]
-0.04
-0.02
0.00
0.02
0.04
Plastic Rotation γp [rad]

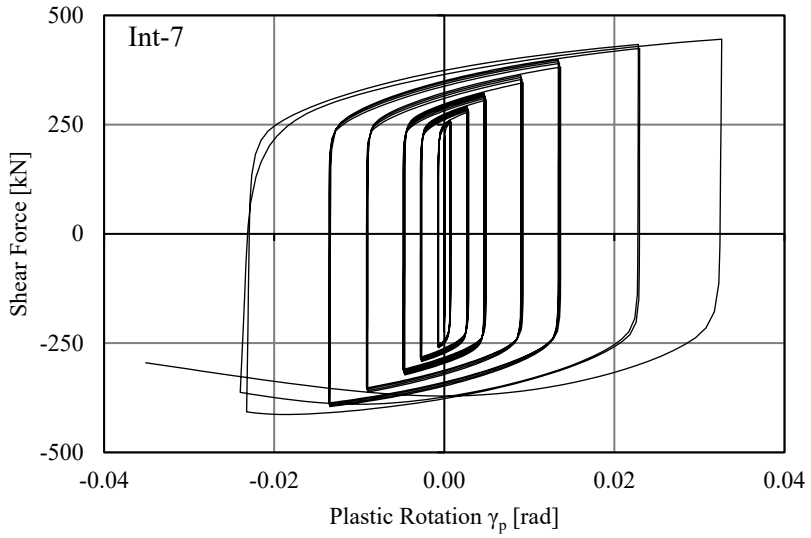
Int-7
500
250
0
-250
-500
Shear Force [kN]
-0.04
-0.02
0.00
0.02
0.04
Plastic Rotation γ_p [rad]

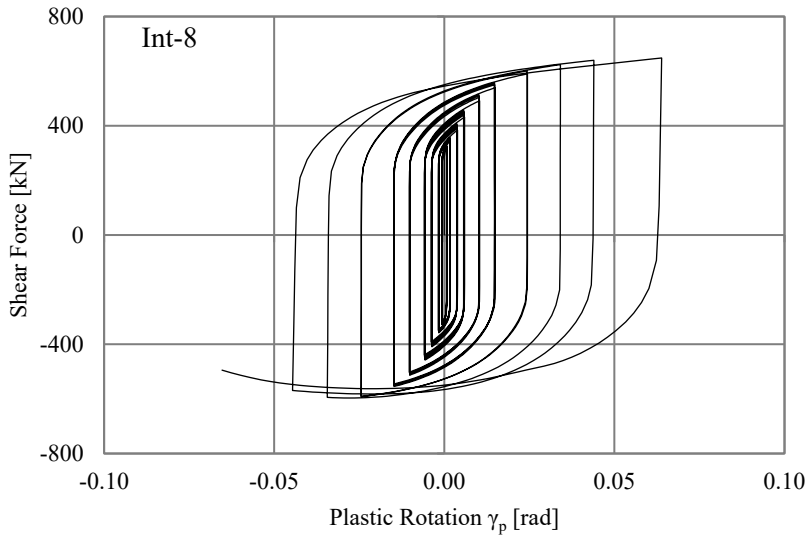
Int-8
800
400
0
-400
-800
Shear Force [kN]
-0.10
-0.05
0.00
0.05
0.10
Plastic Rotation γ_p [rad]

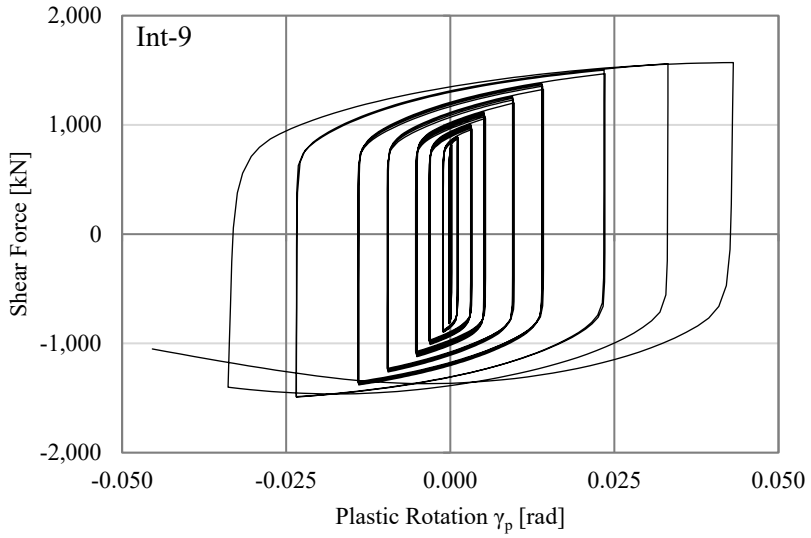
Int-9
2,000
1,000
0
-1,000
-2,000
Shear Force [kN]
-0.050
-0.025
0.000
0.025
0.050
Plastic Rotation γ_p [rad]

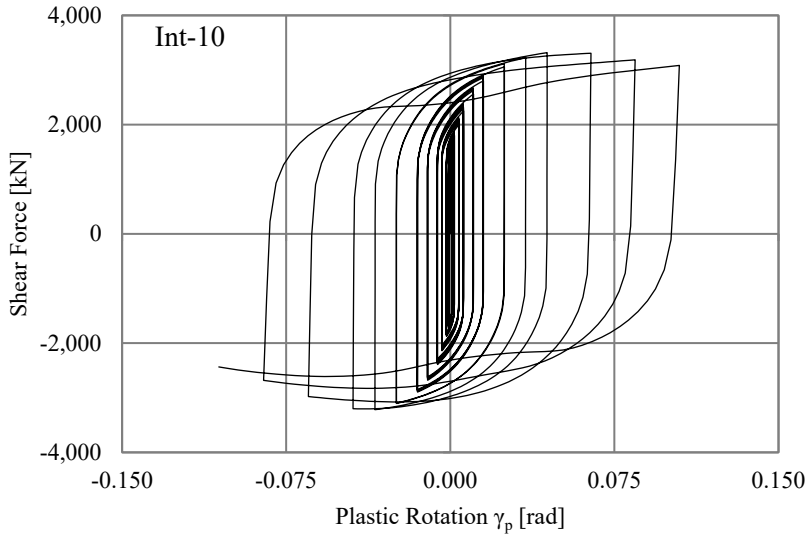
Int-10
4,000
2,000
0
-2,000
-4,000
Shear Force [kN]
-0.150
-0.075
0.000
0.075
0.150
Plastic Rotation γ_p [rad]

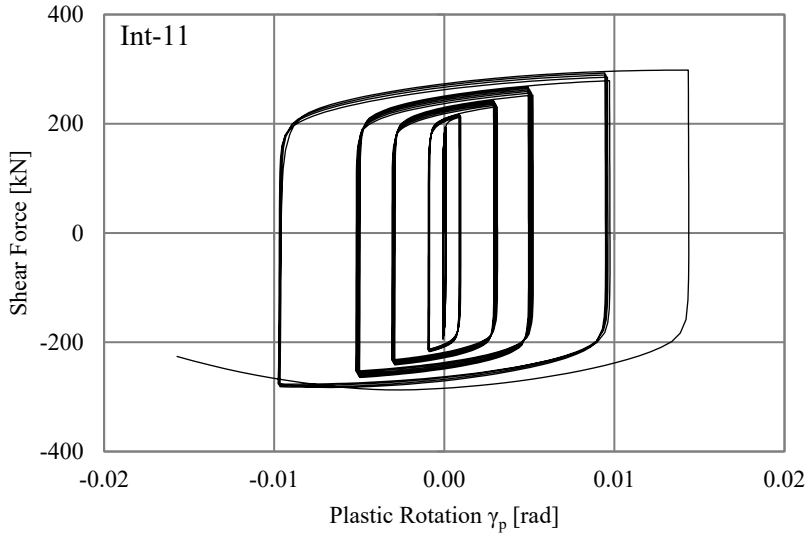
Int-11
400
200
0
-200
-400
Shear Force [kN]
-0.02
-0.01
0.00
0.01
0.02
Plastic Rotation γ_p [rad]

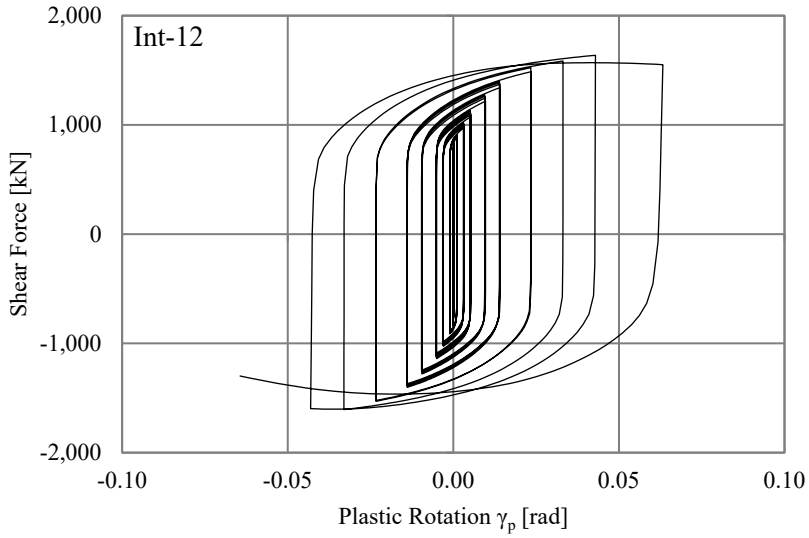
Int-12
2,000
1,000
0
-1,000
-2,000
Shear Force [kN]
-0.10
-0.05
0.00
0.05
0.10
Plastic Rotation γ_p [rad]

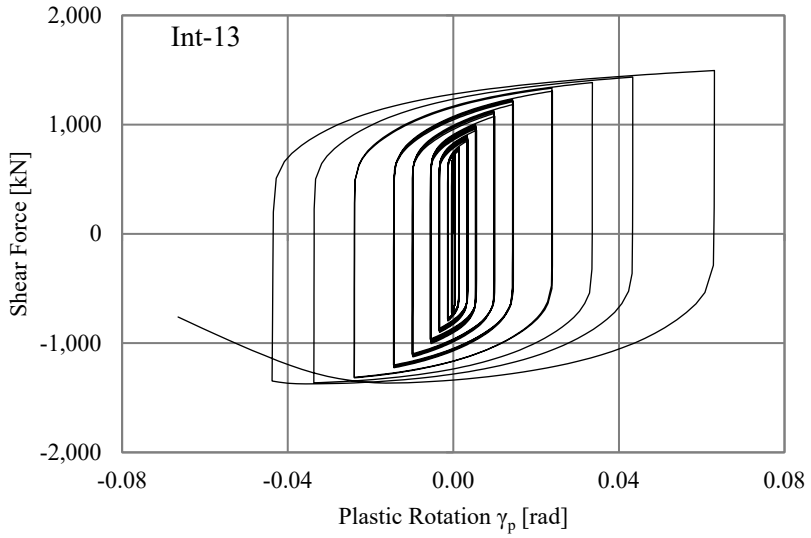
Int-13
2,000
1,000
0
-1,000
-2,000
Shear Force [kN]
-0.08
-0.04
0.00
0.04
0.08
Plastic Rotation γp [rad]

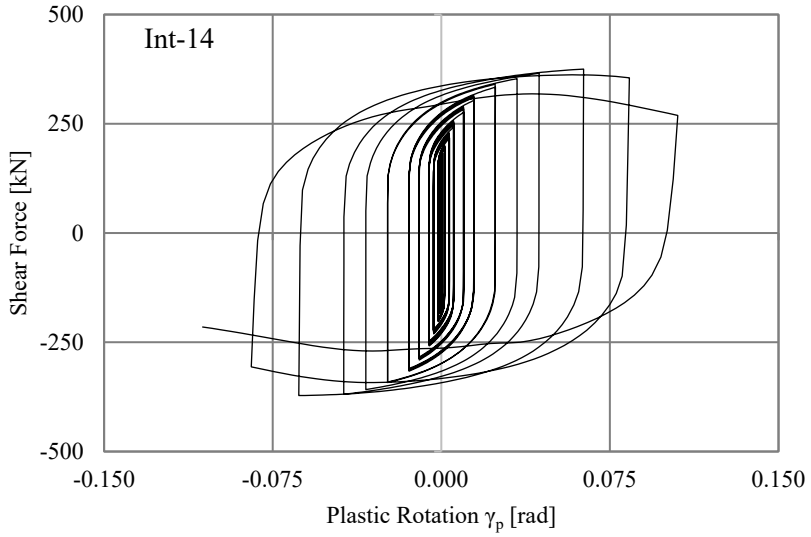
Int-14
500
250
0
-250
-500
Shear Force [kN]
-0.150
-0.075
0.000
0.075
0.150
Plastic Rotation γp [rad]

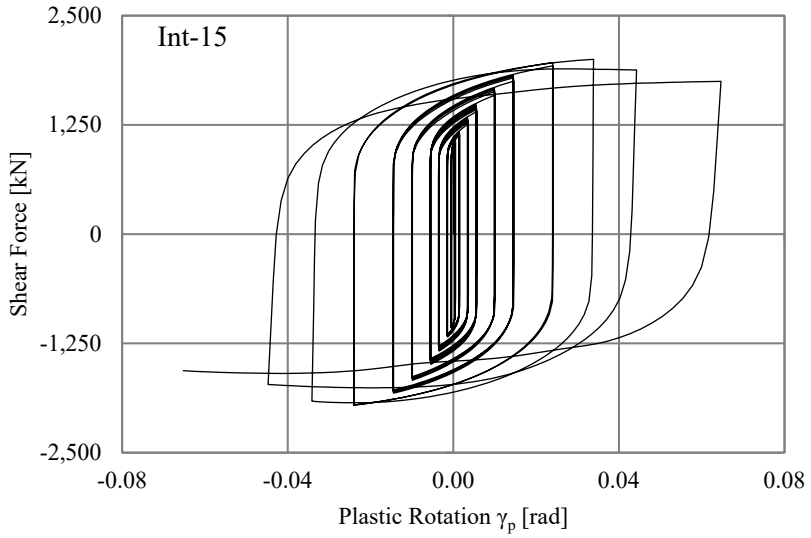
Int-15
2,500
1,250
0
-1,250
-2,500
Shear Force [kN]
-0.08
-0.04
0.00
0.04
0.08
Plastic Rotation γp [rad]

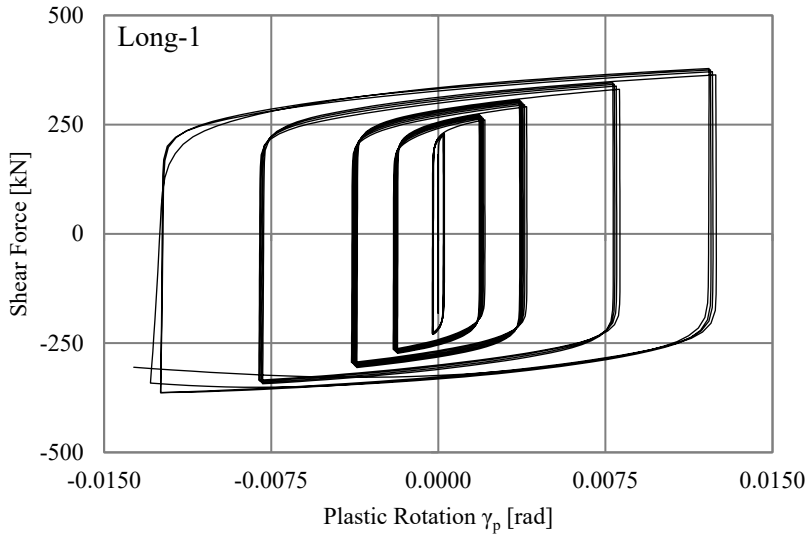
Long-1
500
250
0
-250
-500
Shear Force [kN]
-0.0150
-0.0075
0.0000
0.0075
0.0150
Plastic Rotation γ_p [rad]

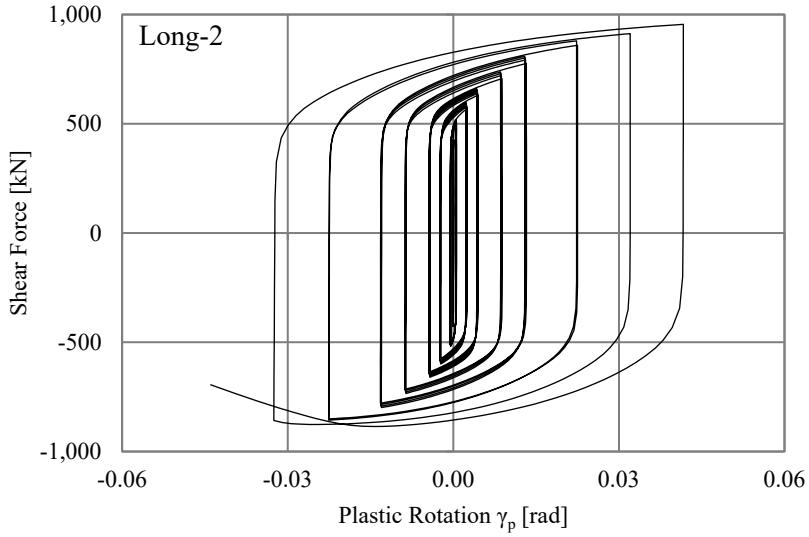
Long-2
1,000
500
0
-500
-1,000
Shear Force [kN]
-0.06
-0.03
0.00
0.03
0.06
Plastic Rotation γ_p [rad]

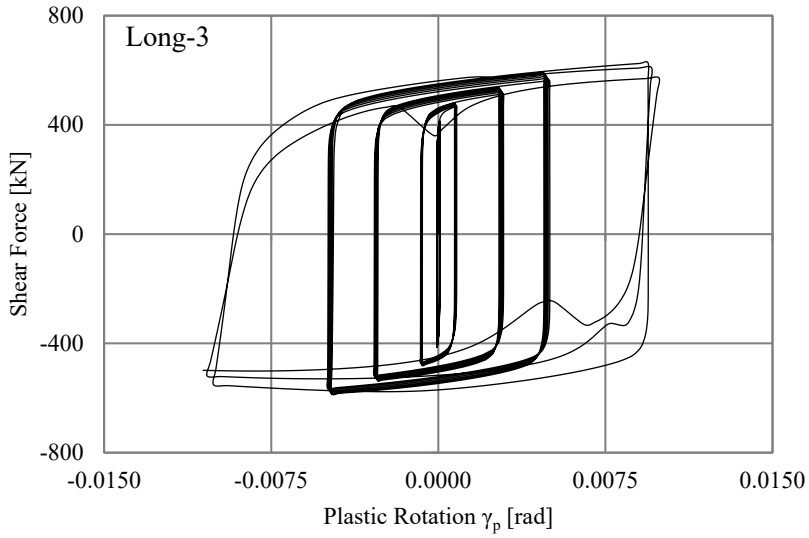
Long-3
800
400
0
-400
-800
Shear Force [kN]
-0.0150
-0.0075
0.0000
0.0075
0.0150
Plastic Rotation γ_p [rad]

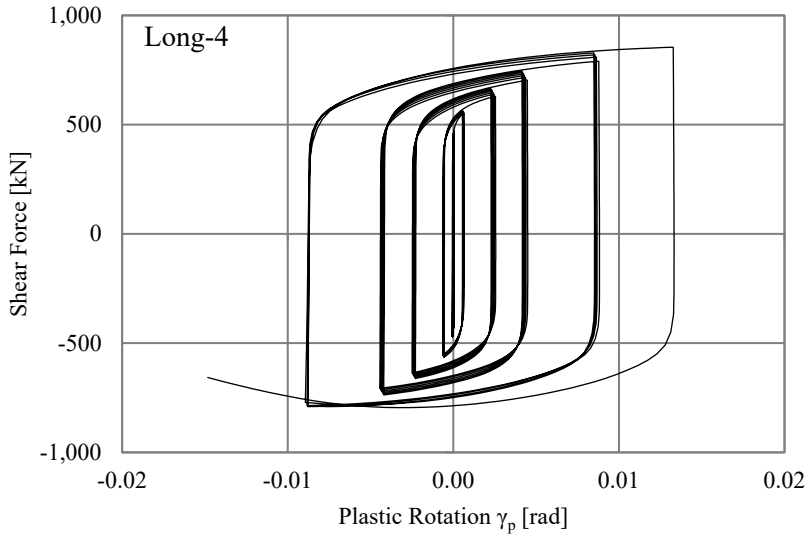
Long-4
1,000
500
0
-500
-1,000
Shear Force [kN]
-0.02
-0.01
0.00
0.01
0.02
Plastic Rotation γp [rad]

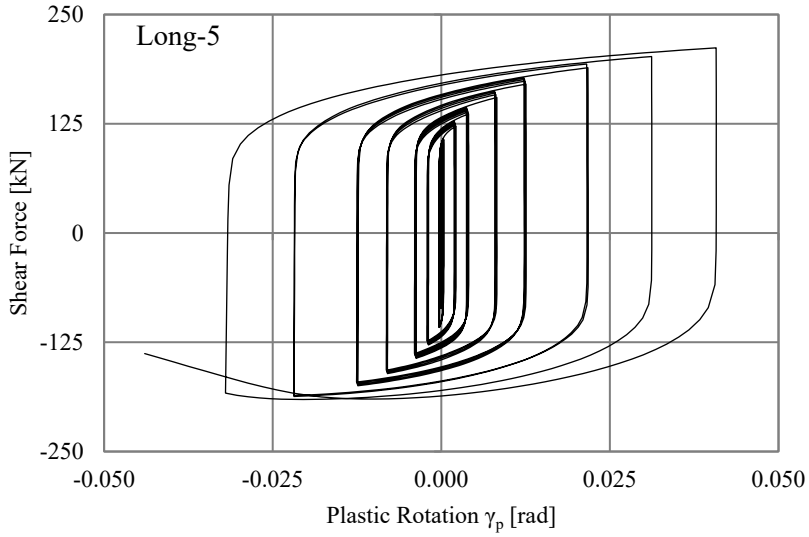
Long-5
250
125
0
-125
-250
Shear Force [kN]
-0.050
-0.025
0.000
0.025
0.050
Plastic Rotation γp [rad]

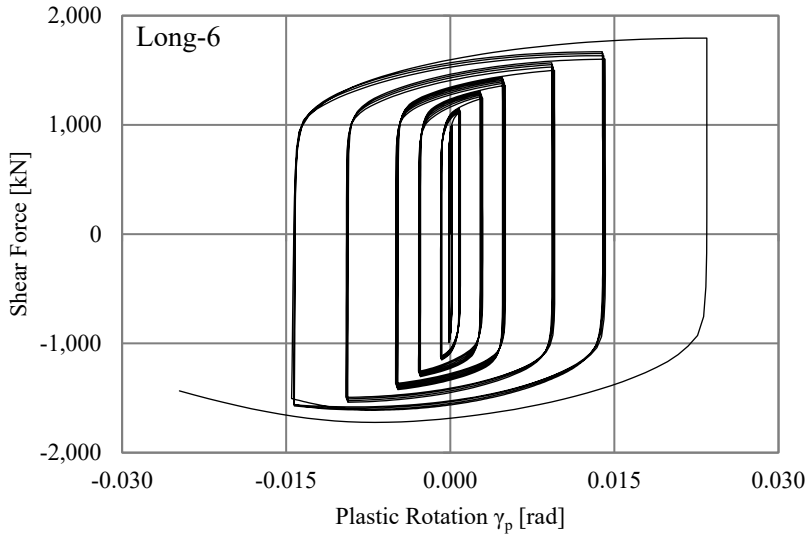
Long-6
2,000
1,000
0
-1,000
-2,000
Shear Force [kN]
-0.030
-0.015
0.000
0.015
0.030
Plastic Rotation γp [rad]

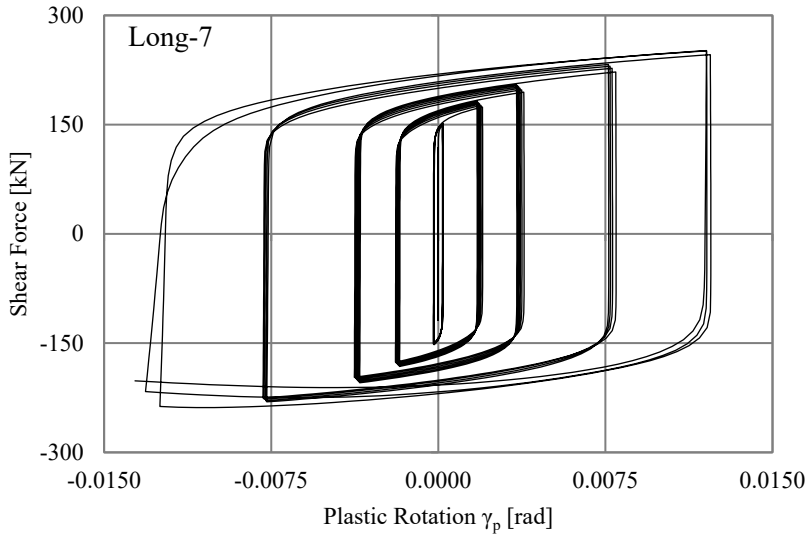
Long-7
300
150
0
-150
-300
Shear Force [kN]
-0.0150
-0.0075
0.0000
0.0075
0.0150
Plastic Rotation γp [rad]

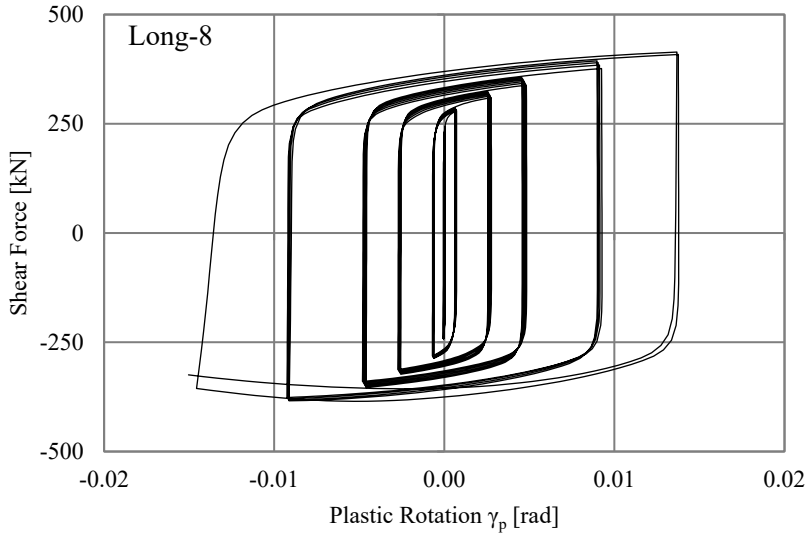
Long-8
500
250
0
-250
-500
Shear Force [kN]
-0.02
-0.01
0.00
0.01
0.02
Plastic Rotation γp [rad]

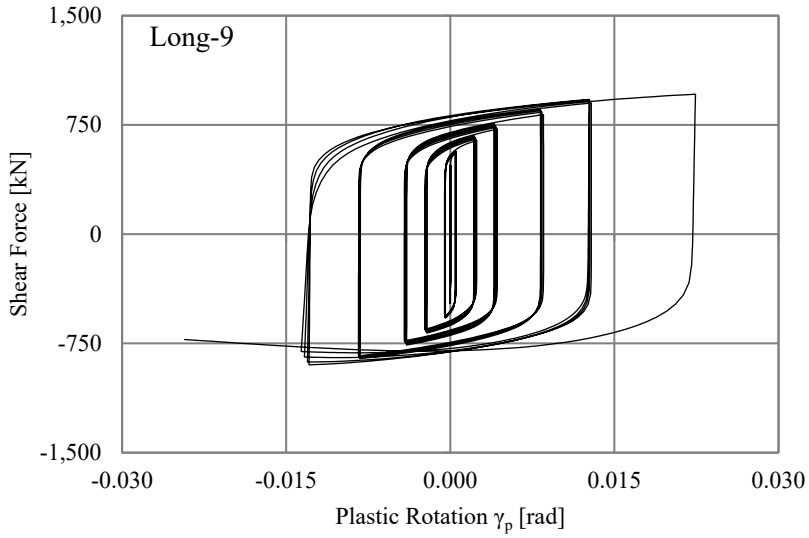
Long-9
1,500
750
0
-750
-1,500
Shear Force [kN]
-0.030
-0.015
0.000
0.015
0.030
Plastic Rotation γp [rad]

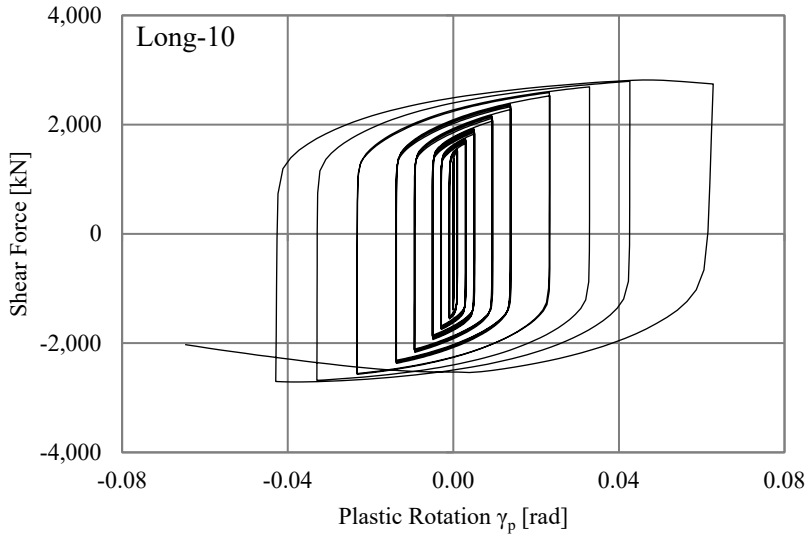
Long-10
4,000
2,000
0
-2,000
-4,000
Shear Force [kN]
-0.08
-0.04
0.00
0.04
0.08
Plastic Rotation γp [rad]

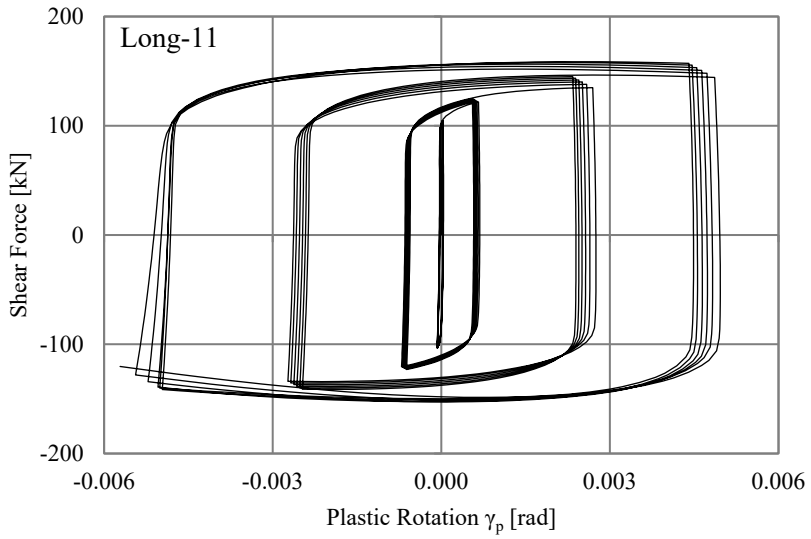
Long-11
200
100
0
-100
-200
Shear Force [kN]
-0.006
-0.003
0.000
0.003
0.006
Plastic Rotation γp [rad]

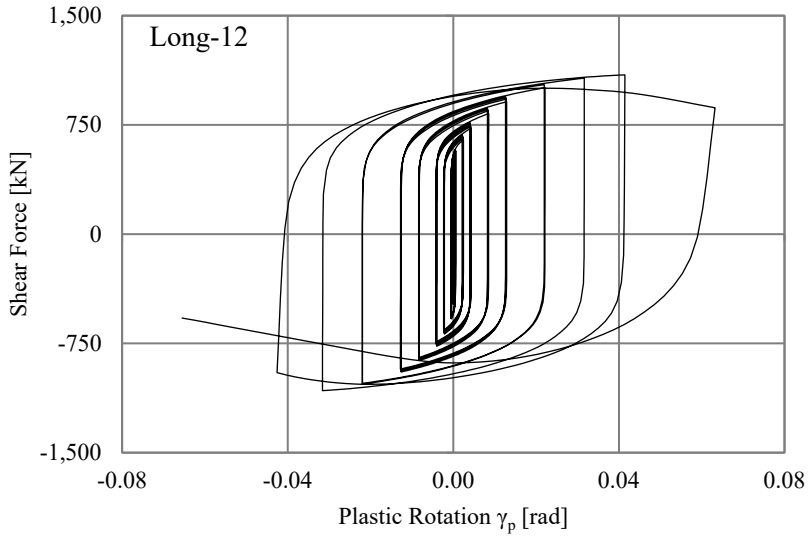
Long-12
1,500
750
0
-750
-1,500
Shear Force [kN]
-0.08
-0.04
0.00
0.04
0.08
Plastic Rotation γp [rad]

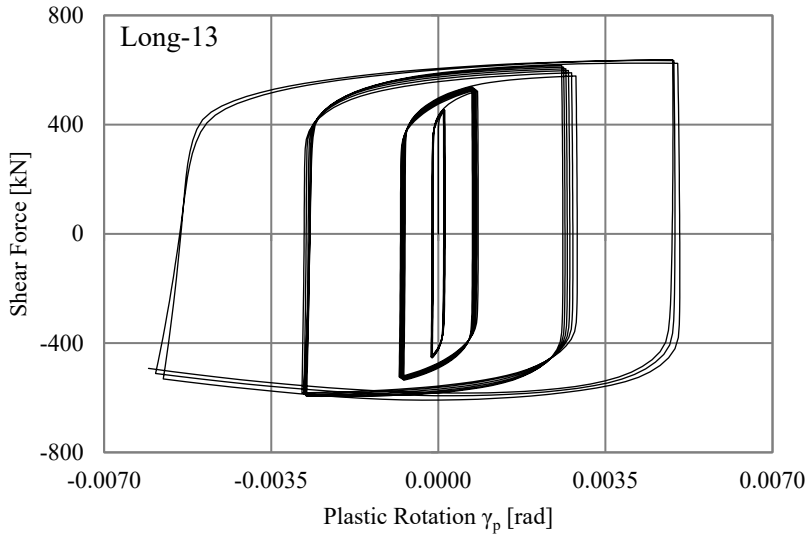
Long-13
800
400
0
-400
-800
Shear Force [kN]
-0.0070
-0.0035
0.0000
0.0035
0.0070
Plastic Rotation γp [rad]

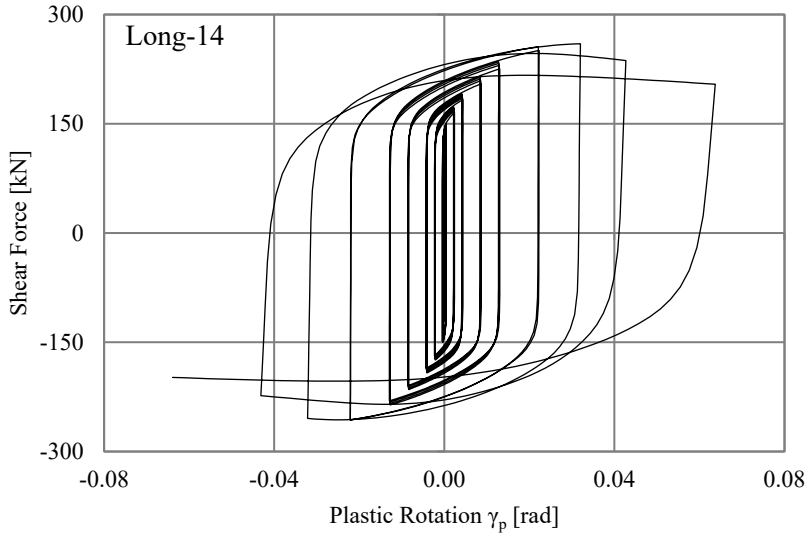
Long-14
300
150
0
-150
-300
Shear Force [kN]
-0.08
-0.04
0.00
0.04
0.08
Plastic Rotation γp [rad]

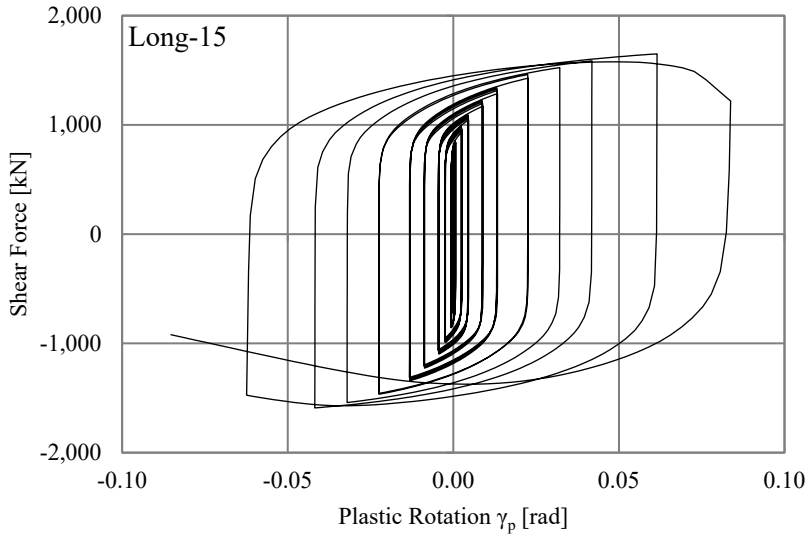
Long-15
2,000
1,000
0
-1,000
-2,000
Shear Force [kN]
-0.10
-0.05
0.00
0.05
0.10
Plastic Rotation γp [rad]